

AD-A054 152

HERCULES INC WILMINGTON DEL SYSTEMS GROUP

F/G 21/8.2

STUDY OF STRUCTURAL DAMPING IN SOLID PROPELLANT ROCKET MOTORS U--ETC(U)

DEC 77 F R JESEN

F04611-76-C-0039

UNCLASSIFIED

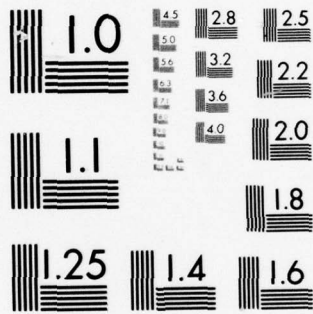
AFRPL-TR-77-84

NL

1 OF 2

AD  
A064152





MICROCOPY RESOLUTION TEST CHART  
NATIONAL BUREAU OF STANDARDS-1963-A



AFRPL-TR-77-84

2

FOR FURTHER TRANSMISSION

AD A 054152

**STUDY OF STRUCTURAL DAMPING IN SOLID PROPELLANT  
ROCKET MOTORS UNDERGOING UNSTABLE  
ACOUSTIC OSCILLATIONS**

F. R. JENSEN  
HERCULES INCORPORATED  
SYSTEMS GROUP  
WILMINGTON, DELAWARE 19899

DECEMBER 1977  
FINAL REPORT

APPROVED FOR PUBLIC RELEASE  
DISTRIBUTION UNLIMITED

Prepared for  
AIR FORCE ROCKET PROPULSION LABORATORY  
DIRECTOR OF SCIENCE AND TECHNOLOGY  
AIR FORCE SYSTEMS COMMAND  
EDWARDS A. F. B., CALIFORNIA 93523

AD No. 1  
DDC FILE COPY

DDC  
RECEIVED  
MAY 16 1978  
D

## NOTICES

When U. S. Government drawings, specifications, or other data are used for any purpose other than a definitely related Government procurement operation, the Government thereby incurs no responsibility nor any obligation whatsoever, and the fact that the Government may have formulated, furnished, or in any way supplied the said drawings, specifications, or other data, is not to be regarded by implication or otherwise, or in any manner licensing the holder or any other person or corporation, or conveying any rights or permission to manufacture, use, or sell any patented invention that may in any way be related thereto.

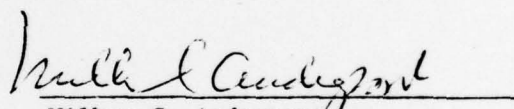
## APPROVAL STATEMENT

This report was submitted by Hercules Incorporated, P.O. Box 98, Magna, Utah 84044, under contract F04611-76-C-0039, job order 573010 BT, with the Air Force Rocket Propulsion Laboratory, Edwards AFB, Ca 93523.

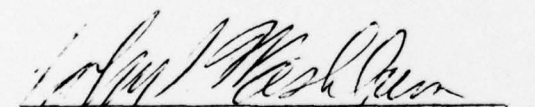
The report has been reviewed by the Information Office/DOZ and is releasable to the National Technical Information Service (NTIS). At NTIS, the report will be available to the general public, including foreign nations.

This technical report has been reviewed and is approved for publication.

  
J. J. Dunn, Capt., USAF  
Project Manager

  
Wilbur C. Andrepond  
Chief, Combustion Section

For The Commander

  
John I. Washburn, Major, USAF  
Chief, Propulsion Analysis Division

UNCLASSIFIED

Final Repts Apr 76 - Jul 77

SECURITY CLASSIFICATION OF THIS PAGE (When Data Entered)

19 REPORT DOCUMENTATION PAGE		READ INSTRUCTIONS BEFORE COMPLETING FORM
1. REPORT NUMBER AFRPL-TR-77-84 ✓	2. GOVT ACCESSION NO. --	3. RECIPIENT'S CATALOG NUMBER --
4. TITLE (and Subtitle) STUDY OF STRUCTURAL DAMPING IN SOLID PROPELLANT ROCKET MOTORS UNDERGOING UNSTABLE ACOUSTIC OSCILLATIONS.		5. TYPE OF REPORT & PERIOD COVERED Final Report 4/76 to 7/77
		6. PERFORMING ORG. REPORT NUMBER
7. AUTHOR(s) F. R. Jensen	8. CONTRACT OR GRANT NUMBER(s) F04611-76-C-0039 New	
9. PERFORMING ORGANIZATION NAME AND ADDRESS Hercules Incorporated Systems Group Wilmington, Delaware 19899		10. PROGRAM ELEMENT, PROJECT, TASK AREA & WORK UNIT NUMBERS 573010BT --
11. CONTROLLING OFFICE NAME AND ADDRESS Air Force Rocket Propulsion Laboratory Edwards Air Force Base, CA 93523		12. REPORT DATE 11 December 1977
		13. NUMBER OF PAGES 160 (12) 163p
14. MONITORING AGENCY NAME & ADDRESS (if different from Controlling Office) 16 57301 17 10		15. SECURITY CLASS. (of this report) UNCLASSIFIED
15a. DECLASSIFICATION/DOWNGRADING SCHEDULE		
16. DISTRIBUTION STATEMENT (of this Report) Approved for public release. Distribution unlimited		
17. DISTRIBUTION STATEMENT (of the abstract entered in Block 20, if different from Report) --		
18. SUPPLEMENTARY NOTES --		
19. KEY WORDS (Continue on reverse side if necessary and identify by block number) Structural damping, propellant damping, <u>acoustic oscillations</u> in solid rocket motors, acoustic testing, damping measurements		
20. ABSTRACT (Continue on reverse side if necessary and identify by block number) The objective of the program was to establish the role of structural damping in regulating acoustic pressure growth rates in solid-propellant rocket motors and to show the accuracy to which structural damping calcula- tions can be made. The planned approach called for testing to be conducted on subscale rocket motors to provide data for verification of analysis results. Because of various technical problems experienced in the testing task, the program objectives were not achieved. For example, a test		

407 928

JOB



UNCLASSIFIED

SECURITY CLASSIFICATION OF THIS PAGE(When Data Entered)

20. ABSTRACT (Cont)

configuration that yields accurate acoustic natural frequencies and mode shapes was found to be entirely inadequate for damping measurements. This problem, which was ultimately found to be the major problem with the experimental task, was traced to an unwanted acoustic coupling between the driver cavity and the main acoustic cavity in the test model. In spite of the problems, the coverage of the testing task given in this report should be of interest to anyone planning to measure structural dampening of acoustic modes in rocket motors.

An analytical study of the structural damping problem was conducted using finite element models of subscale motors and simple rod-organ pipe models that exhibit the basic structural damping characteristics of interest. A detailed study was conducted using a closed form solution for a rod-organ pipe model. Results from the closed form solution and the finite element solutions show how damping response is related to variations in static pressure level, properties variations, and variations in the ratios of gas-phase to solid-phase uncoupled natural frequencies.

Recommendations are given for further structural damping investigations based on the experience gained in the present program.

ACCESSION for	
DTIC	White Section <input checked="" type="checkbox"/>
DDC	Buff Section <input type="checkbox"/>
UNANNOUNCED	<input type="checkbox"/>
JUSTIFICATION.....	
BY.....	
DISTRIBUTION/AVAILABILITY CODES	
Dist.	AVAIL. and/or SPECIAL
A	

UNCLASSIFIED

SECURITY CLASSIFICATION OF THIS PAGE(When Data Entered)

## PREFACE

This is the final report for the program entitled Study of Structural Damping in Solid Propellant Rocket Motors Undergoing Unstable Acoustic Oscillations, Contract F04611-76-C-0039. The work was accomplished at Hercules Incorporated, Bacchus Works, Magna, Utah. The report is submitted in accordance with data item B005 of the contract. The contract was issued to Hercules by the Air Force Rocket Propulsion Laboratory, Edwards, Ca., 93523. Captain J. J. Donn was the AFRPL project manager for the program.

At Hercules, Mr. L. R. West assisted with the acoustics testing work on this program. Mr. Lanny Myers assisted with the propellant dynamic testing work and Dr. Scott Beckwith provided values of dynamic propellant moduli for use in the NASTRAN analyses. Dr. Dean Wang performed NASTRAN analyses and Mr. Norm Peterson studied a rod-organ pipe model in support of the Structural Damping program. Dr. Merrill Beckstead was a technical consultant and Mr. McKay Anderson was the Technical Program Manager. Dr. F. R. Jensen was the Principal Investigator. Dr. F. E. C. Culick of the California Institute of Technology also consulted on the project.

# CONTENTS

<u>Section</u>		<u>Page</u>
I	INTRODUCTION . . . . .	8
II	APPROACH	
	A. Task I - Experimental Measurement of Structural Damping . . . . .	11
	B. Task II - Structural Damping Analysis Verification . . . . .	12
III	ACOUSTIC TEST SET-UPS AND PROCEDURES	
	A. Rigid-Walled Model . . . . .	13
	B. Instrumentation . . . . .	13
	C. Mode Shape Determination . . . . .	15
	D. Damping Factor ( $\alpha$ ) Measurement . . . . .	15
	E. Lightweight Analog Motors (LAM's) . . . . .	16
IV	ACOUSTIC TEST RESULTS AND DISCUSSION	
	A. Initial Inert Model Experimentation . . . . .	17
	1. Natural Modes and Frequencies . . . . .	17
	2. Damping and Natural Frequency Measurements Under Various Conditions . . . . .	22
	3. Attempt to Model a Cylinder . . . . .	26
	4. Check on Linearity . . . . .	27
	5. Initial Inert Model Baseline Data . . . . .	33
	B. LAM-179 Testing . . . . .	33
	1. Thermal Tests . . . . .	33
	2. Mode Shapes and Natural Frequencies . . . . .	34
	3. Mode Shapes and Frequencies Using Helium Gas . . . . .	34
	4. Damping and Frequency Measurements Using Nitrogen and Helium . . . . .	42
	5. Damping and Frequency in LAM-179 as a Function of Pressure . . . . .	42
	C. LAM-180 Testing . . . . .	44
	D. Additional Inert Model Testing . . . . .	44
	1. Additional Baseline Data . . . . .	44
	2. Investigation of Speaker Coupling . . . . .	47
V	PROPELLANT DYNAMIC PROPERTIES DETERMINATION	
	A. Dynamic Moduli from Stress Relaxation Data . . . . .	50
	B. The Gottenberg Torsional Shear Testing Machine . . . . .	50
VI	STRUCTURAL DAMPING AND ACOUSTIC ANALYSES . . . . .	52
	A. Approach . . . . .	54
	1. LAM NASTRAN Model . . . . .	54
	2. Acoustic Cavity Model . . . . .	54
	3. Rod-Organ Pipe Model . . . . .	56

## CONTENTS (Cont)

<u>Section</u>		<u>Page</u>
B.	Results and Comparisons . . . . .	60
1.	LAM NASTRAN Model. . . . .	63
2.	Acoustic Cavity Model. . . . .	63
3.	Rod-Organ Pipe Model . . . . .	72
C.	Conclusions . . . . .	72
1.	LAM NASTRAN Model. . . . .	72
2.	Acoustic Cavity Model. . . . .	75
3.	Rod-Organ Pipe Model . . . . .	75
VII	RECOMMENDATIONS FOR FURTHER STUDY. . . . .	77
VIII	SUMMARY AND CONCLUSIONS	
A.	Task I. . . . .	78
B.	Task II . . . . .	79
	LIST OF REFERENCES . . . . .	81
 <u>Appendix</u>		
A	DYNAMIC MODULUS VALUES FOR VRA-7, VRX-2, VSF-3, AND FKM PROPELLANTS. . . . .	A-1
B	ANALYSIS OF ROD-ORGAN PIPE STRUCTURAL DAMPING MODEL. . .	B-1



# LIST OF ILLUSTRATIONS

<u>Number</u>	<u>Title</u>	<u>Page</u>
1	Inert Model Constructed to Represent a Rigid Walled LAM . . . . .	14
2	Mode Shapes for the First Acoustic Mode at 151 Hz (Inert Model with 1/4-Inch Gap) . . . . .	18
3	Second Acoustic Mode, Occurring at 371 Hz (Inert Model with 1/4-Inch Gap) . . . . .	19
4	Mode Shape of the 900 Hz Mode (Inert Model with 1/4-Inch Gap) . . . . .	20
5	Mode Shape of the 1178 Hz Mode (Inert Model with 1/4-Inch Gap) . . . . .	21
6	Damping and Frequency for the 150 Hz Mode at 10 psi . . .	28
7	Damping and Frequency for the 370 Hz Mode at 10 psi . . .	28
8	Damping and Frequency for the 900 Hz Mode at 10 psi . . .	29
9	Damping and Frequency for the 1180 Hz Mode at 10 psi . . .	29
10	Damping and Frequency for the 1450 Hz Mode at 10 psi . . .	30
11	Damping and Frequency for the 150 Hz Mode at 300 psi . . .	30
12	Damping and Frequency for the 370 Hz Mode at 300 psi . . .	31
13	Damping and Frequency for the 900 Hz Mode at 300 psi . . .	31
14	Damping and Frequency for the 1180 Hz Mode at 300 psi . .	32
15	Damping and Frequency for the 1450 Hz Mode at 300 psi . .	32
16	Acoustic Mode Shape for the 154 Hz Mode in LAM-179 Using Nitrogen at 10 psi . . . . .	35
17	Acoustic Mode Shape for the 378 Hz Mode in LAM-179 Using Nitrogen at 10 psi . . . . .	36
18	Acoustic Mode Shape for the 858 Hz Mode in LAM-179 Using Nitrogen at 10 psi . . . . .	37
19	Acoustic Mode Shape for the 1040 Hz Mode in LAM-179 Using Nitrogen at 10 psi . . . . .	38



# LIST OF ILLUSTRATIONS (Cont)

<u>Number</u>	<u>Title</u>	<u>Page</u>
20	Frequency Response Plot for LAM-179 from 100 Hz to 900 Hz Using Nitrogen at 10 psi . . . . .	39
21	Frequency Response Plot for LAM-179 from 900 to 2500 Hz Using Nitrogen at 10 psi . . . . .	40
22	Acoustic Mode Shape for the First Longitudinal Mode in LAM-179 Using Helium at 10 psi ( $f = 250$ Hz) . . . . .	41
23	Damping and Frequency Measured for the First Mode in LAM-179 as a Function of Pressure . . . . .	43
24	Baseline Damping Data from Inert Model Compared to Results from LAM-179 . . . . .	46
25	Damping Factor Versus Pressure for End Plate with 1/16 Inch Diameter Hole . . . . .	48
26	Frequency Versus Pressure for End Plate with 1/16 Inch Diameter Hole . . . . .	48
27	Computer Plot of the Grid for the LAM Finite Element Model . . . . .	55
28	Rod-Organ Pipe . . . . .	57
29	Comparison of LAM Experimental and Analytical (NASTRAN) Results . . . . .	62
30	Comparison of Measured and Analytical First Acoustic Mode Shape . . . . .	64
31	Acoustic Decay-Pressure Predictions of Finite Element and Analytical Procedures . . . . .	68
32	Frequency Predictions of Finite Element and Analytical Procedures . . . . .	69
33	Acoustic Decay - Rod Length for Several Density Ratios . .	70
34	Frequency Shift, Rod Length for Several Density Ratios . .	71
35	Reduced Decay Formulation for Variation of Component Lengths . . . . .	73
36	Reduced Frequency Formulation for Variation of Component Lengths . . . . .	74

# LIST OF TABLES

<u>Number</u>	<u>Title</u>	<u>Page</u>
1	Frequencies and Mode Shapes for the Inert Model with 1/4-Inch Gap . . . . .	17
2	Variation in Frequency and Damping as a Function of Probe Position for the Two Different Damping Measurement Methods (Measurements Made from Probe Transducer) . .	23
3	Variation in Frequency and Damping as a Function of Probe Position for the Two Different Damping Measurement Methods (Measurements Made at Wall Position No. 9) .	24
4	Variation in Frequency and Damping as a Function of Measurement Location for the Two Different Damping Measurement Methods . . . . .	25
5	Damping and Frequency Measurements Using Two Methods at Two Pressures . . . . .	26
6	Simple Cylinder Test Results . . . . .	27
7	Damping and Frequency as a Function of Pressure for LAM-179 . . . . .	44
8	Damping and Frequency as a Function of Pressure for LAM-180 . . . . .	45
9	Additional Frequency and Damping Data for the Inert Model . . . . .	45
10	Damping and Frequency Measurements Made on the Inert Model Using an End Plate with 1/4-Inch Diameter Hole (Gap = 0.49-Inch) . . . . .	47
11	Damping and Frequency Measurements Made on the Inert Model Using a 1/16-Inch Diameter Hole in the End Plate (Gap = 0.49-Inch) . . . . .	49
12	Rod-Organ Pipe Parameters for Finite-Element Solution Comparison . . . . .	59
13	Analysis Results of the LAM Model . . . . .	61

# LIST OF TABLES (Cont)

<u>Number</u>	<u>Title</u>	<u>Page</u>
14	Results of Acoustic Cavity Analyses . . . . .	65
15	NASTRAN and Overlapping Element Calculations of Rod-Organ Pipe Acoustic Frequency and Decay Parameters . .	66
16	Base Values of Rod-Organ Pipe Parameters for Analytical Parameter Study . . . . .	67

## SECTION I

### INTRODUCTION

Almost all solid propellant rocket motors exhibit some degree of combustion instability. Combustion instability is characterized by chamber pressure oscillations in a burning motor that increase in an unstable ( $e^{\alpha t}$  envelope) fashion until some limiting amplitude is reached. As burning in the motor continues, the conditions required to sustain oscillation in a particular mode change and the oscillations themselves typically die away before the end of motor operation.

The hot combustion gases in the combustion cavity can oscillate in various natural acoustic modes much the same way that the column of air in an organ pipe resonates. A small perturbation in combustion cavity pressure can start acoustic oscillations in one or more of the natural acoustic modes. If the mode is unstable, the small pressure perturbation causes the mode to grow in amplitude at a rate determined by combined growth and loss mechanisms. One potential loss mechanism is the structural damping inherent in the motor case and grain structure. Since the motor can absorb energy from an oscillating acoustic mode, structural damping can have a significant stabilizing effect. An earlier study<sup>(1)</sup> indicated the potential role of structural damping in stabilizing acoustic oscillations.

High level vibration (as high as 300 g's), has been attributed to unstable acoustic pressure oscillations in some modern ballistic missile motors. Such high level vibration response is potentially hazardous to the safe and reliable operation of a missile. Because of this, a considerable amount of effort has been devoted to the study of unstable acoustic pressure oscillations in solid rocket motors over the past several years. As a part of such studies, the Aerojet Solid Propulsion Company (ASPC) was commissioned by the Air Force Rocket Propulsion Laboratory (AFRPL) to develop a Standard Stability Program (a computer program that could serve as a standard for the industry for predicting the acoustic stability of new rocket motor designs).

The plans for the Standard Stability Program did not include consideration of structural damping as a stabilizing mechanism. Therefore, the AFRPL issued contract F04611-76-C-0039, to Hercules Incorporated, Bacchus Works, Magna, Utah, to do the work required to incorporate structural damping considerations into the ASPC Standard Stability Program. This final report covers the work performed by Hercules on the AFRPL Structural Damping Program.

---

(1) Anderson, J. McKay, "Structural Damping of Acoustic Oscillations in Solid Propellant Rocket Motors", Eighth JANNAF Combustion Meeting, Monterey, Cal. 14-16 September 1971.



The objectives of the Structural Damping Program were to establish the role of structural damping in regulating acoustic pressure growth rates in solid propellant rocket motors and to show the accuracy to which structural damping calculations can be made. The program was organized into the five tasks discussed below.

#### TASK I - EXPERIMENTAL MEASUREMENT OF STRUCTURAL DAMPING

Objective - Experimentally determine the magnitude of structural damping in a 10-inch-diameter test motor and demonstrate how damping is affected by changes in acoustic frequency and motor chamber pressure.

#### TASK II - VERIFICATION OF STRUCTURAL DAMPING CALCULATIONS

Objective - Demonstrate the accuracy to which the measured structural damping rates can be calculated using the NASTRAN computer program. This task required that dynamic propellant moduli be obtained for use in the analysis models.

#### TASK III - GUIDELINES AND PROCEDURES FOR STRUCTURAL DAMPING ANALYSES

Objective - Establish guidelines and procedures that would enable analysts to routinely carry out structural damping analyses.

#### TASK IV - DEVELOP PARAMETRIC STRUCTURAL DAMPING CURVES

Objective - Develop a series of parametric charts which will allow analysts to estimate structural damping magnitudes for simple stability analyses.

#### TASK V - INCORPORATION OF STRUCTURAL DAMPING INTO ASPC ACOUSTIC STABILITY PROGRAM

Objective - Ensure compatibility of the structural damping analysis computer program with the ASPC Standard Stability Program nomenclature and procedures and provide a single reference source for all calculations necessary for an all-up acoustic stability analysis.

Tasks I and II of the program were scheduled to run concurrently. The program plan included provisions for reviewing and replanning the program if any trouble precluded successful completion of Tasks I and II. Various technical problems were encountered in Tasks I and II and neither task was successfully completed. This report documents the work performed on Tasks I and II, discusses the technical problems encountered, and makes suggestions for a future study of structural damping.

Problems experienced with the experimental work of Task I are the main reason the project was not completed as planned. Initially, damping measurements indicated that the damping coefficient,  $\alpha$ , is a strong function of geometry, (gap width), and pressure. The expected result of a monotonically increasing value of  $\alpha$  with increasing pressure was not achieved. Later experiments indicated that the acoustic driver used for the testing was not uncoupled from the acoustic cavity and most of the test data contained the influence of the driver as well as the characteristics of the acoustic cavity. The final experiment in the program, using a 1/16-inch-diameter hole between acoustic cavity and driver to uncouple the two cavities, resulted in a significantly different  $\alpha$  versus pressure response.

The second section of this report covers the general approach to Tasks I and II. Section III covers the basic test installations and procedures, and Section IV contains a discussion of the corresponding test data. Dynamic moduli testing using the Gottenberg apparatus and modulus conversion from relaxation data are discussed in Section V. The analyses that were performed to support the program, mostly using NASTRAN, are discussed in Section VI. Sections VII and VIII contain recommendations and conclusions, respectively. Mr. Normand Peterson's report of his study of the rod-organ pipe model is included as an appendix to this report.

## SECTION II

### APPROACH

The five tasks into which this project was organized were listed in Section I. Only Tasks I and II are discussed here.

#### A. TASK I - EXPERIMENTAL MEASUREMENT OF STRUCTURAL DAMPING

Plans for Task I called for performing damping measurements on three different test motors. The damping was to have been measured by introducing an acoustic wave in the motor combustion cavity and then either measuring the pressure decay after the input to the driver was removed or measuring the width of a frequency response curve. Such measurements would indicate the total damping in the system. Sources of damping included in the damping data would be structural damping in the grain, structural damping in the case, boundary layer shear damping, and flow damping due to the particular motor geometry. Since the damping source of major interest in the study was structural damping of the grain, a comparison between a model with a live propellant grain and a model with a rigid-walled grain was planned in order to isolate the value of structural damping due to the grain.

Original plans called for a motor with a rigid-walled grain (plaster-of-paris) to be constructed as nearly as possible like the motors with the live propellant grains. However, a cursory stress analysis of a motor with a plaster-of-paris grain indicated that the grain and case bond system could not withstand the high loads associated with pressurization to 1500 psi. For this reason, an all steel rigid-walled model with internal geometry similar to that of the live propellant motors was used.

The main difference in geometry between the live propellant motors and the rigid-walled model is in the area of the flapped dome. When one of the live propellant motors is pressurized, the forward dome cavity opens up to an extent that depends on the pressure level. When the dome cavity opens up, it is wide near the centerbore and tapers down to a small crack at the bond termination near the dome tangent line. Thus, the dome cavity is a variable thickness gap with an outside surface approximately in the shape of a hemisphere. The inert (rigid-walled) model was designed with a forward dome gap of uniform thickness extending along a radial line from the centerbore to the motor inside radius. Thus the gap model and the actual motor gap are of different geometries. The uniform width (thickness) of the gap model in the inert motor was designed to be adjustable from 0.0 to 0.5 inch to allow modeling of the live propellant motors at various pressure levels.

A low cost, 10-inch-diameter motor design that has been used at Hercules for other experimental work was selected as the test vehicle. The lightweight analog motor (LAM) was designed for and has been proof tested for pressures greater than 2000 psi. For this program, damping measurements

were made at pressures up to 1500 psi. Two different types of propellant, hydroxy-terminated polybutadiene (HTPB) and a crosslinked double-base (XLDB) were selected for use in the program. The two propellant types were expected to have sufficiently different damping characteristics to make the differences measurable. LAM 179, (motor serial number 179), was cast at the end of April 1976, with VSF-3 propellant. The VSF-3 propellant is an HTPB type propellant. LAM 180 was cast at the end of May 1976, with VRX-2, an XLDB propellant. Both motors were cast, rather than cartridge loaded, because the casting operation happened to be more convenient and efficient at the time.

#### B. TASK II - STRUCTURAL DAMPING ANALYSIS VERIFICATION

The objective of Task II was to verify that structural damping factors can be calculated using the NASTRAN computer program and an appropriate finite element model. Plans called for an analysis of the model at each test condition used in Task I so that a direct comparison could be made between test and analysis data. The comparison would result in a qualitative measure of the accuracy to which structural damping calculations can be made.

A required input to the NASTRAN finite element model is the propellant dynamic moduli (the model includes case, propellant, and gas elements). The work to determine the moduli was a part of this task. Plans called for use of the Gottenberg torsional shear testing apparatus to determine the propellant dynamic moduli. The determination of propellant properties actually carried out in the program is discussed in Section V. The NASTRAN and other analyses conducted are discussed in Section VI.



## SECTION III

### ACOUSTIC TEST SET-UPS AND PROCEDURES

#### A. RIGID-WALLED MODEL

A sketch of the inert model designed to represent a rigid-walled LAM is shown in Figure 1. The nine threaded holes along the tube wall are sized to accept PCB model 116A11 pressure transducers. The pressure transducers are used to measure the oscillatory component of the acoustic cavity pressure. The nine transducer locations along the wall and one in the end plate were used to determine acoustic mode shapes. Cap screws with seal washers were placed in all holes not being used. A probe system (not shown in Figure 1) was also used to determine acoustic mode shapes. The probe system consisted of a rod about 1/2-inch in diameter with a pressure transducer connected to one end. A special end plate with a seal around the rod was used with the probe system. The probe-mounted transducer could be continuously adjusted from one end of the centerbore cavity to the other.

The radial gap in the inert model opposite the driver end was adjustable from 0.0 to 0.5 inch in width. The adjustment was made by putting spacers between the end plate and the outer bolt ring. The end plate is held against the spacers by friction and chamber pressure.

Most of the tests were performed with the driver fitting loosely into the aluminum end plate as shown in Figure 1. Using a loose fit between the driver flange and the end plate allowed chamber pressure to be all around the driver. Having the pressure equalized between the main cavity and the speaker cavity assured that the driver would not be under a pressure load during the high pressure tests. The cavity around the driver was tightly packed with polyurethane foam to hold the driver in place against the end plate.

The last few tests were performed with a modified driver configuration. An end plate with a 1/16-inch-diameter hole between the main cavity and the driver cavity was used in place of the end plate shown in Figure 1. The new end plate had a provision for rigid attachment of the driver to the end plate.

#### B. INSTRUMENTATION

All response measurements were made using PCB model 116A11 pressure transducers. Output from the pressure transducers was input to charge amplifiers. Output from the amplifiers was observed on an oscilloscope and recorded on an oscillograph or an X-Y recorder. Steady state measurements were read on an HP model 3400A RMS voltmeter. A digital frequency counter was used for precise determination of frequencies.



The driver was a University model ID-75 loudspeaker driver. An audio oscillator was connected to the driver through a McIntosh power amplifier. The audio oscillator was adjusted for a 2 volt output at 200 Hz. The power amplifier gain was adjusted to put out a constant 8 volts (rms) into the 16 ohm (nominal) driver.

#### C. MODE SHAPE DETERMINATION

Acoustic cavity mode shapes are mapped by using the probe and the transducer locations along the tube wall. Prior to mapping mode shapes, a frequency sweep is made with the pressure transducer in a particular fixed position. The response amplitude is plotted as a function of frequency on an X-Y recorder. The plot shows peaks at the acoustic resonant frequencies. A particular mode is "tuned in" by adjusting the frequency knob on the oscillator while observing the pressure transducer output on the voltage meter. The frequency which produces a maximum voltage output is noted on the frequency counter and the frequency knob is left untouched during mode mapping.

When the resonant frequency has been tuned in, an acoustic mode is mapped using the probe by moving the probe in increments from one end of the cavity to the other. At each setting of the probe, the voltmeter reading is recorded along with the probe position.

The wall positions are used to map mode shapes by removing the cap screws one at a time and replacing them with the pressure transducer. The same transducer is used for all readings so that differences between transducers will not have an effect on the results. Mapping the mode shapes using the wall transducer positions with and without the probe in place gives an indication of the amount of mode shape distortion caused by the presence of the probe.

#### D. DAMPING FACTOR ( $\alpha$ ) MEASUREMENT

Two different kinds of tests can be performed to measure the damping factor,  $\alpha$ . Using the frequency response method, the frequency bandwidth at the half power points,  $\Delta f$ , will yield  $\alpha$  according to

$$\alpha = \pi \cdot \Delta f$$

When a resonant frequency,  $f_o$ , has been tuned in, as described above, the voltage  $V_o$ , is recorded from the voltmeter reading. The half power points are determined by dividing the maximum voltage  $V_o$  by  $\sqrt{2}$ . With the frequency set at the resonance frequency, the frequency knob on the oscillator is adjusted to a slightly lower frequency until a value of  $V_o/\sqrt{2}$  is read on the voltmeter and the new frequency,  $f_1$ , is recorded. The same procedure for a slightly higher frequency,  $f_2$ , gives  $\Delta f = f_2 - f_1$ .

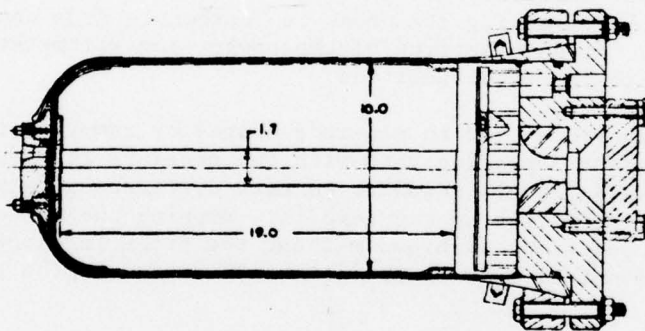
The decay method is used by recording the pressure decay signal after power to the driver has been cut off. The decay signal is recorded on an oscillograph and the damping factor is given by:

$$\alpha = \frac{f_o}{n} \ln \left( \frac{X_{i+n}}{X_i} \right)$$

The value of  $(\alpha/f_o)$  is commonly known as the logarithmic decrement. The  $X_i$  represents the amplitude of the pressure from the pressure decay curve at the peak of any cycle and  $X_{i+1}$  is the corresponding amplitude  $n$  cycles later.

#### E. LIGHTWEIGHT ANALOG MOTORS (LAM'S)

A sketch giving the configuration of a LAM is shown below.



In the acoustic tests performed for this program, the end closure with the driver (as shown in Figure 1) was substituted for the end closure with the nozzle that is shown in the sketch. The forward closure of Figure 1 was also used for the LAM tests in place of the closure shown above.

The LAM's used for testing in this program had a flap in the forward dome so that the dome and propellant separated when the motor was pressurized.

The acoustic tests on the LAM's were performed remotely on the static test firing range at the Bacchus Works facility. The motor was mounted securely to a metal test stand using the bolts in the heavy LAM aft closure. The test stand was, in turn, securely bolted to the floor of the static firing test bay. The usual safety procedures were followed in testing the LAM's.



## SECTION IV

### ACOUSTIC TEST RESULTS AND DISCUSSION

#### A. INITIAL INERT MODEL EXPERIMENTATION

##### 1. Natural Modes and Frequencies

With the inert model containing air at ambient pressure and temperature, and with the variable gap set at 1/4-inch, a frequency sweep was made to determine the model acoustic cavity natural frequencies. The pressure transducer was located at wall position No. 9 and the probe was at station No. 1 (approximately 1.0 inch from the forward end plate). The wall transducer peaked at the frequency and voltage values shown in Table 1 (values from the NASTRAN analysis are shown for comparison):

TABLE 1. FREQUENCIES AND MODE SHAPES FOR THE  
INERT MODEL WITH 1/4-INCH GAP

Frequency (Hz)	Normalized Pressure	Frequencies From NASTRAN Analysis (Hz)
151	0.015	144.7
371	0.034	372.9
625	0.018	635.0
900	0.113	911.1
1178	0.132	1190.0
1445	0.082	--

The mode shape of the 151 Hz mode was measured using both wall transducer locations and the probe. The results are shown in Figure 2. The probe was kept at station No. 1 while the wall measurements were being made. Mode shapes in the cavities at either end of the centerbore were not included in the mode verification measurements.

Mode shapes for the 371, 900, and 1178 Hz modes are shown in Figures 3, 4, and 5, respectively. The 625 Hz mode was weak and not well defined and was not plotted. The 1445 Hz mode is a high frequency mode the study of which is beyond the scope of this program. This program was limited to a study of a few lower frequency modes.

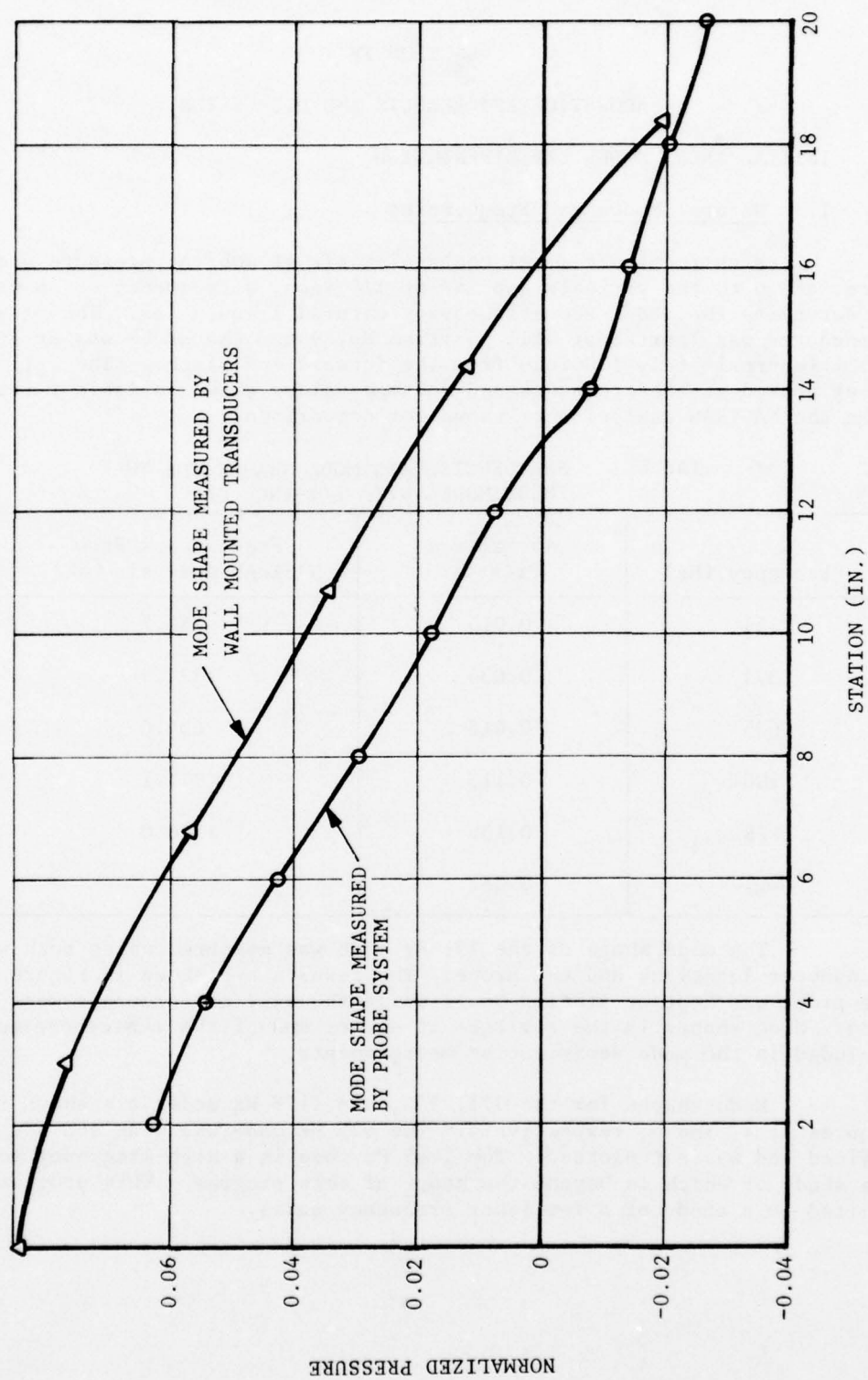


Figure 2. Mode Shapes for the First Acoustic Mode at 151 Hz (Inert Model with 1/4-Inch Gap)

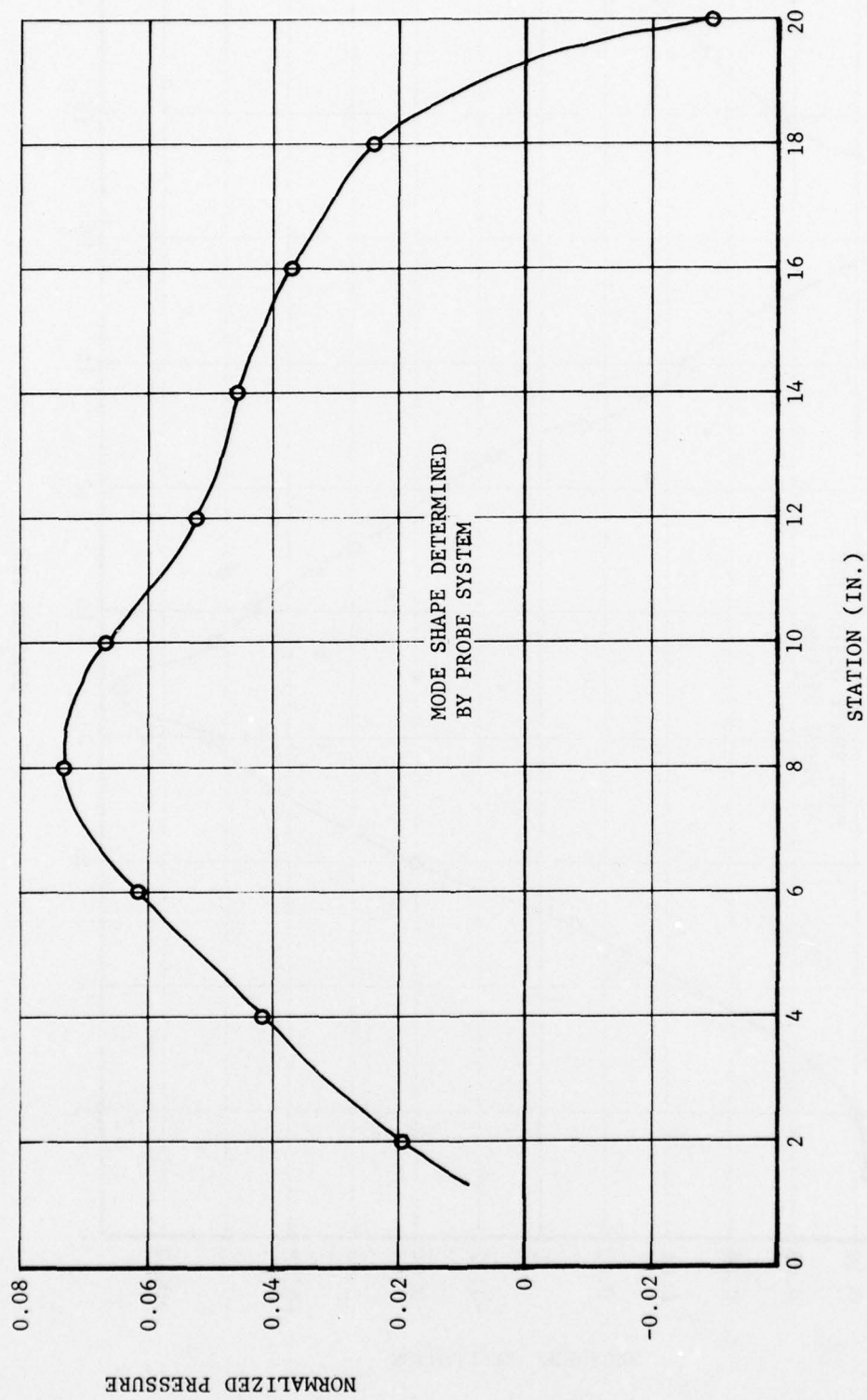


Figure 3. Second Acoustic Mode, Occurring at 371 Hz (Inert Model with 1/4-Inch Gap)

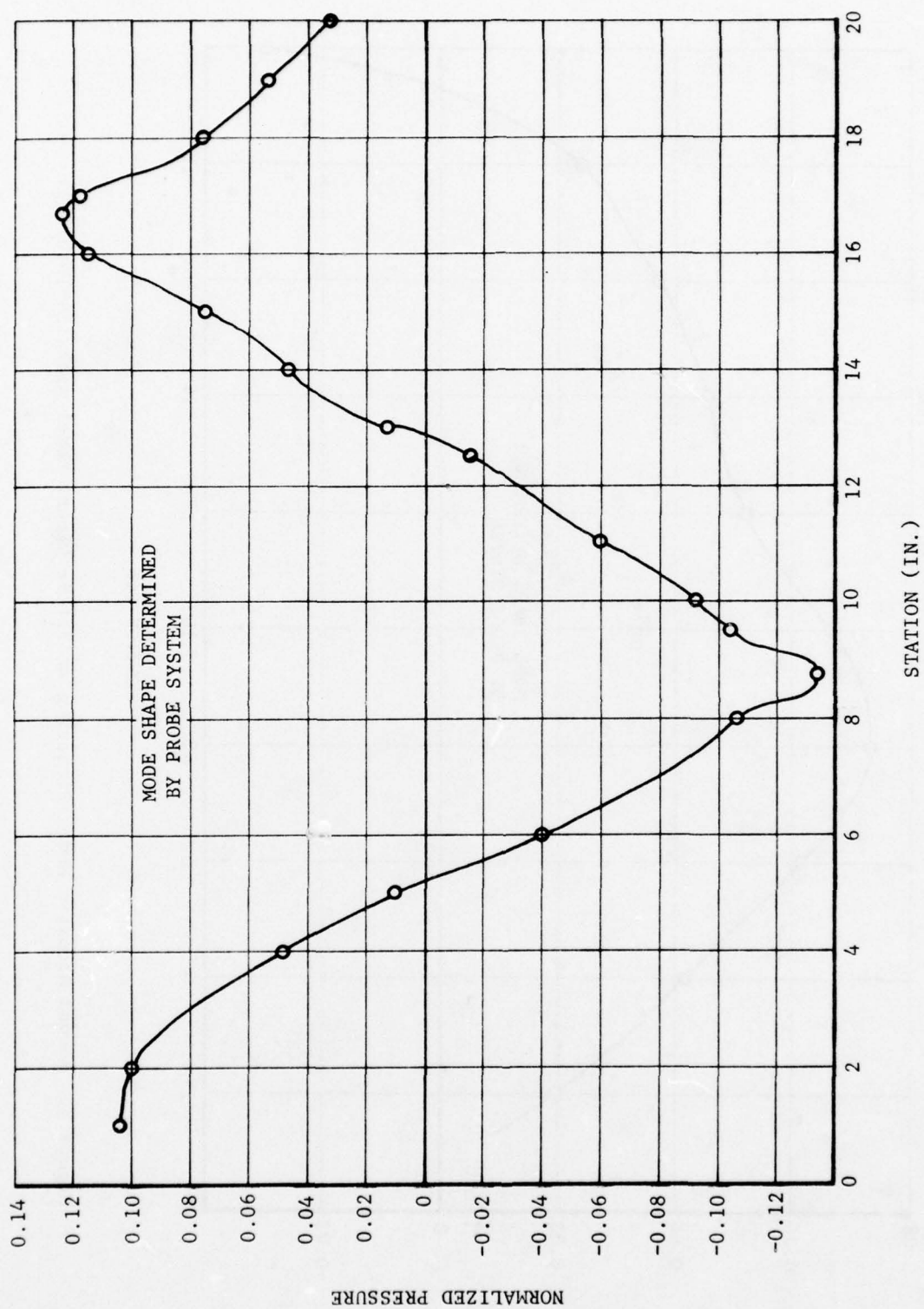


Figure 4. Mode Shape of the 900 Hz Mode (Inert Model with 1/4-Inch Gap)



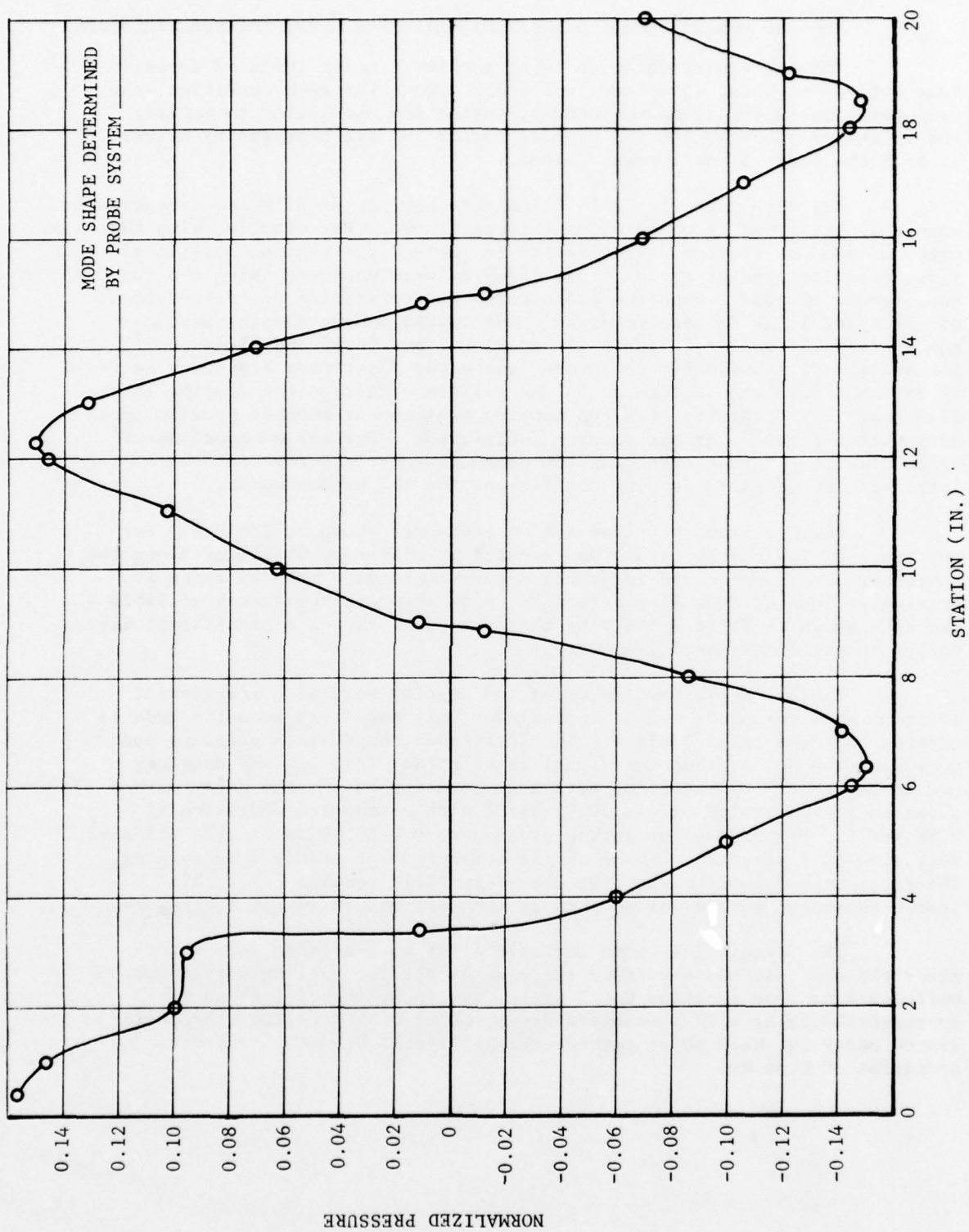


Figure 5. Mode Shape of the 1178 Hz Mode (Inert Model with 1/4-Inch Gap)

## 2. Damping and Natural Frequency Measurements Under Various Conditions

Initial experimentation using the inert model included comparisons between methods, locations, and probe uses. For each condition, the resonant frequency ( $f$ ) was measured by tuning the oscillator to maximize the voltmeter reading, and the damping factor ( $\alpha$ ) was measured by either or both the decay or half power method.

The data given in Table 2 indicate how the damping and frequency change as the probe is moved along the centerbore. For example, with the probe located at station 2 (see sketch in Table 2 for station locations) first mode frequencies of 147.0 and 147.9 Hz were measured using the two measurement methods. When the probe was moved to station 20, frequencies of 141.4 and 142.4 Hz were measured. The corresponding damping measurements are 37.07 and 38.10  $\text{sec}^{-1}$  for station 2 and 36.13 and 37.33  $\text{sec}^{-1}$  for station 20. Evidently the probe lowers the first mode frequency as it is extended into the centerbore but has little effect on the damping in the first mode. In addition, the two damping measurement methods provide agreement within 1  $\text{sec}^{-1}$  for the damping coefficient. Further examination of Table 2 indicates that extending the probe further into the centerbore increases the measured damping coefficient for the higher modes.

Results from a similar set of tests are shown in Table 3. For the tests of Table 3 the probe was located at different positions along the centerbore but damping and frequency measurements were made by using a transducer located at wall position No. 9 as shown in the sketch of Table 3. The data shown in Table 3 indicate that the probe causes a significant distortion in the inert model response.

Table 4 shows how frequency and damping vary with measurement location when the probe is not installed. Only the first acoustic mode is covered by the data of Table 4. The first mode shape has a pressure node near location No. 7, thus the signal level at No. 7 is low and data may not be reliable. Disregarding data from location No. 7, the decay method gives an average value of  $\bar{\alpha} = 30.95 \text{ sec}^{-1}$  with a standard deviation of 0.88  $\text{sec}^{-1}$ . The half power method yielded an  $\bar{\alpha} = 30.40 \text{ sec}^{-1}$  with standard deviation of 3.08  $\text{sec}^{-1}$ . Based on the comparison of standard deviations, the decay method appeared to give more repeatable results. For this reason the decay method was adopted as the main method in the later work.

The frequencies shown in Table 4 for both methods were determined the same way and should be the same except for testing variations. Omitting data from location No. 7 again, the decay method frequencies averaged 143.22 Hz with a standard deviation of 0.59 Hz. The frequencies listed under the half power method averaged 145.08 Hz with a standard deviation of 0.54 Hz.

TABLE 2. VARIATION IN FREQUENCY AND DAMPING AS A FUNCTION OF PROBE POSITION FOR THE TWO DIFFERENT DAMPING MEASUREMENT METHODS (MEASUREMENTS MADE FROM PROBE TRANSDUCER)

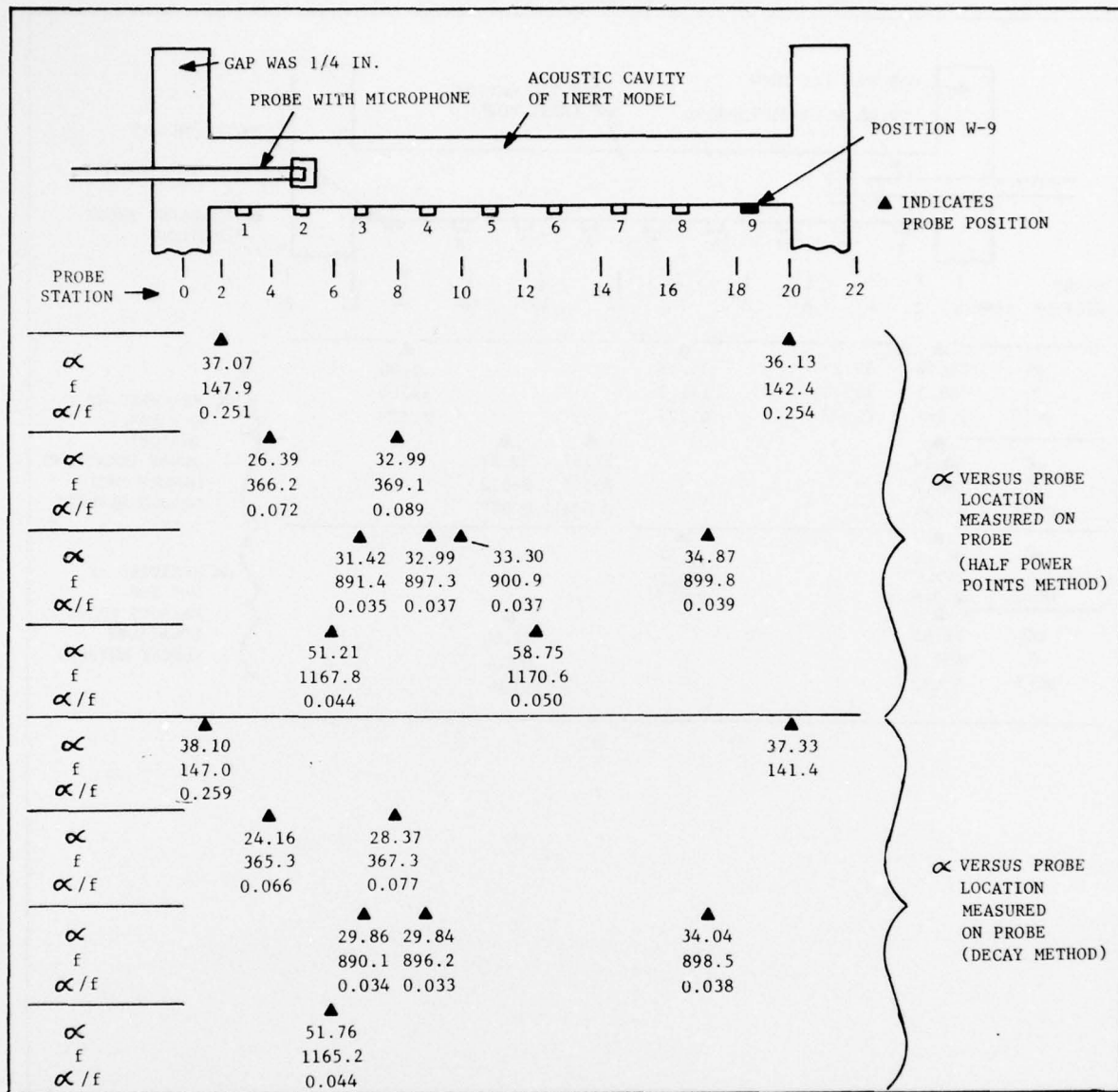


TABLE 3. VARIATION IN FREQUENCY AND DAMPING AS A FUNCTION OF PROBE POSITION  
FOR THE TWO DIFFERENT DAMPING MEASUREMENT METHODS  
(MEASUREMENTS MADE AT WALL POSITION NO. 9)

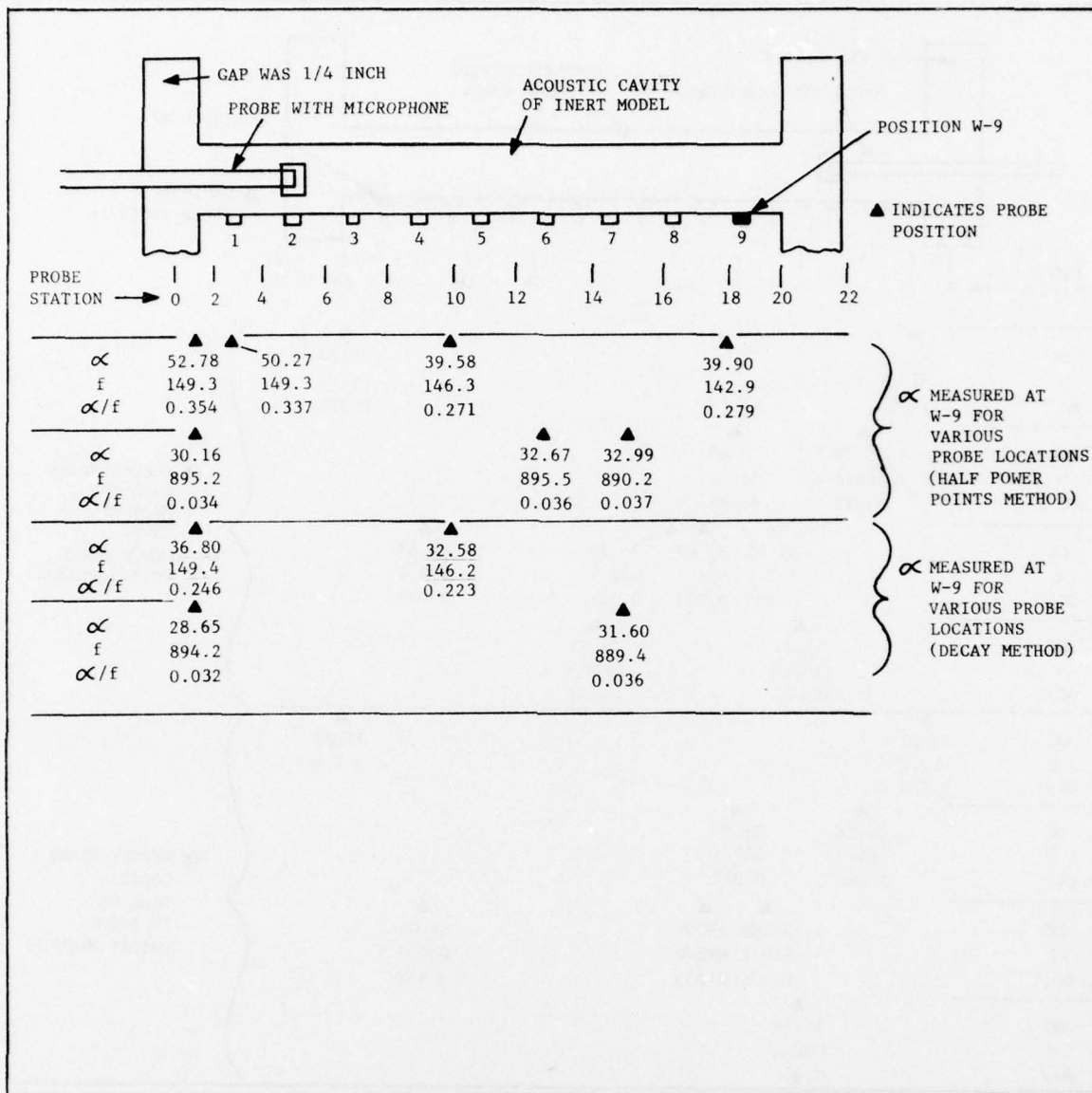
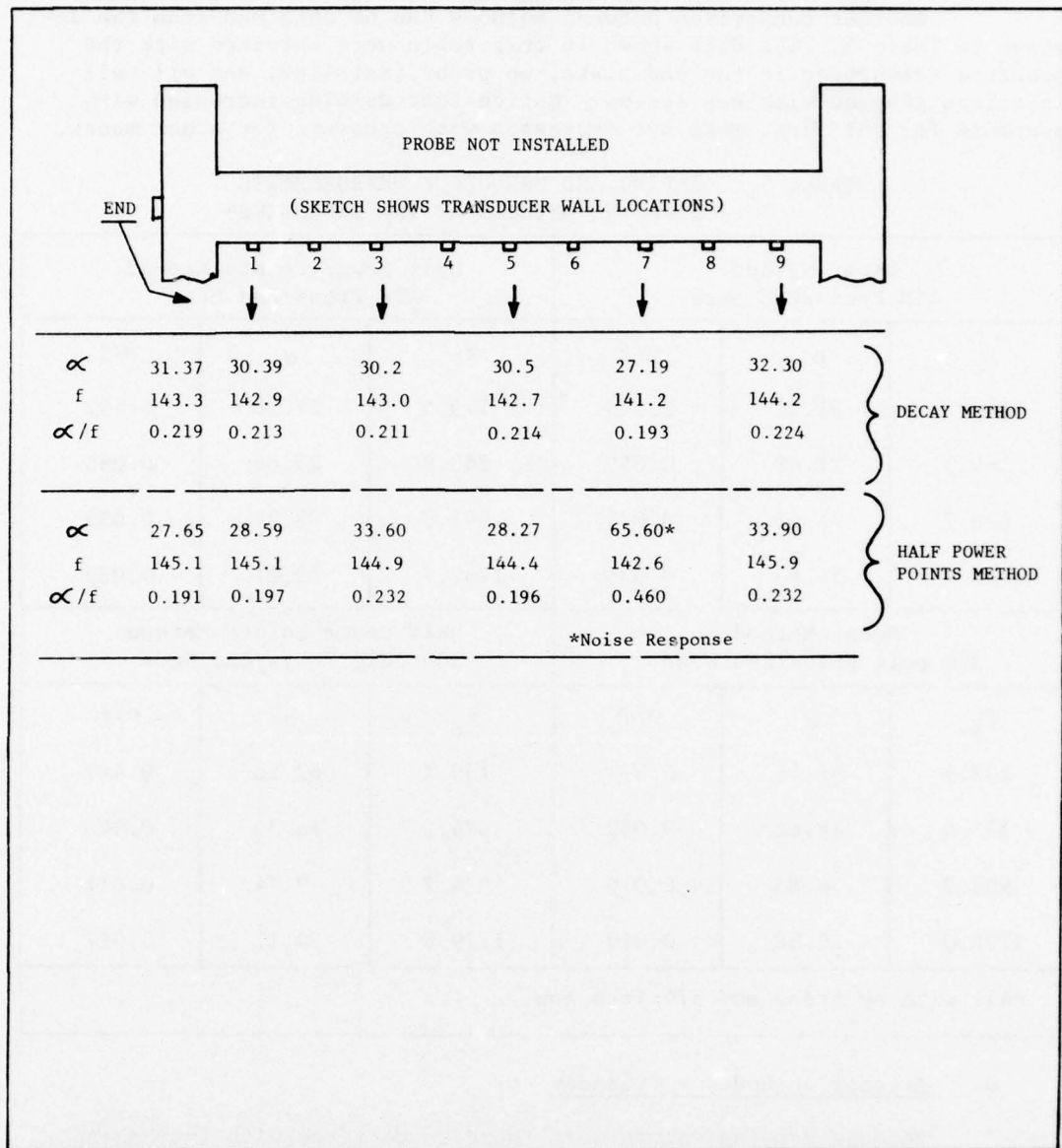




TABLE 4. VARIATION IN FREQUENCY AND DAMPING AS A FUNCTION OF MEASUREMENT LOCATION FOR THE TWO DIFFERENT DAMPING MEASUREMENT METHODS



Another comparison between methods can be obtained from the data shown in Table 5. The data shown in this table were obtained with the pressure transducer in the end plate, no probe installed, and all wall locations plugged with cap screws. Notice that damping increased with pressure for the first mode but decreased with pressure for other modes.

TABLE 5. DAMPING AND FREQUENCY MEASUREMENTS  
USING TWO METHODS AT TWO PRESSURES\*

Decay Method ATM Press/End Meas			Half Power Points Method ATM Press/End Meas		
$f_o$	$\alpha$	$\alpha/f$	$f_o$	$\alpha$	$\alpha/f$
143.3	31.37	0.219	145.4	27.96	0.192
364.3	21.49	0.059	369.9	23.88	0.065
878.7	25.58	0.029	891.3	29.22	0.033
1146.1	34.63	0.030	1162.7	38.01	0.033
Decay Method 300 psig Press/End Meas			Half Power Points Method 300 psig Press/End Meas		
$f_o$	$\alpha$	$\alpha/f$	$f_o$	$\alpha$	$\alpha/f$
138.5	51.45	0.371	139.1	62.20	0.447
373.4	18.64	0.050	374.2	16.34	0.044
903.3	8.83	0.010	904.7	9.74	0.011
1178.0	22.88	0.019	1179.8	20.11	0.017
*All with no probe and 1/4-inch gap.					

### 3. Attempt to Model a Cylinder

Because damping values were found to decrease with increasing pressure for the higher frequency modes, an attempt was made to simplify the test configuration so that results could be more easily interpreted. The variable gap on one end of the inert model was adjusted for a 0.0 inch gap width. On the other end of the model, a plastic spacer was machined to fit into the gap to give a cylindrical tube configuration. Results from the simple cylinder are shown in Table 6.

TABLE 6. SIMPLE CYLINDER TEST RESULTS

	First Longitudinal Mode	Second Longitudinal Mode
0 psi	$f = 316 \text{ Hz}$ $\alpha = 384 \text{ sec}^{-1}$	$f = 626 \text{ Hz}$ $\alpha = 305 \text{ sec}^{-1}$
300 psi	$f = 380 \text{ Hz}$ $\alpha = 182 \text{ sec}^{-1}$	$f = 658 \text{ Hz}$ $\alpha = 98.9 \text{ sec}^{-1}$

The results shown in Table 6 show that damping values are unrealistically high for the cylinder configuration. The various small cracks in the cylinder model were suspected to have caused the extra high damping values. Therefore, the cylinder was modified by using O-rings on each side of the plastic spacer and by using a sealing putty (CS) in all cracks. The modified cylinder at 0 psi yielded the data shown below.

First Longitudinal Mode

$$f = 296 \text{ Hz}$$

$$\alpha = 71.9 \text{ sec}^{-1}$$

Second Longitudinal Mode

$$f = 604 \text{ Hz}$$

$$\alpha = 150 \text{ sec}^{-1}$$

The damping values were greatly reduced by the modifications made to the original cylinder but the question of the effect of CS on the damping was not ascertained. The plan to study a simple cylinder was abandoned because of the high sensitivity of damping to small changes in the model configuration. To study damping in a simple cylinder, a new model of clean design and an uncoupled driver would be required.

4. Check on Linearity

Most of the tests were conducted with an 8 volt (rms) input to the driver. To evaluate whether measured values would be sensitive to variation in the input power, damping and frequency measurements were made with input levels of 2, 4, and 8 volts. The results are shown below:

Input Level (V)	Decay Method ( $\text{sec}^{-1}$ )	Half Power Method ( $\text{sec}^{-1}$ )	Frequency (Hz)
8	$\alpha = 84$	$\alpha = 64$	297.7
4	$\alpha = 83$	$\alpha = 78$	297.8
2	$\alpha = 84$	$\alpha = 84$	296.9

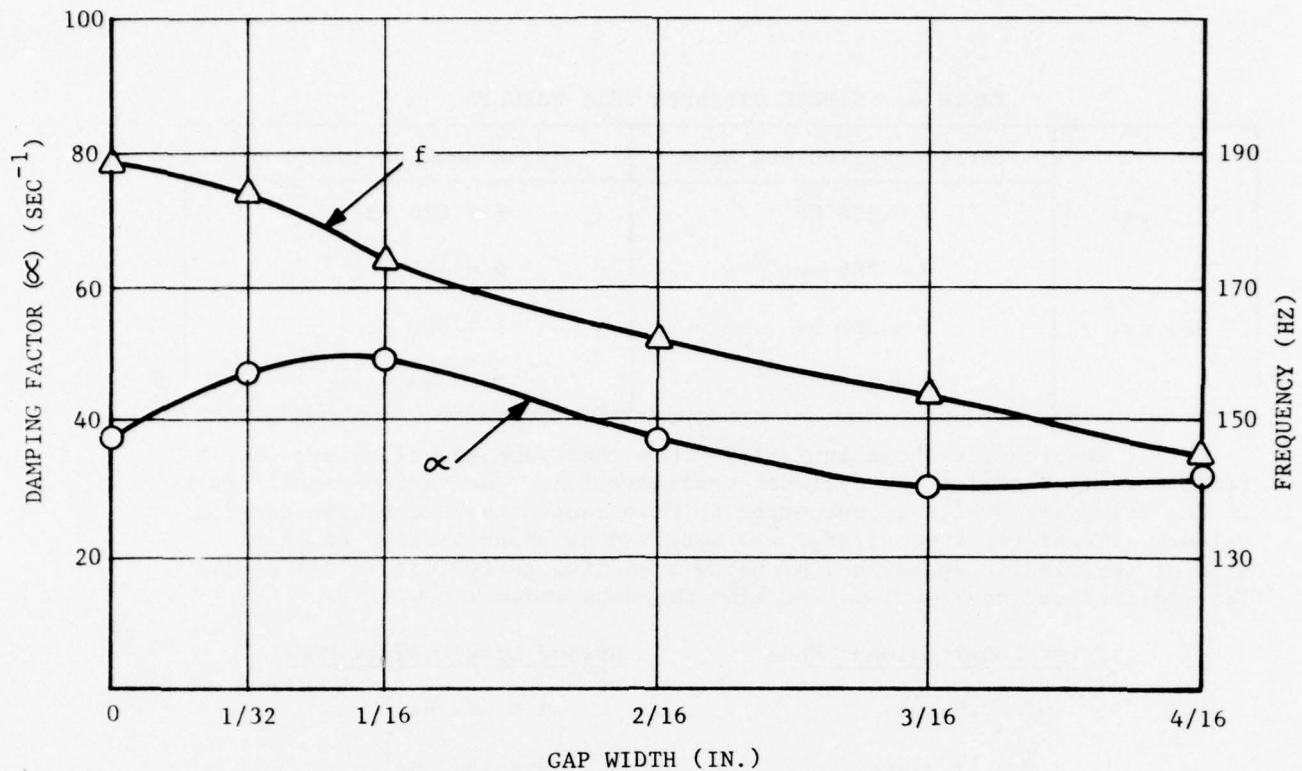


Figure 6. Damping and Frequency for the 150 Hz Mode at 10 psi

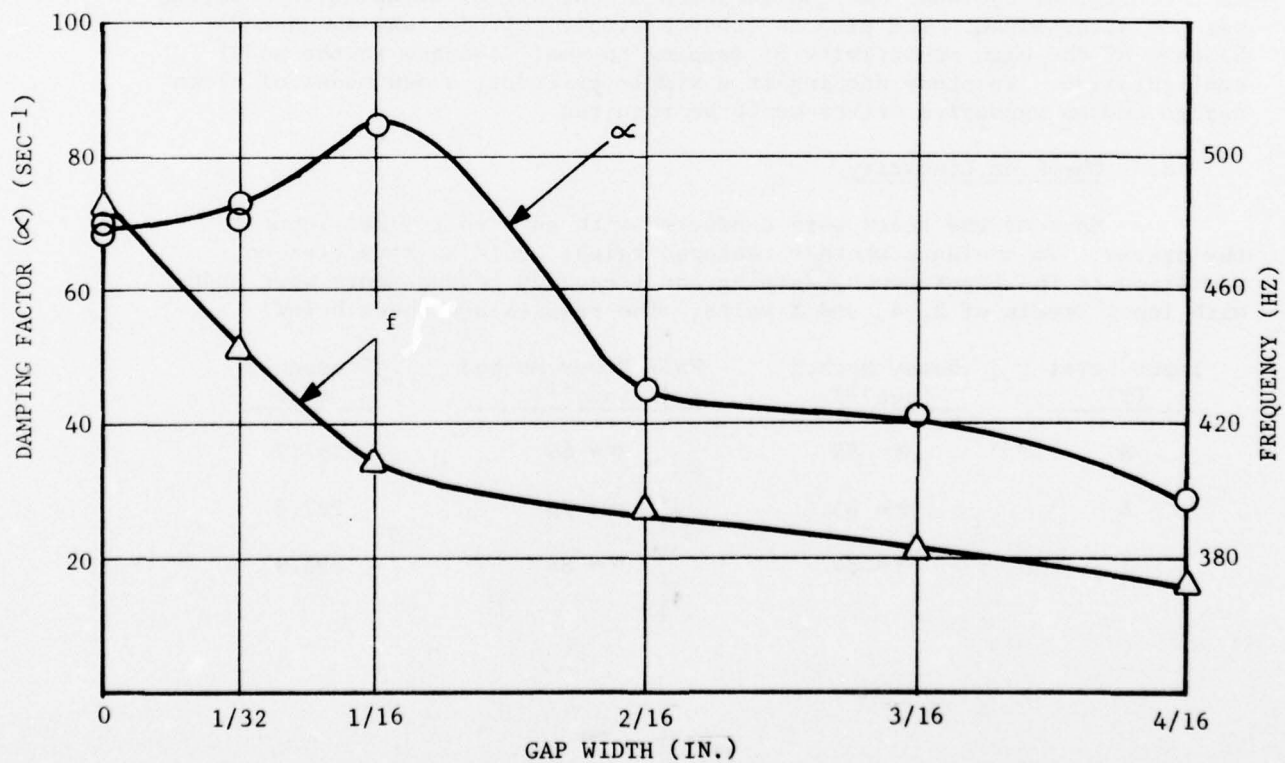


Figure 7. Damping and Frequency for the 370 Hz Mode at 10 psi



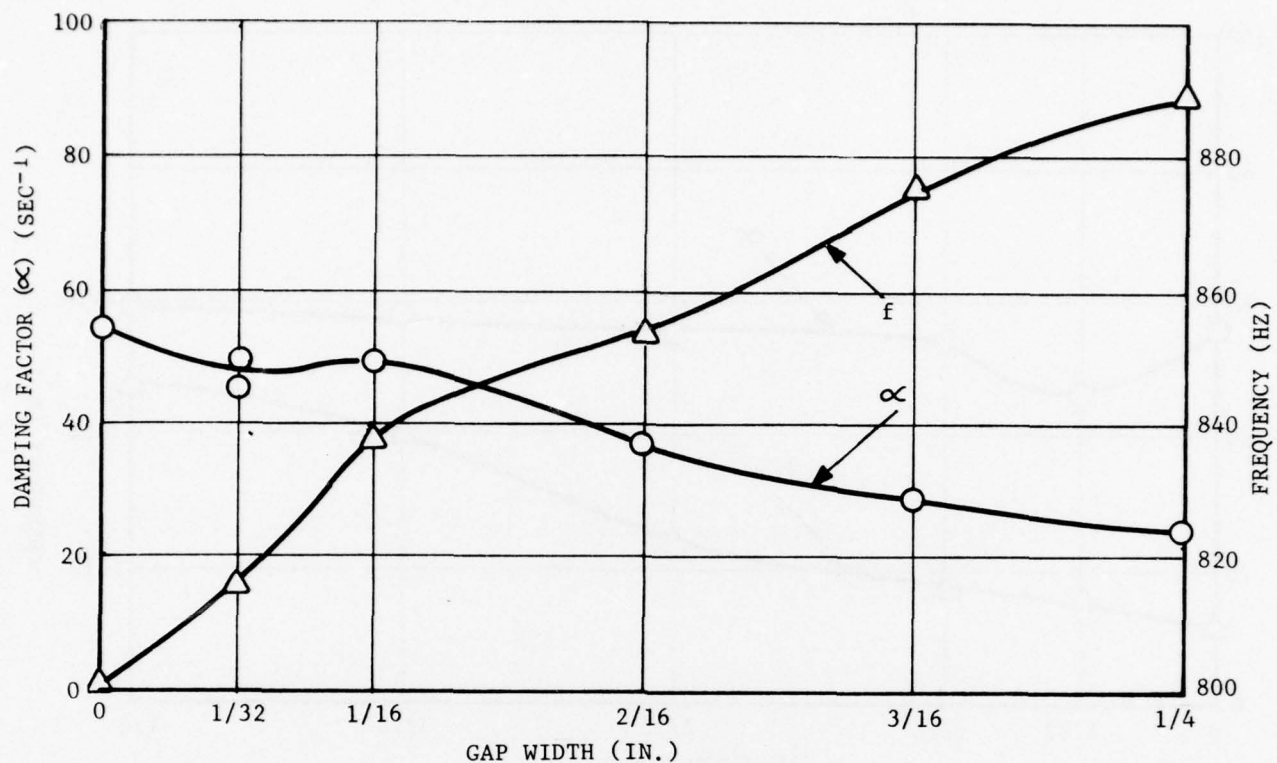


Figure 8. Damping and Frequency for the 900 Hz Mode at 10 psi

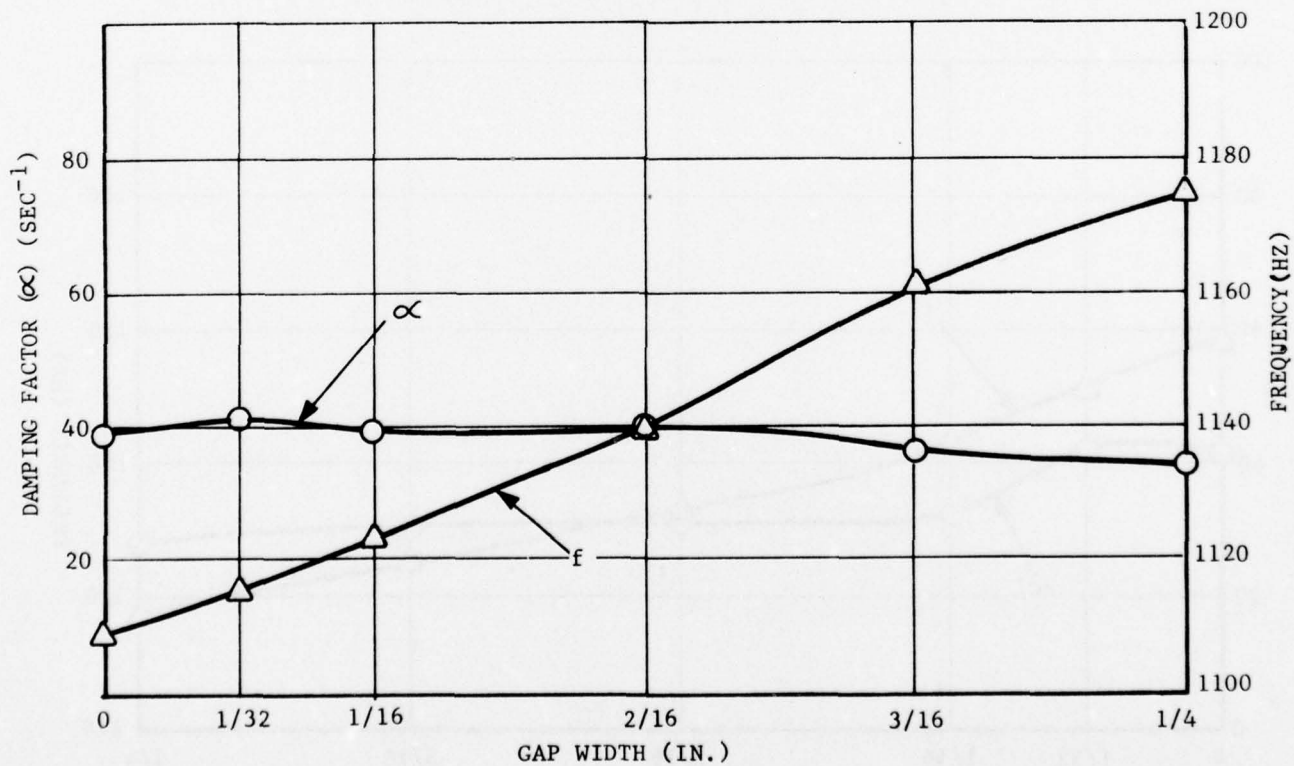


Figure 9. Damping and Frequency for the 1180 Hz Mode at 10 psi

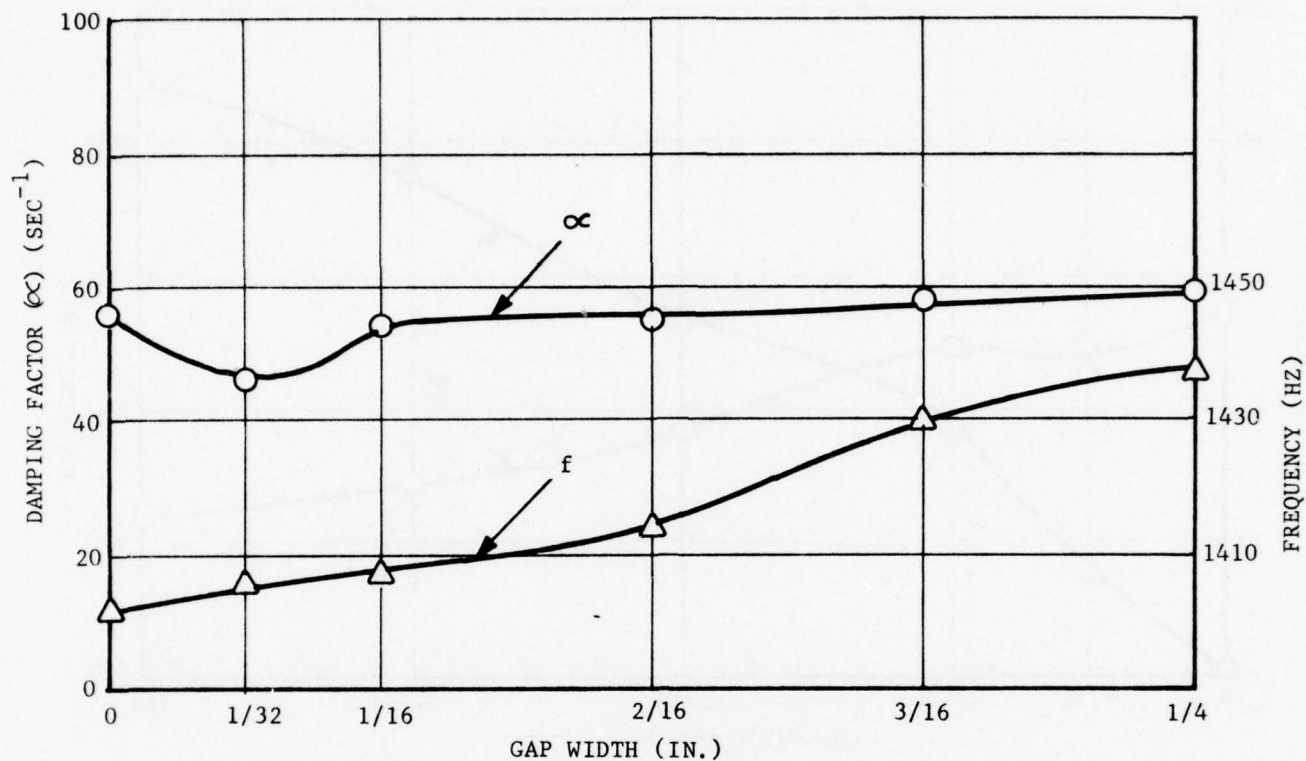


Figure 10. Damping and Frequency for the 1450 Hz Mode at 10 psi

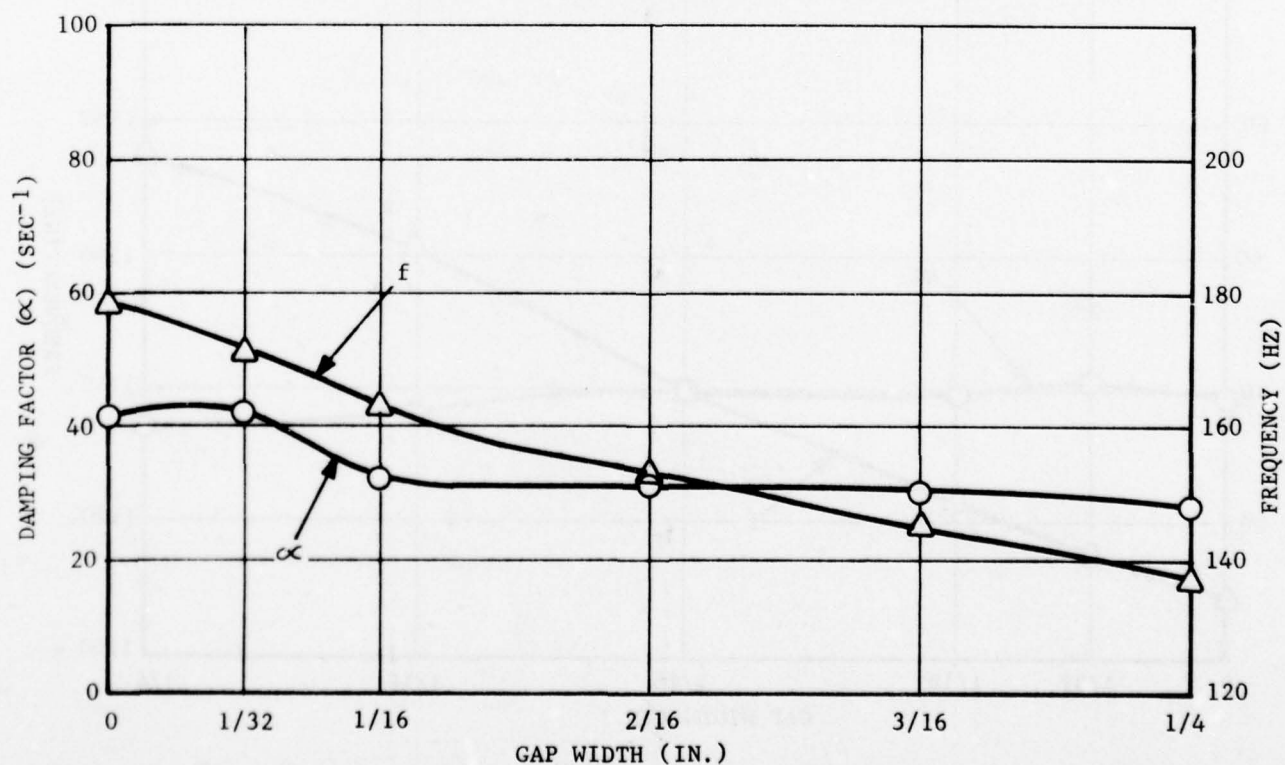


Figure 11. Damping and Frequency for the 150 Hz Mode at 300 psi

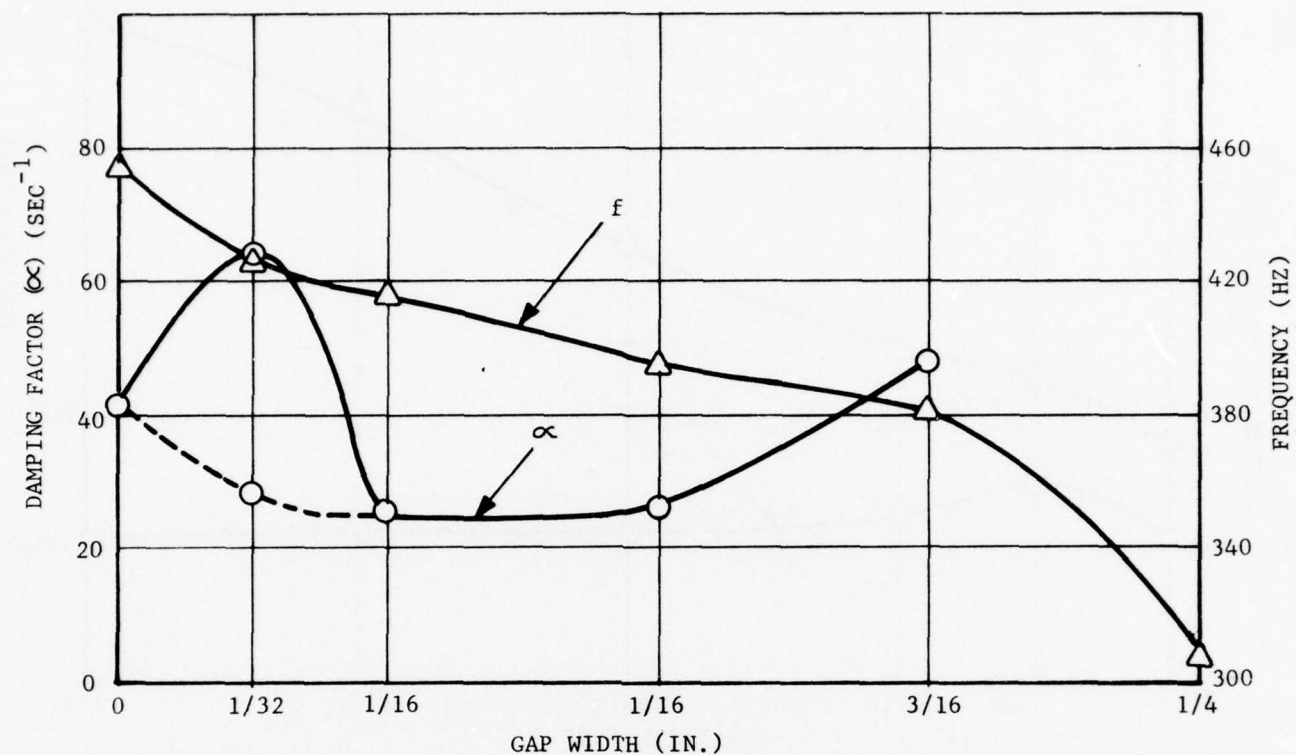


Figure 12. Damping and Frequency for the 370 Hz Mode at 300 psi

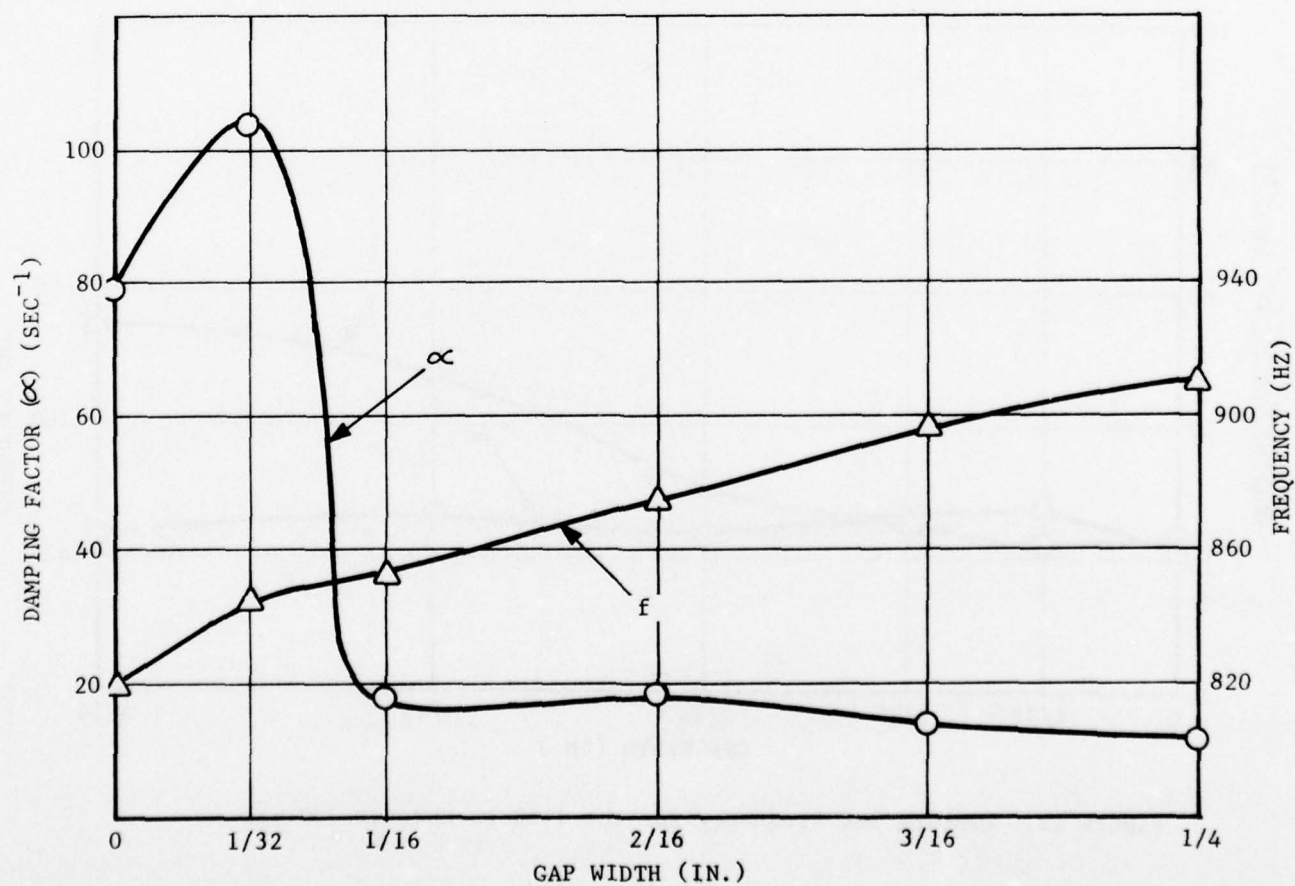


Figure 13. Damping and Frequency for the 900 Hz Mode at 300 psi

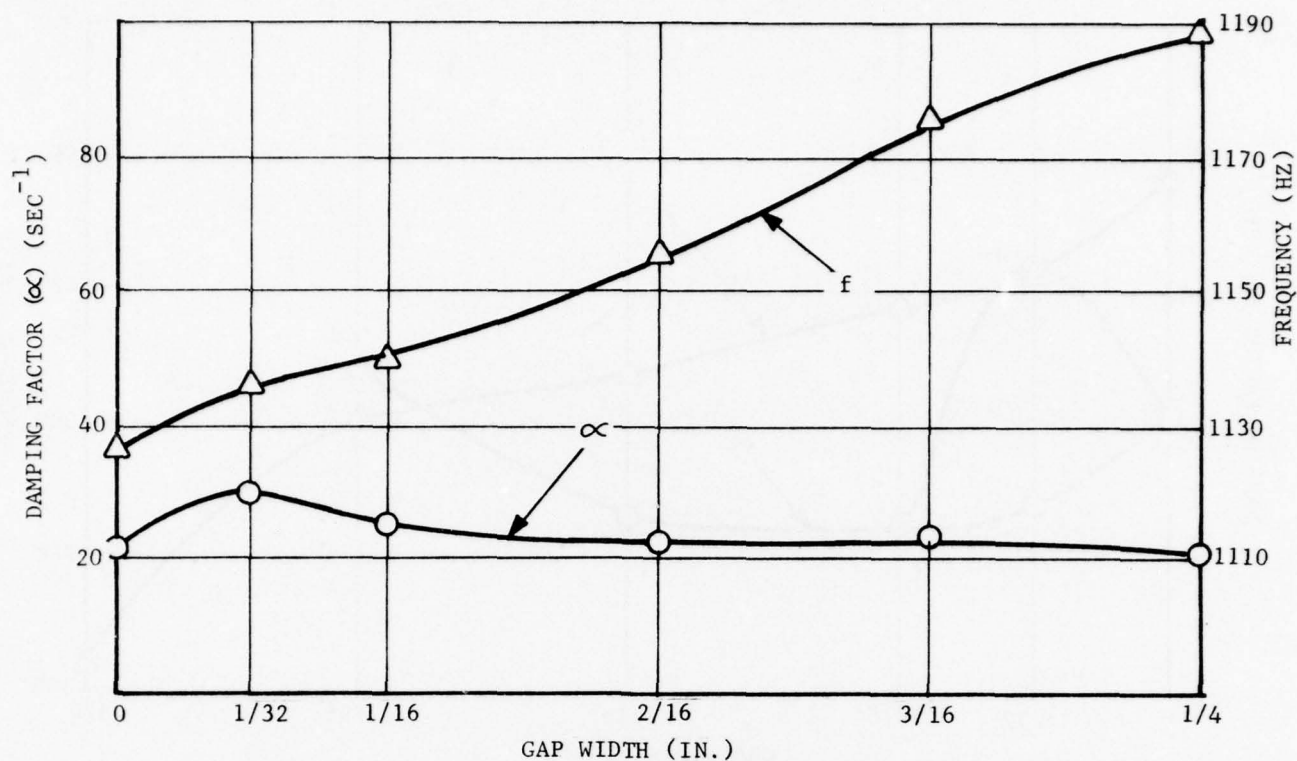


Figure 14. Damping and Frequency for the 1180 Hz Mode at 300 psi

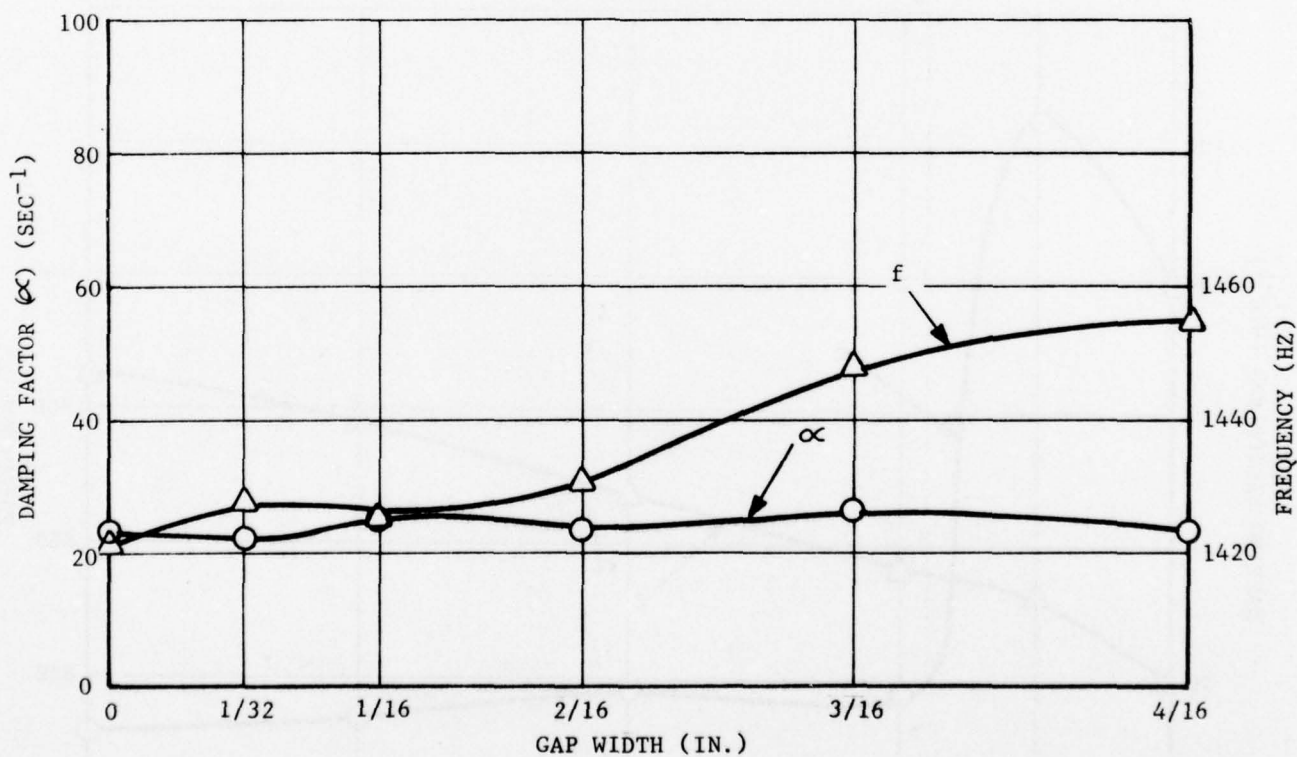


Figure 15. Damping and Frequency for the 1450 Hz Mode at 300 psi



The test configuration used to obtain the data in the tabulation was the simple cylinder sealed with CS as previously described.

#### 5. Initial Inert Model Baseline Data

The inert model was designed with an adjustable gap width so the gap could be varied to approximate conditions in a live-propellant LAM at various pressures. Several schemes were considered for comparing data from the inert model with data from the LAM. For example, the gap configuration in a LAM as a function of pressure could be estimated from finite element static pressure analyses. Then the variable gap in the inert model could be adjusted to give an equal gap volume at the particular comparison pressure. Another method was to adjust the inert model gap to give the same resonant frequency as that measured for a LAM at a particular pressure.

To definitely characterize the inert model, the frequency and damping were measured at gap widths of 0, 1/32, 1/16, 1/8, 3/16, and 1/4 inch for the first 5 strong modes, (the 625 Hz mode was omitted), at 10 psi and 300 psi chamber pressures. The results are shown in Figures 6 through 10 for 10 psi chamber pressure and in Figures 11 through 15 for 300 psi chamber pressure. The decay method was used to measure the damping factors.

#### B. LAM-179 TESTING

##### 1. Thermal Tests

When a motor with live propellant is pressurized to high pressure levels, care must be taken not to pressurize fast enough to cause dangerous heating. To ensure safe heating rates, some temperature measurements were made during pressurization through different sizes of orifices.

The motor was pressurized with nitrogen gas through a hole in the heavy aft closure plate. A thermocouple was taped to the grain near the forward end of the LAM. An orifice of approximately 0.012-inch-diameter was partially blocked by inserting a wire of approximately 0.008-inch-diameter. Using the partially blocked orifice, the motor was pressurized to 1400 psi at a rate of less than 5 psi/sec. Initially, a temperature rise of 6° F was measured. After the initial temperature increase, no further increase was detected.

The orifice was then changed to give an unrestricted hole with an approximate diameter of 0.010 inch. The new orifice allowed pressurization to 1500 psi at a rate of approximately 9 psi/sec. The maximum temperature increase for this pressurization was 18° F. Most of the temperature increase occurred during pressurization from 0 to 250 psi with little temperature change being detected from 500 to 1500 psi.

## 2. Mode Shapes and Natural Frequencies

LAM-179 was pressurized to 10 psi with nitrogen gas and acoustic resonances were found at 154, 378, 631, 858, and 1096 Hz. Using the probe system, the mode shapes were plotted for all except the 631 Hz mode. The 631 Hz mode was weak and not well defined, as was the case with the inert model at 625 Hz. The mode shapes are shown in Figures 16 through 19.

After the mode shapes were measured, the probe system was removed and the forward end closure containing a pressure transducer was installed. A frequency sweep was made and the transducer response was plotted using an X-Y recorder. The results are shown in Figures 20 and 21. The value of the voltage read on the voltmeter at each resonance peak is noted near the peak on the plots of Figures 20 and 21. Since the voltage is directly proportional to pressure, the voltage values can be considered to be normalized pressures. The values of normalized pressure show the relative magnitudes between peaks but give no indication of absolute pressure level with respect to a known reference.

Comparing the LAM frequencies with the inert model frequencies, both measured at 10 psi and with the inert model having a gap of 1/4-inch, shows good correlation between the two tests. For example, first mode frequencies of 154 Hz for the LAM versus 151 Hz for the inert model; second mode frequencies of 378 Hz for the LAM compared with 371 Hz for the inert model, etc., indicate that a 1/4-inch gap inert model nearly matches a LAM with 10 psi pressure. This was surprising since finite element results indicated a very small gap would occur in the LAM at 10 psi. However, closer examination of the LAM indicated an initial (0 pressure) gap of 0.10-inch to 0.15-inch. The LAM's were constructed in a standard configuration which included a nylon (or similar material) netting in the dome cavity to prevent dome sticking under ignition pressurization.

## 3. Mode Shapes and Frequencies Using Helium Gas

The original program plan called for the use of helium and nitrogen gas mixtures to shift the acoustic natural frequencies with respect to the structural natural frequencies. Therefore, acoustic modes and frequencies were studied with helium in the LAM. The LAM was pressurized to 100 psi using helium and then depressurized to a level of 10 psi. With helium in the motor, the first mode occurred at 250 Hz and the second mode at 611 Hz. The mode shape for the 250 Hz mode is shown in Figure 22.

At this point in the testing, the driver failed. When the driver was replaced and the LAM was again pressurized to 10 psi with helium, the 250 Hz mode had shifted to 340 Hz and the 611 Hz mode had shifted to 822 Hz. Apparently different amounts of residual nitrogen or air was present in the LAM for the two tests. An attempt was made to clear out residual gases by pressurizing and depressurizing the LAM with helium four times. The first, second, fourth, and fifth modes were then found to occur at frequencies of 406, 978, 2228, and 2873 Hz, respectively. The corresponding modes using nitrogen occurred at 154, 378, 858, and 1096 Hz. The ratio of frequency with helium to frequency with nitrogen averaged 2.6.

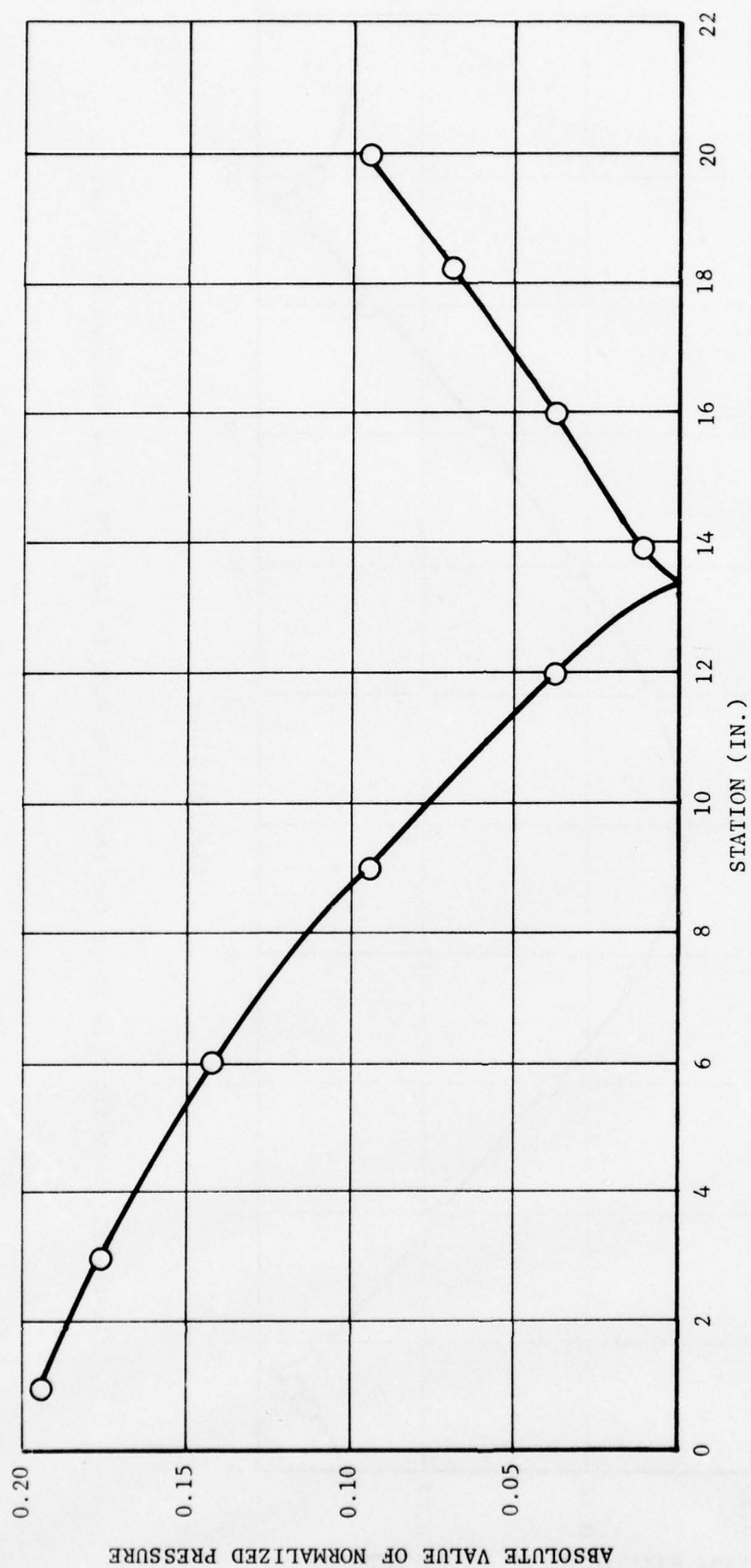


Figure 16. Acoustic Mode Shape for the 154 Hz Mode in LAM-179 Using Nitrogen at 10 psi

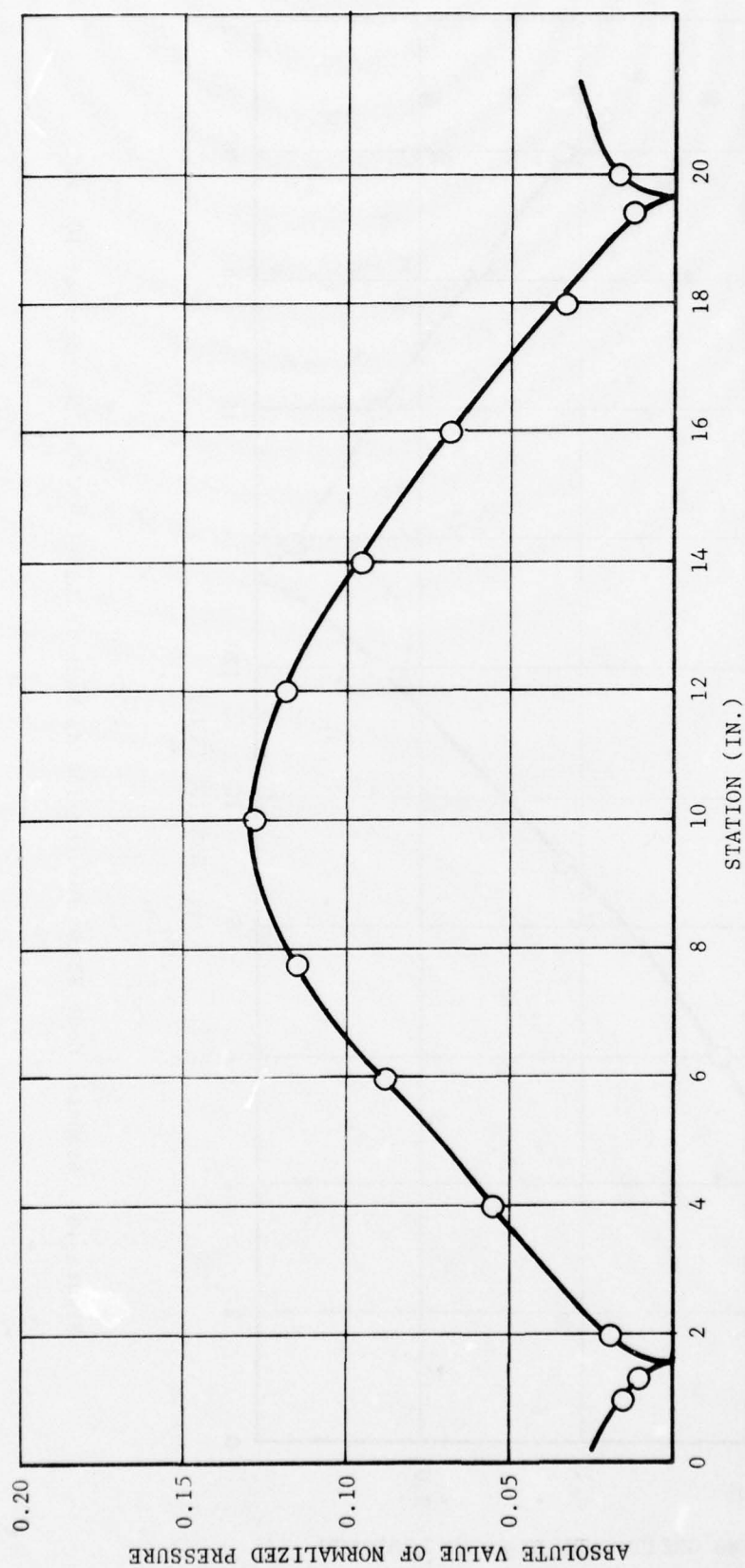


Figure 17. Acoustic Mode Shape for the 378 Hz Mode in LAM-179 Using Nitrogen at 10 psi



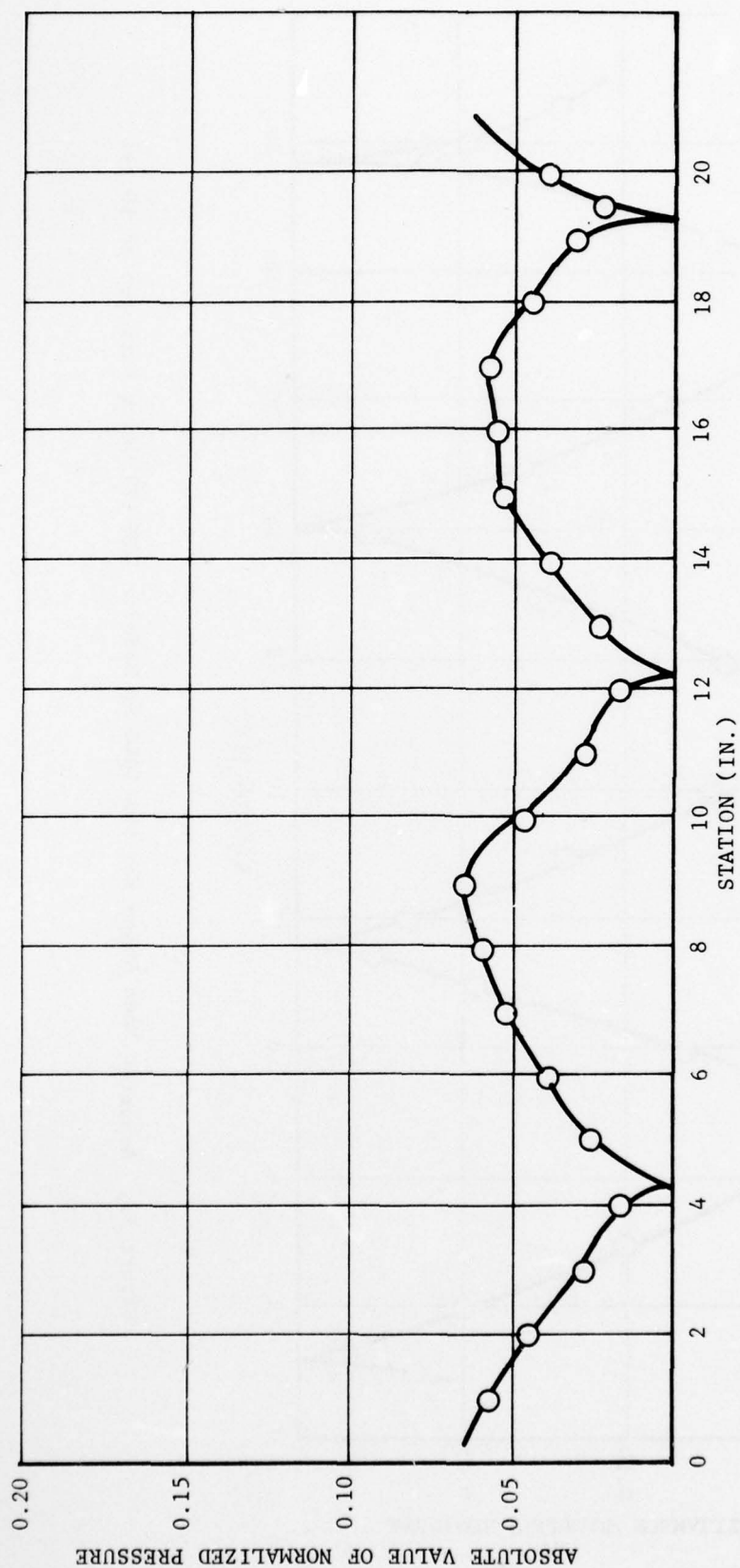


Figure 18. Acoustic Mode Shape for the 858 Hz Mode in LAM-179 Using Nitrogen at 10 psi

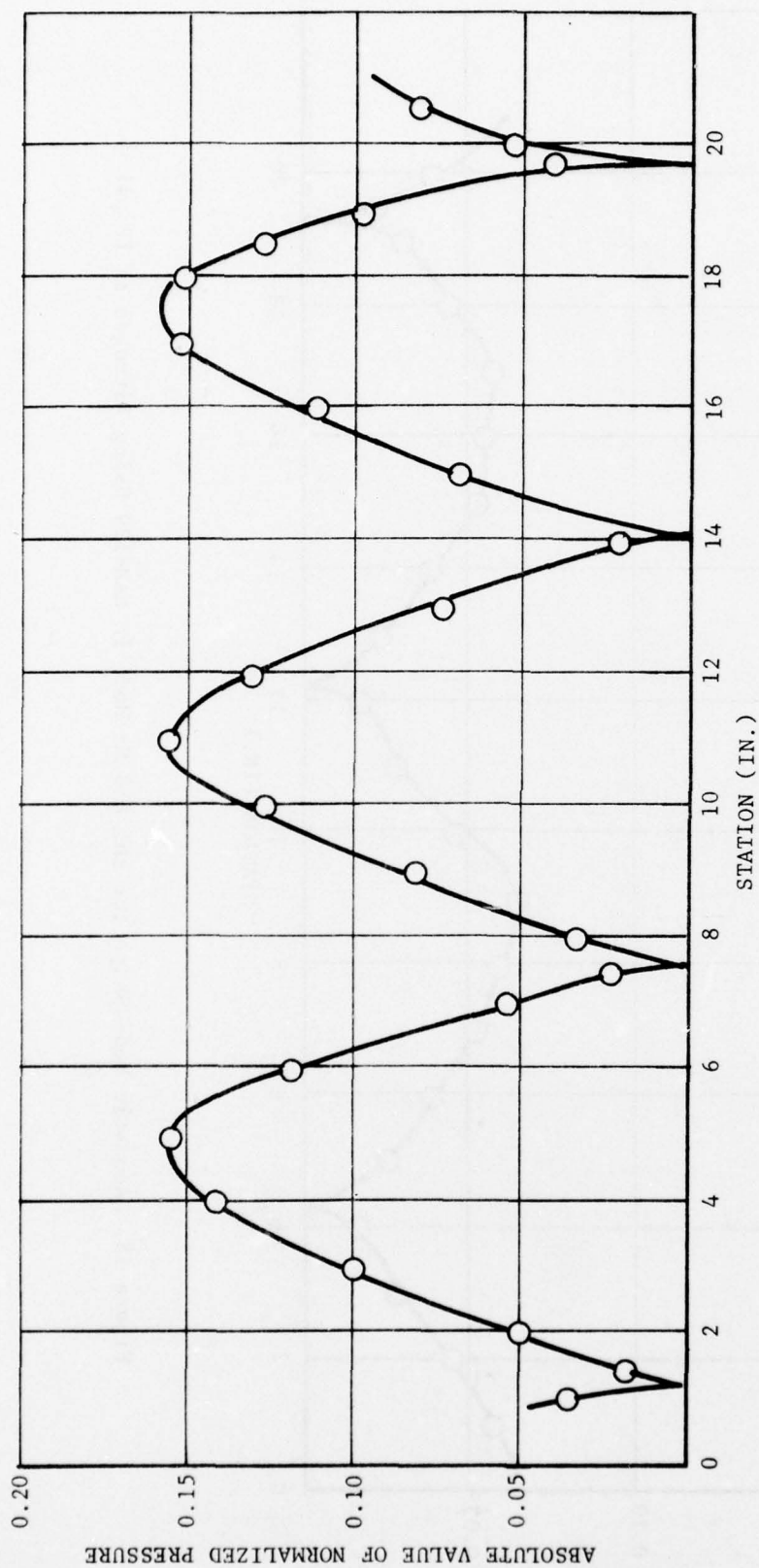


Figure 19. Acoustic Mode Shape for the 1040 Hz Mode in LAM-179 Using Nitrogen at 10 psi

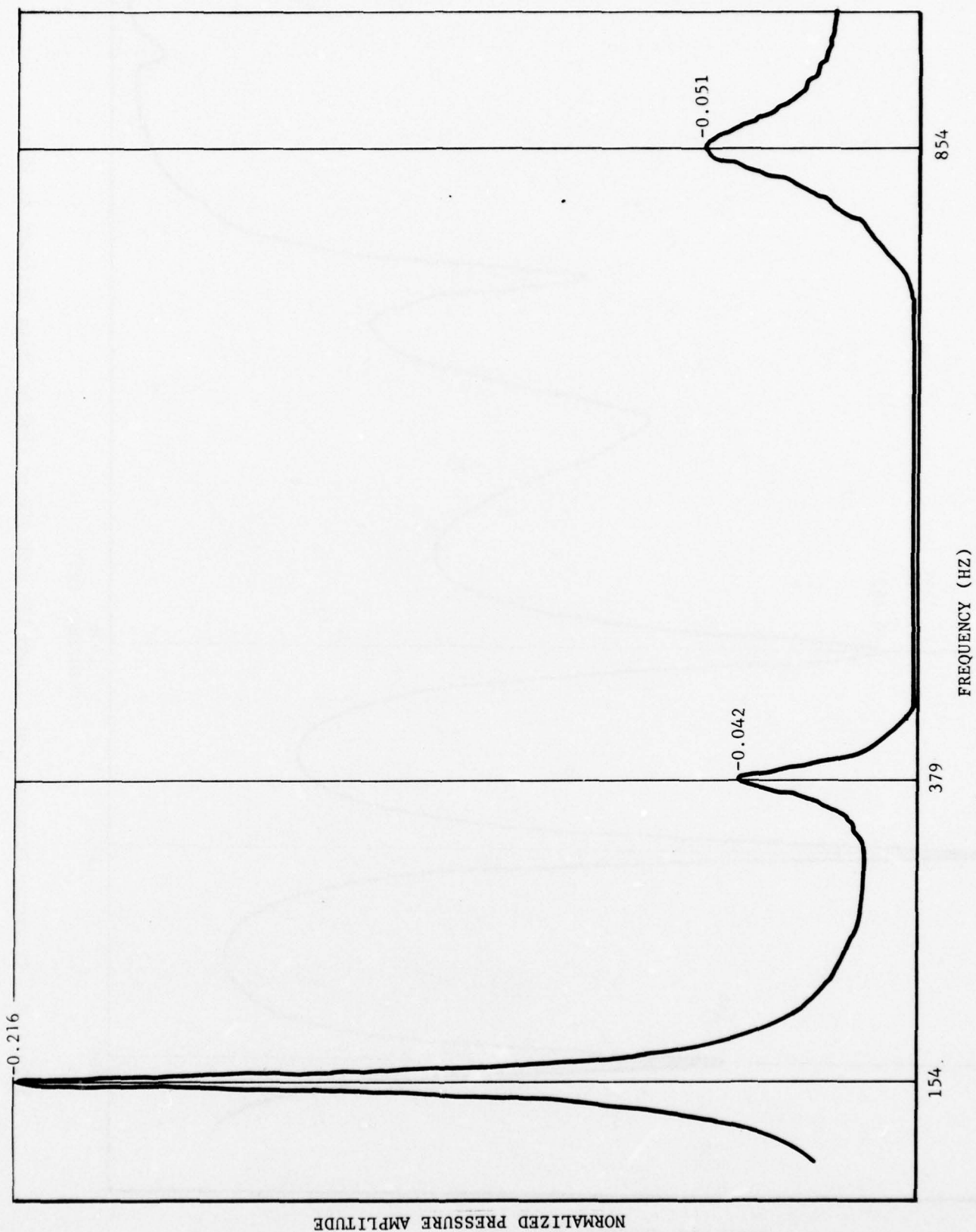


Figure 20. Frequency Response Plot for LAN-179 from 100 Hz to 900 Hz Using Nitrogen at 10 psi

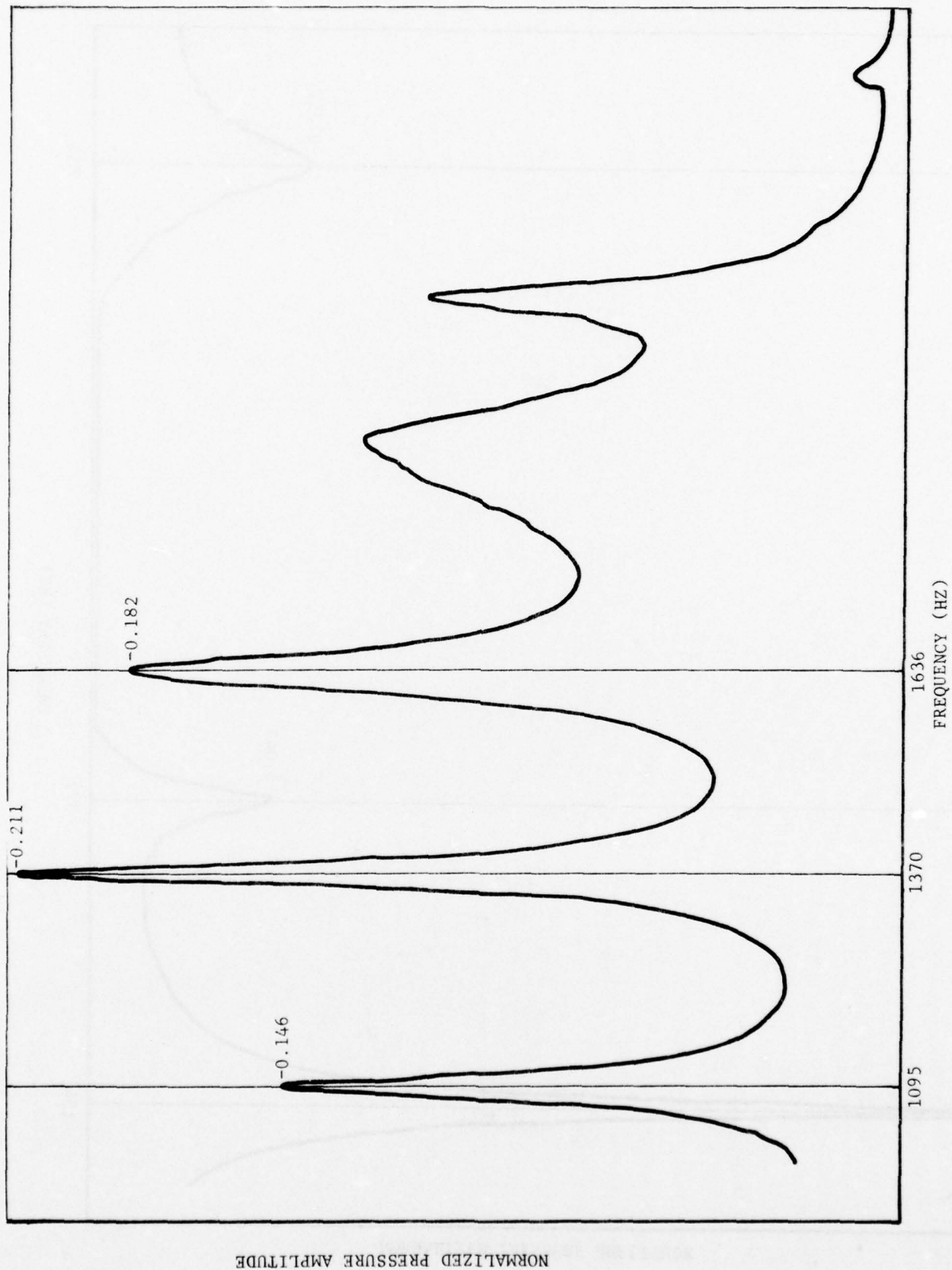


Figure 21. Frequency Response Plot for LAM-179 from 900 to 2500 Hz Using Nitrogen at 10 psi



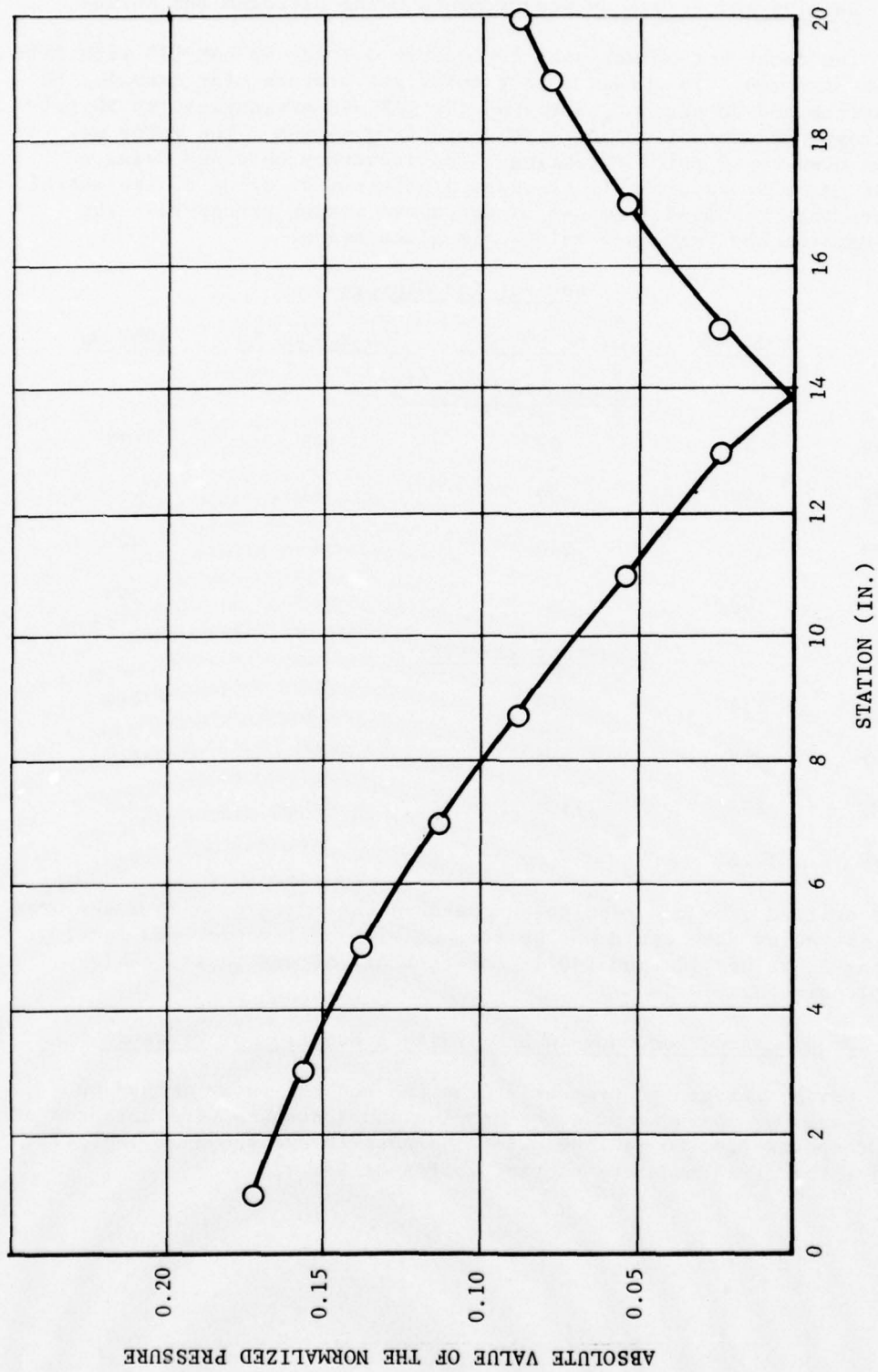


Figure 22. Acoustic Mode Shape for the First Longitudinal Mode in LAM-179 Using Helium at 10 psi ( $f = 250$  Hz)

#### 4. Damping and Frequency Measurements Using Nitrogen and Helium

The decay method was used to measure damping in LAM-179 with different gas mixtures. To obtain a particular gas mixture, for example, 50 percent helium and 50 percent nitrogen, the LAM was pressurized to 50 psi using nitrogen and then from 50 to 100 psi using helium. The motor was then blown down to 10 psi for testing. The frequency obtained using a particular gas mixture probably provides a better indication of the actual gas mixture that resulted from use of the above mixing procedure. The measured damping and frequency values are given below:

<u>Nominal Gas Mixture</u>				
<u>Mode</u>	<u>100% N<sub>2</sub></u>	<u>10% N<sub>2</sub>-90% He</u>	<u>50% N<sub>2</sub>-50% He</u>	<u>100% He</u>
<u>Damping (<math>\alpha</math>) (sec<sup>-1</sup>)</u>				
154 Hz	43	67	109	133
378 Hz	59	77	75	--
858 Hz	130	214	--	--
1096 Hz	83	--	--	290
<u>Frequency (f) (Hz)</u>				
154 Hz	154	203	257	406
378 Hz	378	501	665	978
858 Hz	858	1131	--	2228
1096 Hz	1096	--	--	2873

Data were omitted from the tabulations because the corresponding modes were weak and the noisy data could not be reduced with confidence. In fact, the damping of values 130 and 290 in the tabulations are questionable because of noisy data.

#### 5. Damping and Frequency in LAM-179 as a Function of Pressure

Using nitrogen to pressurize the LAM and the decay method to reduce the damping measurements, the damping and frequency were measured at various pressures from 10 to 1500 psi. The results are shown in Table 7. Results for the first mode are plotted in Figure 23.

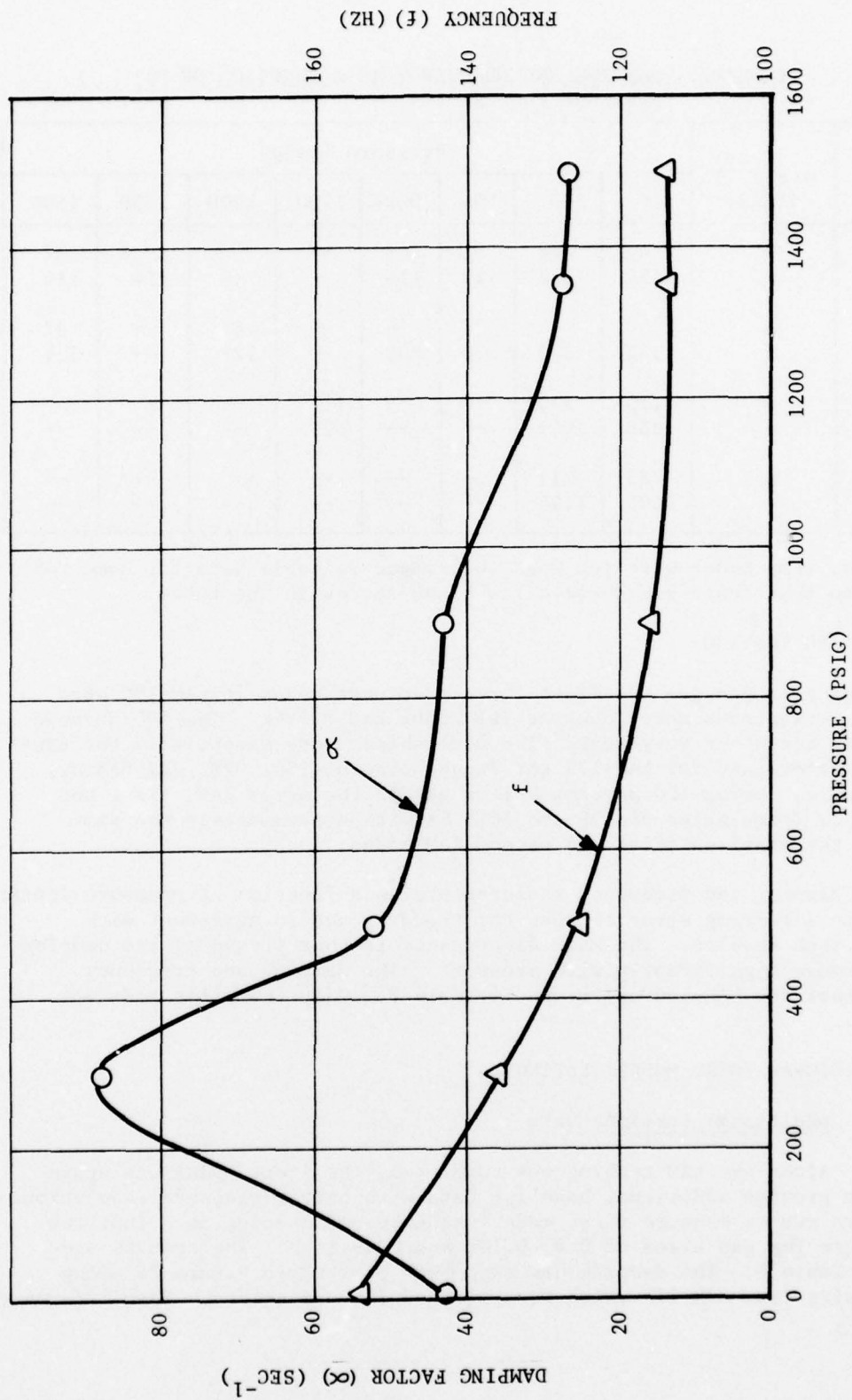


Figure 23. Damping and Frequency Measured for the First Mode in LAM-179 as a Function of Pressure

TABLE 7. DAMPING AND FREQUENCY AS A FUNCTION OF PRESSURE FOR LAM-179

Mode	$\alpha(\text{sec}^{-1})$ f(Hz)	Pressure (psig)							
		10	300	500	900	1100	1200	1350	1500
154 Hz	$\alpha$	43	88	52	43	--	--	27.6	27
	f	154	136	125	116	--	--	114	114
378 Hz	$\alpha$	59	49	74	--	--	81	--	37
	f	378	353	330	332	--	321	--	324
858 Hz	$\alpha$	130	346	--	--	112	--	--	--
	f	858	945	--	--	621	--	--	--
1096 Hz	$\alpha$	83	217	--	--	--	--	--	--
	f	1096	1145	--	--	--	--	--	--

As before, some modes were too weak to produce reliable data for some conditions so that there are quite a few blank spaces in the table.

#### C. LAM-180 TESTING

Using nitrogen gas the first three prominent modes in LAM-180 were checked. Resonances were found at 161, 386, and 805 Hz. The 600 Hz mode was either absent or very weak. The mode shapes were essentially the same as those determined for LAM-179 for frequencies of 154, 378, and 858 Hz, respectively. Using 100 percent helium gas in the motor gave first and second mode frequencies of 429 and 1018 Hz with approximately the same shape as the previous first and second LAM modes.

The damping and frequency measurements as a function of pressure appear to contain a testing error because the trend is not in agreement with previous test results. The main discrepancy is that frequency and damping do not change significantly with pressure. The damping and frequency measurements for LAM-180 are given in Table 8. Only the first mode was examined.

#### D. ADDITIONAL INERT MODEL TESTING

##### 1. Additional Baseline Data

After the LAM testing was completed, the inert model was again tested to provide additional baseline data with better pressure resolution. Tests were run to measure first mode frequency and damping as a function of pressure for gap sizes of 0.0, 0.18, and 0.49 inch. The results are shown in Table 9. The damping has also been plotted in Figure 24 along with results from LAM-179 which were plotted for comparison. The difference



between LAM damping and inert model damping was expected to increase monotonically with increasing pressure. Figure 24 shows that the difference between LAM and inert model damping does not increase monotonically.

TABLE 8. DAMPING AND FREQUENCY AS A FUNCTION OF PRESSURE FOR LAM-180

Pressure (psig)	Frequency (f) (Hz)	Damping ( $\alpha$ ) ( $\text{sec}^{-1}$ )
0	148	44
10	158	44
100	158	97
200	156	43
300	156	42
400	157	47
500	157	49
600	158	43
700	158	41
800	160	43
900	158	47
1000	158	42
1100	159	47
1200	158	46
1300	159	44
1400	159	49
1500	159	47

TABLE 9. ADDITIONAL FREQUENCY AND DAMPING DATA FOR THE INERT MODEL

Pressure (psig)	Gap = 0-Inch		Gap = 0.18-Inch		Gap = 0.49-Inch	
	f(Hz)	$\alpha(\text{sec}^{-1})$	f(Hz)	$\alpha(\text{sec}^{-1})$	f(Hz)	$\alpha(\text{sec}^{-1})$
0	187.2	28.7	151.0	31.6	124.1	31.6
10	190.1	30.2	150.9	36.0	123.3	34.3
100	189.4	36.2	145.2	35.9	121.2	49.6
200	187.5	46.9	141.6	28.3	118.1	37.2
300	186.8	45.4	140.4	24.2	116.5	26.9
400	186.4	51.4	139.4	20.3	115.6	21.6
500	185.0	56.0	139.2	19.4	116.7	19.0
600	180.9	61.7	139.1	18.3	115.1	16.0
800	179.5	62.4	138.8	16.0	114.8	13.4
1000	177.9	59.0	139.2	15.8	115.1	11.2
1200	--	--	--	--	115.8	10.7
1250	117.6	53.4	139.5	15.5	--	--
1300	--	--	--	--	116.3	10.4
1400	--	--	--	--	116.9	11.4
1440	--	--	--	--	117.6	12.7
1500	176.3	56.1	141.5	15.2	--	--

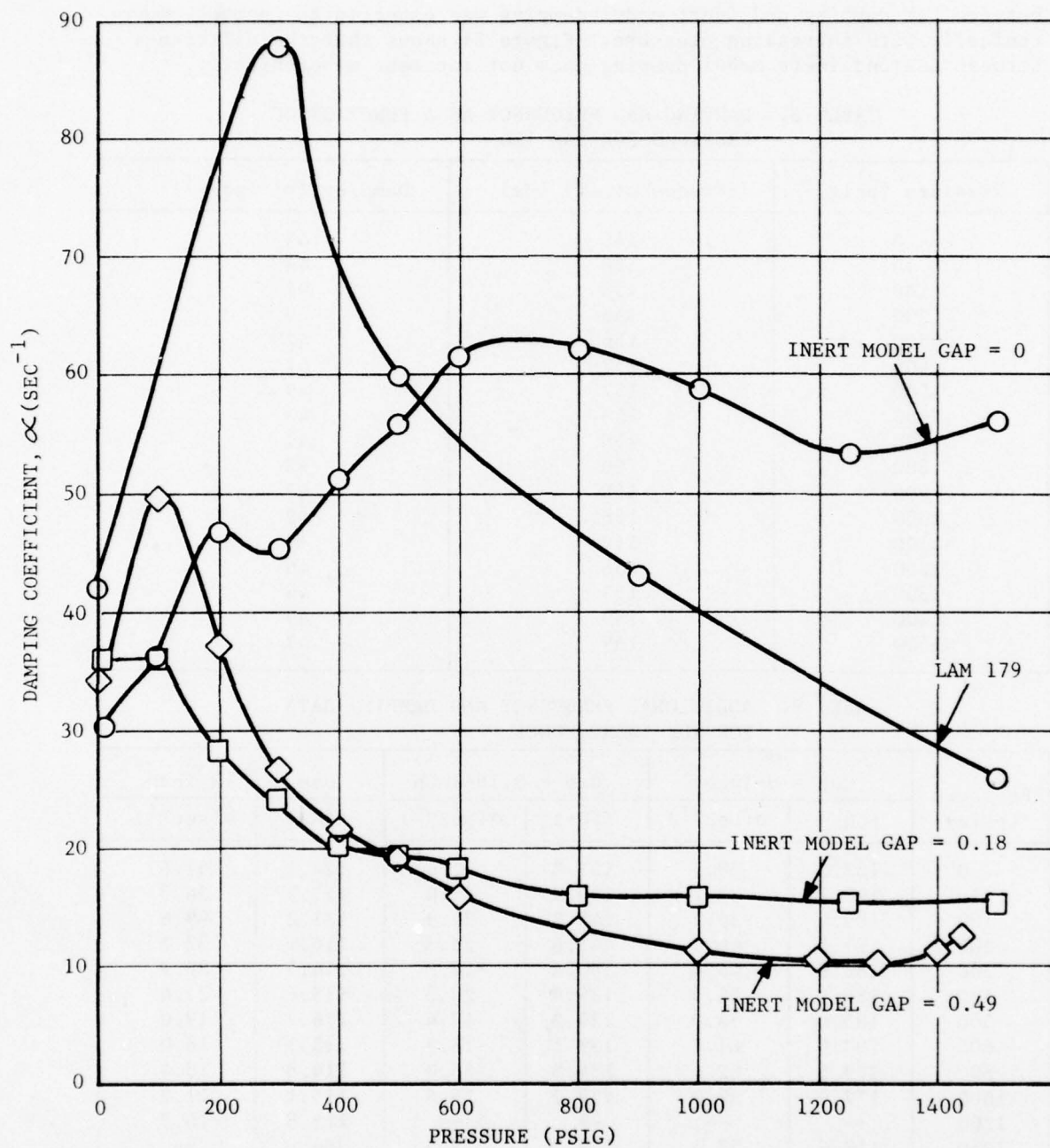


Figure 24. Baseline Damping Data from Inert Model Compared to Results from LAM-179

## 2. Investigation of Speaker Coupling

Because damping measurements on the LAM's and on the inert model did not produce the expected results, consultant Dr. Fred Culick was asked to examine the experimental set-up. Dr. Culick suggested trying a smaller hole between driver and acoustic cavity and fastening the driver down more firmly. The driver had previously been held in place by polyurethane foam packed in the driver cavity.

A new end plate was fabricated with a 1/4-inch diameter hole separating the driver cavity and the acoustic cavity. Measurements made using the 1/4-inch diameter hole are given in Table 10. The results are significantly different than those obtained with the regular end plate with a 1-3/8-inch diameter hole.

TABLE 10. DAMPING AND FREQUENCY MEASUREMENTS MADE ON THE INERT MODEL USING AN END PLATE WITH 1/4-INCH DIAMETER HOLE (GAP = 0.49-INCH)

Pressure (psig)	Frequency f (Hz)	Damping $\alpha$ (sec <sup>-1</sup> )
0	123.7	noisy (26-43)
100	121.4	45.4
200	119.0	44.1
300	117.6	36.4
400	116.1	29.99
500	114.8	24.36
600	114.2	21.60
800	113.7	17.43
1000	113.8	15.78
1250	114.7	14.07
1450	116.2	14.74

Next, an endplate with a 1/16-inch diameter hole and a provision for rigidly mounting the driver, was fabricated. The endplate, complete with new driver, was installed on the inert model. The pressure tests were repeated and the results are shown in Table 11 and are plotted in Figures 25 and 26.

Data in Tables 10 and 11 show that use of the modified endplate resulted in drastically different response measurements. It thus appears likely that all data gathered during this program are invalid. There is no reason to accept the data from the last test (Table 11) as valid until further studies show that the particular driver-endplate design yields an uncoupled acoustic cavity response.

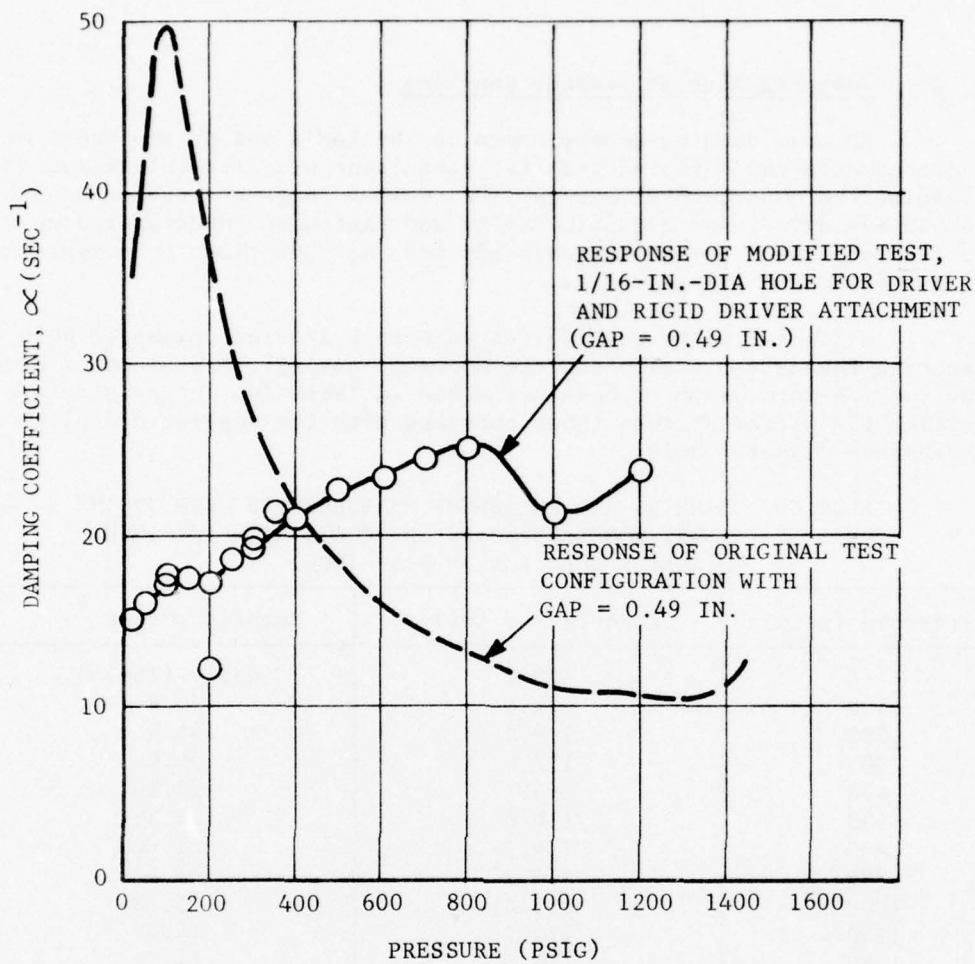


Figure 25. Damping Factor Versus Pressure for End Plate with 1/16 Inch Diameter Hole

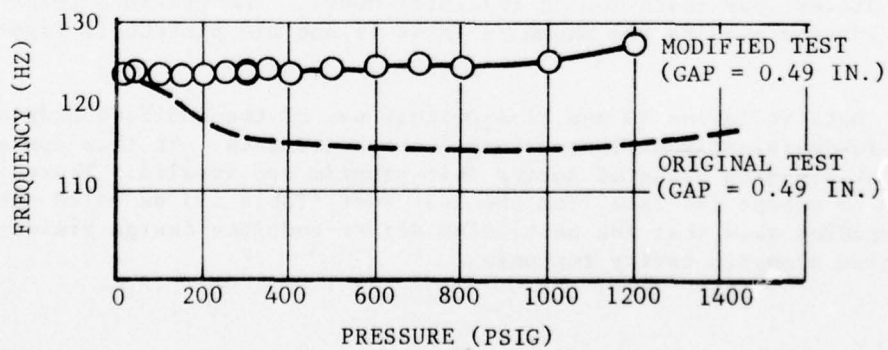


Figure 26. Frequency Versus Pressure for End Plate with 1/16 Inch Diameter Hole



TABLE 11. DAMPING AND FREQUENCY MEASUREMENTS MADE ON THE  
INERT MODEL USING A 1/16-INCH DIAMETER HOLE IN  
THE END PLATE (GAP = 0.49 INCH)

Pressure (psig)	Frequency f (Hz)	Damping $\alpha$ (sec <sup>-1</sup> )
20	123.8	15.19
100	123.9	17.69
200	123.5	12.28 (noisy)
300	123.6	19.86
400	123.9	20.91
500	124.2	22.69
600	124.9	23.48
700	125.1	24.49
800	124.9	25.11
1000	125.5	21.30
1200	127.5	23.83

## SECTION V

### PROPELLANT DYNAMIC PROPERTIES DETERMINATION

Task II of the program called for a NASTRAN analysis of the LAM's. The NASTRAN models included the propellant grain. It was necessary to know the grain dynamic moduli to obtain a reasonable representation of the viscoelastic characteristics of the grain. A well established, reliable, accurate, and universally acceptable method for measuring grain dynamic properties at frequencies up to 1000 Hz does not exist. The program plan stated that the Gottenberg torsional shear testing machine would be used if a better method could not be found.

Various problems were experienced with the Gottenberg machine. To provide data for the program, stress relaxation data were converted to dynamic moduli. This section discusses the efforts to obtain data from the Gottenberg machine and presents the data obtained by converting relaxation moduli.

#### A. DYNAMIC MODULI FROM STRESS RELAXATION DATA

Tensile stress relaxation modulus values were converted to dynamic moduli for the three propellants of interest, VRX-2, VSF-3, and FKM. Two different methods were used to do the conversion: (1) The power law modulus assumption method, and (2) the Fourier transform integral conversion method. A memorandum giving complete details of the conversions is included as Appendix A. The converted moduli are shown in Appendix A, Figures A-3 through A-8.

#### B. THE GOTTENBERG TORSIONAL SHEAR TESTING MACHINE

The apparatus referred to as the Gottenberg Testing Machine is described in a report by Gottenberg and Christensen<sup>(2)</sup> where it is referred to as the High Frequency Apparatus. The apparatus was designed to apply forced torsional oscillations to a right circular cylinder whose ends are bonded to rigid boundaries. The apparatus was acquired by Hercules from Colorado University for use on this and other projects.

Various problems were experienced in attempting to use the testing machine. The fact that the machine is cumbersome slowed the work to resolve the problems. The machine and instrumentation must be calibrated and

(2) Gottenberg, W. G. and Christensen, R. M., On the Experimental Determination of the Complex Shear Modulus of a Linear Isotropic Viscoelastic Solid, 6121-6777-RU000, EM 13-14, Space Technology Laboratories, Inc., One Space Park, Redondo Beach, California, 1 June 1963.

adjusted at each frequency using a steel specimen in place of propellant. The machine must then be disassembled and then reassembled with propellant in place of the steel calibration sample. It must therefore be disassembled and reassembled twice for each different test frequency. Another troublesome feature is that the waveform becomes extremely distorted at a certain input level and the level at which the extreme distortion occurs must be determined at each test frequency. According to the machine designer, Dr. Gottenberg, tests should be run at a level below the distortion threshold.

When the various problems had apparently been overcome, the machine was used to measure the dynamic shear moduli of VSF-3 propellant at two different frequencies. At a frequency of 250 Hz, the real part of the shear modulus was measured to be 8566 psi. This compares with an approximate value of 2366 obtained by converting relaxation modulus data. The test results are higher than the estimated modulus value by a factor of 3.6, but the estimate could be inaccurate. Past experience with converting relaxation modulus data to dynamic moduli indicates that only a moderate degree of accuracy can be expected.

To evaluate the procedure and testing set-up currently being used to obtain data with the Gottenberg machine, samples of FKM propellant were prepared and tested. FKM was selected because data from an earlier use of the Gottenberg machine were available for comparison. Considerable confidence was placed in the earlier FKM data because a careful evaluation indicated that measured values were quite reasonable. Dr. Gottenberg personally assisted in the acquisition of the earlier FKM data approximately 6 years ago. At 250 Hz, the earlier FKM data shows a real shear modulus of 1550 psi. The current test program yielded a value of 2878 psi, still too high by a factor of 1.86. This result was fairly encouraging because small differences in the manufacture of FKM over 6 years time and lot-to-lot variations could explain a large part of the difference. The corresponding FKM modulus from converted relaxation data is 1400 psi.

## SECTION VI

### STRUCTURAL DAMPING AND ACOUSTIC ANALYSES

The analysis work in this program was originally directed toward demonstrating the accuracy to which structural damping rates could be calculated. In keeping with the original objectives of the program, a NASTRAN model of a LAM was constructed and analyzed. Because of problems being experienced with the experimental work of Task I, the analysis effort was expanded to include a rod-organ pipe model and methods of solution other than NASTRAN.

Despite the availability of general purpose dynamics codes that could be easily adapted for structural damping calculations, relatively little effort has been expended in this area. The early experimental and analytical work of Ryan, Coates, and Baer<sup>(3)</sup>, experimental studies at Thiokol<sup>(4)</sup>, and analytical work of Anderson<sup>(5)</sup>, comprise the published structural damping applications in the solid rocket industry. The more recent and extensive work of Anderson involved the application of a Hercules finite-element code, developed originally for grain vibration studies, to the calculation of acoustic modes and frequencies, as well as structural damping. The NASTRAN code<sup>(6)</sup> can also be used for structural damping calculations with little or no modification. In fact, any general purpose dynamics code that considers viscous damping and has an eigenvalue or frequency response capability can be used for structural damping calculations. Fluid behavior can be approximated by assigning solid elements a very low shear modulus in comparison to the bulk modulus.

The code used by Anderson has overlapping tension and shear elements to represent the grain and special fluid elements for the acoustic cavity. The code solves only the frequency response problem. The damping exponent,  $\alpha$ , is obtained from the ratio of the energy loss rate to the stored energy i.e.,  $\alpha = 1/2 \frac{\dot{W}}{W}$ . It is necessary to excite the acoustic cavity at a selected

- (3) Ryan, N. W., Coates, R. L., & Baer, A. D., "Participation of the Solid Phase in the Oscillatory Burning of Solid Rocket Propellants," Ninth Symposium (International) on Combustion, Academic Press, (1963).
- (4) Stibor, G. S., Poseidon C3 First Stage Motor Acoustic Studies Simulation and Analysis of Observed Static Test Phenomena, Report No. TWR-4209, Thiokol Chemical Corporation/Hercules Incorporated Joint Venture, 24 August 1970.
- (5) Anderson, J. M., "Structural Damping of Acoustic Oscillations in Solid Propellant Rocket Motors," Eighth JANNAF Combustion Meeting, CPIA Publication 220, November 1971.
- (6) The NASTRAN User's Manual, Level 16.0, NASA SP-222(03), March 1976.



node and perform a frequency sweep to achieve a resonant condition. Although the code does not use the Herrmann reformulation<sup>(7)</sup> for Poisson's ratio near 0.5, acceptable propellant modeling is still accomplished.<sup>(8)</sup>

The NASTRAN code has previously been used in combustion instability studies to obtain acoustic modes and frequencies and/or component vibration levels. However, in this program, the NASTRAN code was used as the primary tool for structural damping calculations. With the NASTRAN code it was necessary to model the grain with 3-D elements, even though a 2-D solution was desired, because of the solid-fluid coupling procedure used in the formulation. The available versions of NASTRAN do not contain reformulated grain elements. Hercules has installed a reformulated 3-D element into their modified Level-15 version. The damping exponent obtained directly from the complex eigenvalue approach is generally more desirable because the modes and frequencies are obtained directly, without need for a resonant frequency search.

The LAM NASTRAN model was analyzed using both the frequency response method and the eigenvalue method to obtain a comparison. In addition to the LAM analyses, this section of the report covers acoustic cavity analyses and the rod-organ pipe study. The acoustic cavity analyses were conducted to obtain natural frequencies and mode shapes for comparison with data from the inert model. The rod-organ pipe study was conducted to confirm previous analysis results and to provide a better understanding of the effect of pressure on structural damping. The rod-organ pipe model was also used to help resolve differences between NASTRAN and the Hercules finite element code.

A closed-form analytical solution was obtained for a damped rod-organ pipe model to referee a subtle difference in behavior predicted by the two finite element approaches. The analytical solution provided structural damping levels consistent with those of the NASTRAN and the Hercules overlapping element codes. However, complex structural-acoustic coupling behavior with significant frequency shifts is predicted when fundamental structural and acoustic modes are in close proximity. The two finite element codes differ in their ability to match the analytically predicted frequency shifts. The overlapping element code agrees better with the analytical solution than NASTRAN, but both codes provide measurable frequency errors.

---

(7) Herrmann, L. R., "Elasticity Equations for Incompressible and Nearly Incompressible Materials by a Variational Theorem," AIAA Journal 3, No. 10, 1965.

(8) Anderson, J. M., & Christiansen, H. N., "Behavior of the Finite Element Stiffness Method for Nearly Incompressible Materials," Sixth Annual Meeting of the ICRPG Mechanical Behavior Working Group, 1967.

All analysis work mentioned above was performed under Task II of this program. This report section describes the analyses and presents the results.

#### A. APPROACH

##### 1. LAM NASTRAN Model

A finite element model of a LAM was made to include both gas (fluid) and grain (solid) elements for analysis using the hydroelastic analysis capability in NASTRAN. By using a complex eigenvalue solution with such a model, the damping factor ( $\alpha$ ) and natural frequency ( $f$ ) can be determined for any of the natural modes. A computer plot of the LAM model is shown in Figure 27. The complete LAM was simulated by applying symmetrical boundary conditions to the 2 boundary surfaces of a 5-degree segment model. Reformulated solid elements (CDUM) and fluid elements were used to represent the grain and acoustic cavity respectively. The polyurethane foam surrounding the acoustic driver (speaker) was modeled as a low modulus material with no acoustic cavity. The elements representing the gas in the acoustic cavity are not shown in the figure. The gas elements have the same spacing as the grain elements and one gas element covers the distance from the centerline to the grain surface. Note that the particular LAM model shown in Figure 27 has a small dome cavity modeled in the forward end.

Orthotropic stiffness properties were used in the case model. The case thickness used was 0.08 inch in the cylindrical section and case density was  $1.9161 \times 10^{-4}$  lb sec<sup>2</sup>/in.<sup>4</sup>. Propellant density used was  $1.6278 \times 10^{-4}$  lb sec<sup>2</sup>/in.<sup>4</sup>. Propellant stiffness for formulation VSF-3 at 154 Hz was represented by a modulus of 6200 psi (real part of the complex modulus) and a loss tangent of 0.5323 (ratio of imaginary modulus to real modulus). The corresponding Poisson's ratio for the propellant was 0.49898. For the gas, (nitrogen at 10 psig), a density of  $1.638 \times 10^{-7}$  lb sec<sup>2</sup>/in.<sup>4</sup> and a bulk modulus of 31.47 psi were used. The values given are typical and some were varied between computer runs.

##### 2. Acoustic Cavity Model

The acoustic cavity portion of the LAM model was used as a separate model to represent the inert rigid-walled motor. Typical properties used were the same as those given for the nitrogen used in the LAM model. The density and bulk modulus were changed to represent different pressures in the cavity. The configuration of the acoustic cavity model was varied to represent no dome cavity, a straight radial cavity (inert model), and a curved cavity (LAM). Only real eigenvalue analyses were conducted on the acoustic cavity model because no damping was included in the gas elements.

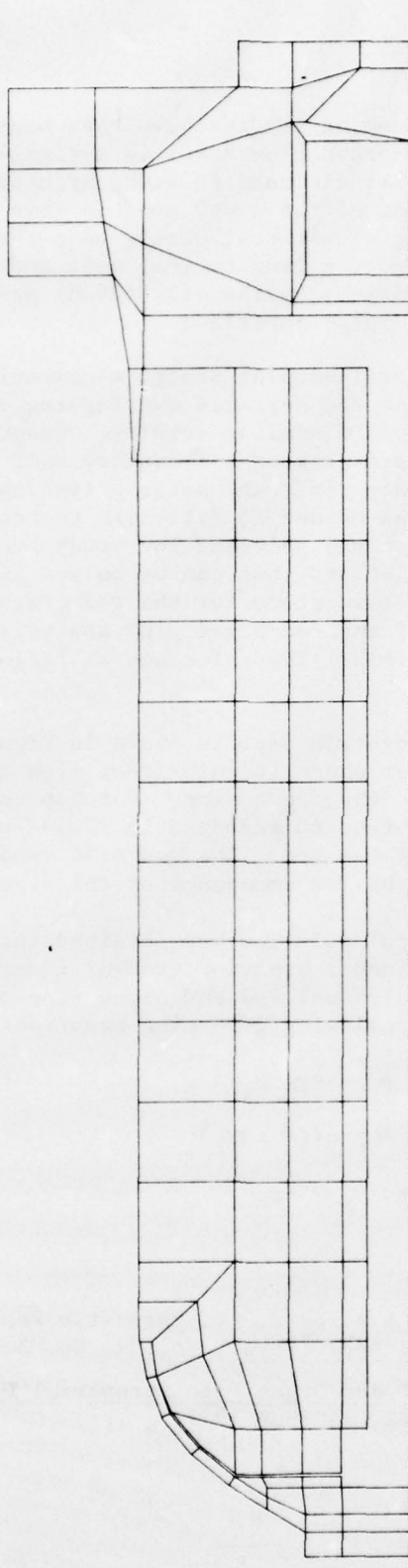


Figure 27. Computer Plot of the Grid for the LAM Finite Element Model

### 3. Rod-Organ Pipe Model

Previous structural damping studies have been based on a rod-organ pipe model.<sup>(8,9)</sup> The rod-organ pipe model is a simple one-dimensional (1-D) model that has the essential elements to study structural damping in a simple form. The configuration of the model used in this program is shown in Figure 28. The damping of interest occurs when the undamped gas in the organ pipe is oscillating in a longitudinal mode and the heavily damped propellant rod is being driven by the oscillating pressure applied to the rod by the gas at the rod-pipe interface.

In the current structural damping study, a comparison was initiated between the NASTRAN and the Hercules overlapping element solutions. In general, the two methods provided similar results. However, there were disturbing differences in predicted resonant frequency shifts as the fluid properties were varied to simulate different motor operating pressures. It became evident that a referee was needed to establish the correct simulation. The rod-organ pipe problem was selected for study because of the earlier work and because it is 1-D and thus can be solved in closed form. A solution comparison and parametric study for the rod-organ pipe are given below. The description of the rod-organ pipe analysis is a condensation of a more extensive report.<sup>(10)</sup> The reference is included in this report as Appendix B.

A schematic of the rod-organ pipe is shown in Figure 28. The organ pipe has rigid walls except where it interfaces with the rod. The rod is fixed on the end opposite the organ pipe. For typical rocket motor properties, the organ pipe will tend to resonate in closed-closed modes because of the high impedance of the rod. The rod will tend to resonate in fixed-free modes because of the low impedance of the organ pipe.

A closed-form analytical solution was obtained for the rod-organ pipe for assumptions of long, slender behavior (radial inertia is neglected). Physical behavior within the individual rod and organ pipe components is assumed to be described by the following governing equations.

$$\text{Continuity} \quad \rho_t = -\rho_o u_x \quad (1)$$

$$\text{Dynamic State} \quad \rho = c^2(\rho_o + \tau \rho_t) \quad (2)$$

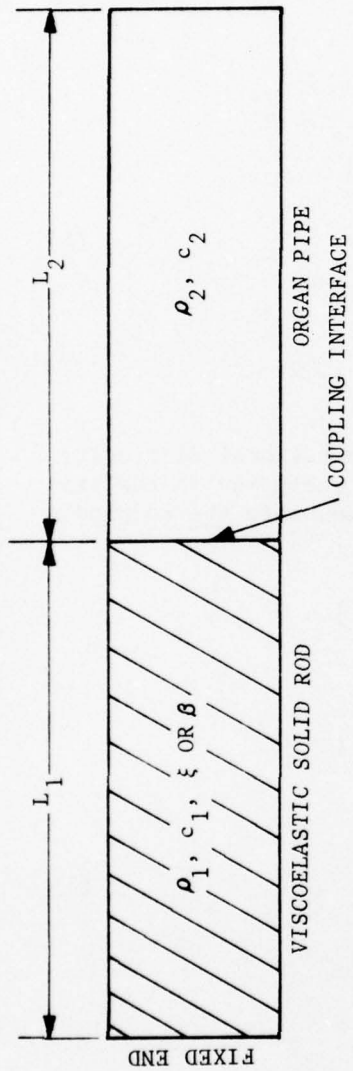
$$\text{Momentum} \quad \rho_o u_t = -p_x \quad (3)$$

(9) McClure, F. T., Hart, R. W., & Bird, J. F., "Acoustic Resonance in Solid Propellant Rockets," J. Appl. Phys., Vol 31, No. 5, May 1960.

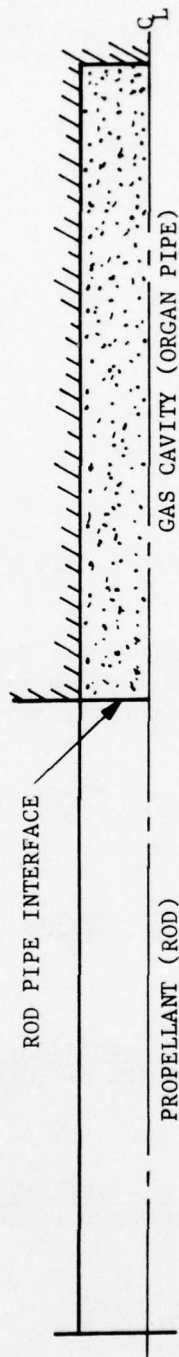
(10) Peterson, N. L., Analysis of Rod-Organ Pipe Structural Damping Model, Hercules Memo, Misc/6/20-7482, 14 June 1977.



(a) SCHEMATIC SHOWING PARAMETERS



(b) SKETCH OF THE ROD-ORGAN PIPE MODEL



(c) FINITE ELEMENT MODEL OF THE ROD-ORGAN PIPE



Figure 28. Rod-Organ Pipe

The assumptions are used that particle velocities are zero on the external ends of the coupled system, and that both pressure and particle velocity are continuous at the coupling interface. From these assumptions, the characteristic equation for free oscillations in the coupled rod-organ pipe is obtained in the form

$$\frac{\tan(K_1 L_1)}{\tan(K_2 L_2)} + \frac{\rho_1 K_1}{\rho_2 K_2} = 0,$$

where

$$K_j = \frac{\omega - i\alpha}{c_j \sqrt{R_j}} e^{i \frac{\varphi_j}{2}} = \gamma_j + i\chi_j$$

$$\varphi_j = \tan^{-1} \frac{\omega \tau_j}{1 - \alpha \tau_j} \quad (4)$$

and

$$\sqrt{R_j} = \{(1 - \alpha \tau_j)^2 + (\omega \tau_j)^2\}^{1/4} \text{ for } j = 1, 2.$$

The complex wave numbers,  $K_j$ , create a computational difficulty in the direct solution of Equations (4) due to their inclusion in the trigonometric functions. The equations may be transformed into the coupled real equations

$$\Theta_1 + R_b \left\{ \Theta_2 \cdot \cos \frac{\varphi_2 - \varphi_1}{2} + \chi_2 \cdot \sin \frac{\varphi_2 - \varphi_1}{2} \right\} = 0$$

and

$$-\chi_1 + R_b \left\{ \Theta_2 \cdot \sin \frac{\varphi_2 - \varphi_1}{2} - \chi_2 \cdot \cos \frac{\varphi_2 - \varphi_1}{2} \right\} = 0$$

where

$$\Theta_j = \frac{\sinh(2X_j)}{\cosh(2X_j) + \cos(2Y_j)} \quad (5)$$

$$\chi_j = \frac{\sin(2Y_j)}{\cosh(2X_j) + \cos(2Y_j)}$$

and

$$R_b = \frac{\rho_1 c_1}{\rho_2 c_2} \sqrt{\frac{R_1}{R_2}} \quad (j = 1, 2)$$

This system of equations was solved on a digital computer using a generalized Newton's method to find the values of  $\omega$  and  $\alpha$  from initial estimates input through an interactive control terminal.

The finite-element solutions for the rod-organ pipe have radial inertia. In the overlapping element solution, only "tension" elements need to be used. The organ pipe is simulated in a pure 1-D sense (no radial inertia) and the rod has lumped radial inertia at its outer boundary nodes. In the NASTRAN solution, some degree of radial inertia is present in both the rod and organ pipe. The organ pipe was represented alternately with NASTRAN using fluid and reformulated solid (CDUM) elements.

Comparison solutions were obtained for the rod-organ pipe parameters given in Table 12. The basic grid networks for the NASTRAN and overlapping element solutions used 28 elements, 14 spaced axially in the rod and 14 axially in the organ pipe. The element lengths were smallest near the rod-organ pipe interface, and graduated as outlined in Table 12. Typical propellant properties were used in the comparison. For one of the NASTRAN solutions, the basic grid was refined by cutting the radial and axial grid spacing in half.

TABLE 12. ROD-ORGAN PIPE PARAMETERS FOR  
FINITE-ELEMENT SOLUTION COMPARISON

Length of rod, $L_1$ (in.)	= 9.5
Length of organ pipe, $L_2$ (in.)	= 9.5
Diameter (in.)	= 2.0
Fluid density (pressure), $\rho_2(P)$ (psi)	= $1.638 \times 10^{-7}$ (10), $3.731 \times 10^{-6}$ (500), $1.101 \times 10^{-5}$ (1500), $\text{lb f sec}^2/\text{in.}^4$
Fluid speed of sound (in./sec)	= 13,860
Rod density, $\rho_1$ ( $\text{lb f sec}^2/\text{in.}^4$ )	= $1.6275 \times 10^{-4}$
Rod bulk modulus (psi)	= $0.95 \times 10^6$
Rod tensile modulus (psi)	= 6200
Rod tensile loss tangent, $\beta$	= 0.5323
Node axial locations away from interface (in.)	= 0.1, 0.3, 0.6, 1.0, 1.5, 2.1, 2.8, 3.6, 4.5, 5.5, 6.5, 7.5, 8.5, 9.5

## B. RESULTS AND COMPARISONS

### 1. LAM NASTRAN Model

Results of the LAM analysis using the NASTRAN computer program are summarized in Table 13. The nomenclature used in the table is listed below:

$E'$  = Propellant storage modulus (psi)

$E''$  = Propellant loss modulus (psi)

$\beta$  =  $E''/E'$  propellant loss tangent

$\nu$  = Poisson's ratio

$\rho$  = Mass density (lb sec<sup>2</sup>/in.<sup>4</sup>)

$B$  = Gas bulk modulus (psi)

$f$  = Frequency (Hz)

$\alpha$  = Structural damping factor (sec<sup>-1</sup>)

Structural damping was determined by the hydroelastic analysis option in NASTRAN. This approach calculates the complex eigenvalue solution for the coupled gas-solid acoustic oscillations. The imaginary part of the complex eigenvalue is the resonant angular frequency of the coupled system, while the real part is the structural damping factor,  $\alpha$ .

Analysis results of the LAM corresponding to three gas pressures (nitrogen at 10, 300, and 1500 psig) are shown in the first three cases of Table 13. In these analyses, a 0.16 inch forward flap gap opening at the grain bore surface (Figure 27) was used for all three pressures. The 0.16 inch gap observed in the unpressurized LAM was probably caused by thermal shrinkage during motor cure and the nylon webbing as previously discussed. As the LAM is pressurized, the flexible case will grow radially and the flap gap will tend to open up more. The radial growth of the LAM case and the forward flap gap opening will increase the total acoustic cavity volume and thus change the coupled acoustic frequency and structural damping. An ideal way is to use the deformed LAM geometry for frequency and structural damping calculations for each pressure load. For preliminary study of the LAM model, the geometry was assumed to be the same for all pressure levels. It should also be pointed out that in these three analyses, the complex eigenvalue output includes a rigid body motion mode and a natural mode for the speaker. These two modes were subsequently eliminated by constraining the axial motion of the LAM and the motion of the speaker to the aft closure. Cases 4 and 5 in Table 13 show the results. Comparison of analytical results with experimental measurements is shown in Figure 29. Frequency agreement is excellent, which indicates the LAM case



TABLE 13. ANALYSIS RESULTS OF THE LAM MODEL

Case No.	Type of Analysis	Fwd Flap Gap Opening (in.)	Propellant Properties				Gas Properties			First Longitudinal Mode		Remarks
			E' (psi)	$\nu$	$\rho$ (lb sec <sup>2</sup> /in. <sup>4</sup> )	$\beta = E''/E'$	B (psi)	$\rho$ (lb sec <sup>2</sup> /in. <sup>4</sup> )	Gas Press. (psig)	f (Hz)	$\alpha$ (sec <sup>-1</sup> )	
1	Hydroelastic	0.16	6200	0.4989	$1.6278 \times 10^{-4}$	0.5323	31.47	$1.638 \times 10^{-7}$	10	156.32	- 3.26	
2	Hydroelastic	0.16	6200	0.4989	$1.6278 \times 10^{-4}$	0.5323	437.07	$2.275 \times 10^{-6}$	300	142.85	-31.86	
3	Hydroelastic	0.16	6200	0.4989	$1.6278 \times 10^{-4}$	0.5323	2115.4	$1.101 \times 10^{-5}$	1500	111.10	-62.23	
4	Hydroelastic	0.16	6200	0.4989	$1.6278 \times 10^{-4}$	0.5323	31.47	$1.638 \times 10^{-7}$	10	156.31	- 3.83	1. Speaker MPC to aft closure
5	Hydroelastic	0.16	6200	0.4989	$1.6278 \times 10^{-4}$	0.5323	2115.4	$1.101 \times 10^{-5}$	1500	111.10	-62.28	2. Axial motion constrained
6	Hydroelastic	0.16	6200	0.4989	$1.6278 \times 10^{-4}$	0.3	2115.4	$1.101 \times 10^{-5}$	1500	108.7	-39.09	
7	Hydroelastic	0.0625	6200	0.4989	$1.6278 \times 10^{-4}$	0.5323	31.47	$1.638 \times 10^{-7}$	10	172.46	- 4.9	
8	Hydroelastic	0.0	6200	0.4989	$1.6278 \times 10^{-4}$	0.5323	31.47	$1.638 \times 10^{-7}$	10	183.1	- 2.28	
9	Real Eigenvalue	0.16	6200	0.4989	$1.6278 \times 10^{-4}$	0	437.07	$2.275 \times 10^{-6}$	300	157.52	--	
10	Real Eigenvalue	0.16	6200	0.4989	$1.6278 \times 10^{-4}$	0	2115.4	$1.101 \times 10^{-5}$	1500	157.52	--	
11	Real Eigenvalue	0.0	6200	0.4989	$1.6278 \times 10^{-4}$	0	31.47	$1.638 \times 10^{-7}$	10	183.74	--	
12	Real Eigenvalue	0.0	6200	0.4989	$1.6278 \times 10^{-4}$	0	--	--	--	253.75	--	Frequency for the first structural mode

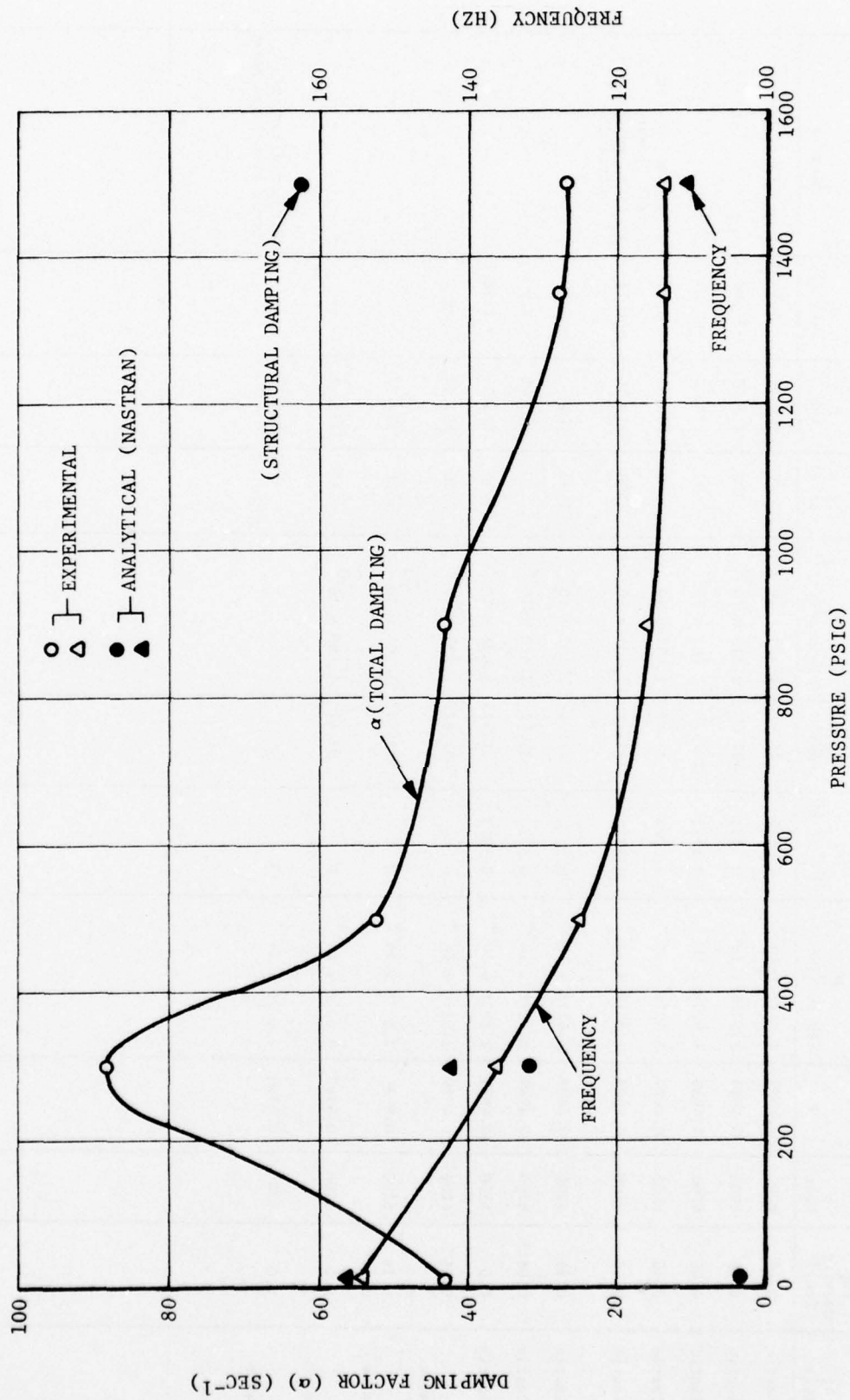


Figure 29. Comparison of LAM Experimental and Analytical (NASTRAN) Results

growth and further flap gap opening as a result of pressurization are small. The damping measurements from the LAM tests are the total damping caused by both structural damping and boundary layer shear damping. To obtain the structural damping comparable to the NASTRAN results, the boundary layer shear damping measured from the rigid-wall motor test must be subtracted from the total damping. The difference in  $\alpha$  shown in Figure 30 is therefore expected.

The dynamic moduli of the propellant used in the NASTRAN analyses were the converted data calculated from tensile stress relaxation modulus values. These data may differ from the dynamic moduli using the Gottenberg torsional shear test. To assess the effect of  $\beta$  on frequency and structural damping, an analysis was performed using  $\beta = 0.3$ . Results shown in case 6 indicates a frequency change of 2.2 percent and a structural damping change of 37.2 percent. It is apparent that structural damping is strongly affected by the propellant dynamic moduli. The effect of the flap gap opening on frequency and structural damping are shown in cases 7 and 8. The frequency drops off as the flap gap opens up, while the structural damping does not follow any definite change pattern. Cases 9 through 12 show some real eigenvalue analyses of the LAM.

## 2. Acoustic Cavity Model

The acoustic cavity analysis results of the inert and LAM models are shown in Table 14. The objective of this analysis was to determine the test measurement accuracy for frequency and mode shape. Results of the NASTRAN analyses indicate that measured frequencies (values in parentheses) are in good agreement with the analytical predictions. Figure 30 shows the first longitudinal mode shape comparison between the measured and analytical data. The measured data were normalized with respect to the maximum pressure which occurred at the extreme radial location of the 1/4 inch gap. The last case in Table 14 shows the acoustic cavity analysis result of the LAM. It is interesting to note the first longitudinal mode frequency from real eigenvalue analysis is identical to the result of a complex eigenvalue analysis (Case 1 in Table 13).

## 3. Rod-Organ Pipe Model

A summary of the finite-element solutions for the rod-organ pipe is given in Table 15. The predicted damping exponent,  $\alpha$ , is seen to increase with the gas pressure because the impedance match between the rod and fluid improves. This behavior is consistent with the earlier work of Anderson. The values for frequency and damping exponent are in general agreement, but there are subtle differences of importance. In particular, the predicted frequency shift with pressure varies with grid refinement and damping level (loss tangent,  $\beta$ ).

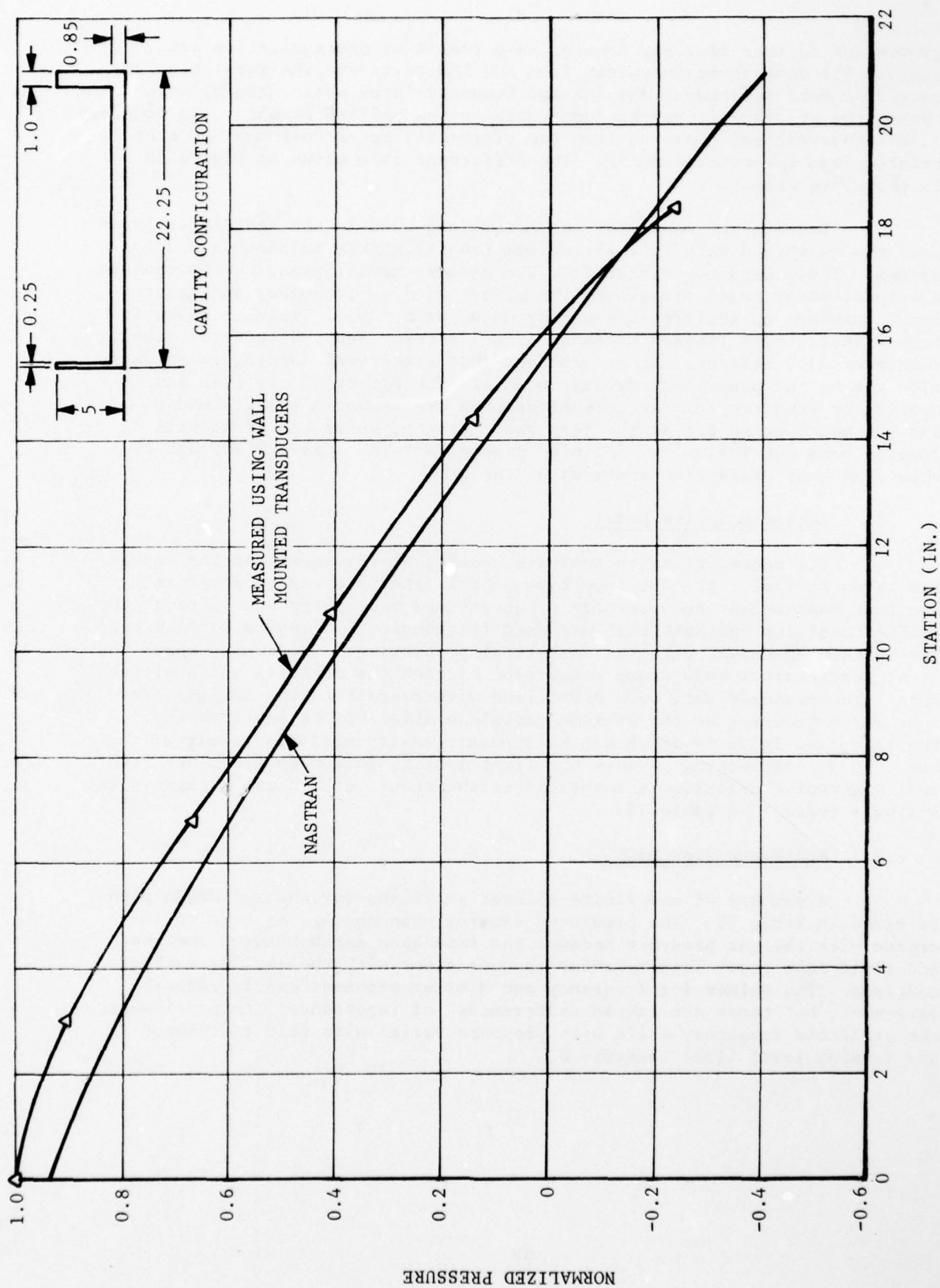


Figure 30. Comparison of Measured and Analytical First Acoustic Mode Shape



TABLE 14. RESULTS OF ACOUSTIC CAVITY ANALYSES

Cavity Configuration (in.)	Gas Properties			First Longitudinal Mode (Hz)	Remarks
	B (psi)	$\rho$ (lb sec <sup>2</sup> /in. <sup>4</sup> )	Gas Press (psig)		
	31.47	$1.638 \times 10^{-7}$	10	194.05 (190.1)	Rigid-wall tube cavity with no gap
	31.47	$1.638 \times 10^{-7}$	10	182.83	LAM cavity with no gap
	437.07	$2.275 \times 10^{-6}$	300	147.49 (151)	Rigid-wall tube cavity with 0.246 inch gap
	437.07	$2.275 \times 10^{-6}$	300	146.35	Rigid-wall tube cavity with 0.256 inch gap
	31.47	$1.638 \times 10^{-7}$	10	156.80	LAM cavity with 0.16 inch gap

TABLE 15. NASTRAN AND OVERLAPPING ELEMENT CALCULATIONS OF ROD-  
ORGAN PIPE ACOUSTIC FREQUENCY AND DECAY PARAMETERS

Code	Gas Element	Grain Element	Eigenvalue Method	Pressure (psig)	Grain	Coupled Gas Mode	
						fc (Hz)	$\alpha$ (sec <sup>-1</sup> )
NASTRAN-15 (Hydroelastic)	Fluid	CDUM	Power	10	0.5323	732.0	2.46
	Fluid	CDUM	Power	500	0.5323	739.0	60.05
	Fluid	CDUM	Power	1500	0.5323	757.0	158.96
NASTRAN-15 (Hydroelastic)	CDUM	CDUM	Power	10	0.5323	729.4	2.71
	CDUM	CDUM	Power	500	0.5323	737.0	59.69
	CDUM	CDUM	Power	1500	0.5323	754.2	162.76
NASTRAN (Very Fine Grid)				1500	0.5323	740.2	174.04
NASTRAN-15 (Hydroelastic)	Fluid	CDUM	Determinant	1500	0.5323	757.0	159.05
NASTRAN-15 (Real Eigenvalue)	Fluid	CDUM	Power	500	0.0	731.64	0.0
	Fluid	CDUM	Power	1500	0.0	731.67	0.0
NASTRAN-15	CDUM	CDUM	Freq Resp	10	0.5323	730.0	0.0
	CDUM	CDUM	Freq Resp	1500	0.5323	760.0	0.0
Overlapping Element Program	Fluid	Solid	Freq Resp	10	0.5323	730.0	2.33
	Fluid	Solid	Freq Resp	500	0.5323	730.0	63.53
	Fluid	Solid	Freq Resp	1500	0.5323	730.0	170.54
Overlapping Element Program	Fluid	Solid	Freq Resp	10	0.0	726.0	0.0
	Fluid	Solid	Freq Resp	500	0.0	710.0	0.0
	Fluid	Solid	Freq Resp	1500	0.0	693.0	0.0

The damping exponent and frequency for the finite-element solutions are compared with the closed-form analytical solution in Figures 31 and 32. The damping exponent comparison as a function of fluid pressure level (density) is quite favorable; whereas the frequency comparison is less impressive. With normal propellant damping, the analytical and overlapping element solutions predict little frequency shift; whereas the NASTRAN solutions indicate a moderate increase in frequency. When the rod loss tangent is set to zero, NASTRAN predicts little frequency shift; whereas the analytical and overlapping element solutions predict a moderate decrease in frequency.

A closed-form parameter study was conducted where the base values for the rod and organ pipe were as given in Table 16. The rod length was then varied and the resulting effects on the decay and frequency parameter calculated (see Figures 33 and 34).

TABLE 16. BASE VALUES OF ROD-ORGAN PIPE PARAMETERS  
FOR ANALYTICAL PARAMETER STUDY

Parameter	Symbol	Value
Density Ratio	$\rho_1/\rho_2$	10
Rod Length (in.)	$L_1$	10
Pipe Length (in.)	$L_2$	10
Rod Sound Speed (ips)	$C_1$	6000
Pipe Sound Speed (ips)	$C_2$	12000
Damping Parameter	$\beta$	0.5

When the length of the rod is 2.5 inches, the uncoupled and undamped resonant frequencies of the rod and organ pipe fall on top of each other. Thus, maximum dynamic participation (damping) of the rod is expected. The greatest damping occurs for the smallest density ratio, where the impedances are best matched. Influences of the second, third, and even the fourth rod modes on the decay parameter are evident, though less impressive than the fundamental.

The influence of the rod length on the (organ pipe) frequency shift is somewhat involved. The greatest frequency shift occurs for the lowest density ratio, as expected. A sinusoidal type behavior is predicted to occur when the uncoupled rod frequencies fall near multiples of the uncoupled organ pipe frequency. The steep nature of the frequency oscillation near the first uncoupled resonance match is profound and somewhat unexpected. The maximum deviation of the coupled gas resonance (fundamental mode) from the uncoupled value occurs when the uncoupled rod and organ pipe resonances are slightly removed from one another, rather than when they are precisely superimposed.

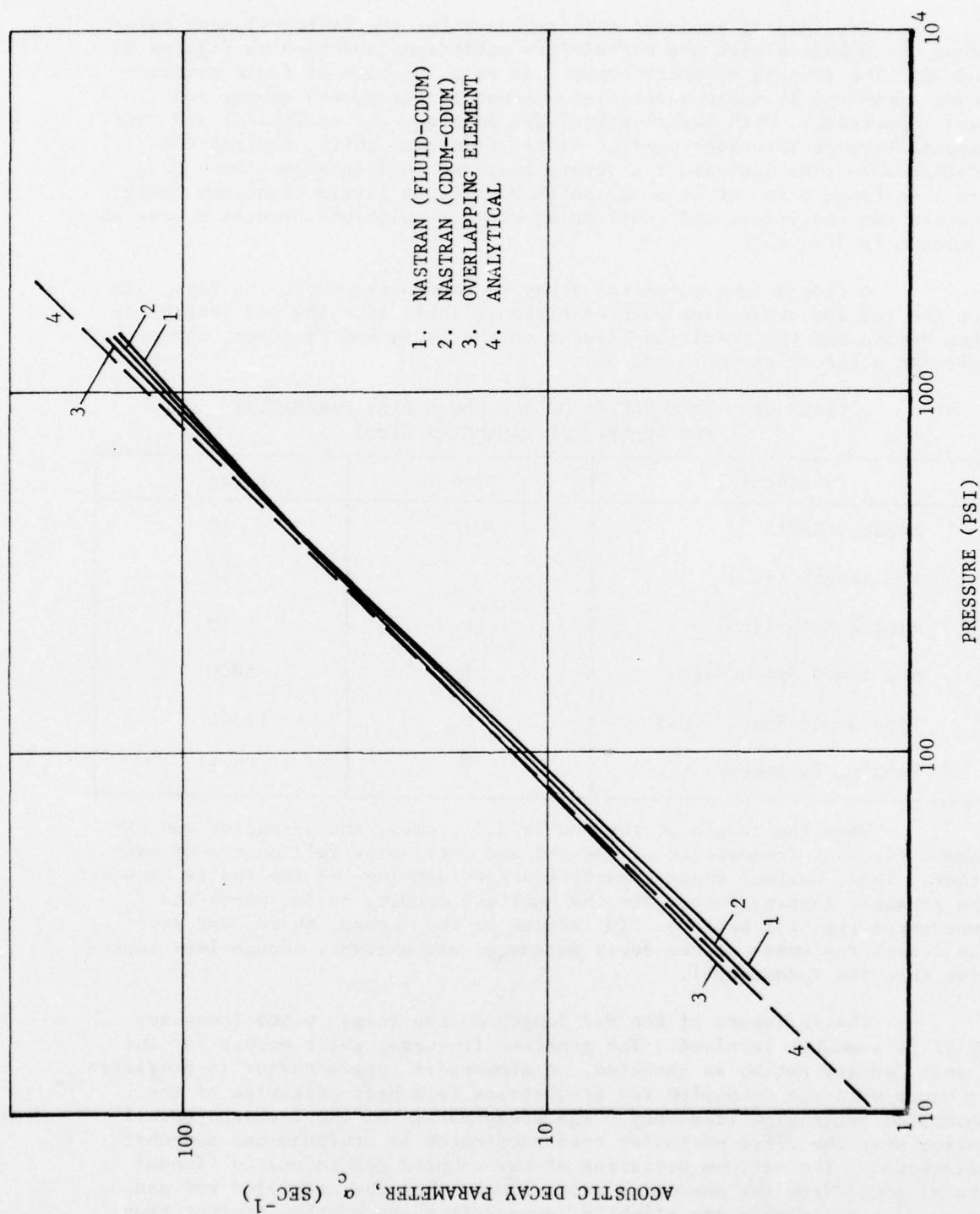


Figure 31. Acoustic Decay-Pressure Predictions of Finite Element and Analytical Procedures



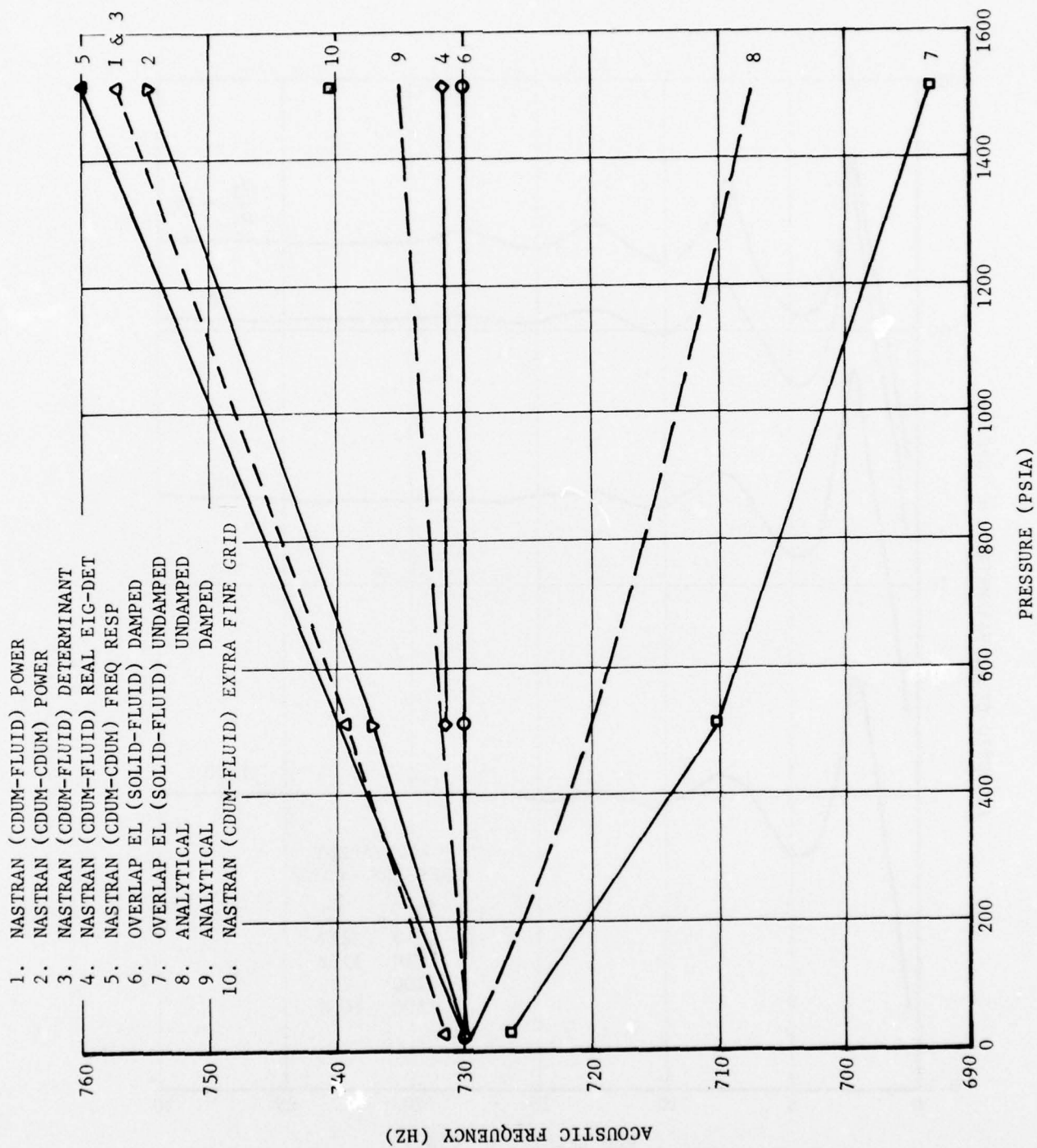


Figure 32. Frequency Predictions of Finite Element and Analytical Procedures

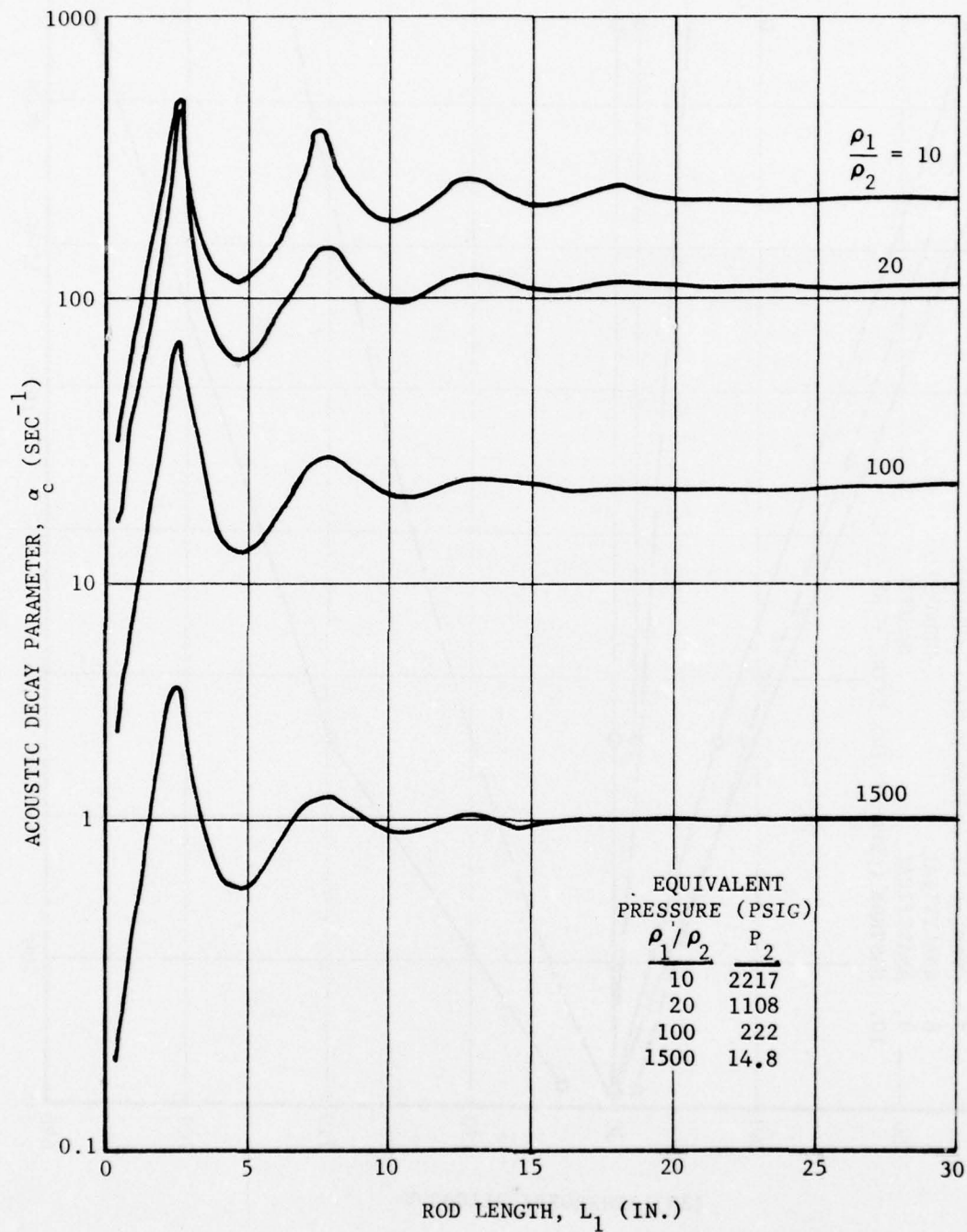


Figure 33. Acoustic Decay - Rod Length for Several Density Ratios

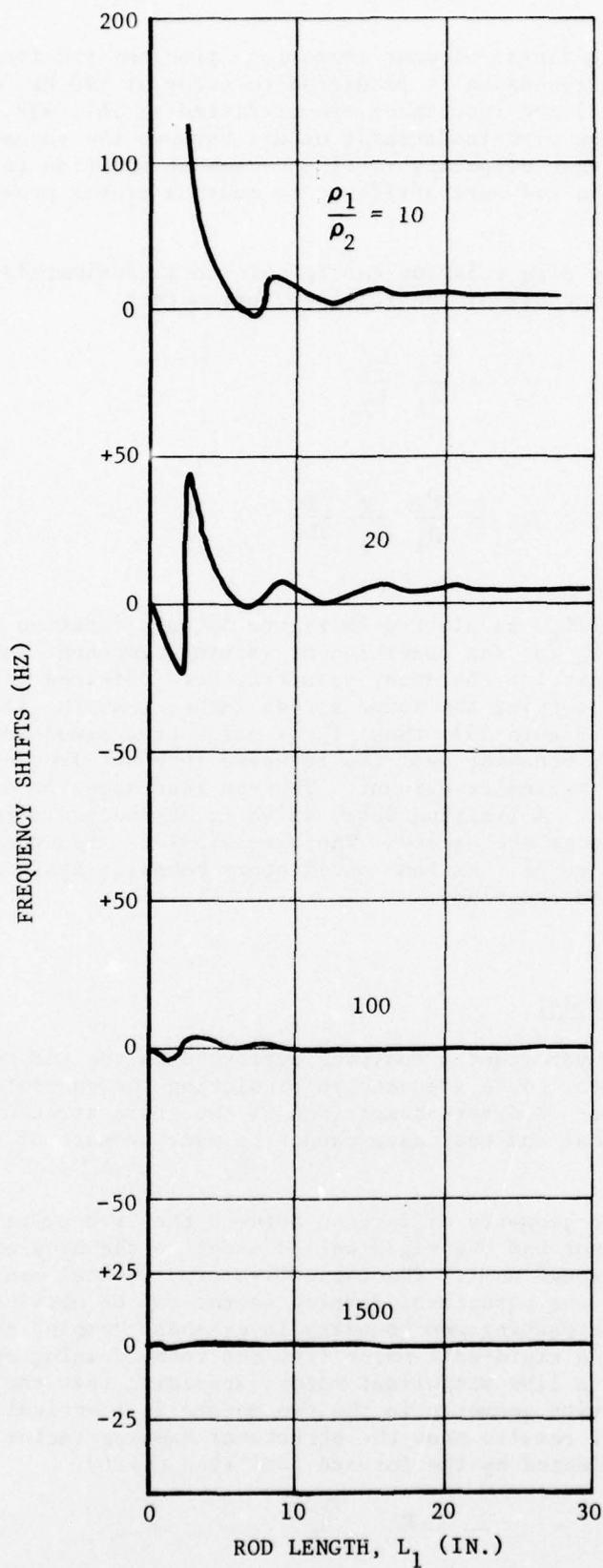


Figure 34. Frequency Shift, Rod Length for Several Density Ratios

For the basic finite-element comparison problem, the fundamental (uncoupled) organ pipe resonance is predicted to occur at 729 Hz, while uncoupled (and undamped) rod resonances are predicted at 162, 487, and 812 Hz. Thus, the organ pipe fundamental occurs between the second and third rod modes. A larger disparity in finite-element solution results could be expected if the rod were stiffened to cause a closer proximity of uncoupled resonances.

The rod-organ pipe solution can be cast in approximately dimensionless form through the use of the following parameters:

$$\Gamma_c = \frac{c_2}{c_1} \frac{L_1}{L_2}$$

$$\Phi_c = \frac{\rho_2}{\rho_1} \frac{c_2}{c_1} \frac{c_2}{2L_2} \quad (6)$$

the decay parameter,  $\alpha_c/\Phi_c$ , is plotted in Figure 35 as a function of the similarity parameter,  $\Gamma_c$  for the condition of varying component lengths. Slightly different values for the decay parameter were obtained near the first rod resonance by varying the sound speeds rather than the lengths (note dashed curves in Figure 35); thus,  $\Gamma_c$  is not a true dimensionless parameter. Oscillatory behavior near the relative resonant frequencies of the rod in the coupled system is evident. The rod resonances occur at  $\Gamma_c = 1/2, 3/2, 5/2$ , etc. A limiting decay value is approached after the first three rod resonances are passed. The dimensionless frequency shift,  $\Delta f/\Phi_c$ , is shown in Figure 36. Extreme oscillatory behavior again occurs near the fundamental rod resonance.

## C. CONCLUSIONS

### 1. LAM NASTRAN Model

The NASTRAN hydroelastic analyses performed on the LAM model shown in Figure 27 appear to be adequate in predicting the gas-solid coupled mode frequency. However, a direct comparison of the grain structural damping factor between analytical and test data cannot be made because of the following difficulties:

- (a) The geometry difference between the live propellant motor and the rigid walled model in the area of the flapped dome. Theoretically, experimental measurement of the structural damping factor can be obtained by subtracting the boundary layer shear damping measured in a rigid-wall motor from the total damping measured in a live propellant motor, providing that the acoustic cavity geometry in the two motors is identical. Analytical results show the structural damping factor is affected by the forward dome flap cavity.



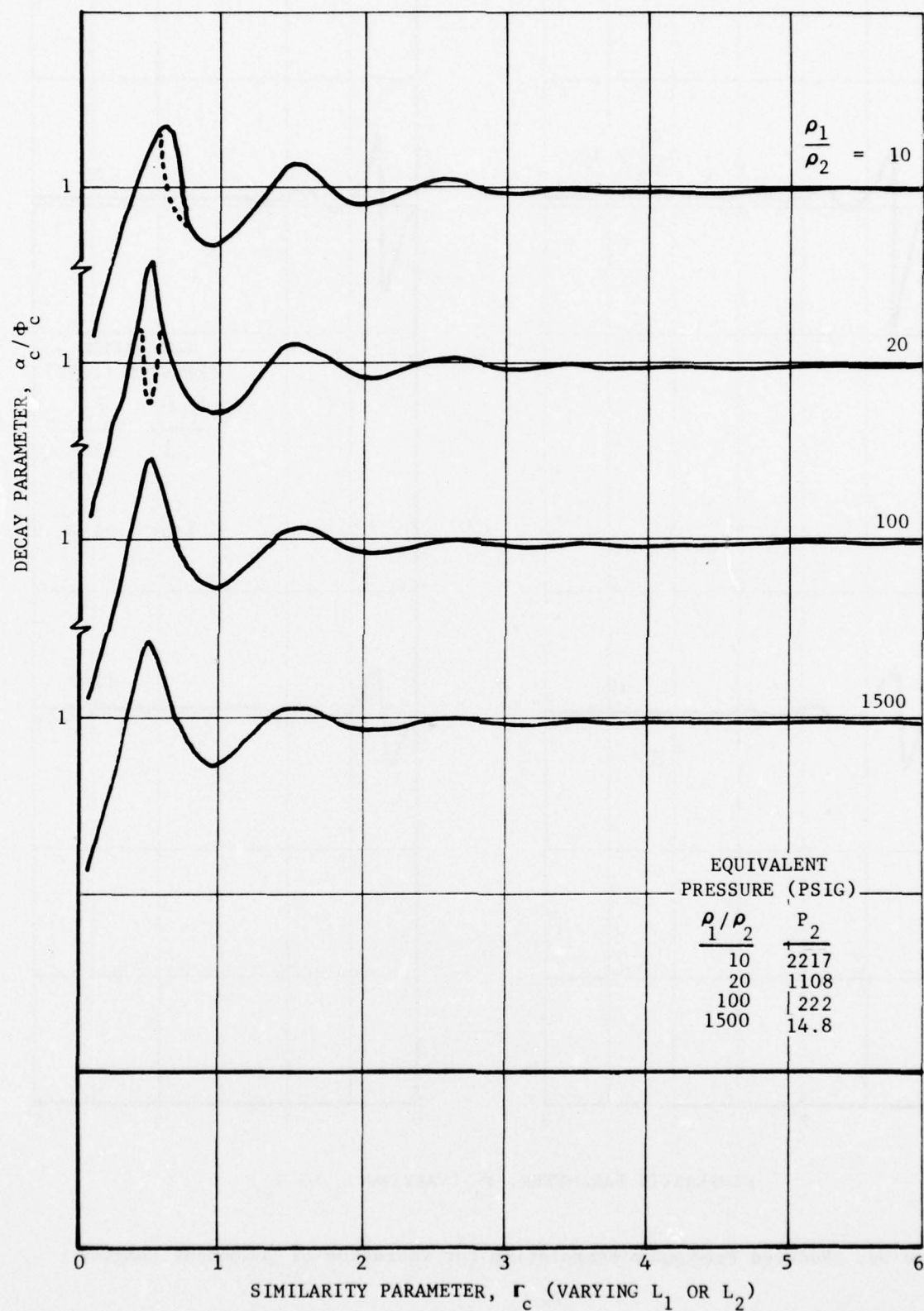


Figure 35. Reduced Decay Formulation for Variation of Component Lengths

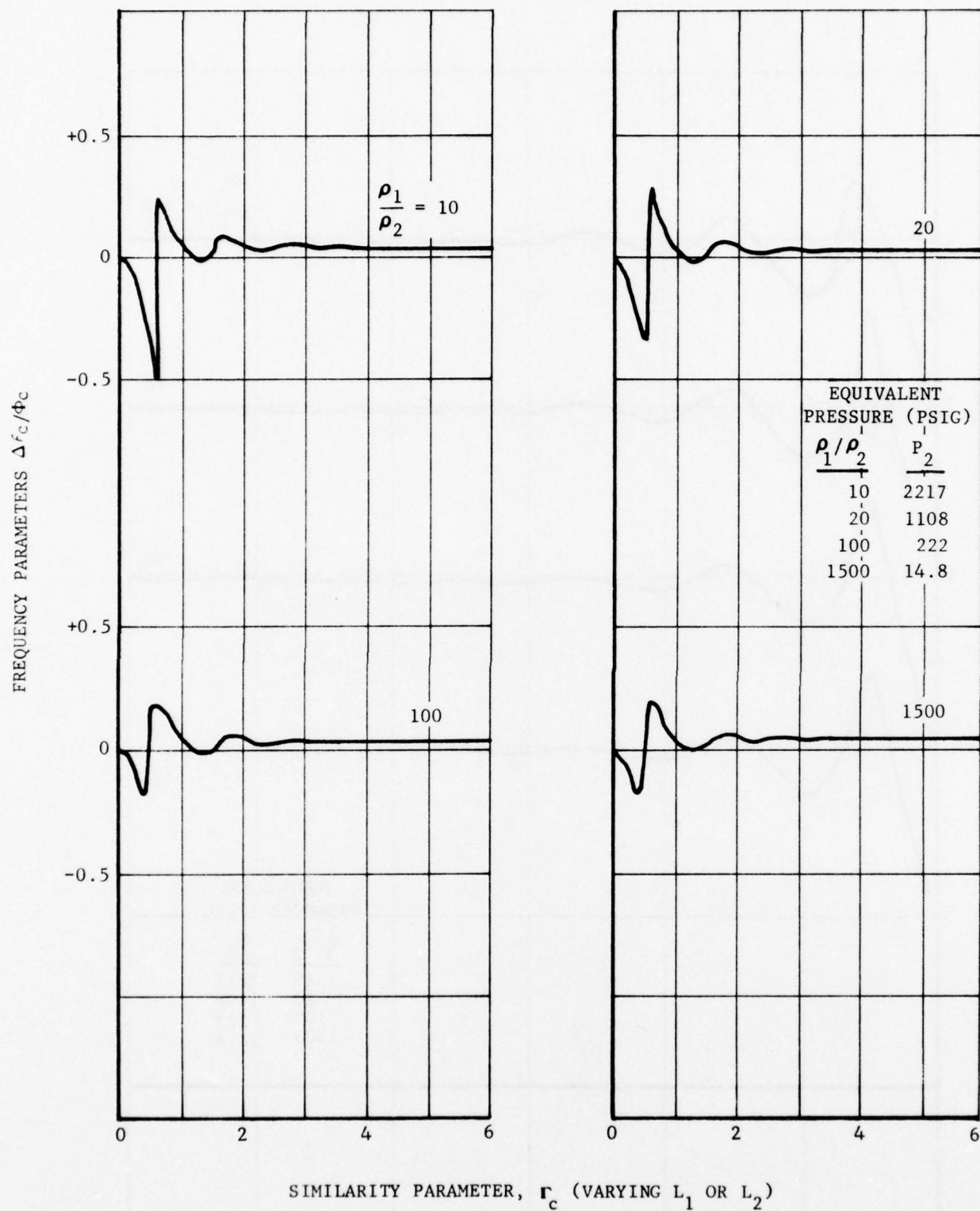


Figure 36. Reduced Frequency Formulation for Variation of Component Lengths

- (b) The degree of accuracy of the propellant dynamic moduli. Propellant dynamic moduli converted from tensile stress relaxation modulus values were used in the NASTRAN analyses. Past experience with converting relaxation modulus data to dynamic moduli indicates that only a moderate degree of accuracy can be expected. Since the structural damping factor is a strong function of the propellant dynamic moduli, as shown in the NASTRAN analyses, accurate dynamic moduli should be used.
- (c) The finite-element grid spacing. Frequency and structural damping factor are affected by the finite-element grid spacing. A study of the rod-organ pipe model showed the coupled gas mode frequency decreased by 2.2 percent and the structural damping increased by 9.5 percent as the number of the solid elements was increased from 14 to 88. Study of the grid refinement in the LAM model was not conducted because of the required long computer time. The finite-element grid shown in Figure 27 consists of 303 grid points, 29 fluid elements, and 125 solid elements. A typical computer run for hydroelastic analysis requires about 65 minutes CPU time on an IBM 370-155 computer.

## 2. Acoustic Cavity Model

The NASTRAN analyses of the rigid-wall model using the real eigenvalue option are in good agreement with the measured frequencies and mode shapes. The mode shape agreed better with the pressure transducer data than did the probe measurements. The analysis predicted a constant frequency for all pressure levels (speed of sound maintained as a constant) which agreed with the modified test results shown in Figure 26.

## 3. Rod-Organ Pipe Model

Predicted values of the decay exponent,  $\alpha$ , agreed reasonably well for the cases studied. However, calculated shifts in acoustic frequency were disturbingly different as the gas density was increased while maintaining a constant speed of sound (pressure effect). The overlapping element method agreed better with the analytical solution than did the NASTRAN. However, this better agreement may be related to the more direct simulation of the rod-organ pipe with the overlapping element program, because of its simpler element forms. This program comparison may not extend into more complex rocket motor simulations.

The analytical rod-organ pipe solution fully supports the presence of high structural damping levels in structural-acoustic systems as predicted previously by Anderson.<sup>(8)</sup> However, the coupled behavior is complex when uncoupled acoustic and structural resonances are in close

proximity. Significant frequency shifts can occur in addition to high values of structural damping, for typical values of the propellant tensile loss tangent. The level of structural damping is almost directly proportional to the motor operating pressure, assuming a fixed motor configuration. This occurs because of the better impedance match between the grain and gas with increased gas density.

A detailed parameter study was performed with the analytical rod-organ pipe solution. This study provides a comprehensive understanding of coupled behavior in structural-acoustic systems with structural damping. Significant dynamic interaction is predicted when structural and acoustic modes are in close proximity, even for typical (high) values of the propellant tensile loss tangent.



## SECTION VII

### RECOMMENDATIONS FOR FURTHER STUDY

Because of problems discussed in previous sections, this program could not be successfully completed as it was originally scheduled and budgeted. The main problem encountered was the unexpected response of the motors as a function of pressure. Testing in the later stages of the program showed that an improved driver configuration could possibly solve the problem. Sufficient data are not available at the present time to establish that any particular driver configuration is satisfactory. Some additional experimentation will be required to obtain a satisfactory driver configuration. This experimentation must be performed before evaluation of existing data or acquisition of additional data will be meaningful. When an adequate driver configuration has been established new structural damping measurements will have to be made. Use of a very simple model for initial structural damping measurements is recommended so that damping caused by cracks, gaps, and other geometric irregularities will not be an important factor.

Problems with the analytical portion of the program (Task II), were caused mainly by the lack of agreement between different analysis techniques for calculating structural damping. The complex eigenvalue solutions obtained by using the NASTRAN code show some frequency shift with increasing pressure; whereas frequency response solutions obtained using the Hercules Potential Energy computer program show essentially no frequency shift with increasing pressure. A rod-organ pipe model closed form solution was obtained to provide an independent estimate of frequency dependence on pressure level.

The closed form solutions show a small frequency shift with increasing pressure. Increasing the grid refinement in the rod portion of the NASTRAN model has been found to yield a significantly smaller frequency shift than the original model. This result, which shows good agreement with the closed form solution, indicates that a study should be made to determine the degree of grid refinement required to obtain acceptable accuracy using the NASTRAN complex eigenvalue analysis.

Various problems have been experienced with use of the Gottenberg dynamic shear modulus tester. Modulus values obtained from the tests are consistently higher than expected. Recent test values have been compared with relaxation modulus data converted to dynamic moduli and with data obtained from the Gottenberg apparatus during the previous test program. Based on the experience gained to date on measurement of propellant dynamic moduli, it is suggested that further work is necessary in this area for the design, fabrication, and verification of a dynamic modulus measuring instrument, applicable to conditions of interest for solid rocket propellants.

## SECTION VIII

### SUMMARY AND CONCLUSIONS

#### A. TASK I

All of the experimental work in the program was performed under Task I. The program plan outlined a series of tests to be performed on each of two LAM's and an inert model. Because preliminary results were not as expected, the experimental task was expanded to study apparent discrepancies and considerably more testing was performed than originally planned.

Acoustic mode shapes and frequencies have been measured successfully in the past at Hercules during various programs. However, this program represents the first attempt to measure the damping associated with an acoustic wave in a cavity. The mode shape and frequency measurements made on the LAM's and on the inert model were successful and were in good agreement with analytical (NASTRAN) results. The damping measurements were not considered to be successful.

Initially, damping measurements were hampered by small details that were apparently unimportant in making mode shape and natural frequency determinations. The damping was found to vary significantly with changes in the width of the simulated dome cavity gap. When a plastic spacer was installed in an effort to convert the inert model into a cylinder, small cracks around the spacer were found to greatly change measured damping values. Another problem with the measured damping was the unexpected measured trend of damping as a function of pressure. These unexpected damping-pressure trends were responsible for initiating a study of possible problems with test techniques.

Near the end of the experimental work, some significant changes in the test set-up were made. The hole between the driver and the acoustic cavity was reduced in diameter from 1-3/8 inches to 1/16 inch in an effort to uncouple the acoustic cavity from the driver cavity. In addition, the driver was mounted rigidly rather than being supported by compressed polyurethane foam. These changes resulted in a completely different trend of measured damping as a function of pressure.

The following conclusions can be drawn as a result of the Task I work:

- (1) Present test methods are sufficient to determine acoustic mode shapes and natural frequencies.
- (2) Small gaps and cracks and other geometric details can have a large affect on damping measurements.

- (3) The driver configuration must be designed with care in order to obtain a response of the acoustic cavity that is not influenced by coupling between the driver and the acoustic cavity. The final driver configuration used in the testing program was found to produce significantly different results from previous configurations but has not been shown to produce satisfactory results. Additional study would be required to obtain a driver design that could be recommended for future damping measurements in an acoustic cavity.

#### B. TASK II

Original plans called for analyses to be performed for the same conditions that were used in corresponding tests so that comparisons could be made between test and analysis results. Initial analyses were conducted on the LAM motor using test conditions. Calculated natural frequencies and mode shapes were found to be in good agreement with test data. However, calculated damping values were not in good agreement with measured values and, furthermore, trends of damping and frequency as a function of pressure were not in agreement with expectations. The expected trends were established from previous analysis work on other programs.

Because of the unexpected trends obtained, the analysis task was diverted from original objectives, and analyses were performed to verify previous analysis results. Analyses previously performed on a simple (rod-organ pipe) model using a Hercules overlapping element finite-element program were repeated and results were compared with corresponding NASTRAN analysis results. The Hercules program showed a nearly constant natural frequency as a function of pressure whereas NASTRAN predicted a decrease in frequency with increasing pressure. To assist in evaluation of the results from the two different finite element programs, an analytical (closed form) solution was obtained for the damped rod-organ pipe model.

Using the rod-organ pipe model, predicted values of the decay exponent,  $\alpha$ , agreed reasonably well for the cases studied. However, calculated shifts in acoustic frequency were disturbingly different as the gas density was increased while maintaining a constant speed of sound (pressure effect). The overlapping element method agreed better with the analytical solution than did NASTRAN. This better agreement, however, may be related to the more direct simulation of the rod-organ pipe with the overlapping element program because of its simpler element forms. The program comparison may not carry over into more complex rocket motor simulations.

The analytical rod-organ pipe solution fully supports the presence of high structural damping levels in structural-acoustic systems as predicted previously by Anderson. However, the coupled behavior is complex when uncoupled acoustic and structural resonances are in close proximity. Significant frequency shifts can occur in addition to high values of structural damping for typical values of the propellant tensile loss tangent. The

level of structural damping is almost directly proportional to the motor operating pressure, assuming a fixed motor configuration. This occurs because of the better impedance match between the grain and gas with increased gas density.

A detailed parameter study was performed with the analytical rod-organ pipe solution. This study provides a comprehensive understanding of coupled behavior in structural-acoustic systems with structural damping. A significant amount of dynamic interaction is predicted when structural and acoustic modes are in close proximity, even for typical (high) values of the propellant tensile loss tangent.

A study of the rod-organ pipe model using NASTRAN indicated that significant changes in model response occurred when the grid refinement was changed. An optimum grid refinement was not determined. A study should be performed to determine guidelines for adequate grid refinement for such analysis.



# LIST OF REFERENCES

1. Anderson, J. McKay, "Structural Damping of Acoustic Oscillations in Solid Propellant Rocket Motors," Eighth JANNAF Combustion Meeting, Monterey, Cal. 14-16 September 1971.
2. Gottenberg, W. G. and Christensen, R. M., On the Experimental Determination of the Complex Shear Modulus of a Linear Isotropic Viscoelastic Solid, 6121-6777-RU000, EM 13-14, Space Technology Laboratories, Inc., One Space Park, Redondo Beach, California, 1 June 1963.
3. Ryan, N. W., Coates, R. L. & Baer, A. D., "Participation of the Solid Phase in the Oscillatory Burning of Solid Rocket Propellants," Ninth Symposium (International) on Combustion, Academic Press, (1963).
4. Stibor, G. S., Poseidon C3 First Stage Motor Acoustic Studies Simulation and Analysis of Observed Static Test Phenomena, Report No. TWR-4209, Thiokol Chemical Corporation/Hercules Incorporated Joint Venture, 24 August 1970.
5. Anderson, J. M., "Structural Damping of Acoustic Oscillations in Solid Propellant Rocket Motors," Eighth JANNAF Combustion Meeting, CPIA Publication 220, November 1971.
6. The NASTRAN User's Manual, Level 16.0, NASA SP-222(03), March 1976.
7. Herrmann, L. R., "Elasticity Equations for Incompressible and Nearly Incompressible Materials by a Variational Theorem," AIAA Journal 3, No. 10, 1965.
8. Anderson, J. M., & Christiansen, H. N., "Behavior of the Finite Element Stiffness Method for Nearly Incompressible Materials," Sixth Annual Meeting of the ICRPG Mechanical Behavior Working Group, 1967.
9. McClure, F. T., Hart, R. W., & Bird, J. F., "Acoustic Resonance in Solid Propellant Rockets," J. Appl. Phys., Vol 31, No. 5, May 1960.
10. Peterson, N. L., Analysis of Rod-Organ Pipe Structural Damping Model, Hercules Memo, Misc/6/20-7482, 14 June 1977.

APPENDIX A

DYNAMIC MODULUS VALUES FOR VRA-7, VRX-2, VSF-3

AND FKM PROPELLANTS

Memo from S. W. Beckwith to F. R. Jensen  
dated 3 December 1976

Hercules Incorporated  
Bacchus Works  
Magna, Utah

3 December 1976

TO: F. R. Jensen  
FROM: S. W. Beckwith *S. W. Beckwith*  
SUBJECT: DYNAMIC MODULUS VALUES FOR VRA-7, VRX-2, VSF-3, and FKM PROPELLANTS

#### INTRODUCTION

The prediction of motor structural damping characteristics by analysis requires the dynamic moduli ( $E'$ ,  $E''$ ) for a given propellant system. Tests are currently underway to generate measured dynamic shear moduli ( $G'$ ,  $G''$ ) using the Gottenberg torsional shear apparatus. In the absence of available experimental measurements one is forced to rely on linear, visco-elastic interconversion techniques to provide engineering values for early analysis. This memorandum summarizes the dynamic tensile moduli ( $E'$ ,  $E''$ ) over the range of frequencies ( $\omega$ ) of interest using stress relaxation data (1% strain) converted by (1) Power Law Modulus assumption, and (2) Fourier transform integral conversion.

#### POWER LAW MODULUS CONVERSION

Most propellants can be represented by the power law model over a wide range of time scale in the following form.

$$E(t) = E_{\infty} + E_1 t^{-n} \quad (1)$$

where  $E_{\infty} \equiv$  long time equilibrium modulus

$E_1, n \equiv$  material constants

The value of  $E_{\infty}$  is estimated from a master stress relaxation curve at the long times (say  $10^4$  to  $10^6$  seconds). The difference,  $E(t) - E_{\infty}$  is plotted against time,  $t$ , on log-log paper. The correct value of  $E_{\infty}$  will lead to a linear curve from which the values of  $E_1$  (taken at  $t = 1$ ) and  $n$  (slope of line) may be determined. This procedure was followed and the constants determined for VRA-7, VRX-2, VSF-3, and FKM propellants as shown in Table A-1. One may check the fit by calculating distinct points on the master

stress relaxation curve. In all cases the fit was within a few percent except at very short times (less than  $10^{-5}$  sec). However, this is important in that short times represent higher frequencies where the deviation, after conversion may be important.

With the power law constants ( $E_\infty$ ,  $E_1$ , and  $n$ ) we may now calculate the dynamic tensile moduli ( $E'$ ,  $E''$ ) using the following relationships derived by linear, viscoelasticity assumptions,

$$E'(\omega) = E_\infty + E_1 \Gamma(1-n) \omega^n \cos \frac{n\pi}{2} \quad (2)$$

$$E''(\omega) = E_1 \Gamma(1-n) \omega^n \sin \frac{n\pi}{2} \quad (3)$$

$$\phi_{\text{LIMIT}} = \frac{n\pi}{2} \quad (4)$$

where  $\Gamma$  = gamma function

$\omega$  = frequency (Hz)

$\phi_{\text{LIMIT}}$  = phase angle in radians

This conversion works very well for the long time, low frequency range but does not represent short times (high frequency) because of the divergent  $E_1 t^{-n}$  term. One typically needs the creep compliance power law for the short time range,

$$D(t) = D_0 + D_1 t^n \quad (5)$$

where  $D_0$   $\equiv$  short time (glassy) compliance

$D_1, n$   $\equiv$  material constants

Using this set of models (equations 1 and 5), the low frequencies are modeled by the modulus representation and the high frequencies by the compliance representation,

$$D'(\omega) = D_0 + D_1 \Gamma(1+n) \omega^{-n} \cos \frac{n\pi}{2} \quad (6)$$

$$D''(\omega) = D_1 \Gamma(1+n) \omega^{-n} \sin \frac{n\pi}{2} \quad (7)$$

where the terms are as described earlier.



STRESS RELAXATION MODULUS COVERSION - FOURIER TRANSFORMS

The second approach was to use Hercules computer program 62501 which converts stress relaxation data to dynamic tensile moduli ( $E'$ ,  $E''$ ).

The dynamic moduli are expressed in terms of the relaxation modulus in the form

$$E'(\omega) = \omega \int_0^{\infty} E(t) \sin \omega t \, dt \quad (8)$$

$$E''(\omega) = \omega \int_0^{\infty} E(t) \cos \omega t \, dt \quad (9)$$

from which the integrals are evaluated by numerical procedures. The representation of  $E'$  usually is smooth while that for  $E''$  often shows some numerical oscillations.

PROPELLANT RESULTS

The dynamic tensile moduli ( $E'$ ,  $E''$ ) for VRA-7, VRX-2, VSF-3, and FKM propellants are shown in the attached figures. Table A-II gives power law equations and the limit phase angle for the same propellants. The following observations can be made from the data:

1. Both VRA-7 and VRX-2, XLDB propellants, exhibit little visco-elastic behavior as evidenced by the low value of  $n$  (.098 to .116), whereas FKM (CMDB propellant) is intermediate ( $n = .215$ ), and VSF-3 (HTPB propellant) is high ( $n = .281$ ).
2. Better agreement between the two conversion methods exists when the time dependence is weak as shown by VRA-7 and VRX-2.
3. In all cases the conversion methods agree better in the low frequency range as we noted they would earlier. Compliance data would probably fit better at the high frequencies but is not available.
4. The loss modulus,  $E''$ , exhibits considerable numerical oscillation at low frequencies and, in the case of VRA-7, diverges about  $10^3$  cycles (Hz).
5. For analysis purposes, one should use the converted relaxation modulus curves ( $E'$ ) and a smooth curve through the corresponding loss modulus ( $E''$ ) curve.
6. If one must work with dynamic shear moduli, then the dynamic tensile moduli values must be divided by 3,

From: S. W. Beckwith

- 4 -

$$G' = \frac{E'}{3} \quad (10a)$$

$$G'' = \frac{E''}{3} \quad (10b)$$

SWB:pc

cc:	J. M. Anderson	K17
	L. F. Myers	K17
	D. T. Wang	K16
	F. M. Norton	K19

TABLE A-I. POWER LAW COEFFICIENTS FOR

$$E = E_{\infty} + E_1 t^{-n}$$

<u>Propellant</u>	<u>Type</u>	<u><math>E_{\infty}</math> (psi)</u>	<u><math>E_1</math></u>	<u><math>n</math></u>
VRA-7	XLDB	300	419	.098
VRX-2	XLDB	300	280	.116
VSF-3	HTPB	50	738	.281
FKM	CMDB	400	769	.215

TABLE A-II. POWER LAW COEFFICIENTS FOR

## DYNAMIC MODULUS

<u>Propellant</u>	<u><math>E'</math></u>	<u><math>E''</math></u>	<u><math>\phi_{\text{LIMIT}}</math></u>
VRA-7	$300 + 442 \omega^{.098}$	$68.6 \omega^{.098}$	.154
VRX-2	$300 + 298 \omega^{.116}$	$54.9 \omega^{.116}$	.182
VSF-3	$50 + 847 \omega^{.281}$	$400 \omega^{.281}$	.441
FKM	$400 + 858 \omega^{.215}$	$301 \omega^{.215}$	.338

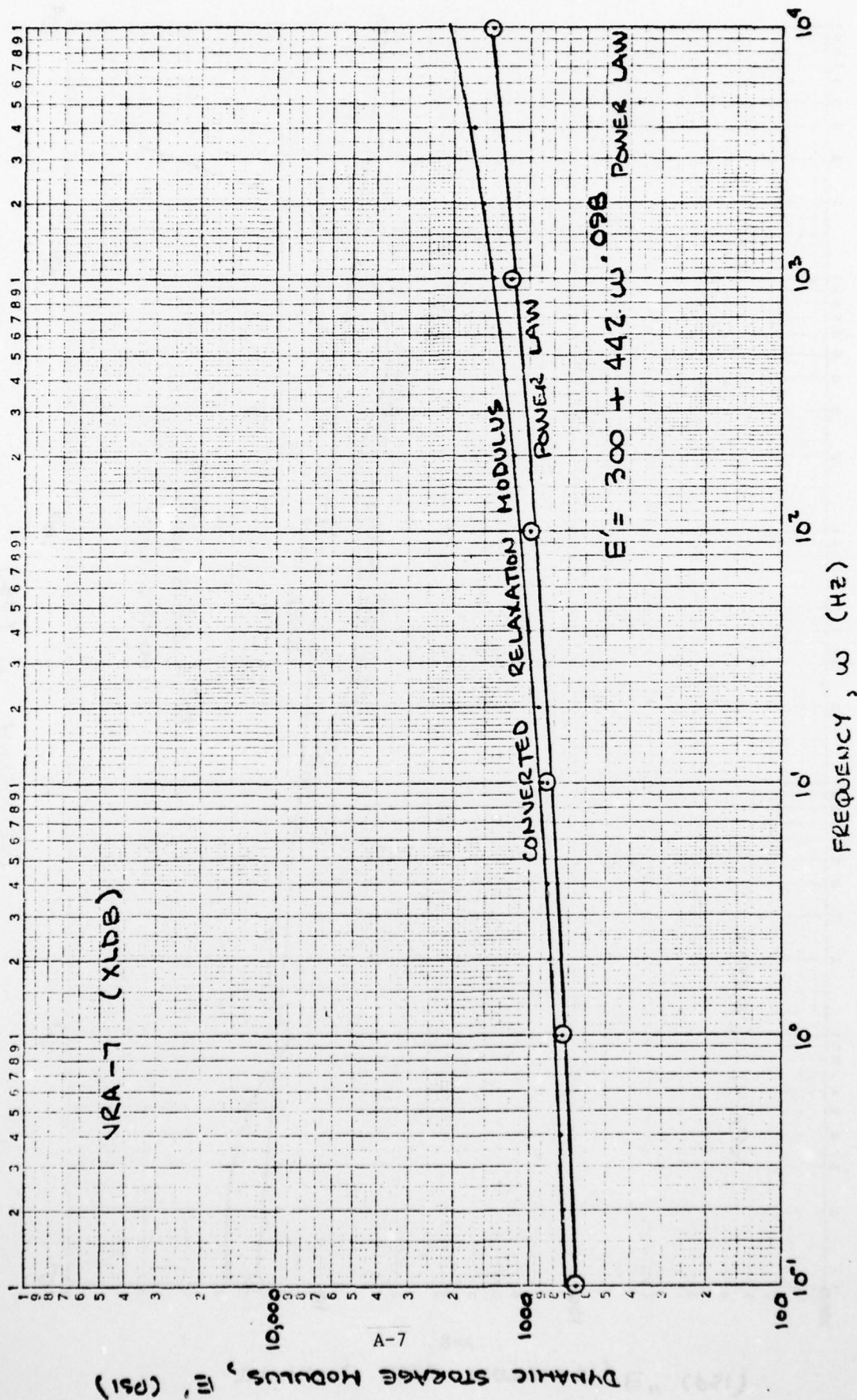


Figure A-1. Storage Modulus For VRA-7 Propellant



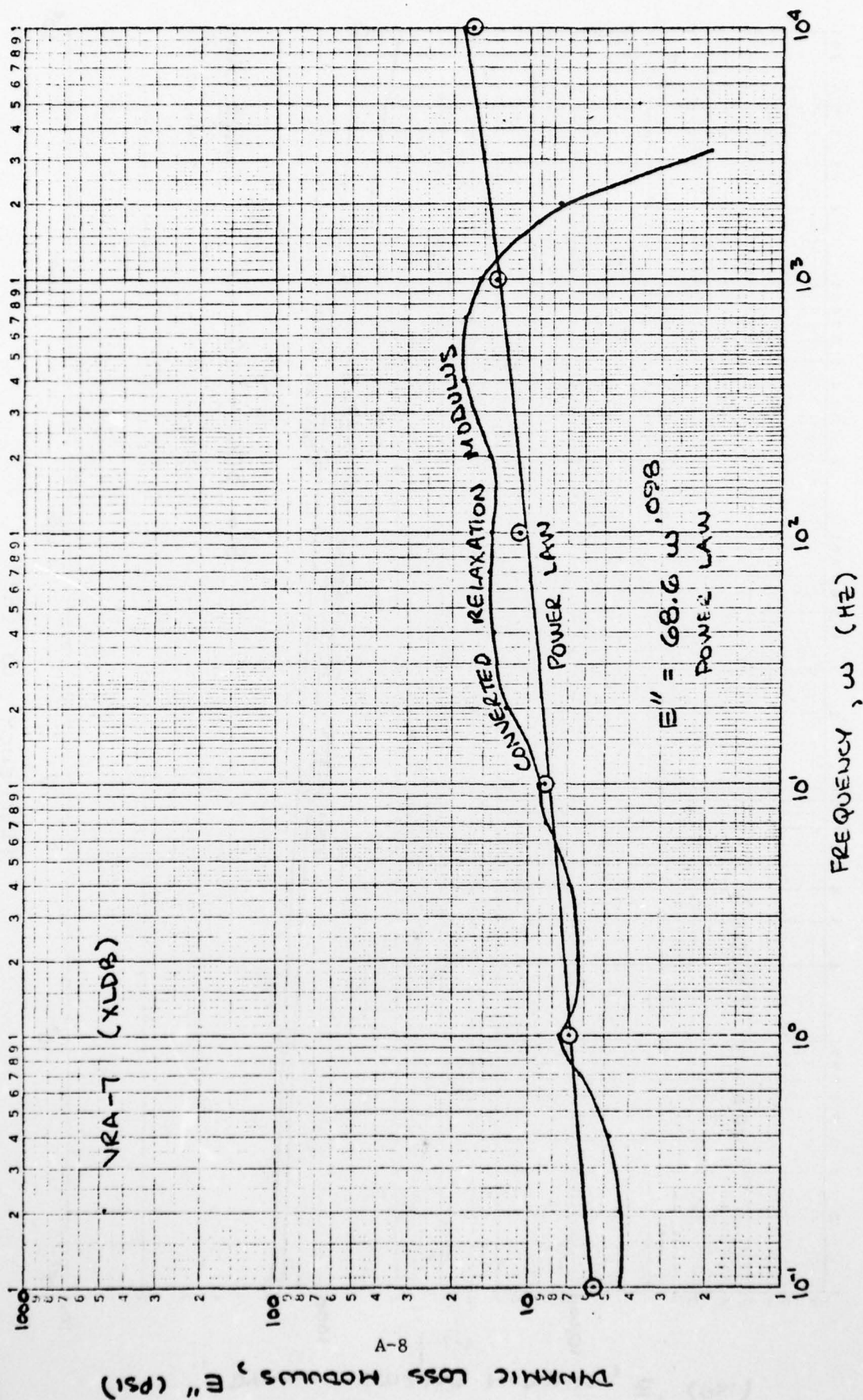


Figure A-2. Loss Modulus for VRA-7 Propellant

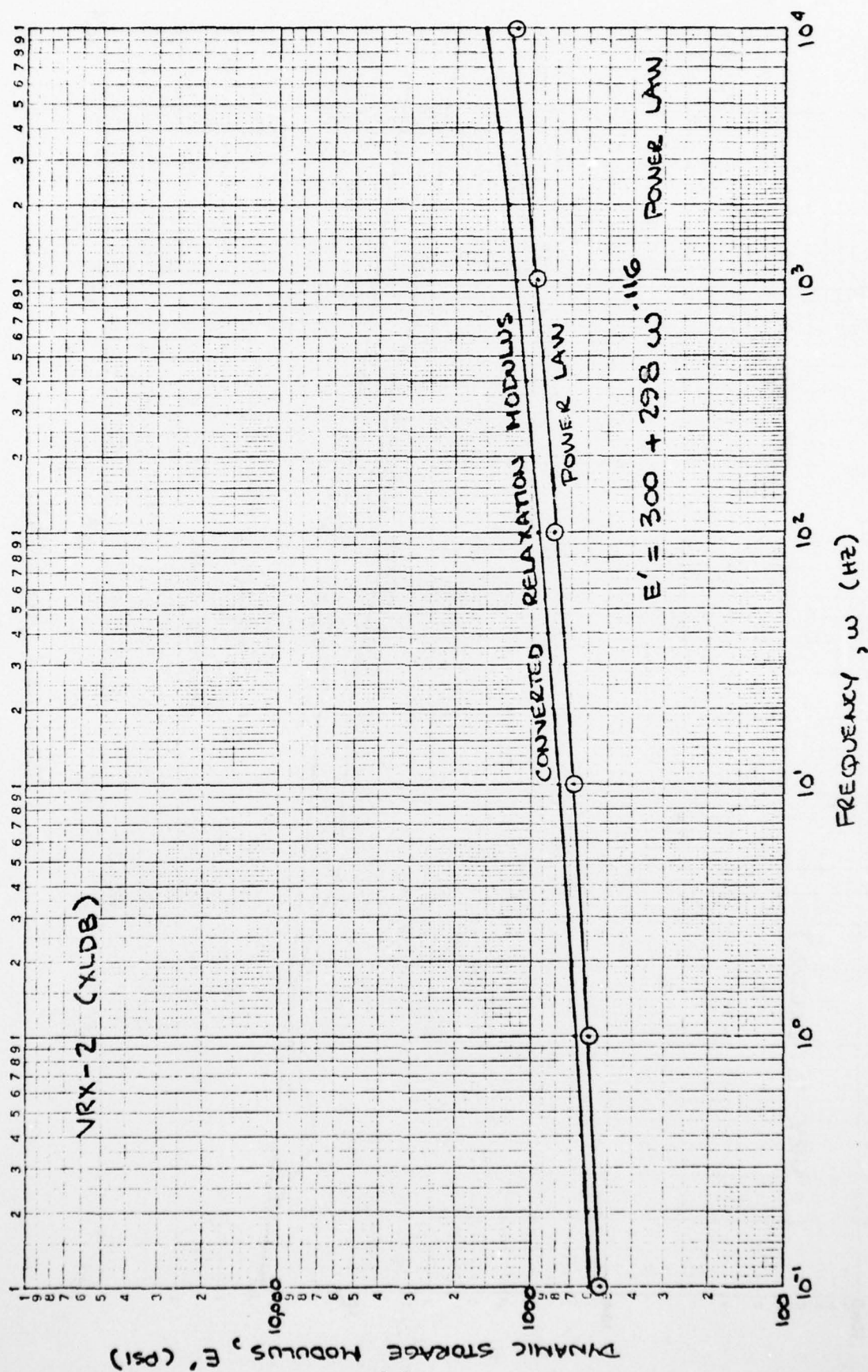


Figure A-3. Storage Modulus for VRX-2 Propellant

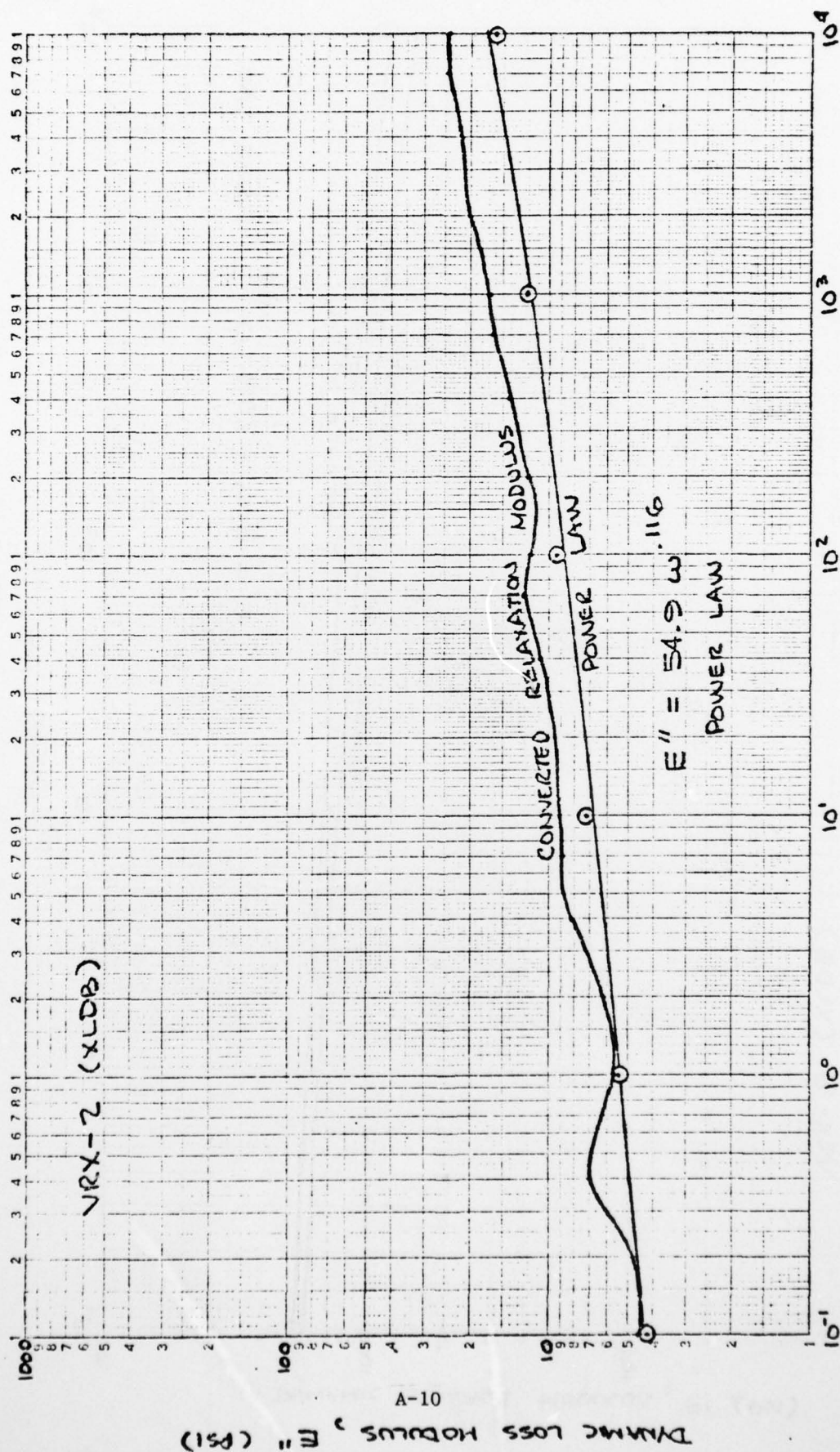


Figure A-4. Loss Modulus for VRX-2 Propellant



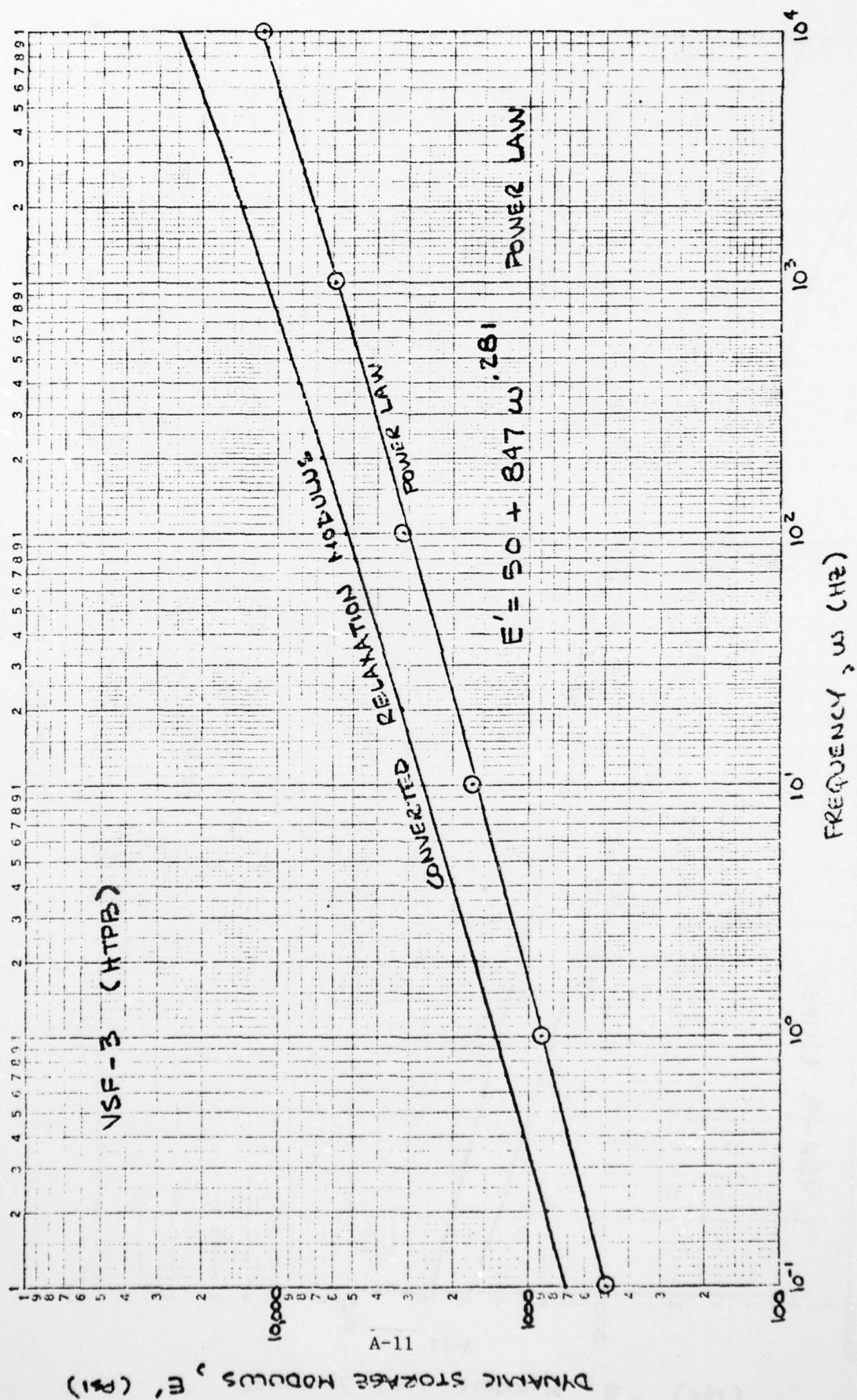


Figure A-5. Storage Modulus for VSF-3 Propellant



AD-A054 152

HERCULES INC WILMINGTON DEL SYSTEMS GROUP

STUDY OF STRUCTURAL DAMPING IN SOLID PROPELLANT

DEC 77 F R JESEN

F/G 21/8.2  
ROCKET MOTORS U--ETC(U)

F04611-76-C-0039

NL

UNCLASSIFIED

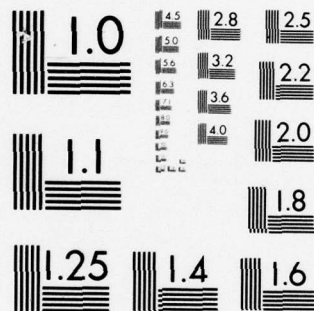
AFRPL-TR-77-84

2 OF 2

AD  
A054152



END  
DATE  
FILMED  
6-78  
DDC



MICROCOPY RESOLUTION TEST CHART  
NATIONAL BUREAU OF STANDARDS-1963-A

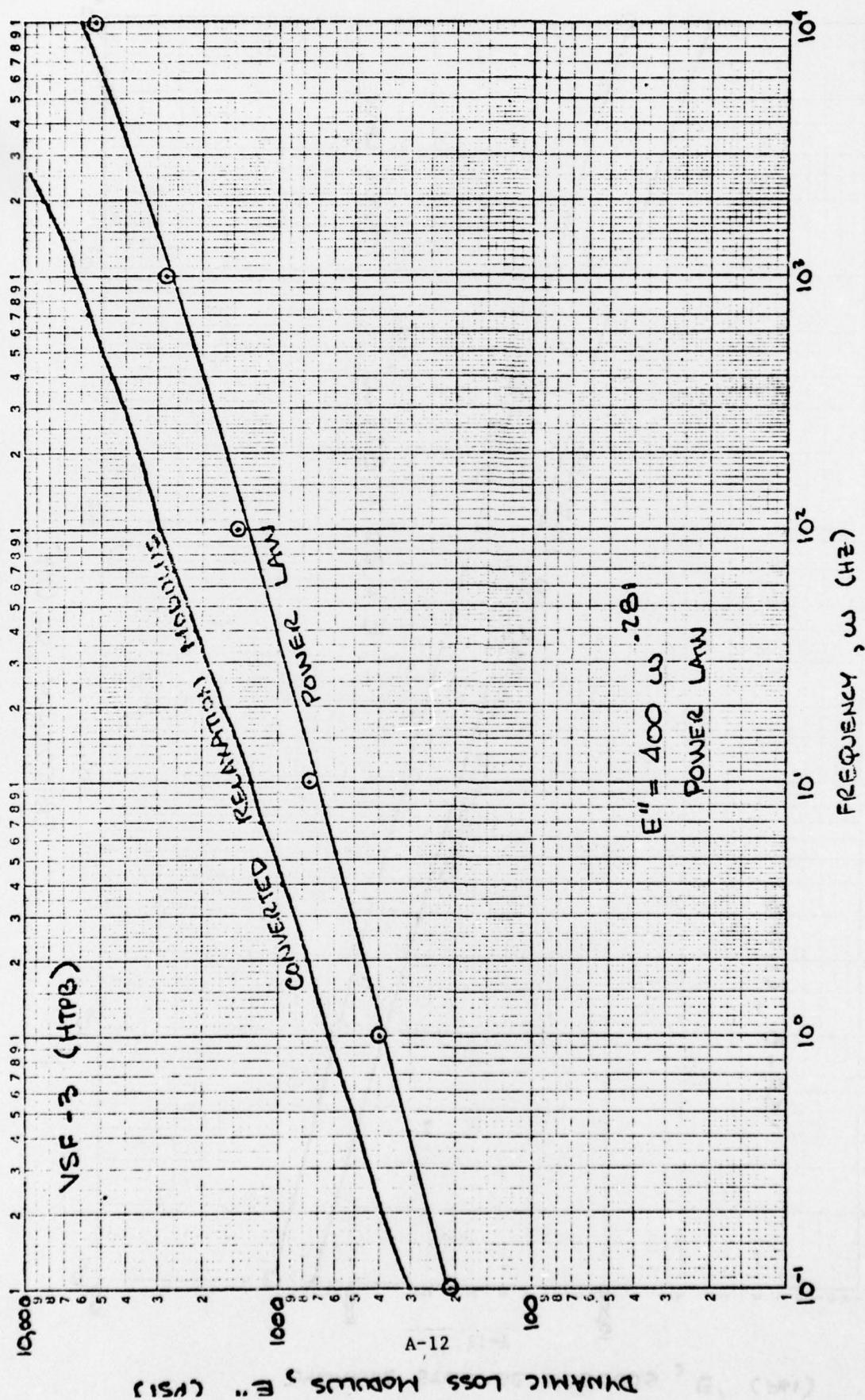


Figure A-6. Loss Modulus for VSF-3 Propellant

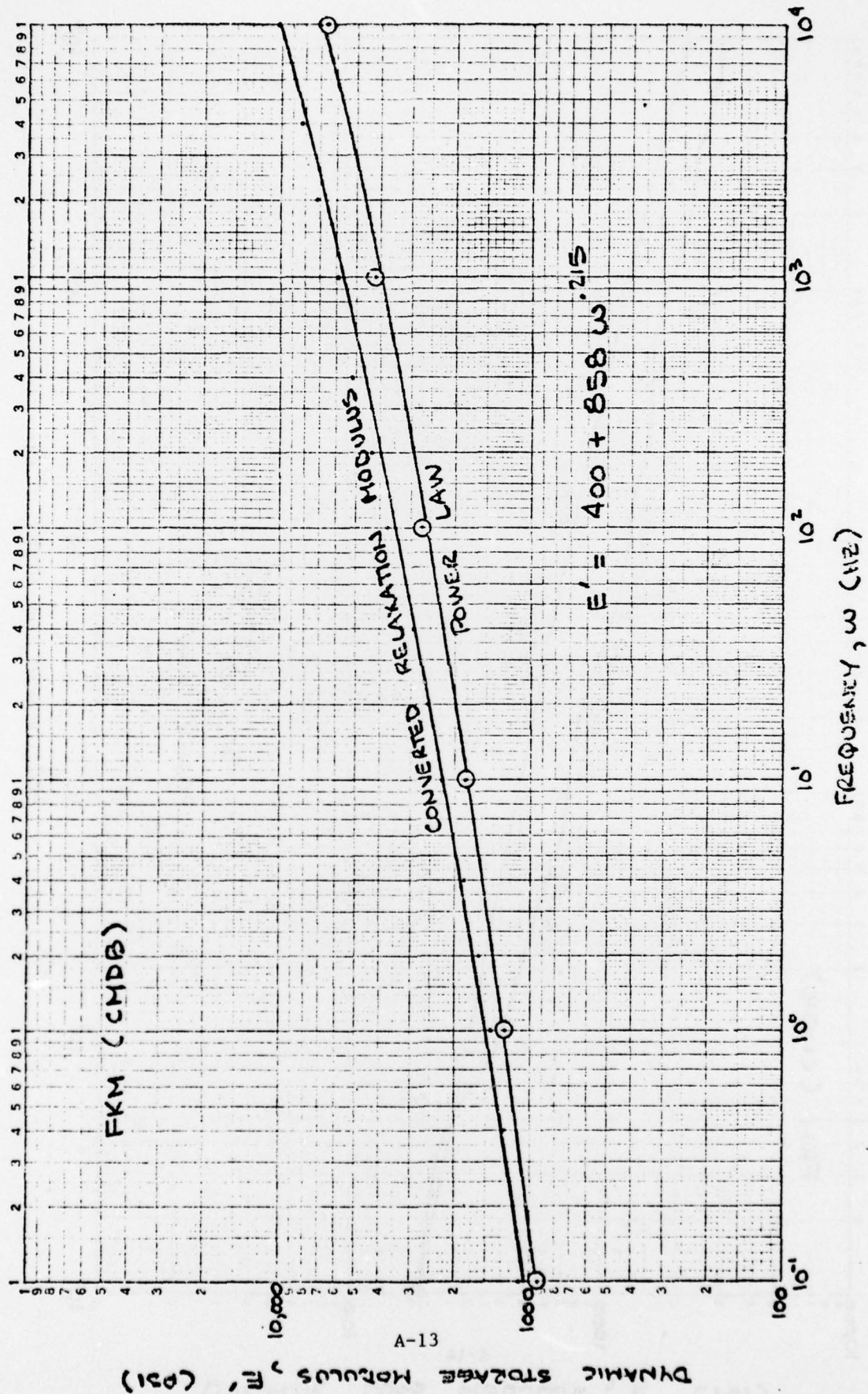


Figure A-7. Storage Modulus for FKM Propellant



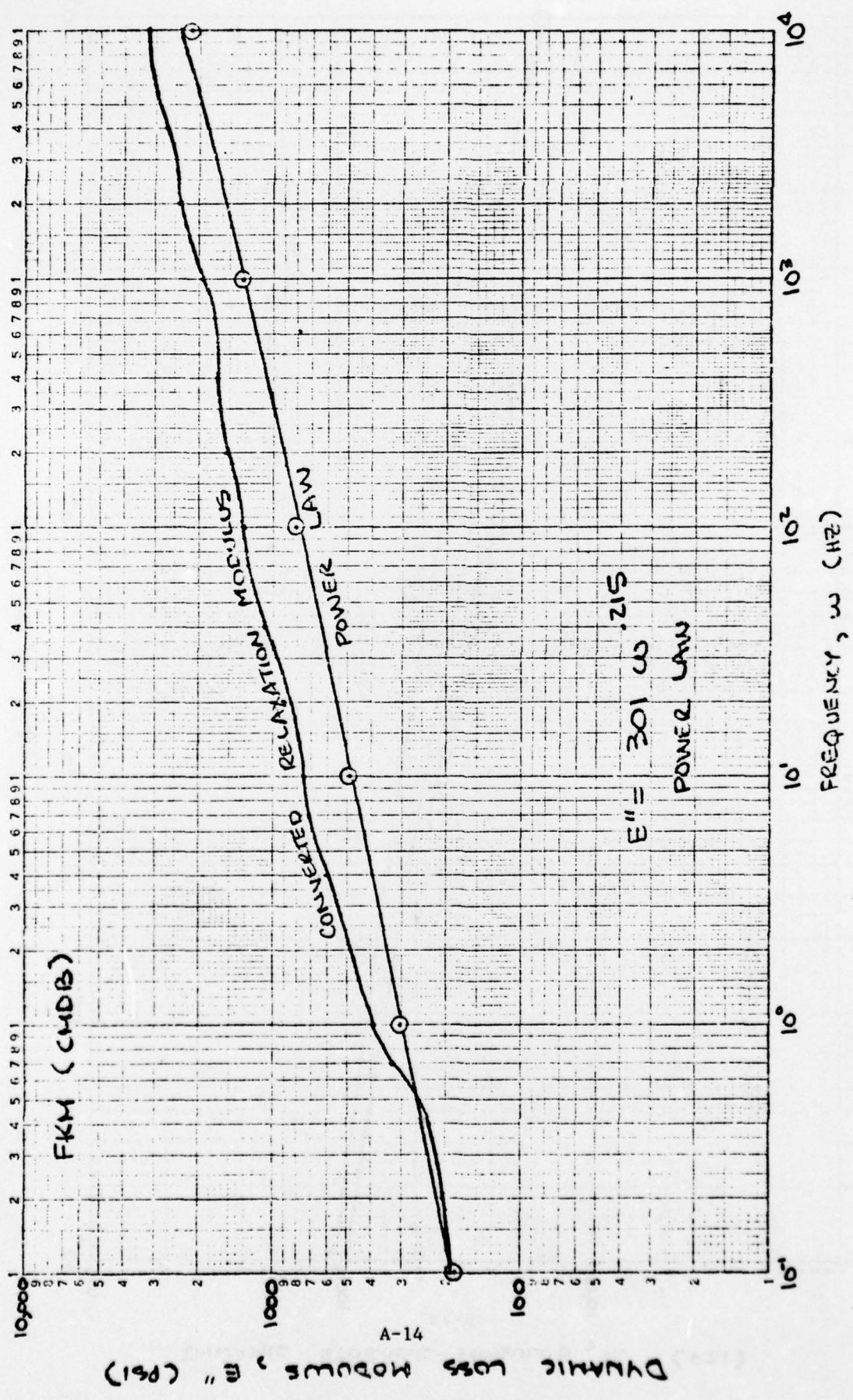


Figure A-8. Loss Modulus for FKM Propellant

## APPENDIX B

### ANALYSIS OF ROD-ORGAN PIPE STRUCTURAL DAMPING MODEL

Memo: N. L. Peterson to J. M. Anderson, Hercules Incorporated,  
Bacchus Works, Magna, Utah, 14 June 1977.

Hercules Incorporated  
Bacchus Works  
Magna, Utah

14 June 1977

In Reply Refer to:  
Misc/6/20-7482

TO: J. M. Anderson  
FROM: N. L. Peterson  
SUBJECT: ANALYSIS OF ROD-ORGANPIPE STRUCTURAL DAMPING MODEL

SUMMARY OF RESULTS AND CONCLUSIONS

A study was performed to referee differences between NASTRAN and Hercules potential energy (PE) program calculations of eigenvalues for an acoustically coupled viscoelastic rod and organpipe. Predicted values of the damping parameter,  $\alpha$ , agreed reasonably well for the few cases studied. Previous structural damping predictions showing moderately high  $\alpha$  are also supported by the analytical solution, but there were complex differences between the calculations of frequency shift with pressure.

For an undamped rod the analytical procedure predicts a 3.2% frequency decrease from a base value of 730 Hertz at ambient to 707 Hertz at 1500 psi; the PE predicts a 4.7% shift and NASTRAN predicts no shift over the same range of pressure. All of the procedures predicted roughly comparable increases of frequency from their undamped condition, for an increase of the damping coefficient  $\beta$  from 0 to 0.5323. At 15 psi there is general agreement that the shift with increasing  $\beta$  is small. At 1500 psi the net analytical frequency shift due to damping and increased pressure is 0.7% above the ambient value. The net increase percentages for the PE and NASTRAN procedures are respectively 0.2% and 3.3%. Thus, the PE prediction again agrees better than NASTRAN with the analytical solution.

The better agreement between the analytical and PE solutions, than with that of NASTRAN, may be fortuitous, considering all of the parameters involved. Neither of the finite element programs directly enforce continuity of pressure at the RO interface, as the analytical method does, but this condition may fall into place more effectively in the PE program due to its simpler approximation procedures for 1-D problems.

NASTRAN calculations were performed with several solution routines and using both the FLUID and reformulated (for Poisson ratio nearly 0.5) CDUM elements. The insensitivity of frequency to a pressure increase



therefore appears to be related to the reformulated element, rather than the method of solution.

The analytical procedure is computationally fast, so it was used to perform a more detailed study of eigenvalue variation with  $R_0$  physical variables. A dimensional study of the results and the characteristic equation used to obtain them, ultimately led to a reduction of seven physical variables to essentially three nondimensional variables and a semianalytical solution for eigenvalues. This formulation displays coupling characteristics that may be extended to a rationale of the more general structural damping problem. The rationale permits grouping of problems, according to values of the nondimensional parameters, as a simple or a complex problem. Thus, solutions approach a constant value in the  $R_0$ , when the uncoupled gas organpipe frequency is 3 or 4 times that of the rod and their characteristic impedances are not closely matched. This result is of practical importance in motor design because it permits very simple preliminary estimates of structural damping.

The parametric study showed that both damping and frequency may increase or decrease by increasing  $\beta$  from its nominal value, according the relative magnitude of the uncoupled frequencies of the rod and organpipe. This result was predicted by Anderson in his structural damping paper (8th JANNAF Combustion Meeting, CPIA Publication 220, November 1971).

The parametric study also showed that a large shift of the operating frequency may occur as the result of certain combinations of the physical variables. Maximum shift occurs when the uncoupled fundamental frequencies, without damping, are slightly separated. Anderson's structural damping analysis did not disclose this fact, and incorrectly concluded that damping suppresses frequency shift, because he only studied the case where these uncoupled frequencies were identical. The analytical procedure predicts a minimum shift for this case.

The parametric and dimensional similarity studies have disclosed and simplified a broad range of behavioral characteristics in structural damping. Valuable guidelines for future structural damping studies are contained in the results. The conclusions drawn are important and merit confirmation by independent procedures.



### NOMENCLATURE

A, B, C, D, E, H	Rod-organpipe eigenvector subfunctions
DO	Disk-organpipe
F	Force per unit mass; eigenvalue vector
G	Characteristic matrix
H	Rod-organpipe eigenvector subfunction
$Q$	Acoustic intensity
J	Jacobian of characteristic matrix
K	Complex wave number
L	Rod or organpipe length
M	Zener model modulus parameter
P	Total acoustic wave pressure
R	Acoustic wave number subfunction
RO	Rod-organpipe
U	Acoustic velocity amplitude
V	Phase velocity
X	Oscillatory displacement amplitude; imaginary part of complex wave number
Y	Real part of complex wave number

### NOMENCLATURE

e	Base of Napierian logarithms
f	Acoustic cycle frequency; force parameter
i	Imaginary unit
j	RO component index
k	Spring stiffness, real wave number
<del>k</del>	Hypothetical undamped wave number ( $\omega/C$ )
m	Mass
n	Mode number
p	Pressure
r	Ratio of characteristic impedances, dashpot damping parameter
s	Complex eigenvalue of discrete system
t	Time
u	Acoustic velocity
x	distance

### NOMENCLATURE

$\Gamma$	Nondimensional frequency variable
$\Delta$	Small variation
$\theta$	Acoustic characteristic subfunction
$\alpha$	Acoustic decay parameter; acoustic transmission deficient
$\beta$	Structural damping
$\epsilon$	Acoustic strain
$\zeta$	Acoustic damping parameter
$k$	Real wave number
$\xi$	Acoustic displacement
$\pi$	3.14159.....
$\rho$	Density
$\Sigma$	Total structural wave stress
$\Phi$	Eigenvalue perturbation function
$\chi$	Acoustic characteristic subfunction
$\Omega$	Complex acoustic eigenvalue
$\sigma$	Dynamic stress
$\tau$	Relaxation time
$\varphi$	Acoustic phase angle
$\omega$	Acoustic radian frequency

## NOMENCLATURE

### SUBSCRIPTS\*

- 1 Acoustic variable in viscoelastic rod; first mode; first component of acoustic characteristic matrix.
- 2 Acoustic variable in organ pipe gas
- c Coupled condition
- j Rod-organ pipe component variable index
- o Steady state value; amplitude; current eigen value estimate
- f Partial derivative with respect to frequency
- n  $n^{\text{th}}$  mode
- N Undamped free oscillation
- p Phase
- t Partial derivative with respect to time; displacement parameter
- x Partial derivative with respect to distance
- $\alpha$  Partial derivative with respect to decay coefficient
- 1+ Incident wave
- 1- Reflected wave
- 2+ Transmitted wave

### SUPERSCRIPTS

- R Real
- I Imaginary

Overhead dot implies total time derivative.

\* Unsubscripted variable such as  $p$ ,  $u$ ,  $\sigma$ ,  $\epsilon$ ,  $\zeta$  are acoustic perturbations of steady values.



## INTRODUCTION

Calculations of acoustic frequencies and loss parameters for structural damping have been performed with the NASTRAN and potential energy (PE) computer programs in support of the AFRPL structural damping contract. Apparent differences between the results using two types of NASTRAN elements and the PE elements occurred and could not be readily resolved. One of the configurations studied was that of a viscoelastic rod that is acoustically coupled with an organpipe. The coupled combination is called the rod-organpipe (RO).

The objectives in this study were to develop a closed-form analytical model of the RO acoustic behavior; apply it as a referee of the computer programs; and then apply the model in a parametric study of structural damping. The latter study was intended as a cost effective means to help understand the dependence of acoustic coupling, decay, and frequency shift on the geometry and material properties of the RO model.

The RO configuration was acoustically modeled by Prof. F.E.C. Culick of California Institute of Technology with coupled analytical characteristic equations. The model is one-dimensional (1-D) and uses the tensile modulus to specify undamped sonic speed in the solid. This model was programmed for calculation on the Bacchus computer.

The program initially failed to obtain a solution so a review of the model and program was undertaken. An interpretive sign error was found and the coupled characteristic equations were found to have large irregularities close to their zeros. These irregularities caused confusion in the search for the solutions.

The sign error was corrected and the characteristic equations were algebraically transformed into more suitable forms. Several aspects of the model were also modified to obtain a more direct representation of the governing equations by the wave equation. A generalized Newton's method was also formulated to solve the characteristic equations so that the model could be programmed for machine search of solutions on an ITF terminal.

Many of the features of the coupled RO configuration are also contained in its uncoupled components and in a simple wave guide with an abrupt change of acoustic characteristics. Other features are analogous to a simple discrete spring-mass-dashpot system. Analyses of several relevant systems that help explain the RO behavior are outlined in the subappendices, with some discussion pertinent to that behavior. However, the primary intention is that the outlines serve as a basis for technical argument and achievement of a common understanding among those interested. A preliminary review of the appendices might be helpful to those interested in studying the report in detail.

## COMPARISON OF FINITE ELEMENT AND ANALYTICAL RESULTS

A schematic diagram of the coupled RO configuration is shown in Figure B-1. For simplicity in this study, damping was considered to be entirely within the viscoelastic rod, but the analyses can easily be modified to account for internal damping in the organpipe. The analytical model was programmed on ITF and was used for comparison with the NASTRAN and PE

program calculations of acoustic behavior. The finite element calculations with 10, 500, and 1500 psig gas pressure in the organpipe are listed in Table B-I. Results of the comparison of predicted acoustic damping and frequency variations with pressure are, plotted in Figures B-2 and B-3.

Predictions of the acoustic decay parameter,  $\alpha$ , by all of the programs are in reasonable agreement with a small, but possibly important, difference at the 1500 psi pressure condition. At this condition there is about  $12 \text{ sec}^{-1}$  spread in the finite element predictions for  $\alpha$ , but the analytical prediction is about  $24 \text{ sec}^{-1}$  above their average. A reason for this difference has not been conclusively determined, but it may be associated with fundamental inadequacy of displacement-type finite element procedures. This inadequacy will be discussed after comparison of the frequency predictions of the several procedures. Overall, the level of agreement shown in Figure B-2 is encouraging.

Predictions of resonant frequency shifts with pressure, shown in Figure B-3 for the several computational procedures, are not in as good agreement as those for damping. The temptation might exist to disregard differences between the several predictions because the shift is only about 10% of the frequency or less, and its effect appears to be less important than damping. However, as will be shown later in the parameter study, there are situations where a small frequency shift causes a significant change in the decay parameter.

In Figure B-3, the several predictions have a common frequency near zero pressure, which is the uncoupled organpipe fundamental frequency. This is because, at very low pressures, the more dense propellant acts as a hard wall to the gas. As the pressure in the organpipe is increased, the characteristic impedance (product of density and sound speed) of the gas becomes more nearly equal to that of the rod. The result is greater acoustic coupling between the organpipe and the rod. Coupling strength and frequency are also influenced by the damping, through its effect on the sound speed (see Subappendix B.E). As the coupling becomes greater, acoustic amplitudes in the rod approach those in the organpipe and the two oscillate more like a single homogeneous system. The result is that the frequency becomes that of a simple uniform system.

An example of frequency sensitivity to pressure, consider the hypothetical experiment in which (1) damping in the rod is negligible, (2) sound speeds in the rod and organpipe are the same, (3) gas density is negligible in comparison to that in the rod and (4) the organpipe length is three-fourths that of the rod. In this condition the organpipe will oscillate essentially uncoupled at its fundamental frequency. If the organ pipe is then isothermally pressurized to the same density as the rod, the two will have nearly identical acoustic properties and the combination will oscillate like a homogeneous unit. The fundamental frequency will be decreased to three-sevenths of the previous uncoupled organpipe frequency. If the pressure is changed gradually, there will be a gradual transition of frequency. This example is based on simple acoustic theory for coupled oscillators. The effect may also be recognized analytically by considering isothermal variations of  $\rho_2$  in the characteristic equation for an undamped system (see Equation 10 of Subappendix B.C). The same holds for the damped system variations of  $R$ , as induced by changes of  $\rho_2$  or  $\beta$  in Equations (39a, b) of Subappendix B.H.

Coupling of the rod and organpipe acoustic fields is determined by two conditions at the interface, as described in Subappendices B.C and B.H. These two conditions are continuity of both displacement and pressure. They are properly considered in the analytical models but the NASTRAN and PE procedures are of the displacement type and directly consider only continuity of displacement at the interface. The displacement condition provides coupling between the two components, but it does not control the interface slopes of displacement, as is inferred by continuity of pressure. Loose approximations of the pressure conditions presumed to be enforced by elemental force balance in the finite element procedures, but lack of explicit control at the interface leaves the accuracy of results somewhat dependent on chance. This lack of complete simulation may be overcome by use of a mixed (pressure displacement) type element.

The foregoing discussion is helpful in diagnosing the frequency calculations plotted in Figure B-3. Two types of calculations, for  $\beta = 0$  and  $\beta = .5323$ , are involved, and the predictions fall into reasonably close groups. Both NASTRAN procedures predict zero shift for zero damping ( $\beta = 0$ ). In contrast to this, the analytical procedures predict a frequency drop with increasing pressure for  $\beta = 0$ , as might be anticipated from the foregoing discussion of coupling. The frequency drop is caused by the isothermal changes of pressure, and thus of  $\rho_2$ . This frequency drop will help explain the difference between the finite element and analytical calculations for nonzero damping in the following paragraphs.

The NASTRAN predictions of frequency dependence on pressure with damping ( $\beta = .5323$ ) are again reasonably grouped, in both base frequency and variation with pressure. The analytical and PE procedures again contradict the NASTRAN group prediction. In this case they predict a considerably smaller positive slope than NASTRAN. However, the difference between the slopes of each of the procedures, as calculated with and without damping are very nearly the hypothetical frequency shift in Figure B-3 which was obtained by adding positive values of the analytical frequency drop for  $\beta = 0$  to the corresponding values for  $\beta = .5323$ . It hypothesizes the prediction of frequency shift by the analytical procedure with damping, if it was intensive to the basic undamped coupling with frequency as NASTRAN is. The agreement with the NASTRAN calculations is remarkably good, but it is only used to demonstrate a consistency between calculations for the two conditions. It is not a correction of the analytical procedure. Indeed, the indications are that the NASTRAN calculations should be adjusted downward by the analytical frequency drop for  $\beta = 0$ . Analytical, PE and adjusted NASTRAN predictions for coupling with damping are shown in Figure B-4. Reasonable agreement is achieved with this adjustment.

This comparison is made to appear more superficial, but most likely not to be so, by considering the effect of refining the NASTRAN grid. A calculation with  $\beta = .5323$  at 1500 psi with roughly four times finer mesh reduced the predicted frequency from 757 Herz to 740 Hertz. The difference between this and the analytical prediction is only .7%, but the grid was much finer than could be afforded for practical motor stability studies. Furthermore without damping, the refined mesh gave identical results to the coarser mesh calculation. These results are also shown in Figure B-1. Thus, the grid refinement calculation with damping appears to give a fortuitously good result by partly eliminating a frequency shift that is real.



The temptation again might be to state a general rule, from the tendency toward cancellation of the two frequency coupling effects in the RO configuration, as predicted by the analytical procedure. The parametric study shows this would be reckless even for the RO, let alone rocket motor configurations. The conclusions that should be drawn from the comparison of results are (1) there is encouraging agreement between all the procedures on the important prediction of decay exponent, (2) a strong likelihood of erroneous frequency coupling calculations and their sources in the NASTRAN procedures has been detected by the analytical procedure, and (3) there is real value in the use of analytical test models to trouble shoot and validate finite element procedures. Reliability of the analytical test procedure is dependent on the careful attention to detail. Further attention to such detail in the present procedure may be needed to obtain a completely satisfactory check.

After consideration of NASTRAN, PE, and analytical solution differences the decision was made to further review the 1-D model and to perform a parametric study of its independent variables. One possibility considered was that the model might be better able to resolve problems if it were expanded to incorporate two-dimensional (2-D) strain using a Bessel formulation. Bruce Hopkins expanded the calculation to a first order in the Bessel function and found that use of the modified sound speed (based on tensile modulus) in the present 1-D model was the correct procedure. Analysis of higher order terms for cylindrical symmetry has not been performed.

The remainder of this report contains a review of components and concepts that are involved in the RO model and the results of a parametric study of the sensitivity of its eigenvalues to variations of geometric and physical property characteristics.

#### CONCEPTS AND COMPONENTS OF THE ROD-ORGANPIPE

The factors that influence behavior of a 1-D acoustic model are its length and its distribution of sound speed, density and damping behavior. Abrupt changes in the material properties, such as that at the RO interface, and the relative acoustic periods of these components influence acoustic transmission from one component to another through the specific acoustic impedances at the interface. The relative lengths and speeds of sound influence the transmission by their effects on wave frequency and phase relations at the interface.

A preliminary review of the rod and the organpipe, as individual uncoupled systems, helps to more clearly define their interaction in the coupled RO configuration. A description of the uncoupled organpipe is given in Subappendix B.A. As in all of the configurations analysis in this report, both the stress and strain fields are assumed to be 1-D. The damping is considered negligible and, since the end is uncoupled from the rod, no reactive response is assumed. For this reason the eigenvalues are real quantities which are the frequencies  $f_n = nC_0/2L$ . This analysis is briefly extended to that for an undamped rod with fixed-free boundary conditions, which are closely related to the coupled RO problem. The frequencies obtained for the rod are  $f_n = nC_0/4L$ .

The analysis in Subappendix B.A was for a closed-closed organpipe. The double closure is more appropriate for the consideration of coupling with



the rod where the changes of density and speed of sound cause a reasonably large increase in the characteristic impedance to a wave traveling toward the rod. The exponential,  $e^{i(kx-\omega t)}$  is used to represent the spatial and temporal distributions of the wave, assuming the real part as representing the physical phenomena. This approach is based on convenience in mathematical operations and interpretation, and is justified on the basis that the acoustic equations are both real and linear. These conditions permit the modeling to be performed with the complex operator to obtain a representation of the physical solution as the real part of the mathematical solution. This validity also extends to the conditions, to be encountered later, where the terms for  $k$  and  $\omega$  are also complex.

The effect of a sudden change of characteristic impedance is derived in Subappendix B.B. That analysis shows that the transmission of a simple unidirectional wave traveling from one medium to another can be expressed in terms of the ratio of the characteristic impedances. This ratio is the only characteristic needed to account for the influence of material properties on wave transmission through an interface of two undamped materials, if no reflection other than at the interface occurs. This fact is very important to analysis of the RO, because its wave system is formed by the superposition of unidirectional waves that cross the interface.

However, hard walls at the ends of the RO configuration cause reflected waves, they therefore modify the impedance at the interface. This modification is accounted for by use of a complex factor that multiplies the characteristic impedance and is determined by the relative amplitudes and phase angles of the waves reflected from the fixed ends of the RO. Impedance at the interface is therefore influenced by the relative acoustic frequencies and damping which might occur in either end. The acoustic frequencies, in turn, depend on the geometric lengths and sound velocities. As will be shown later, the sound velocities are modified by damping.

No special analysis of free acoustic oscillation in an undamped rod was performed due to its similarity to the organpipe. But special consideration should be given to the assumption that both the stress and strain fields in the rod are 1-D. This infers that the oscillations are only in dilatation. In the analyses of this report, the assumption was made that use of the shear modulus (rather than that for dilatation) in the 1-D strain model is an acceptable approximation of 2-D laterally unconstrained rod oscillations in a fundamentally longitudinal mode. As mentioned previously this was found to be a reasonable first approximation for the 2-D stress field.

An analysis of an undamped RO configuration is developed in Subappendix B.C. The characteristic equation, reproduced here as

$$\frac{\tan\left(\pi f \frac{2L_1}{C_1}\right)}{\tan\left(\pi f \frac{2L_2}{C_2}\right)} + \left(\frac{\rho_1 C_1}{\rho_2 C_2}\right) = 0$$

implicitly but forcefully shows the importance of both the characteristic impedance ratio,  $\rho_1 C_1 / \rho_2 C_2$ , and the relative magnitudes of the uncoupled acoustic frequencies of the rod and the organpipe,  $C_1/2L_1$  and  $C_2/2L_2$ , in

determining the characteristic frequencies. Care must be exercised in using the impedance ratio as a dimensionless similarity parameter because the sound speeds, which it contains as a ratio factor, appear otherwise in the trigonometric functions. Even though coupling effects involve the entire ratio, independent variations of the sound speed ratio should be considered separately.

The units of time and distance can be separately chosen so that  $C_1 = 2L_1$  in magnitude. With this transformation the characteristic equation would demonstrate another important similarity parameter  $(C_2L_1)/(C_1L_2)$ . Again, this parameter is not exact, because the acoustic velocities are involved differently in the impedance ratio. Thus, the coupled, but undamped RO configuration  $\rho_1/\rho_2$ ,  $L_1/L_2$  and  $C_1/C_2$  appear as exact dimensionless similarity parameters while  $(\rho_1C_1)/(\rho_2C_2)$  and  $(C_2L_1)/(C_1L_2)$  appear as important, but coupled parameters. These facts will be realized in analysing behavior of the coupled RO in the parameter study.

The influence of damping (caused by internal friction or viscosity) on the wave amplitude and frequency is not as intuitively nor analytically simple as that for a discrete spring-mass-dashpot system, but similarities in the behavior of the two warrant preliminary consideration of the latter to gain insight. Analyses of two common (Voigt and Zener) systems are presented in Subappendix B.D.

The Voigt model eigenvalue,  $\Omega = -\alpha + \frac{1}{2}\omega = -\zeta\omega_n + \omega_n\sqrt{1-\zeta^2}$  clearly shows the influence of damping on both the frequency and amplitude of free oscillations. Shifts of the damped eigenvalue frequency and the frequency response peak are both downward from the undamped condition as shown in Figure B.D-1. It is important to recognize that the displacement frequency response peak is shifted down from the undamped resonance frequency by approximately twice the shift of eigenvalue frequency obtained for the free damped oscillations but the velocity response peak is not shifted by damping.

A discrete model cannot satisfy a comprehensive analysis of the continuous RO configuration, but the latter can (at least theoretically) be posed in a discrete modal form in which the analogies described in Subappendix B.D can be made exact. The Voigt model is unimodal so it cannot predict direction of frequency shift with damping in coupled systems, where the shifts can be in either direction according to phase relations between transmitted and reflected waves at the interface. Pursuit of the exact analogies between discrete and continuous models is beyond the scope here, but the results of Appendix D are qualitatively important for understanding damping effects and their calculation by eigenvalue and frequency response methods.

The simplest form of damped continuous system is the 1-D damped rod. An analysis of this system is presented in Subappendix B.E to demonstrate damping analysis terms in the uncoupled components of the damped RO configuration. This continuous system analog to the complex compliance, discussed in Subappendix B.D, is applied here as the only change to the governing equations used for Subappendix B.A. The compliance analog enters as a time-rate-dependent part of the equation of state so that it forms a dynamic state equation. This form of the dynamic state equation is similar in character to the Voigt model in Subappendix B.D. In comparison with the Zener model, it has the weakness of not characterizing the pressure relaxation time for a step change of density. Neither the magnitude of the pressure relaxation term nor its influence on the analysis are known. Time was not available to determine

either in this analysis, however, the difference might be crucial in obtaining satisfactory correlation of test and analysis data.

In addition to the complex frequency, as used in Subappendix B.D for the damped discrete system, the damped rod analysis develops the concept of the complex wave number, which defines both the wavelength and its spatial amplitude decrement. In the sense of this wave number being the ratio of angular frequency to the sound velocity in the case of an undamped system, some analysts define a complex wave velocity for the damped system and develop their analysis using it. This is not essential to the development since the temporal and spatial aspects of the damped wave are completely defined by the complex frequency and wave number.

The complex characteristic equation is also introduced in Equation 15 of Subappendix B.E. Hyperbolic terms, that involve the spatial wave amplitude, combine with the trigonometric terms, that involve the wavelength. The real parts of the wave equation and boundary conditions require both the real and imaginary parts of the characteristic equation to be satisfied. It is therefore separated into two coupled real equations to be simultaneously solved for the components,  $f$  and  $\alpha$ , of the complex eigenvalue.

Analysis of frequency response of the damped rod is helpful for understanding problems involved in utilizing test data. The frequency response for a damped rod is developed in Subappendix B.F as a basis for understanding these problems. This development is similar to that for eigenvalues of free oscillations. The governing equations are identical, but the oscillations are assumed to have a steady value so that a real frequency is assumed. The other essential difference in assumptions is that some part of the body (the rod end in Subappendix B.F) is assumed to have a constant oscillatory amplitude and frequency.

Although there is no temporal damping, the time-rate dependence in the dynamic state equation interacts with the real frequency to create a complex wave number and, therefore, spatial damping. The temporal damping coefficient may be obtained by inference either from the resonant frequency and half-power bandwidth or the loss tangent in the ways used for discrete system analyses, but any such estimates should be based on careful analysis.

All of the analyses of this report, including that for the RO configuration, were developed using acoustic terminology. However, in consideration of the direct applicability to possible structural dynamic testing by conventional engineering methods, the frequency response of the damped rod was redeveloped in Subappendix B.G, using structural nomenclature and the test data convention for the structural damping coefficient  $\beta$ , loosely called the loss tangent.

The relation between the acoustical and structural damping coefficients was determined by comparison of acoustic and structural damping developments in Subappendices B.F and B.G, to be

$$\beta = -\omega \zeta / C^2 = -\omega \tau$$

where  $\zeta$  is the acoustic damping coefficient and  $C$  is the sound velocity in the damped material, as approximately determined from the static modulus. Some questions relating to sign conventions in test and analysis have not



been conclusively resolved. Although experimental tests would show that both  $\zeta$  and  $\beta$  vary with oscillation frequency (and amplitude), the analyses of this report assume that  $\beta$  is a constant (0.5 for the parametric study and .5323 for the PE and NASTRAN programs) for all test parameter variations but that of itself. The close relations between analyses of free and damped oscillations in the continuum model and those in the Voigt model should motivate careful consideration of the differences between frequency response and free oscillation analyses, as they relate to experimental data and acoustic damping predictions.

The review of the preceding paragraphs and the developments in Subappendices B.A through B.G display the components, and concepts involved in the analysis of the damped RO configuration. An analysis of this configuration is provided in Subappendix B.H. The complications of its behavior, due to coupling of components and due to damping, are interrelated but, to a reasonable approximation, may be considered separately. Some analysis of the RO behavior for variations of its geometry and material characteristics are discussed later in the parametric study.

Subappendix B.H also includes the development and application of a generalized Newton's method to obtain the simultaneous solution of the two characteristic equations as functions of the frequency and temporal damping parameters. This procedure is applied, in the ITF program, to iteratively search the zeros of the eigenfunctions. Accuracy of the solution depends on the precision available in the ITF system and on the stability of the eigenvalues  $f$  and  $\alpha$  through repeated iterations. If, through an iteration, the respective changes  $df$  and  $d\alpha$  are made and

$$\left| \frac{df}{f} \right| + \left| \frac{d\alpha}{\alpha} \right| < .0002$$

the solution is accepted. The computer program is listed and discussed in Subappendix B.I.

The ITF-operated analytical procedure is a very cost effective and instructive tool. Its validity is sufficient that it can provide valuable insight and data to complement the finite element study and help guide the remaining effort in the structural damping program. The parameter study in the following paragraphs is intended to define the sensitivities of the RO to the several system parameters and to develop the similarity relations by which analysis of the modes can be reduced to simplest form.

#### PARAMETRIC STUDY OF ROD-ORGANPIPE BEHAVIOR

The dependent variables of interest in defining the RO acoustic behavior are its eigenvalues and eigenfunctions. The eigenfunctions are helpful in understanding the distribution and flow of acoustic energy, but they will be disregarded in this analysis to focus attention on eigenvalues. This will permit summarization of the temporal behavior for a large range of parametric variation in a few graphs of frequency,  $f_c$ , and amplitude decay rate,  $\alpha_c$ .

The independent variables of interest are the lengths,  $L_1$  and  $L_2$  of the rod and organpipe respectively, and the material properties associated with wave travel and damping as shown in Figure B-1. In the analytical model those properties are characterized by the sonic speeds,  $C_1$  and  $C_2$  the steady-state densities,  $\rho_1$  and  $\rho_2$ , of the solid and gas respectively, and the temporal damping coefficient,  $\beta$ , of the solid.



The characteristic equations define the eigenvalues implicitly so a preliminary study of the variations for the acoustic parameters ( $L_1$ ,  $L_2$ ,  $C_1$ ,  $C_2$ ,  $\rho_1$ , and  $\rho_2$ ) was performed to find the trends that would infer functional similarities as discussed earlier. Also, since the densities enter the analysis only in the form of a ratio, they are combined in that form as a single parameter. Base values of the parameters are shown in the list below.

Base Values of the RO Configuration Parameters		
Parameter	Symbol	Value
Density Ratio	$\rho_1/\rho_2$	10
Rod Length	$L_1$	10 in.
Pipe Length	$L_2$	10 in.
Rod Sound Speed	$C_1$	6000 IPS
Pipe Sound Speed	$C_2$	12000 IPS
Damping Parameter	$\beta$	.5

Results of these calculations are summarized in Figures B.5 through B.12. All results were plotted in dimensional form but the frequency is plotted as a shift,  $\Delta f_c$  of the coupled frequency,  $f_c$  from the uncoupled organpipe frequency,  $f_2 = C_2/(2 * L_2)$ ; thus,  $\Delta f_c = f_c - f_2$ . This permits reducing the scale-range from that required to span the wide ranges of  $f_c$  created by varying  $C_2$  and  $L_2$  and focusing attention on deviations from  $f_2$  for their significance. The data for variations of  $C_1$  and  $L_1$  were plotted similarly for uniformity.

The lengths and velocities were all varied much more than needed for any direct comparison, and more than is physically reasonable for the sonic velocities. This was done to obtain a vivid picture of the functional characteristics of the variations. Thus, the hyperbolic nature of the average variations of  $\alpha_c$  with respect to  $L_2$  and  $C_1$  in Figures B.6 and B.7 plus similar quadratic variation with respect to  $C_2$  in Figure B.8, were readily detected. A roughly proportional variation of all the data with respect to the density ratio  $\rho_2/\rho_1$  is also apparent. This dependency will be considered in greater detail in subsequent paragraphs and in Figure B-20. No average variation of  $\alpha_c$  with respect to  $L_1$  is apparent. This appears to contradict the idea that acoustic decay by structural damping increases with the volume of damping material.

The terms that are involved in the average variations are those related to the characteristic impedances of the gas and solid and to the uncoupled organpipe mode frequency. These dependencies were anticipated and used to reduce the variations to a simpler form.

The variations of  $\Delta f_c$  with respect to these parameters ( $L_2$ ,  $C_1$ ,  $C_2$  and  $\rho_1/\rho_2$ ) involve characteristics similar to those for  $\alpha_c$ , though not as distinct. This similarity might be anticipated on the premise that, in the construction of the wave number in the wave equation, the damping coefficient enters the

real and imaginary parts as an additive and multiplicative factor respectively. The entire complex frequency,  $\omega_c - i\alpha_c$  would therefore be affected in the same manner. Thus, at this level of comparison, the correlations for  $\Delta f_c$  appear to be similar to those for  $\alpha_c$ . The premise that the variations of frequency shift and decay exponent could be reduced to at least a partial analytical description is obtained from considering the characteristic equations in Subappendices B.C and B.H. This is supported by the data presented in Figure B-5 through B-12.

Algebraic trends of the RO frequency shift,  $\Delta f_c$ , and decay exponent  $\alpha_c$ , variations with  $C_1$ ,  $C_2$ ,  $\rho_1/\rho_2$ , and  $L_2$  were previously described. These variations and the functional form of the characteristic equations, were used to reduce a functional approximation to the trends given by  $\Phi_c = (\rho_2 C_2 / \rho_1 C_1) (C_2 / 2L_2)$ . The characteristic impedance ratio and organpipe frequency being considered are contained in this approximation to  $\Delta f_c$  and  $\alpha_c$ . They respectively represent the influence of material properties on coupling effectiveness, and the real eigenvalue which supports its own modification.

Lengths and velocities were combined into a single "mode-coupling" variable  $\Gamma_c = (C_2 * L_1) / (C_1 * L_2)$ , on the assumption that the uncoupled mode characteristics form a single similarity group upon which the variations depend. These variations of  $\Delta f_c$  and  $\alpha_c$  with  $\Gamma_c$  are transcendental and may not be easily resolved in functional form. They were left in empirical form here, but may be further resolved by a more elaborate modal analysis.

The damping coefficient,  $\beta$ , is already a dimensionless parameter. It was not recognized as belonging to the previously mentioned similarity groups. These are closely related in the immediately visible variation trends and the forms of the characteristic equations. Therefore  $\beta$  was left to be considered separately after a preliminary reduction of the data with the variables mentioned above.

The ITF procedure was modified to calculate the values of  $\alpha_c / \Phi_c$  and  $\Delta f_c / \Phi_c$  as functions of  $\Gamma_c$ . Dimensional variables are simultaneously involved in  $\Phi_c$  and  $\Gamma_c$  and, because these dimensionless parameters were only test variables, calculations were performed varying  $\Gamma_c$  by means of the individual dimensional variables as was done in the initial parameter study. Results of these calculations are plotted in Figures B-11 through B-14, and are arranged in identical order with respect to the individual dimensional variations.

A gross analytical reduction and simplification of the relations between the RO system variables is evident in the similarity of the plotted variations. Relevant scale magnitudes of both independent and dependent variables are reduced to the same order. A global picture of the variations is easily perceived as products of (1) the algebraic function,  $\Phi_c$ , and (2) the globally similar plots of  $\alpha_c / \Phi_c$  and  $\Delta f_c / \Phi_c$  with  $\Gamma_c$ . This similarity is strong between variations of any of the components of  $\Gamma_c$  and is essentially exact between variations of either of the lengths or sound speeds. A totally closed form solution was not obtained, but the variations are in suitable form to obtain a simplified image of the total results and to guide further investigations.

Each of the several plots for different density ratios in Figures B-11 through B-14 are quite similar in form. Variations between the forms are either small or uniform. A more detailed perspective of these variations was obtained by calculating the reduced frequency and decay parameters as functions of the density ratio,  $\rho_1/\rho_2$ , for several values of  $\Gamma_c$ . These calculations are plotted in Figures B-15 and B-16.

The plots show several distinct regions of variation with respect to  $\rho_1/\rho_2$ , and  $\Gamma_c$ . At very low values of these parameters the frequency shift parameter,  $\Delta f_c/\bar{\phi}_c$ , and the decay parameter,  $\alpha_c/\bar{\phi}_c$ , vary oppositely with the frequency variable,  $\Gamma_c$ . The approximately linear variations of these parameters with  $\rho_1/\rho_2$  as shown in Figures B-15 and B-16, and with  $\Gamma_c$ , as shown in Figures B-11 - B-14, are reasonably simple to predict. However, this may not be relevant to structural damping because it corresponds to very high pressures (or low temperatures) and to extremely small values of the length ratio,  $L_1/L_2$ .

As  $\rho_1/\rho_2$  and  $\Gamma_c$  are increased, the decay and frequency shift variations both pass through transition regions for each of these variables. Thus, as  $\Gamma_c$  is increased, the variations have strong oscillations as the uncoupled frequencies,  $C_2/(2 L_2)$  and  $C_1/(4 L_1)$  pass through resonance and anti-resonance conditions. As  $\Gamma_c$  becomes larger than 2, the significance of this resonance is diminished by the spatial decay of the reflected wave in the solid so the variation with respect to this variable becomes quite small. A rough check has indicated a reasonable likelihood of this situation existing in practical motor designs.

As the density ratio,  $\rho_1/\rho_2$  is increased in Figures B-15 and B-16, there is a transition in the decay parameter variation, from the linear region to an approximately constant region. The likely region of relevance to tests and motor design is above  $\rho_1/\rho_2 = 10$ . The variation of  $\alpha_c/\bar{\phi}_c$  and  $\Delta f_c/\bar{\phi}_c$  above this value is essentially negligible.

If the foregoing conditions do exist in motor structural damping, the consequence on its analysis may be extremely important, because it might reduce the evaluation of structural damping to that of determining a parameter quite similar to  $\bar{\phi}_c$ . This task would be almost trivial when compared to a complete NASTRAN analysis. If the variations with  $\Gamma_c$  are small but significant, greater reliability in the calculations could be achieved by using NASTRAN. An intermediate possibility is that for some acoustic modes and motor burn conditions, a simplified analysis could be used while others would require analysis involving the uncoupled modes, to obtain the coupled behavior.

As stated earlier, analysis of the influence of the damping coefficient,  $\beta$ , was deferred until simplification of the analysis could be achieved with the other similarity variables. Variations of the reduced decay and frequency parameters with  $\beta$  were then performed for several values  $\Gamma_c$  and  $\rho_1/\rho_2$ . Representative plots of these calculations are shown in Figures B-17 and B-18.

For very small values of  $\beta$  (not shown in the plots), the value of  $\alpha_c/\bar{\phi}_c$  varies linearly and nearly equal to  $\beta$ . The approximate equality indicates an essential closure of the relationship  $\alpha_c = \beta \bar{\phi}_c$  for small  $\beta$ . However, the region of practical interest is near  $\beta = 0.5$  and, for this value, nonlinearities strongly influence the variation. At very high values of  $\beta$ , structural damping dynamically hardens the viscoelastic solid so much that



it behaves more like a solid terminal to the organpipe. This 'hardening' is in addition to that of the characteristic impedance,  $\rho_1/\rho_2$ , in  $\Phi_c$ . It therefore, strongly reduces  $\alpha_c/\Phi_c$  from the linear variation for large  $\beta$ .

Fortuitous matching of the acoustic wave in the rod with the uncoupled organpipe fundamental mode exists for  $\beta = 0$  and  $\Gamma_c = 2, 4$ , and  $6$ . The frequency shift therefore, approaches zero with  $\beta$  because the latter acts to mismatch the transmitted and reflected waves at the RO interface. At  $\Gamma_c = .25$ , the rod and organpipe are not well matched at  $\beta = 0$ , but the match is improved by increasing  $\beta$ . Further study would be required to obtain a strong rationale regarding the influence of  $\beta$  on frequency shift and to assure consistency between experimental methods and data, and damping predictions based upon them.

#### ROD-ORGANPIPE ADVANTAGES AND DISADVANTAGES

The RO configuration has proven to be a valuable analytical tool for evaluating finite element results in the 1-D problem, and for disclosing problems and simplifications of structural damping analysis. Much more insight may yet be obtained by simple calculations. For example solution stability and sensitivity to error can be assessed by calculating partial derivatives of the characteristic functions with respect to uncertain parameters and finite element formulation features. Other applications are to determine the differences that may exist between behavior of Voigt, Maxwell, and Zener models, and between 1-D and 2-D (axisymmetric) models.

The RO is an effective model for simple theoretical exploration on the computer, but its simplicity is achieved by disregarding several practical details in the analytical model. The rod is constrained to axial motion and the interface is assumed to be sealed around the circumference by a perfectly compliant and frictionless seal. Acoustic waves in the rod could be more accurately simulated by accounting for axisymmetric radial expansion with a Bessel formulation, but transverse oscillations would also be parametrically excited in the rod by longitudinal driving at the RO interface.

The rod cannot be appropriately constrained from these modes without impeding the acoustic wave. Nonlinear Floquet stability theory, using the Mathieu-Hill equation, is required for analysis of the parametrically excited transverse waves. New theoretical work would be required to analyze these waves, but the problem would likely be intractable.

Another practical problem of the present RO configuration is the acoustic seal needed around the circumference of the interface. Acoustic losses at the seal would need to be negligible, but its friction and compliance would also need to be extremely small and accountable in any experimental apparatus. Any circumferential nonuniformity would seed the parametrically excited transverse oscillations.

Still another drawback of the RO is its lack of effectiveness in coupling organpipe oscillations with bending and shear strain in the viscoelastic materials. Analytical representation is easy to obtain, using the reasonably high accuracy of a computer, even though the acoustical impedance is high. Experimental work is much less accurate and, therefore, the need for maximum matching of the rod and organpipe impedances is acute.



## CONCLUSIONS

Comparison of the rod-organpipe (RO) analytical model with results from the NASTRAN and PE programs has demonstrated reasonable agreement in the acoustic decay parameter and disagreements in the frequency shift. The likelihood was shown that the disagreements are caused by a weakness of the reformulated CDUM element used in NASTRAN. Further study of this problem should be performed to determine whether a mixed element, that provides for continuity of both pressure and displacement for abrupt material property changes, would calculate the correct frequency shift. Such an element may be valuable for other problems in structural analysis.

A comprehensive parametric study of acoustic decay and frequency shift in the RO configuration was performed, and the results were reduced to a simplified form by analysis of similarity. In the simplified analysis, three nondimensional independent variables essentially replace seven dimensional variables needed in the unreduced form. The results provide considerable insight for the general problem of structural damping analysis. They also disclosed the possibility of achieving an important reduction in the analysis required for structural damping with simple, but powerful, modal analysis methods.

The RO analytical procedure has proved to be a valuable tool in understanding the problem of structural damping and the finite element procedures used to analyze it. Extensions in the use of the model that are recommended are separate modifications to investigate (1) the significance of applying the more comprehensive Zener model for viscoelastic compliance, (2) eigenvalue solution stability and sensitivity to error, and (3) the significance of 2-D effects.

The subappendices of this report provide a heuristic development of many concepts and problems in structural damping analysis and of the modified Culick analysis of the RO configuration. They also provide a rational basis for critical review of problems of the structural damping program with AFRPL.

CODE	GAS ELEMENT	GRAIN ELEMENT	EIGEN VALUE METHOD	PRESSURE (psig)	GRAIN $\beta$	COUPLED GAS MODE	
						$f_c$ (Hz)	$\alpha$ (Sec <sup>-1</sup> )
NASTRAN-15 (Hydroelastic)	Fluid	CDUM	Power	10	.5323	732.0	2.46
	Fluid	CDUM	Power	500	.5323	739.0	60.05
	Fluid	CDUM	Power	1500	.5323	757.0	158.96
NASTRAN-15 (Hydroelastic)	CDUM	CDUM	Power	10	.5323	729.4	2.71
	CDUM	CDUM	Power	500	.5323	737.0	59.69
	CDUM	CDUM	Power	1500	.5323	754.2	162.76
NASTRAN (Very Fine Grid)				1500	.5323	740.2	174.04
NASTRAN - 15 (Hydroelastic)	Fluid	CDUM	Determinant	1500	.5323	757.0	159.05
NASTRAN-15 (Real E.V.)	Fluid	CDUM	Power	500	0	731.64	0
	Fluid	CDUM	Power	1500	0	731.67	0
NASTRAN - 15	CDUM	CDUM	Freq. Resp.	10	.5323	≈730	0
	CDUM	CDUM	Freq. Resp.	1500	.5323	≈760	0
POTENTIAL ENERGY PROGRAM	Fluid	Solid	Freq. Resp.	10	.5323	≈730	2.93
	Fluid	Solid	Freq. Resp.	500	.5323	≈730	63.59
	Fluid	Solid	Freq. Resp.	1500	.5323	≈730	170.54
POTENTIAL ENERGY PROGRAM	Fluid	Solid	Freq. Resp.	10	0	726	0
	Fluid	Solid	Freq. Resp.	500	0	710	0
	Fluid	Solid	Freq. Resp.	1500	0	693	0

TABLE B-I. NASTRAN and Potential Energy Calculations of Rod-Organ Pipe  
Acoustic Frequency and Decay Parameters.

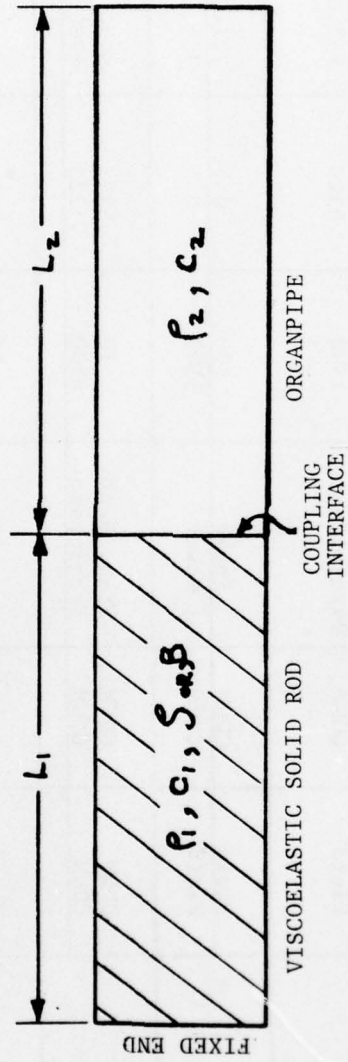


Figure B-1. Schematic of Rod-Organpipe



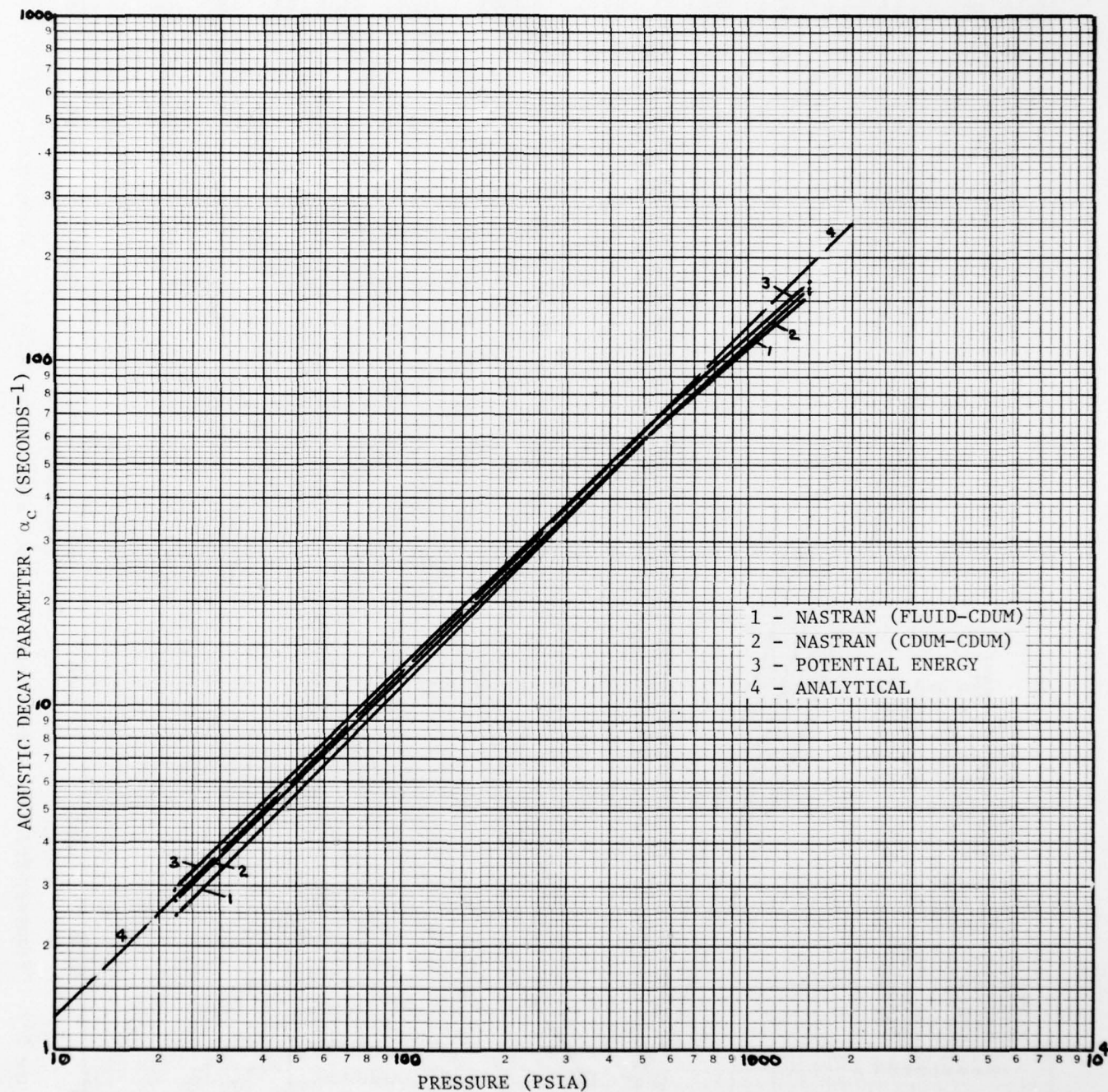


Figure B-2. Acoustic Decay-Pressure Predictions of Finite Element and Analytical Procedures.



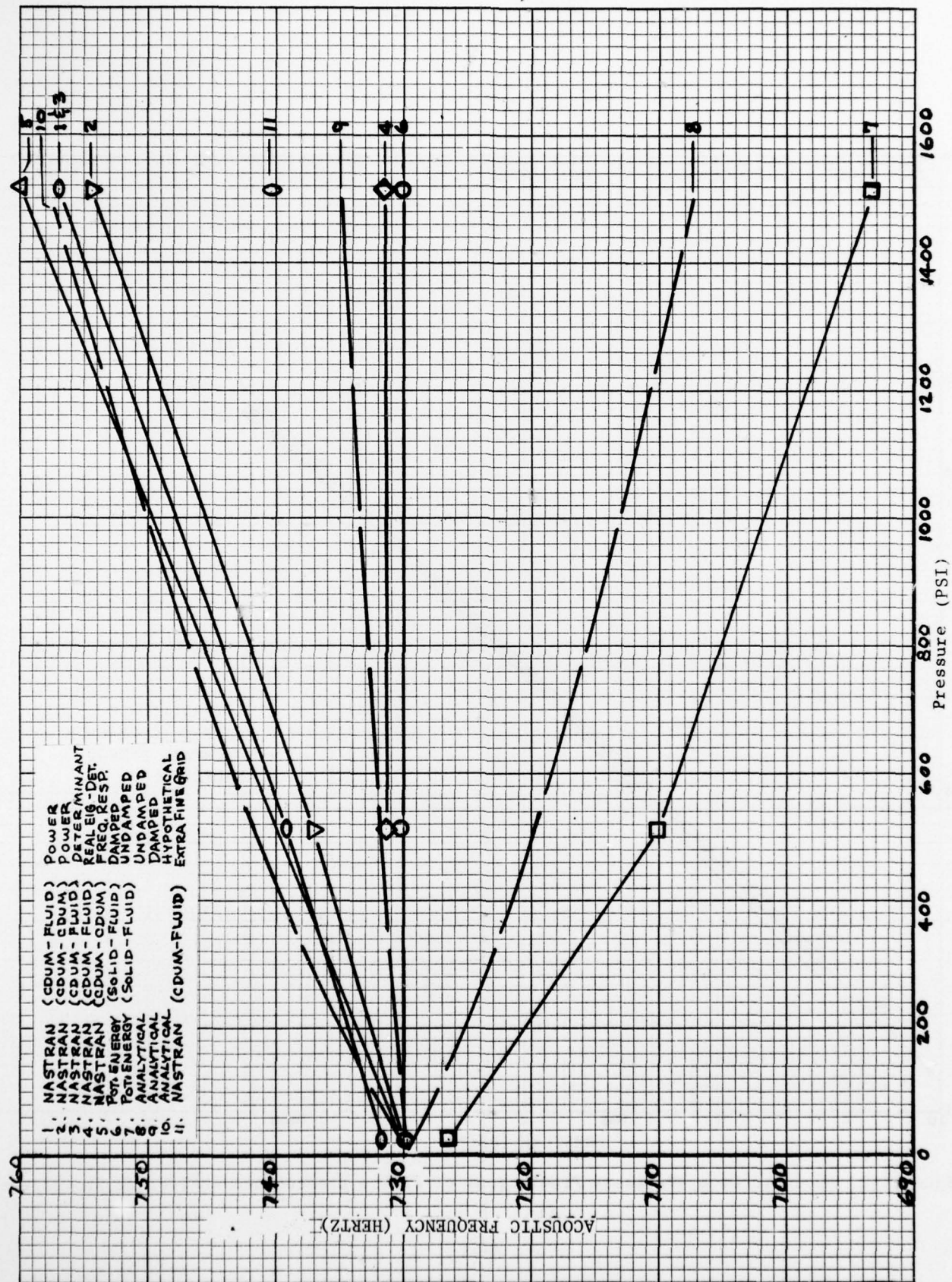


Figure B-3. Frequency-Pressure Predictions of Finite Element and Analytical Procedures.

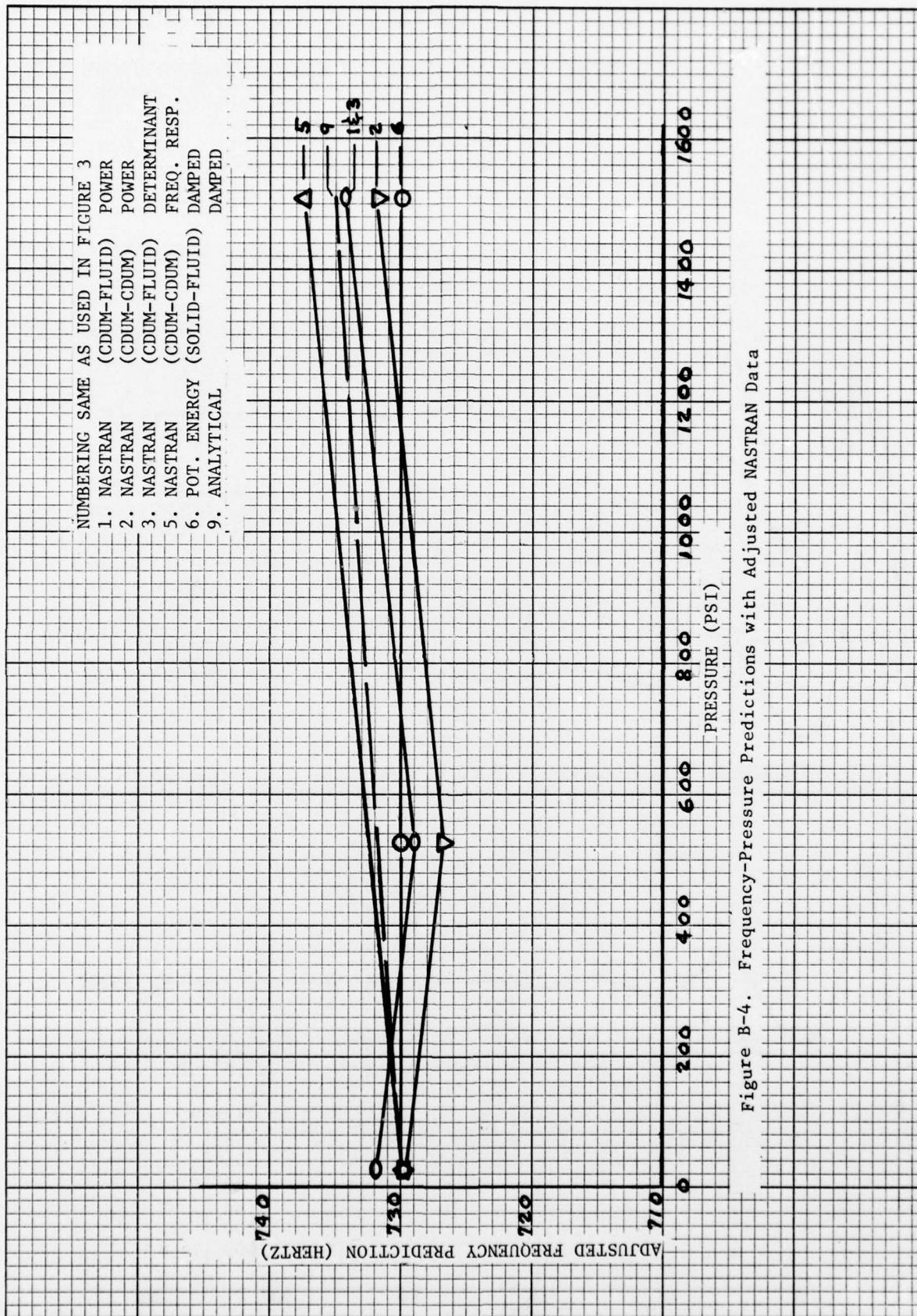


Figure B-4. Frequency-Pressure Predictions with Adjusted NASTRAN Data



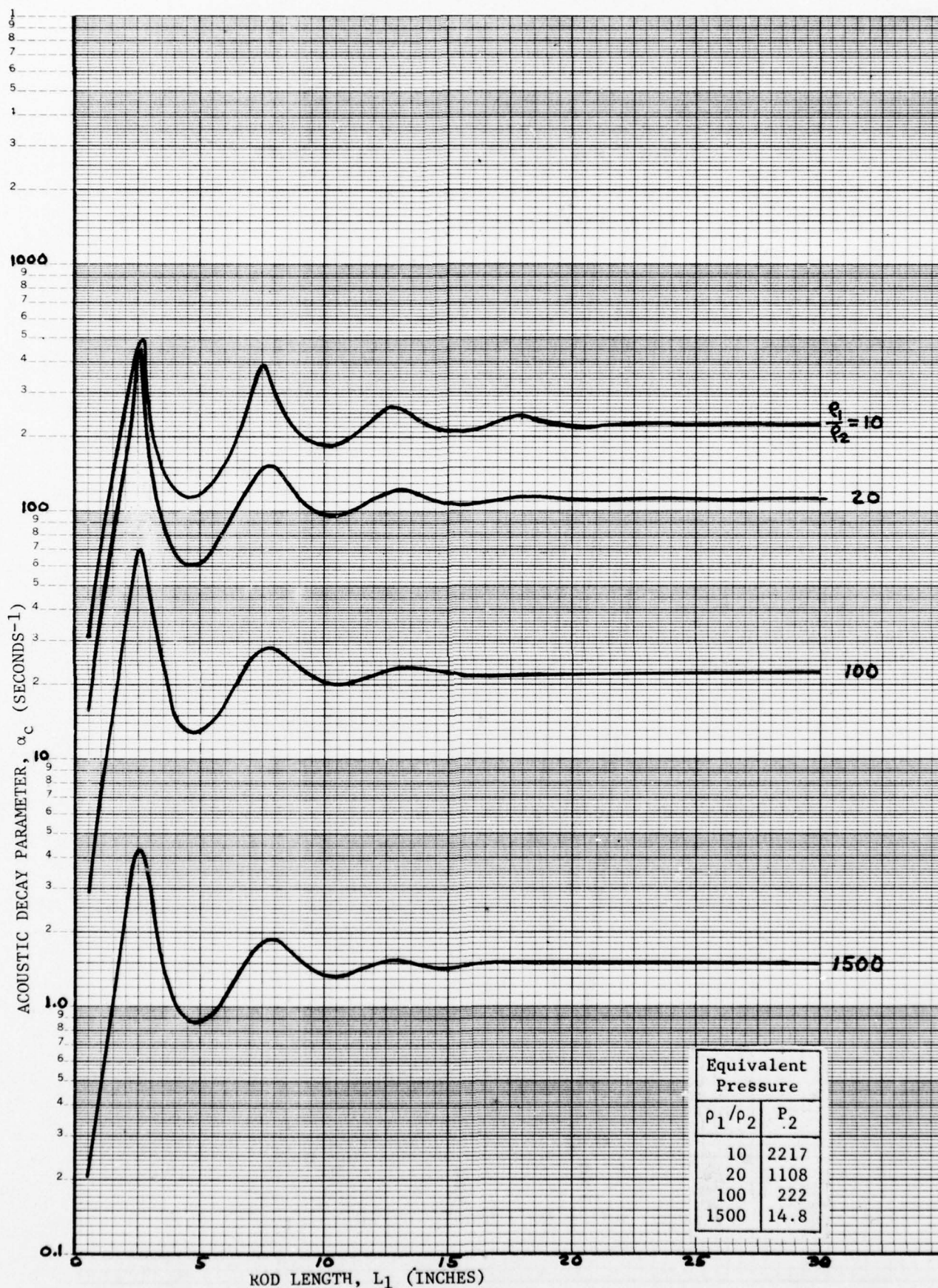


Figure B-5. Acoustic Decay - Rod Length for Several Density Ratios

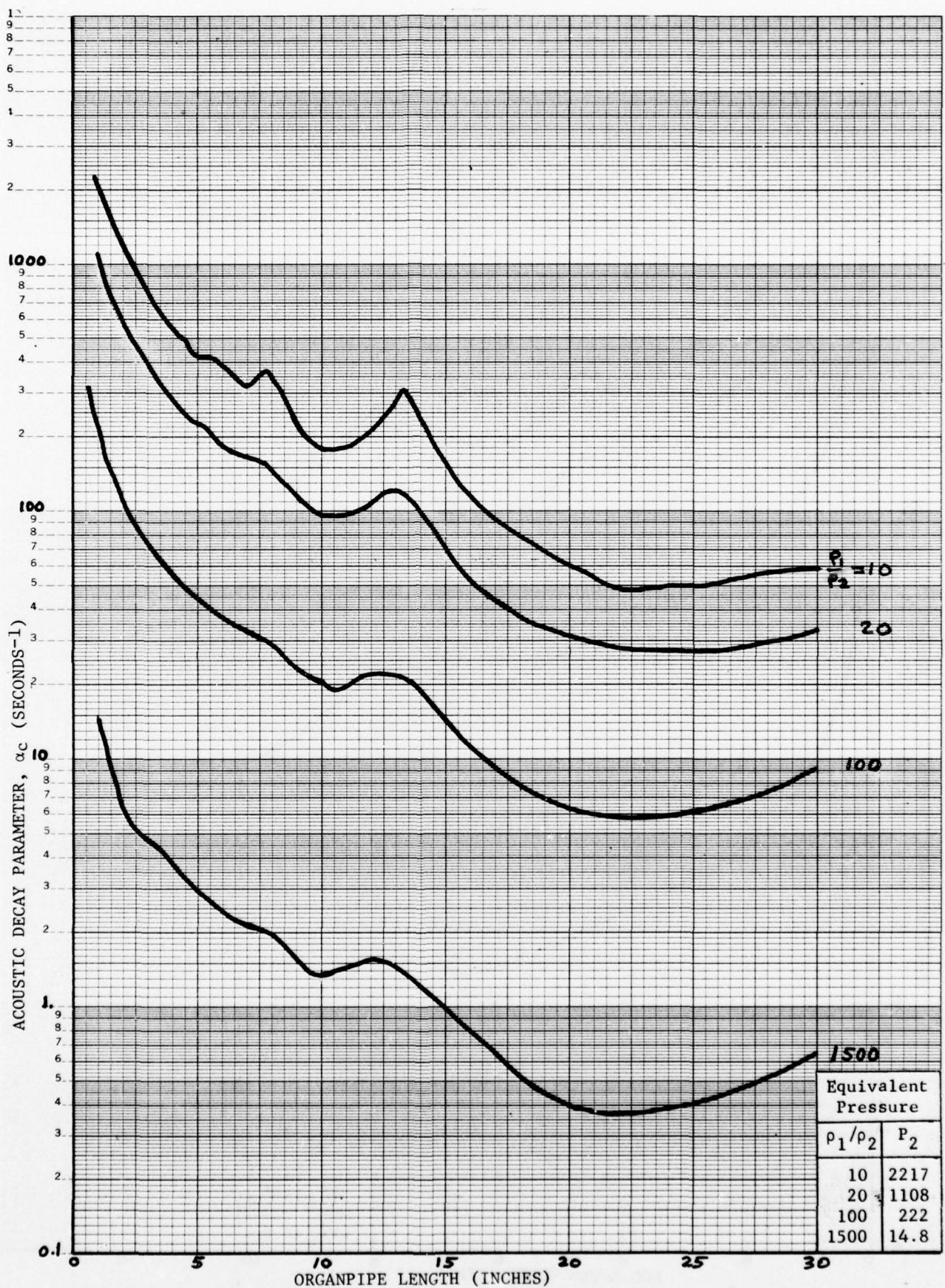


Figure B-6. Acoustic Decay - Organpipe Length for Several Density Ratios



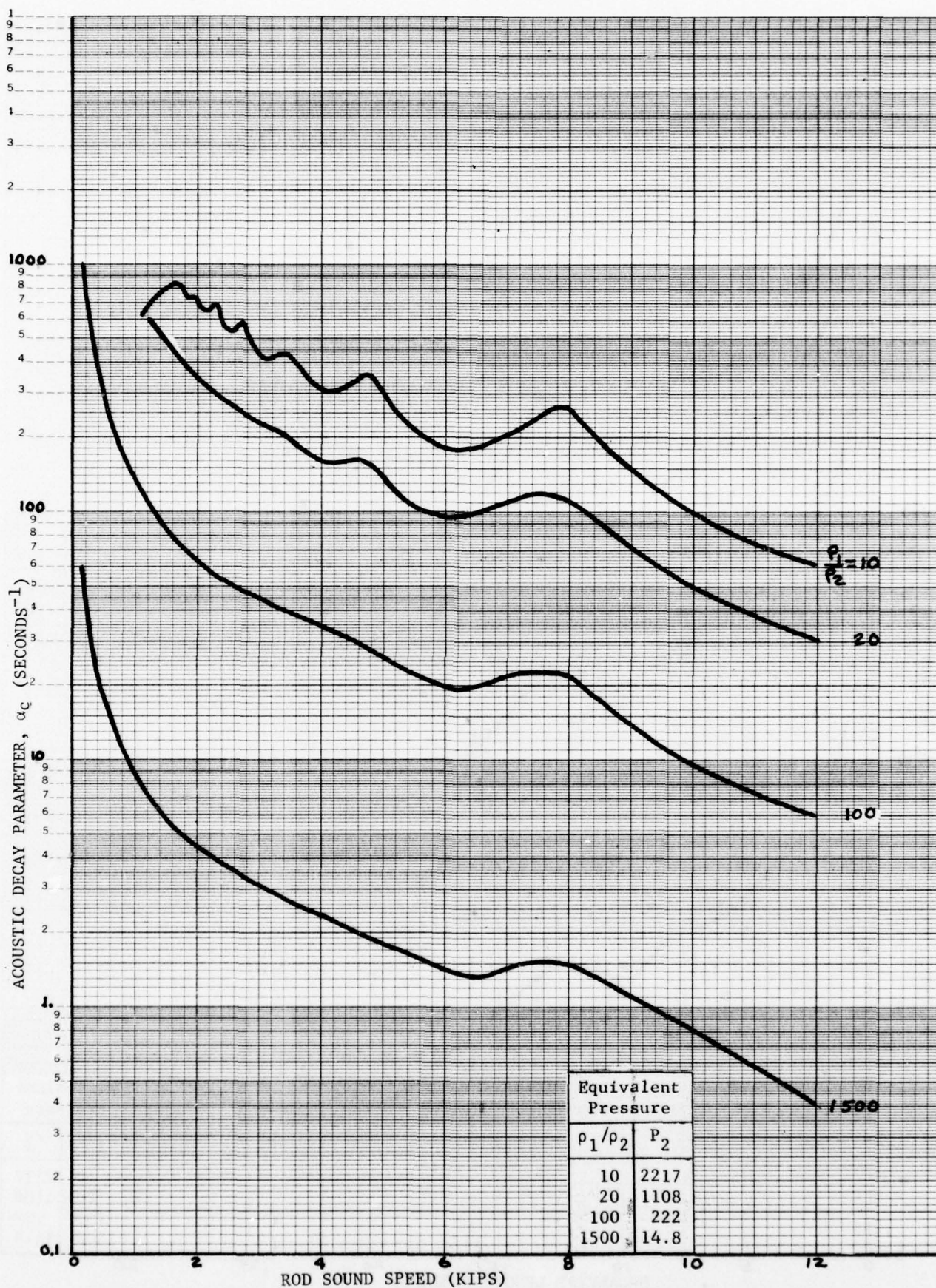


Figure B-7. Acoustic Decay - Rod Sound Speed for Several Density Ratios

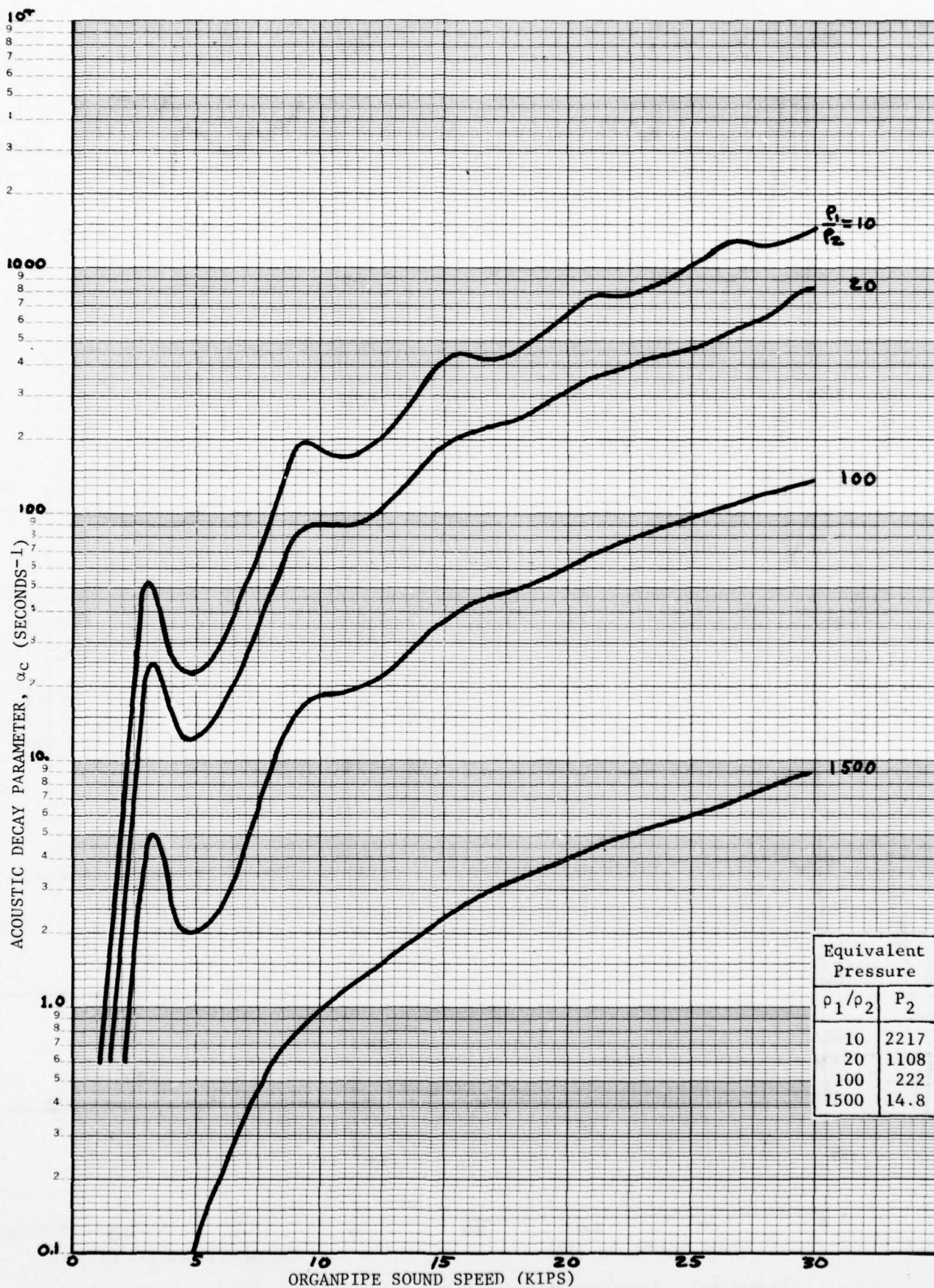


Figure B-8. Acoustic Decay - Organpipe Sound Speed for Several Density Ratios



46 0782

10 X 10 TO THE INCH • 7 X 10 INCHES  
KIEFFEL & ESSER CO. MADE IN U.S.A.

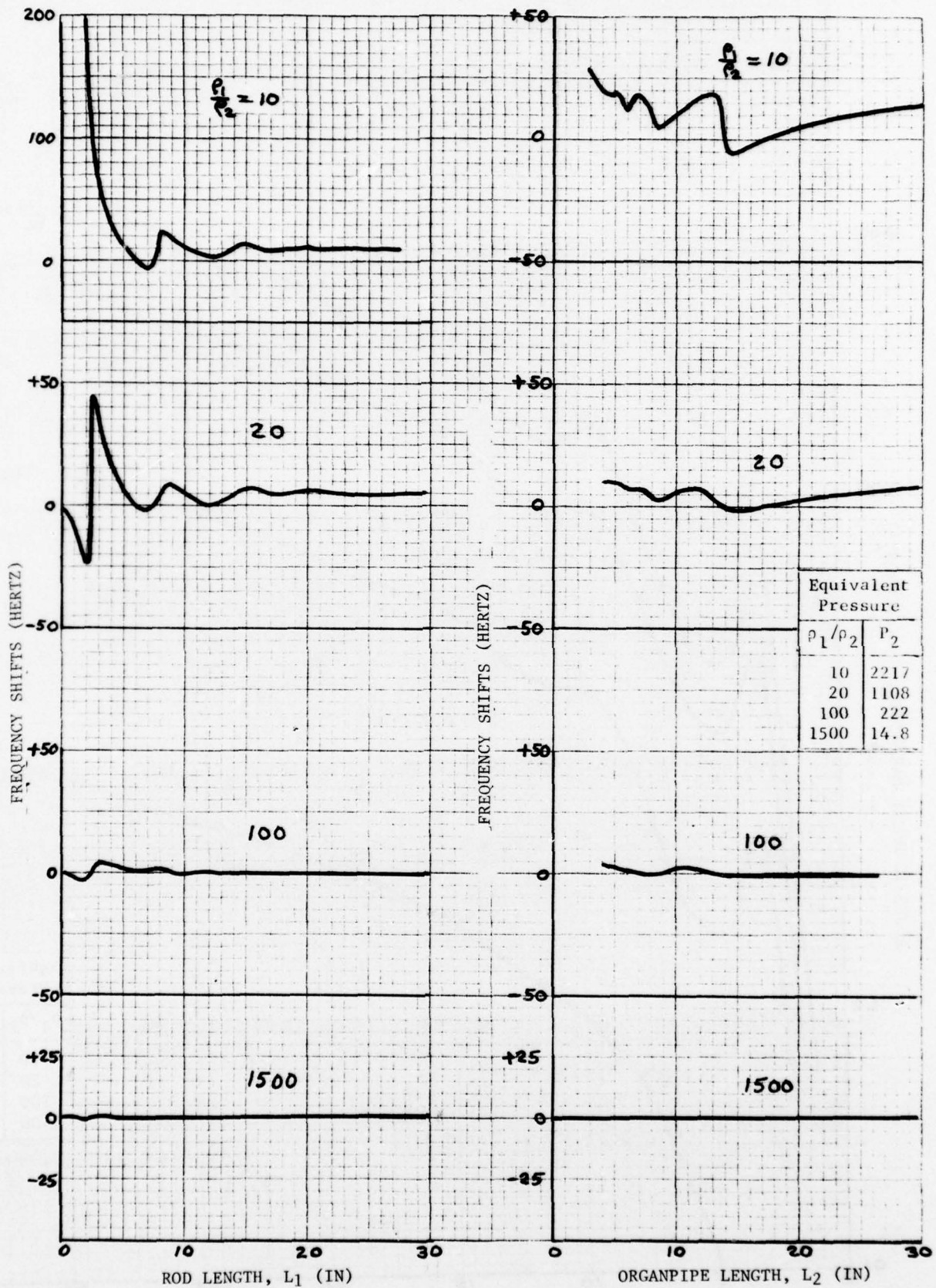


Figure B-9. Frequency Shifts - Component Lengths for Several Density Ratios  
B-30

10 X 10 TO THE INCH • 7 X 10 INCHES  
NEUFEL & ESSER CO. MADE IN U.S.A.

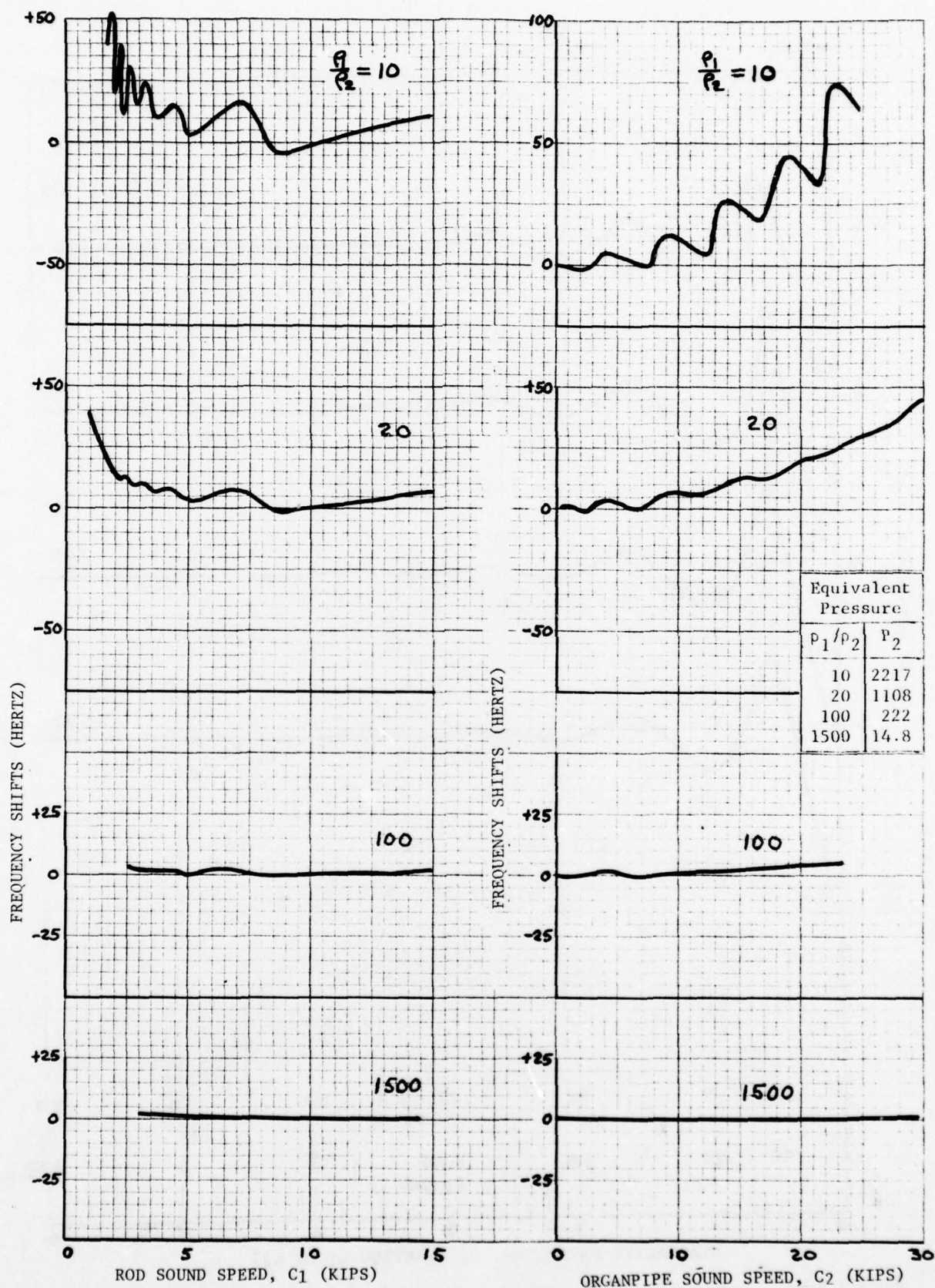


Figure B-10. Frequency Shifts - Component Sound Speeds for Several Density Ratios



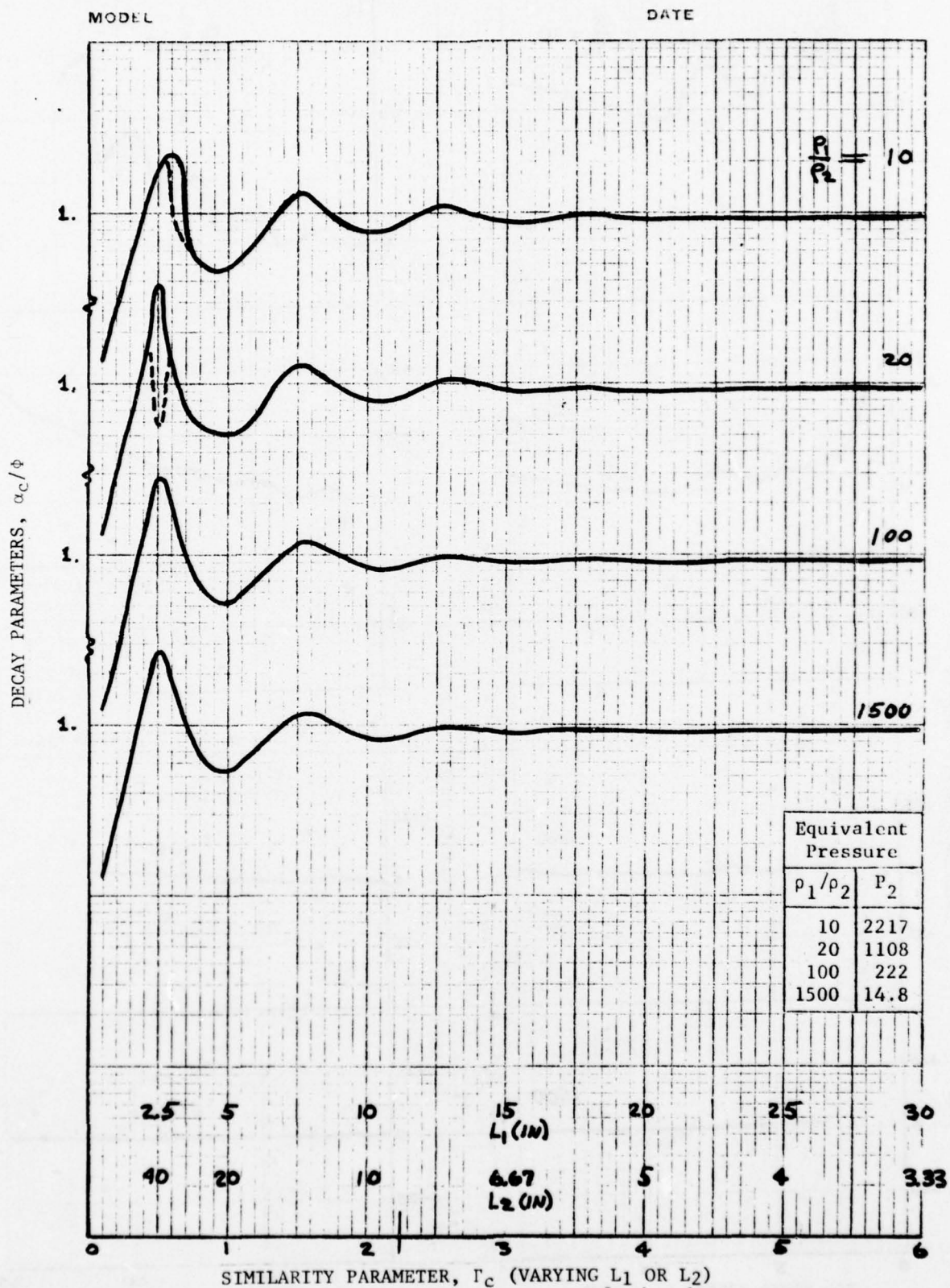


Figure B-11. Reduced Decay Formulation for Variation of Component Lengths

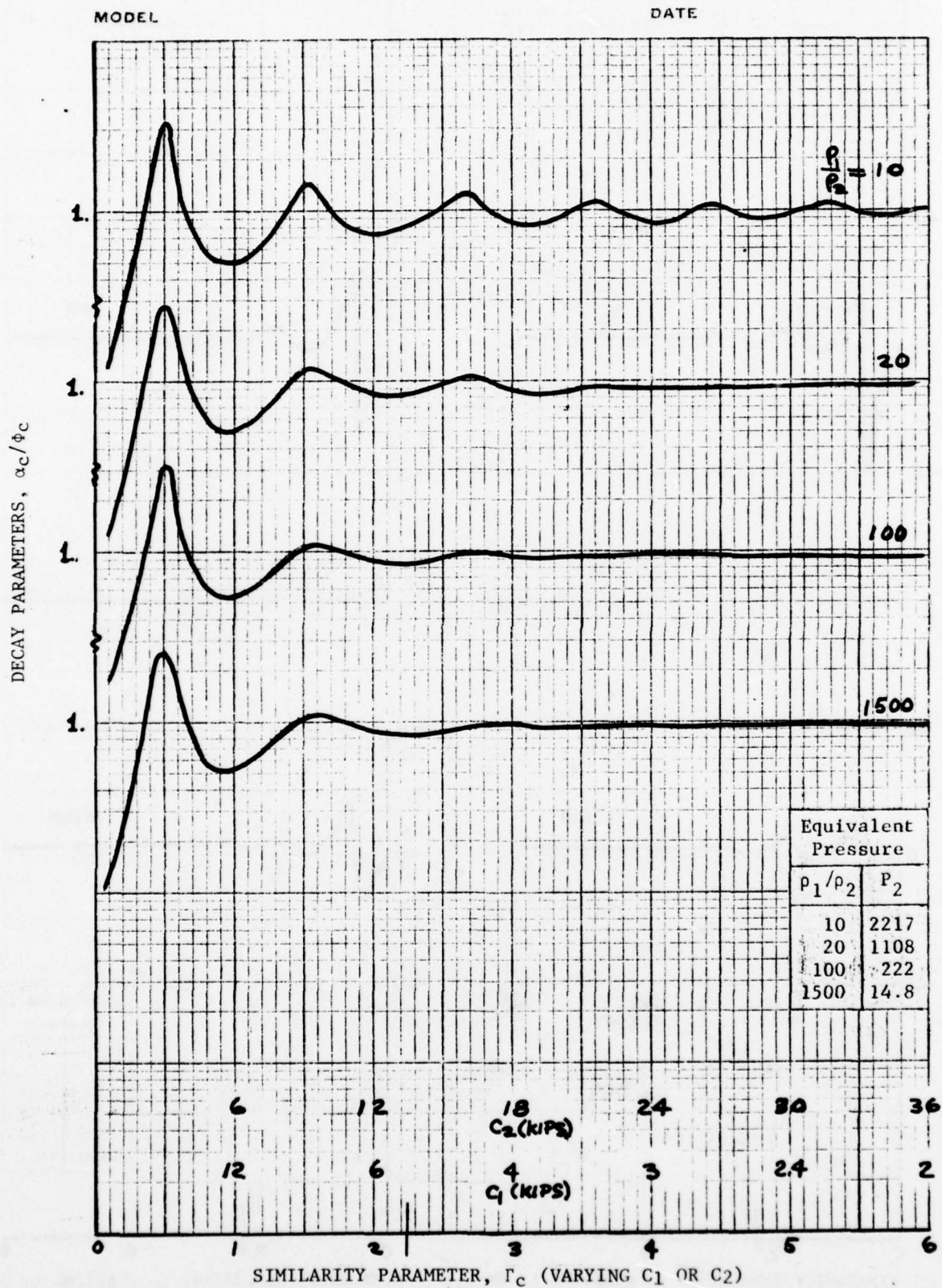


Figure B-12. Reduced Decay Formulation for Variation of Component Sound Speeds

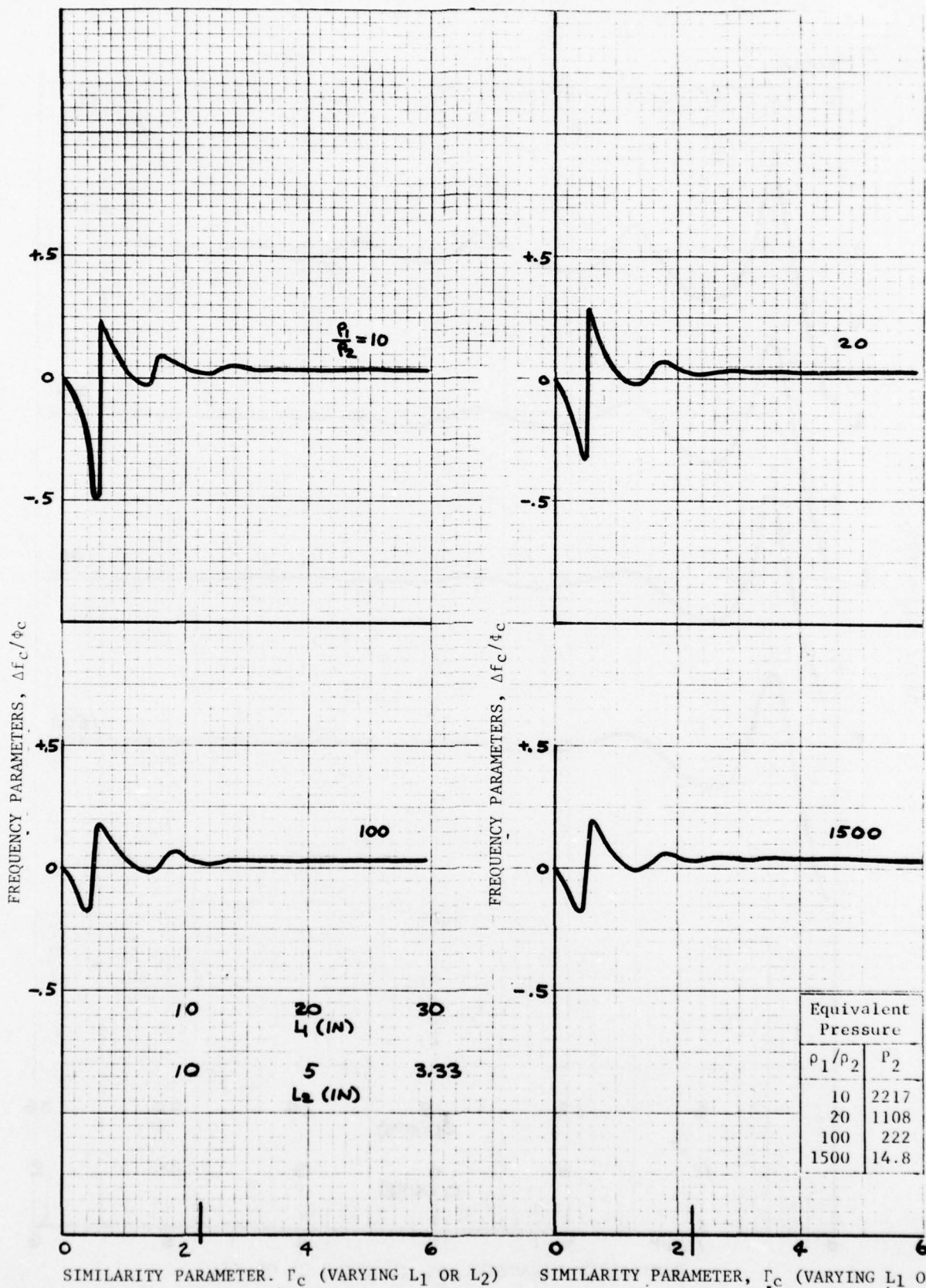


Figure B-13. Reduced Frequency Formulation for Variation of Component Lengths



**10 X 10 TO THE INCH • 7 X 10 INCHES**  
**KEUFFEL & ESSER CO. MADE IN U.S.A.**

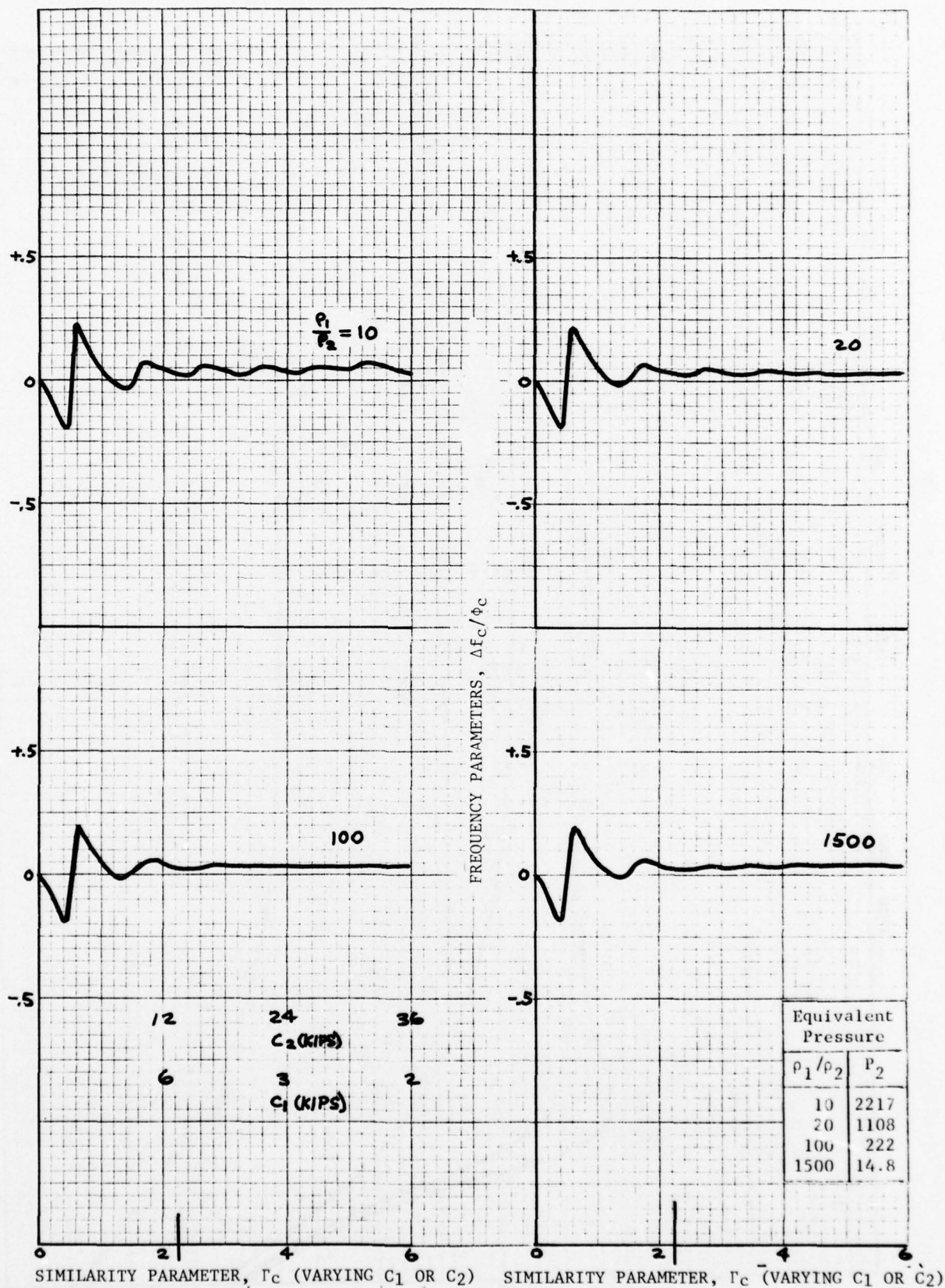


Figure B-14. Reduced Frequency Formulation for Variation of Component Sound Speeds



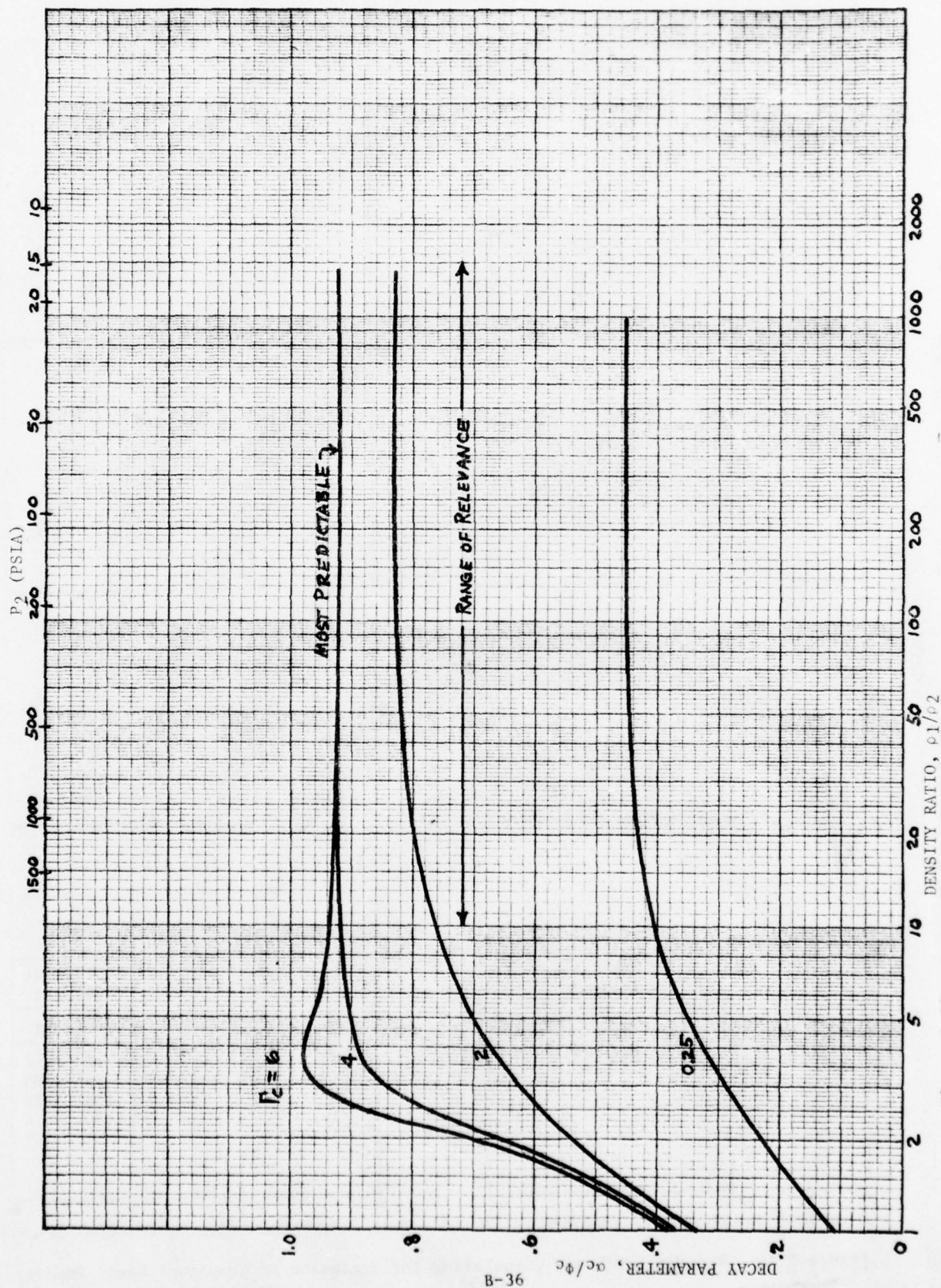


Figure B-15. Reduced Decay Formulation for Variation of Density Ratio

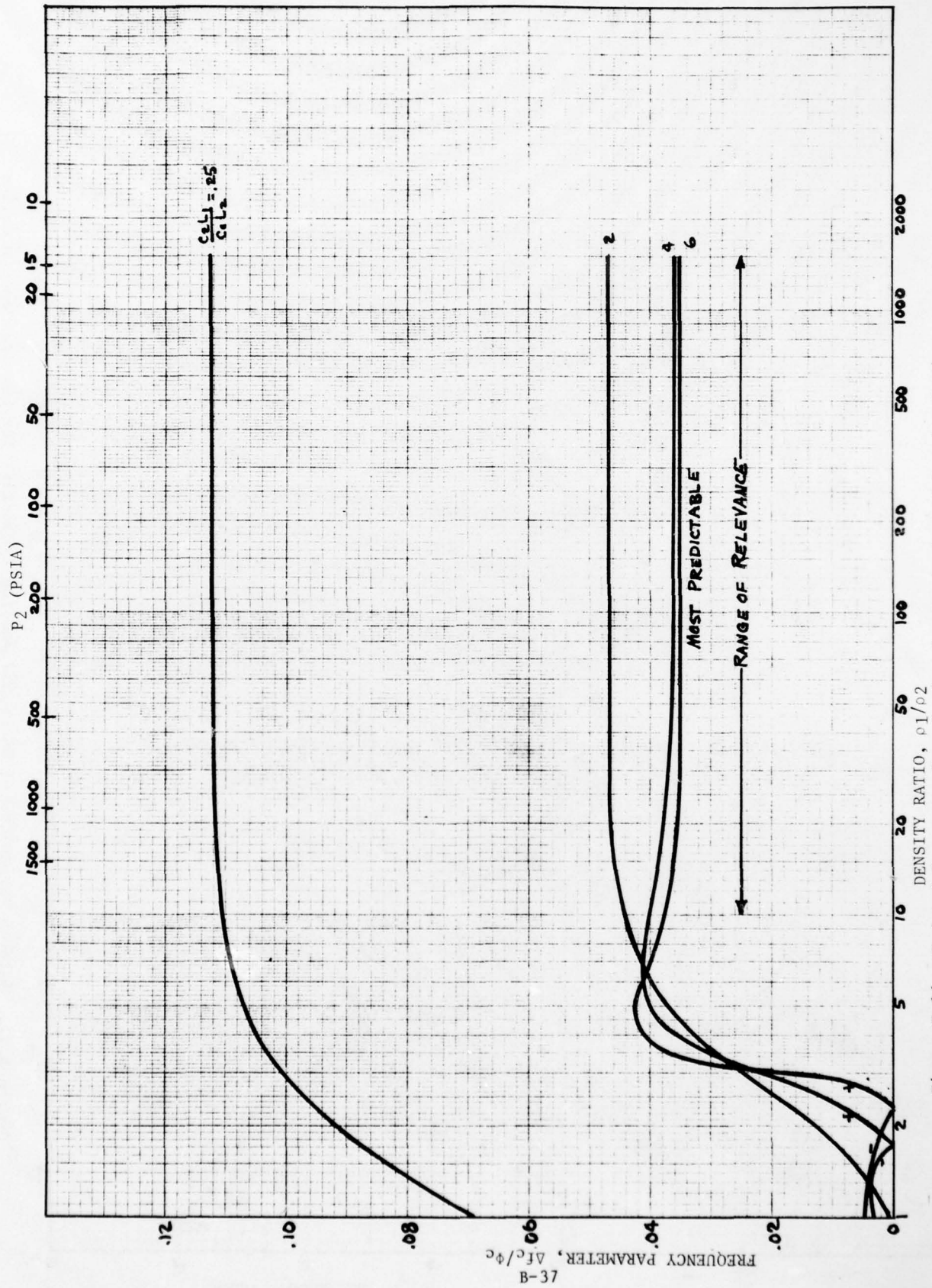


Figure B-16. Reduced Frequency Formulation for Variation of Density Ratio

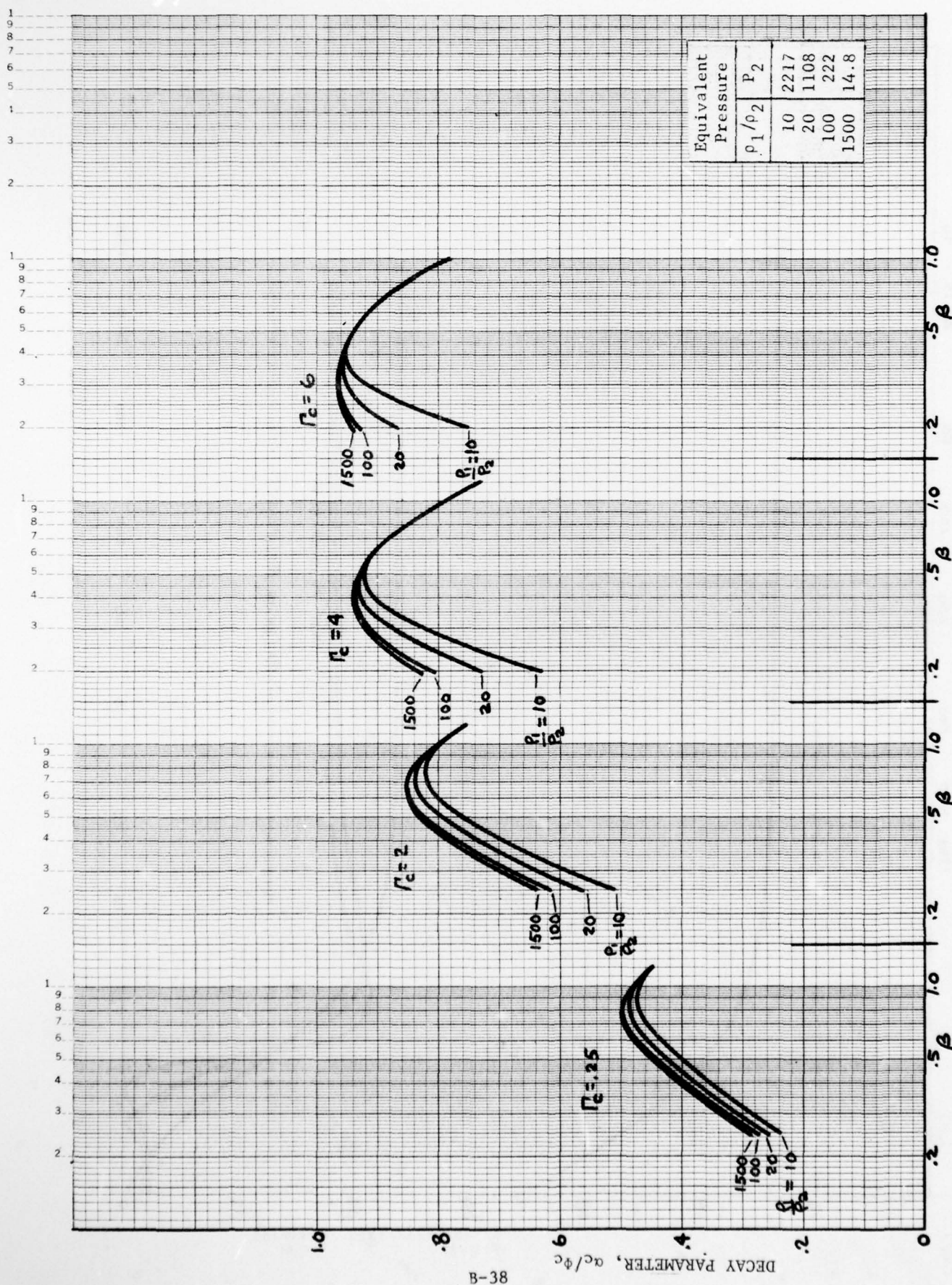


Figure B-17. Related Variations of Decay and Damping Parameters for Several Density Ratios and Similarity Parameter Values



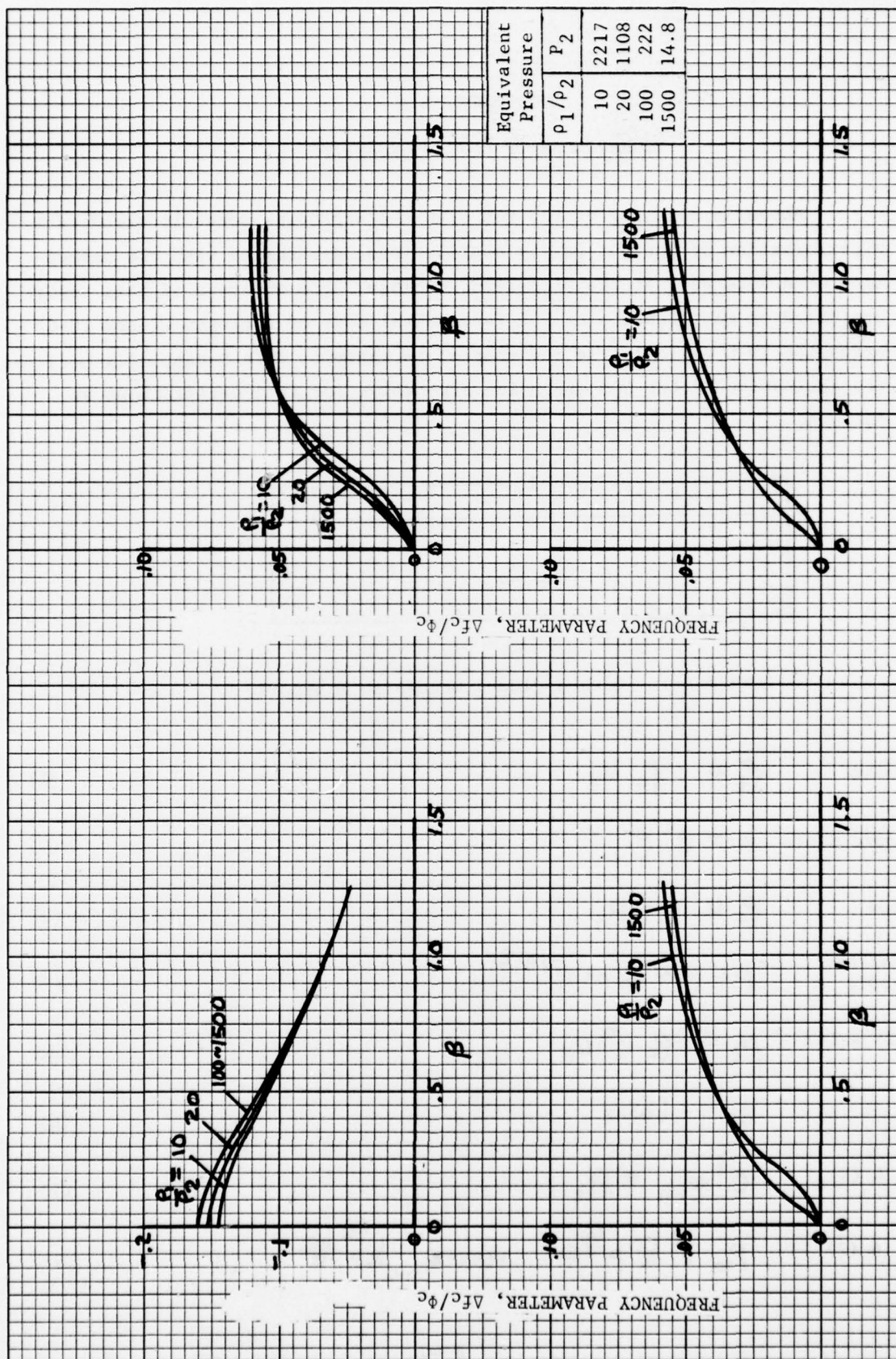


Figure B-18. Related Variations of Frequency and Damping Parameters for Several Density Ratios and Similarity Parameter Values



# SUBAPPENDIX B.A

## EIGENVALUES OF CLOSED ORGANPIPE

Acoustic coupling of the rod with the organpipe modes is essentially a perturbation of the gas cavity oscillations, determined with the assumption of a hard wall at the propellant surface. The analyses of this report are based on modification of the fundamental mode of a closed-closed (C-C) organpipe by a viscoelastic rod coupled in tandem. This Subappendix outlines the derivation of the C-C organpipe eigenvalue for free oscillations as follows:

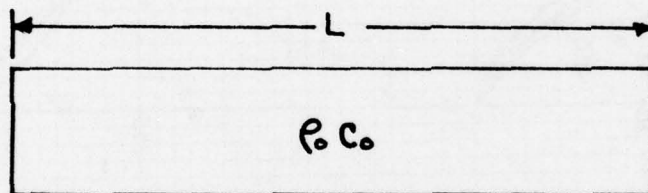


Figure B.A-1. Closed-Closed Organpipe Schematic

Continuity	$p_t = -\rho_0 u_x$	(1)
------------	---------------------	-----

Isentropic State	$p = c^2 \rho$	(2)
------------------	----------------	-----

Momentum	$\rho_0 u_t = -p_x$	(3)
----------	---------------------	-----

Nondecaying Periodic	$p \sim \rho \sim u \sim e^{-i\omega t}$	(4)
-------------------------	--	-----

(1), (2) & (4)	$p_t = -\rho_0 c^2 u_x$	(5)
----------------	-------------------------	-----

(4) <sub>t</sub>	$u_t = -i\omega u$	(6)
------------------	--------------------	-----

-(3) <sub>x</sub> & (5) <sub>t</sub>	$c^2 p_{xx} = p_{tt}$	(7)
--------------------------------------	-----------------------	-----

(4) <sub>tt</sub> & (7)	$p_{xx} + k^2 p \stackrel{(b)}{=} 0$ where $k = \frac{\omega}{c}$	(8)
-------------------------	---	-----

B.C's.

$$u(0) \stackrel{(a)}{=} u(L) \stackrel{(b)}{=} 0 \quad (9)$$

Bidirectional  
Wave

$$p = p_+ e^{ikx} + p_- e^{-ikx} \quad (10)$$

(3) & (6)

$$u = -i p_x / (\rho_0 \omega) \quad (11)$$

(10) & (11)

$$u = \frac{1}{\rho_0 c} (p_+ e^{ikx} - p_- e^{-ikx}) \quad (12)$$

(9-a) & (12)

$$p_+ \stackrel{(a)}{=} p_- = P \quad \& \quad p \stackrel{(b)}{=} P(e^{ikx} + e^{-ikx}) \quad (13)$$

(9-b) & (13)

$$e^{ikL} - e^{-ikL} = 0 \quad \text{or} \quad \sin(kL) = 0 \quad \text{or} \quad k_n = \frac{n\pi}{L} \quad (14)$$

(8-b) & (14)

$$\omega_n = c k_n = \frac{n\pi c}{L} \quad \text{or} \quad f_n = \frac{\omega_n}{2\pi} = \frac{nc}{2L} \quad (15)$$

B.C's. for  
fixed free

$$u(0) \stackrel{(a)}{=} 0 \quad p(L) \stackrel{(b)}{=} 0 \quad (16)$$

(13) & (16-b)

$$\cos(k_n L) = 0 \quad \text{or} \quad k_n = \frac{(2n-1)\pi}{2L} \quad (17)$$

(8-b) & (17)

$$\omega_n = c k_n = \frac{(2n-1)\pi c}{2L} \quad \text{or} \quad f_n = \frac{(2n-1)c}{4L} \quad n=1,2,3,\dots \quad (18)$$

# SUBAPPENDIX B.B

## SIMPLE WAVE TRANSMISSION AND REFLECTION AT ABRUPT CHANGE OF CHARACTERISTIC IMPEDANCE

Changes of density or sound speed, along the path of a wave, split the wave into transmitted and reflected parts. The functional nature of this behavior is important to coupling between the components of the rod-organpipe. The relationship for the ratio of transmitted and reflected amplitudes and intensities is derived here for nondissipative materials.

Consider the pressure amplitudes at the interface of materials designated with subscripts 1 and 2. The wave transmitted into material 2 is assumed to continue without reflection as shown in Figure B.B-1.

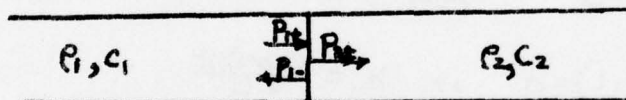


Figure B.B-1. Waveguide with Abrupt Change of Characteristic Impedance

The outline of the derivation is as follows:

$$\left. \begin{array}{l} (10), (11) \& (12) \\ \text{from App. A} \end{array} \right\} \begin{array}{l} P_1 \stackrel{(a)}{=} P_{1+} + P_{1-} \quad P_2 \stackrel{(b)}{=} P_{2+} + P_{2-} \quad P_{2-} \stackrel{(c)}{=} 0 \quad P_1 \stackrel{(d)}{=} P_2 \\ U_1 \stackrel{(e)}{=} \frac{1}{\rho_1 c_1} (P_{1+} - P_{1-}) \quad U_2 \stackrel{(f)}{=} \frac{1}{\rho_2 c_2} (P_{2+} - P_{2-}) \end{array} \quad (1)$$

Eliminate  $P_1$  &  
 $P_2$  and Solve

$$\frac{P_{2+}}{P_{1+}} \stackrel{(a)}{=} \frac{2r}{r+1} \quad \frac{P_{1-}}{P_{1+}} \stackrel{(b)}{=} \frac{r-1}{r+1} \quad \text{where } r = \frac{\rho_2 c_2}{\rho_1 c_1} \quad (2)$$

Definition of  
Intensity

$$I_{1+} \stackrel{(a)}{=} \overline{P_{1+} u_{1+}} \quad I_{2+} \stackrel{(b)}{=} \overline{P_{2+} u_{2+}} \quad I_{1-} \stackrel{(c)}{=} \overline{P_{1-} u_{1-}} \quad (3)$$

Evaluate u in terms  
of p & average over  
cycle

$$d_{1+} \stackrel{(a)}{=} P_{1+}^2 / (2\rho_1 c_1) \quad d_{2+} \stackrel{(b)}{=} P_{2+}^2 / (2\rho_2 c_2) \quad d_{1-} \stackrel{(c)}{=} P_{1-}^2 / (2\rho_1 c_1) \quad (4)$$

Transmission  
Coefficient

$$\alpha_t = \frac{d_{2+}}{d_{1+}} \stackrel{(a)}{=} \left( \frac{P_{2+}}{P_{1+}} \right)^2 \left( \frac{\rho_1 c_1}{\rho_2 c_2} \right) \stackrel{(a)}{=} \frac{4r}{(r+1)^2}$$

Reflection  
Coefficient

$$\alpha_r = \frac{d_{1-}}{d_{1+}} \stackrel{(b)}{=} \left( \frac{P_{1-}}{P_{1+}} \right)^2 \stackrel{(b)}{=} \left( \frac{r-1}{r+1} \right)^2$$

(5)

It is important to recognize that

$$\alpha_t \left( \frac{1}{r} \right) \stackrel{(a)}{=} \alpha_t(r) \quad \& \quad \alpha_r \left( \frac{1}{r} \right) \stackrel{(b)}{=} \alpha_r(r)$$

and

$$\left. \begin{aligned} \frac{P_{2+}}{P_{1+}} \Big|_{r \rightarrow \frac{1}{r}} &\stackrel{(c)}{=} \frac{P_{2+}}{P_{1+}} \Big|_r \quad \text{but} \quad \frac{P_{1-}}{P_{1+}} \Big|_{r \rightarrow \frac{1}{r}} &\stackrel{(d)}{=} - \frac{P_{1-}}{P_{1+}} \Big|_r \end{aligned} \right\} \quad (6)$$

These relations help understand a peaking of the coupling action at the

condition  $r = \frac{\rho_2 c_2}{\rho_1 c_1} = 1$ . Equations (6-c&d) are plotted in Figure B.B-2.



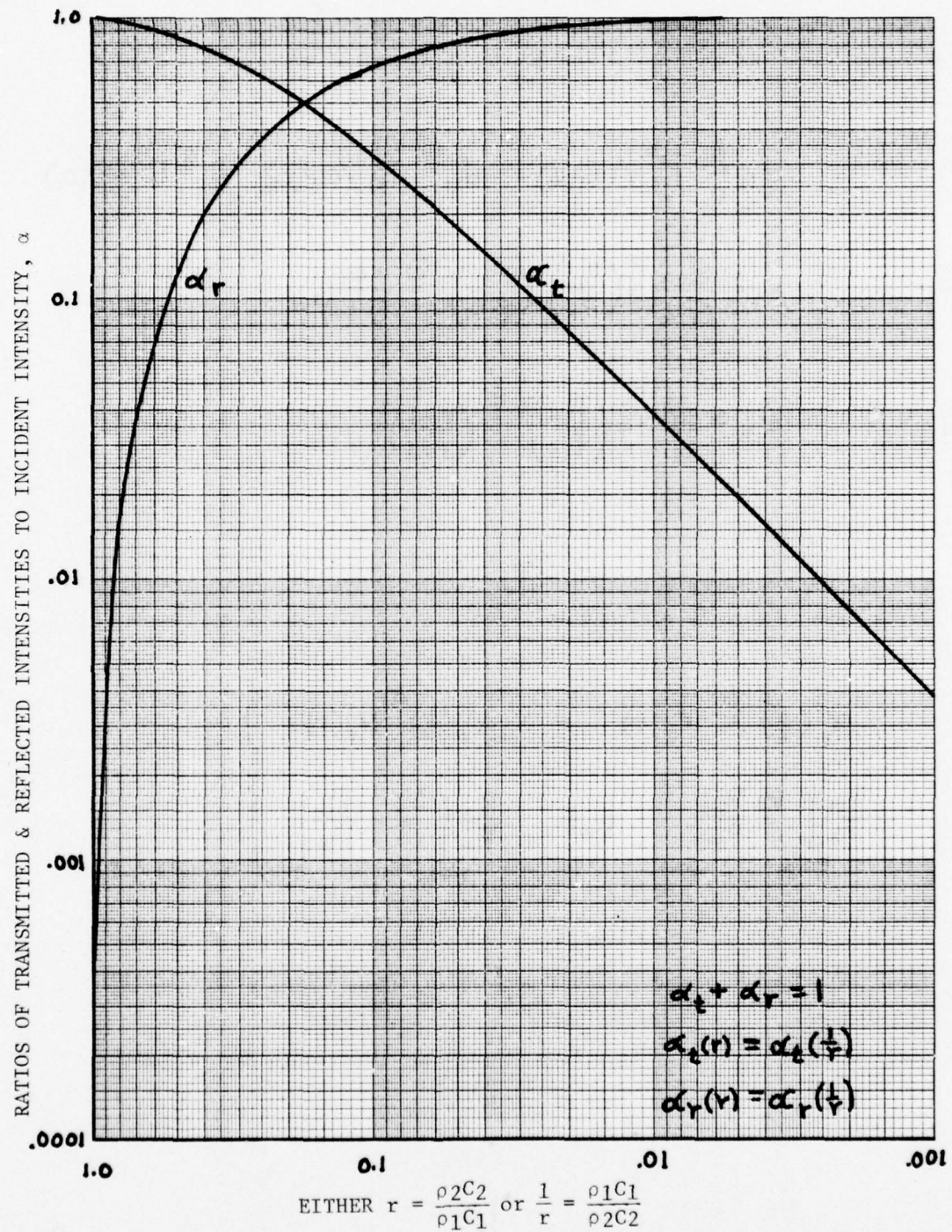


Figure B.B-2. Transmission and Reflection of Incident Wave at Interface with Change of Characteristic Impedance

## SUBAPPENDIX B.C

### CHARACTERISTIC EQUATION OF UNDAMPED ROD-ORGANPIPE

The undamped RO configuration is the limiting case for small damping coefficient  $\beta$ . Its characteristic function is therefore a check for the damped RO at the condition  $\beta = 0$ . It also provides a simpler example to perceive the handling of those features not related to damping.

The analysis here utilizes that of the organpipe in Subappendix B.A by assigning subscripts, 1 and 2, to the terms of Equations (A-10, 12), corresponding respectively to the rod and organpipe. The analyses are then coupled as follows:

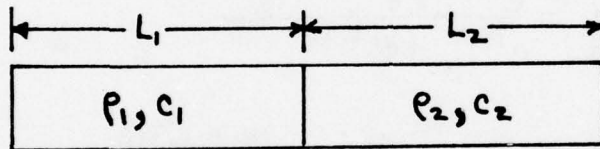


Figure B.C-1. Undamped Rod-Organpipe Schematic

$$\begin{array}{ll}
 \underline{0 \leq x \leq L_1} & \underline{L_1 \leq x \leq L_1 + L_2} \\
 p_1^{(a)} = p_{1+} e^{ik_1 x} + p_{1-} e^{-ik_1 x} & p_2^{(b)} = p_{2+} e^{ik_2 x} + p_{2-} e^{-ik_2 x} \quad (10) \\
 u_1^{(a)} = \frac{1}{\rho_1 c_1} [p_{1+} e^{ik_1 x} - p_{1-} e^{-ik_1 x}] & u_2^{(b)} = \frac{1}{\rho_2 c_2} [p_{2+} e^{ik_2 x} - p_{2-} e^{-ik_2 x}] \quad (12)
 \end{array}$$

$$\text{B.C's.} \left\{ \begin{array}{l} u_1(0) \stackrel{(a)}{=} 0 \\ u_2(L_1+L_2) \stackrel{(a)}{=} 0 \end{array} \right. \quad \begin{array}{l} P_{1-} \stackrel{(b)}{=} P_{1+} = P_1 \\ P_{2-} \stackrel{(b)}{=} P_{2+} e^{2k_2(L_1+L_2)} = P_2 e^{2k_2(L_1+L_2)} \end{array} \quad \begin{array}{l} (13) \\ (14) \end{array}$$

$$\begin{array}{cc} \underline{0 \leq x \leq L_1} & \underline{L_1 \leq x \leq L_1+L_2} \\ (10) \& (13) \quad P_1 \stackrel{(a)}{=} P_1 (e^{ik_1x} + e^{-ik_1x}) & P_2 \stackrel{(b)}{=} P_2 \{ e^{ik_2x} + e^{-ik_2[x-2(L_1+L_2)]} \} \end{array} \quad \begin{array}{l} (15) \\ (16) \end{array}$$

$$(12), (13) \& (14) \quad u_1 \stackrel{(a)}{=} \frac{P_1}{P_1 C_1} (e^{ik_1x} - e^{-ik_1x}) \quad u_2 \stackrel{(b)}{=} P_2 \{ e^{ik_2x} - e^{-ik_2[x-2(L_1+L_2)]} \}$$

$$\text{Interface Conditions} \left\{ \begin{array}{l} P_1(L_1) \stackrel{(a)}{=} P_2(L_1) \\ \frac{P_1}{P_2} \stackrel{(b)}{=} \frac{e^{ik_2L_1} + e^{ik_2(2L_2+L_1)}}{e^{ik_1L_1} + e^{-ik_1L_1}} \end{array} \right. \quad \begin{array}{l} (17) \\ (18) \end{array}$$

$$\frac{P_1}{P_2} \stackrel{(b)}{=} \frac{P_1 C_1}{P_2 C_2} \frac{e^{ik_2L_1} - e^{ik_2(2L_2+L_1)}}{e^{ik_1L_1} - e^{-ik_1L_1}}$$

$$\frac{e^{ik_1L_1} - e^{-ik_1L_1}}{e^{ik_1L_1} + e^{-ik_1L_1}} \stackrel{(a)}{=} - \frac{P_1 C_1}{P_2 C_2} \frac{e^{ik_2(2L_2+L_1)} - e^{ik_2L_1}}{e^{ik_2(2L_2+L_1)} + e^{ik_2L_1}} \stackrel{(b)}{=} - \frac{P_1 C_1}{P_2 C_2} \cdot \frac{e^{ik_2L_2} - e^{-ik_2L_2}}{e^{ik_2L_2} + e^{-ik_2L_2}} \quad (19)$$

$$\frac{\tan k_1 L_1}{\tan k_2 L_2} + \frac{P_1 C_1}{P_2 C_2} = 0 \quad (20)$$

$$\frac{\tan \left( \frac{n\pi f_n}{C_1/2L_1} \right)}{\tan \left( \frac{\pi f_n}{C_2/2L_2} \right)} + \frac{P_1 C_1}{P_2 C_2} = 0 \quad \text{where } f_n = \frac{\omega_n}{2\pi} \quad (21)$$

are the coupled, but undamped, RO natural frequencies.

SUBAPPENDIX B.D  
EIGENVALUES AND FREQUENCY RESPONSE  
OF DISCRETE DAMPED OSCILLATIONS

The Voigt model shown in Figure B.D-1 is the simplest discrete model that can be used as an analog for comparison with damped continuous systems. Analysis of its eigenvalues and frequency response is as follows:

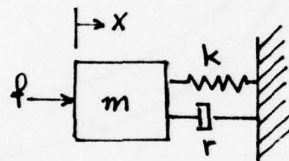


Figure B.D-1 Voigt Oscillator Schematic

Momentum  $m\ddot{x} + r\dot{x} + kx = f$  <sup>(a)</sup> or  $\ddot{x} + 2\zeta\omega_N\dot{x} + \omega_N^2 x = F$  <sup>(b)</sup> where  $\begin{cases} \omega_N = \sqrt{k/m} \\ \zeta = \frac{r}{2m\omega_N} \\ F = \frac{f}{m} \end{cases}$  (1)

Char. Eqn.  $F=0 \nmid x \sim e^{st}$  so  $(s^2 + 2\zeta\omega_N s + \omega_N^2)x = 0$  (2)

Eigenvalue  $s = -\alpha + i\omega = -\zeta\omega_N + i\omega_N\sqrt{1-\zeta^2}$  (3)

% Freq. Shift  $\frac{\Delta\omega}{\omega_N} = \frac{\omega - \omega_N}{\omega_N} = \sqrt{1-\zeta^2} - 1 \approx -\frac{1}{2}\zeta^2$  (4)

Driven Freq.  $F = F_0 e^{i\omega t}$  <sup>(a)</sup> so, using Eqn (1-b),  $X_0 = \frac{F_0}{(\omega_N^2 - \omega^2) + 2i\zeta\omega_N\omega}$  <sup>(b)</sup> (5)  
Resp. Eqn.

$|\ddot{x}|_{\max}$  occurs at the frequency where  $|(\omega_N^2 - \omega^2) + i(2\zeta\omega_N\omega)|$  or  $(\omega_N^2 - \omega^2)^2 + 4\zeta^2\omega_N^2\omega^2$  (6)

is at a maximum. Differentiating <sup>(b)</sup> with respect to  $\omega$  and equating the results

to zero obtains the amplitude resonance at  $\omega = \omega_N\sqrt{1-2\zeta^2}$  (7)

% Freq. Shift  $\frac{\Delta\omega}{\omega_N} \approx -\zeta^2$  (8)



Consideration of the velocity resonance frequency condition is sometimes important because measurements or calculations may be velocity related. The velocity is given by  $\dot{X} = i\omega X$  (9)

and the frequency for  $|\dot{X}|_{\max}$  is the same as that for  $\{|\dot{X}|^2\}_{\max}$  so the velocity resonance is at  $d\{|\dot{X}|^2\}/d\omega = 0$  (10)

$$\text{But } \frac{d\{|\dot{X}|^2\}}{d\omega} = \frac{d}{d\omega} \left[ \frac{\omega^2 F_0^2}{\{(\omega_N^2 - \omega^2)^2 + (2\zeta\omega\omega_N)^2\}} \right] = \frac{\omega_N^2(\omega_N^2 - \omega^2)F_0^2}{\{(\omega_N^2 - \omega^2) + (2\zeta\omega\omega_N)^2\}^2} \quad (11)$$

Thus the velocity resonance is at  $\omega = \omega_N$ .

Three frequencies have been found which characterize the Voigt model (12) They are schematically represented in Figure B.D-2. Distinct frequency peak

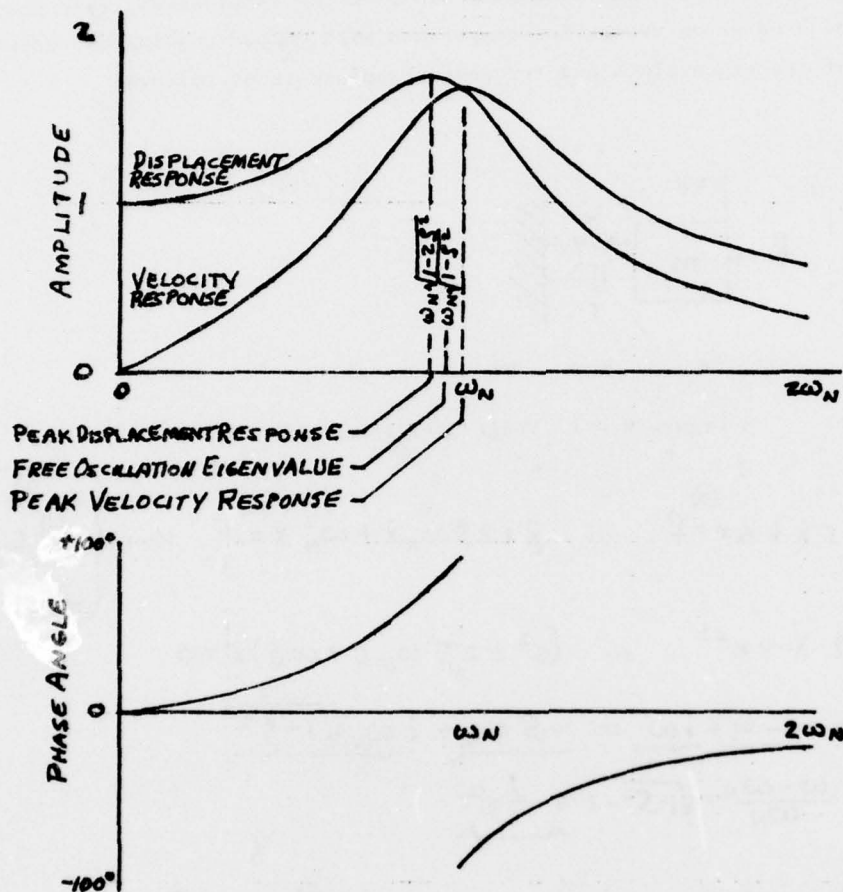


Figure B.D-2. Voigt Model Frequency-Peak Characteristics

characteristics also exist in continuous systems, however, direction and magnitude are not simply related with those of the discrete model if a coupled system is involved. The analogies for such cases are more complicated.

The Zener, or standard linear compliance, model (see Figure B.D-3) is a more exact analog of damped continuous material. It is similar to the Voigt model but has a linear spring in series with the dashpot. This allows the model to account for pressure relaxation that is observed after sudden compression. The Zener model can best be compared directly with the continuous system by considering only the complex compliance as relates between the two systems. The analysis of the compliance is as follows:

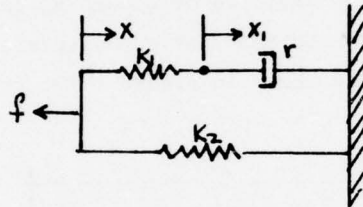


Figure B.D-3. Zener Compliance Model Schematic

$$\text{Force Balance} \left\{ \begin{aligned} K_2 x + K_1 (x - x_1) &= -f & (13) \\ K_1 (x - x_1) - r \dot{x}_1 &= 0 & (14) \end{aligned} \right.$$

$$x \sim x \sim e^{st} \text{ and (2)} \quad x_1 = \frac{x}{\left(\frac{r}{K_1}\right)s + 1} \quad (15)$$

$$(1) \& (3) \quad (1 + \tau_x s) f = -K_2 (\tau_p s + 1) x \quad \text{where} \quad \tau_x = \frac{r}{K_1} \quad \& \quad \tau_p = \tau_x \left( \frac{K_2 + K_1}{K_2} \right) \quad (16)$$

$$\text{The continuum analog to Eqn 4-a is} \quad (1 + \tau_p s) P = M (\tau_p s + 1) \epsilon. \quad (17)$$

Analytical solution using such a compliance analog would be considerably more difficult than with the Voigt model unless the equivalent form

$$P = M \left( \frac{\tau_p s + 1}{\tau_p s + 1} \right) \epsilon \quad (18)$$

could be approximated with an iteratively refined continuum analog of the Voigt model. The form of this analog is

$$P = c^2 (1 + s s) \epsilon, \quad (19)$$

where  $s$  is related, but not equal, to the parameter  $r$ .

This procedure could also be used in finite element analyses in which the global matrix equation is solved iteratively.

# SUBAPPENDIX B.E

## CHARACTERISTIC EQUATIONS OF VISCOELASTIC (DAMPED) ROD

Consideration of the uncoupled viscoelastic rod will introduce the development of coupled, complex characteristic equations and complex eigenvalues for a simpler configuration than the RO. This will help make the features of coupling and damping more distinguishable in the RO. The only difference in the configuration and governing equations, from those of the uncoupled organpipe, is the addition of a damping term to the state (or stiffness) equation similar to that for the discrete model. Analysis of the damped viscoelastic rod shown in Figure B.E-1 is as follows:

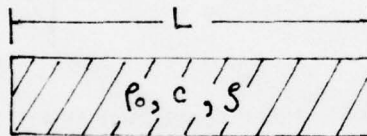


Figure B.E-1. Damped Rod Schematic

$$\text{Continuity} \quad \rho_t^{(a)} = -\rho_0 u_x \quad (\epsilon = \epsilon_x \text{ \& } u = \epsilon_t \text{ so } \epsilon_t = u_x; \text{ also } \epsilon = -\frac{p}{\rho_0} \text{ so } \rho_t = -\rho_0 \epsilon_t) \quad (1)$$

$$\text{Dynamic State} \quad p^{(a)} = c^2 \rho + S \rho_t \quad (c^2 = \frac{\gamma \rho_0}{\rho_0}) \quad (2)$$

$$\text{Momentum} \quad \rho_0 u_t = -p_x \quad (3)$$

$$\text{Definition} \quad \Omega = \omega - i\alpha \quad (4)$$

$$\text{Periodic Expon. Decay All acoustic variable } \propto e^{-i\Omega t} \quad (5)$$

$$(5) \quad u_t = -i\Omega u \quad (6)$$

$$(1) \& (2) \quad p_t = -\rho_0 (c^2 u_x + \mathcal{S} u_{xt}) \quad (7)$$

$$(6) \& (7) \quad p_t \stackrel{(a)}{=} -\rho_0 (c^2 - i \mathcal{S} \Omega) u_x \quad \left\{ \text{Also } p \stackrel{(b)}{=} -\rho_0 (c^2 - i \mathcal{S} \Omega) \xi_x \right. \quad (8)$$

$$(3)_t \& (8)_x \quad (c^2 - i \mathcal{S} \Omega) u_{xx} \stackrel{(a)}{=} u_{tt} \quad \left\{ \text{Also } (c^2 - i \mathcal{S} \Omega) \xi_{xx} \stackrel{(b)}{=} \xi_{tt} + \phi(x) \right\} \quad (9)$$

$$(3)_x \& (8)_t \quad (c^2 - i \mathcal{S} \Omega) p_{xx} = p_{tt} \quad (10)$$

$$(5) \quad p_{tt} = -\Omega^2 p \quad (11)$$

$$(10) \& (11) \quad p_{xx} + \frac{\Omega^2}{(c^2 - i \mathcal{S} \Omega)} p = 0 \quad (12)$$

$$\text{Definitions} \quad k \stackrel{(a)}{=} \Omega/c, \quad \tau \stackrel{(b)}{=} \mathcal{S}/c^2 \quad (13)$$

$$(12) \& (13) \quad p_{xx} + \frac{k^2}{(1 - i \Omega \tau)} p = 0 \quad (14)$$

$$\begin{aligned} \text{Defin. (4) \& (13)} \quad k &\stackrel{(a)}{=} \frac{k}{\sqrt{1 - i \Omega \tau}} \stackrel{(b)}{=} \frac{(\omega - i \alpha)/c}{\sqrt{(1 - \alpha \tau) - i \omega \tau}} \stackrel{(c)}{=} \frac{(\omega - i \alpha)}{c \sqrt{R}} e^{i(\frac{\phi}{2})} \stackrel{(d)}{=} k^R + i k^I \quad \text{where} \\ \text{Trig. Iden.} \quad \phi &\stackrel{(e)}{=} \tan^{-1} \left( \frac{\omega \tau}{1 - \alpha \tau} \right), \quad \sqrt{R} \stackrel{(f)}{=} \left\{ (1 - \alpha \tau)^2 + (\omega \tau)^2 \right\}^{\frac{1}{4}}, \\ (15-c, d, e \& f) \quad k^R &\stackrel{(g)}{=} \frac{1}{c \sqrt{R}} (\omega \cos \frac{\phi}{2} + \alpha \sin \frac{\phi}{2}) \neq k^I \stackrel{(h)}{=} \frac{1}{c \sqrt{R}} (\omega \sin \frac{\phi}{2} - \alpha \cos \frac{\phi}{2}) \end{aligned} \quad (15)$$

$$\text{B.C's.} \quad u(0) \stackrel{(a)}{=} 0 \quad u(L) \stackrel{(b)}{=} 0 \quad (16)$$

$$\text{Bidir. Wave, (14) \& (15)} \quad p = (p_+ e^{ikx} + p_- e^{-ikx}) \quad (17)$$

$$(3), (5) \& (17) \quad u = \frac{k}{\rho_0 \Omega} (p_+ e^{ikx} - p_- e^{-ikx}) \quad (18)$$

$$(16-a) \quad p \stackrel{(a)}{=} P (e^{ikx} + e^{-ikx}) \quad u \stackrel{(b)}{=} \frac{kP}{\rho_0 \Omega} (e^{ikx} - e^{-ikx}) \quad (19)$$



$$(16-b), (19-b) \& (15-d) \quad \sin(KL) \stackrel{(a)}{=} \sin\{(K^R + i K^I)\} \stackrel{(b)}{=} \cosh(K^I L) \cdot \sin(K^R L) + i \sinh(K^I L) \cdot \cos(K^R L) \stackrel{(a)}{=} 0 \quad (20)$$

$$(20-c) \quad \cosh(K^I L) \cdot \sin(K^R L) \stackrel{(a)}{=} 0 \quad \sinh(K^I L) \cdot \cos(K^R L) \stackrel{(b)}{=} 0 \quad (21)$$

$$(21-a \& b) \quad \cosh(K^I L) \stackrel{(a)}{\neq} 0 \quad \text{so} \quad \sin(K^R L) \stackrel{(b)}{=} 0 \quad \& \quad \sin(K^R L) \stackrel{(c)}{\neq} 0 \quad \text{so} \quad \sinh(K^I L) \stackrel{(d)}{=} 0 \quad (22)$$

$$(21-b \& d) \quad K^R L \stackrel{(a)}{=} n\pi \quad \text{so} \quad K^R \stackrel{(b)}{=} \frac{n\pi}{L} \quad \text{and also} \quad K^I \stackrel{(c)}{=} 0 \quad (23)$$

$$(15-h) \& (23-c) \quad \omega \cdot \sin \frac{\phi}{2} - \alpha \cdot \cos \frac{\phi}{2} \stackrel{(a)}{=} 0 \quad \text{or} \quad \tan \frac{\phi}{2} \stackrel{(b)}{=} \left( \frac{\alpha}{\omega} \right) \quad \text{so} \quad \sin \frac{\phi}{2} \stackrel{(c)}{=} \frac{\alpha}{\sqrt{\alpha^2 + \omega^2}} \neq \cos \frac{\phi}{2} \stackrel{(d)}{=} \frac{\omega}{\sqrt{\alpha^2 + \omega^2}} \quad (24)$$

$$(15-g), (24-c \& d) \& (23-b) \quad \frac{\omega \cdot \cos \frac{\phi}{2} + \alpha \cdot \sin \frac{\phi}{2}}{c \sqrt{R}} \stackrel{(a)}{=} \frac{\omega^2 + \alpha^2}{c \sqrt{R}} \stackrel{(b)}{=} \frac{n\pi}{L} \quad (25)$$

$$(25-b) \quad \sqrt{\omega^2 + \alpha^2} L - n\pi c \sqrt{R} = 0 \quad (26)$$

$$\text{Trig. Ident.}, (24-b) \& (15-e) \quad \tan \phi \stackrel{(a)}{=} \frac{2 \cdot \tan \frac{\phi}{2}}{1 + \tan^2 \frac{\phi}{2}} \stackrel{(b)}{=} \frac{2\alpha/\omega}{1 + (\alpha/\omega)^2} \stackrel{(c)}{=} \frac{2\alpha\omega}{\omega^2 + \alpha^2} \stackrel{(d)}{=} \frac{\omega T}{1 - \alpha T} \quad (27)$$

$$(27-d) \quad (\omega^2 + 3\alpha^2) T - 2\alpha = 0 \quad (28)$$

Equations (26) and (28) are two coupled characteristic equations to be solved for the acoustic decay,  $\alpha$ , and angular frequency,  $\omega$ .

# SUBAPPENDIX B.F

## FREQUENCY RESPONSE OF DAMPED ROD (ACOUSTIC NOMENCLATURE)

Testing of material to obtain its viscoelastic characteristics generally involves determining its frequency response to forced oscillations. If the driver has a low output impedance the driving condition is characterized by an interface pressure and the driving point displacement or velocity response is measured. If the driver output impedance is high the response of the driving point stress or force is measured. Both of these approaches are depicted in Figure B.F-1 and outlined as follows:

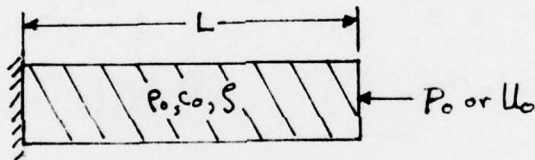


Figure B.F-1. Acoustically Driven Rod Schematic

Continuity	$\rho_t = -\rho_0 u_x$	(1)
------------	------------------------	-----

Dynamic State	$p = c_0^2 \rho + \zeta \rho_t$	(2)
---------------	---------------------------------	-----

Momentum	$\rho_0 u_t = -p_x$	(3)
----------	---------------------	-----

Periodic Driving a Steady Amplitude Response	$p \sim \rho \sim u \sim e^{i[(k^r + i k^i)x - \omega t]}$	(4)
--	--	-----

(1), (1) <sub>t</sub> & (2)	$\rho_t = -\rho_0 (c_0^2 u_x + \zeta u_{xt})$	(5)
-----------------------------	---	-----

$$(4) \& (5) \quad p_t = -\rho_0 (c^2 - i\beta\omega) u_x \quad (6)$$

$$(3)_x \& (6)_t \quad (c^2 - i\beta\omega) p_{xx} = p_{tt} \quad (7)$$

$$(4) \& (7) \quad p_{xx} + \left( \frac{\omega^2}{c^2 - i\beta\omega} \right) p = 0 \quad (8)$$

$$\text{Definitions} \quad k^{(a)} = \omega/c, \quad r^{(b)} = \beta/c^2, \quad K^{(c)} = \frac{k}{\sqrt{1 - i\omega r}} \quad (9)$$

$$(9), (8) \& \text{B.C.'s.} \quad p_{xx} + K^2 p = 0, \quad u^{(b)}(0) = 0, \quad u^{(c)}(L) = U_0 e^{-i\omega t} \text{ or } p^{(d)}(L) = P_0 e^{-i\omega t} \quad (10)$$

$$\text{Def. \& Trig.} \quad R^{(a)} = 1 - \omega r^{(b)} = \sqrt{1 + \omega^2 r^2} e^{-\phi} \quad \text{where } \phi^{(c)} = \tan^{-1}(\omega r) \quad (11)$$

$$(9) \& (11) \quad K = \frac{K}{\sqrt{R}} \left( \cos \frac{\phi}{2} + i \sin \frac{\phi}{2} \right) \quad (12)$$

$$\text{Bidirectional Wave, (3) \& (4)} \quad p = p_+^{(a)} e^{ikx} + p_-^{(a)} e^{-ikx} \quad u = \frac{K}{\rho_0 \omega} (p_+ e^{ikx} - p_- e^{-ikx})^{(b)} \quad (13)$$

$$(10-b), (13-a \& b) \quad p = P^{(a)} (e^{ikx} + e^{-ikx}), \quad u = \frac{K P}{\rho_0 \omega} (e^{ikx} - e^{-ikx}) \quad \& \quad P = P_0^{(c)} e^{-i\omega t} \quad (14)$$

Velocity (High Impedance) Driver

$$(10-c) \& (14-a \& b) \quad U_0 e^{-i\omega t} = \frac{z i K P}{\rho_0 \omega} \sin(kL) \quad \& \quad p = z P \cos(kx)^{(b)} \quad (15)$$

$$(15-a \& b) \quad p = -i \rho_0 \omega \cdot U_0 \cos(kx) \cdot e^{-i\omega t} / (k \sin(kL)) \quad (16)$$

Pressure (Low Impedance) Driver

$$(10-d) \& (14-a \& b) \quad P_0 e^{-i\omega t} = z P \cos(kL) \quad \& \quad u = \frac{z i K P}{\rho_0 \omega} \sin(kx)^{(b)} \quad (17)$$

$$(17-a \& b) \quad u = i K \cdot P_0 \sin(kx) \cdot e^{-i\omega t} / (\rho_0 \omega \cos(kL)) \quad (18)$$

# SUBAPPENDIX B.G

## FREQUENCY RESPONSE OF DAMPED ROD (STRUCTURAL DYNAMICS NOMENCLATURE)

Terms and procedures used in material testing are not identical to the common acoustic terms used in this report. Accurate predictions of structural damping in combustion instability requires that analyses and testing at least can be consistent in transfer and use of data. No sufficiently comprehensive and generally accepted definition of terms and standard procedures were found for dynamic testing. Therefore, a trial is made here to outline the frequency response analysis of Subappendix B.F with assumed structural dynamics terms. This is presented to instigate constructive criticism and initiate other efforts to obtain a comprehensive and compatible procedure for testing and analysis

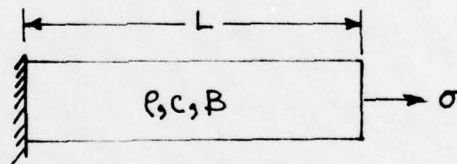


Figure B.G-1. Acoustically Driven Rod Schematic

Continuity	$\rho_t = -\rho_0 u_x$ (a)	$\epsilon = \epsilon_x$ & $u = \epsilon_t$ (b) (c)	so $\epsilon_t = u_x$ (d)	(1)
Dynamic State	$\sigma = \rho_0 c^2 (1 + i\beta) \epsilon$			(2)
Momentum	$\rho_0 u_t = \sigma_x$			(3)
Periodic-Steady	$\sigma \sim \rho \sim u \sim \epsilon \sim e^{i[(k^r + i k^i)x - \omega t]}$			(4)
(1-d) & (2)	$\sigma_t = \rho_0 c^2 (1 + i\beta)$			(5)



Structural-Acoustic  
Comparison

$$\left\{ \begin{array}{l} \sigma = -p \\ \epsilon = -p/\rho_0 \end{array} \right\} \text{ so, comparing Eqs. F-2\&G-2}$$

$$\begin{array}{l} c^2 \beta = -\omega \zeta \\ \beta = -\omega \frac{\zeta}{c^2} = -\omega \tau \end{array} \quad (6)$$

$$(3)_x \& (4)_t \quad c^2(1+i\beta) \sigma_{xx} = \sigma_{tt} \quad (7)$$

$$(4)\&(7) \quad \sigma_{xx} + \frac{\omega^2}{c^2(1+i\beta)} \sigma = 0 \quad (8)$$

$$\text{Definitions} \quad k = \frac{\omega}{c}, \quad \tau = \zeta/c^2, \quad K = \frac{k}{\sqrt{1-i\omega\tau}} \quad (9)$$

$$(8), (9)\&(B.C.'s.) \quad \sigma_{xx} + K^2 \sigma = 0, \quad u(0) = 0, \quad u(L) = U_0 e^{-i\omega t} \text{ or } \sigma(L) = \epsilon_0 e^{-i\omega t} \quad (10)$$

$$\text{Def. \& Trig.} \quad R = 1 - \beta = (1 + \beta^2)^{\frac{1}{2}} e^{-i\phi} \quad \text{where} \quad \phi = \tan^{-1} \beta \quad (11)$$

$$(9)\&(11) \quad K = \frac{k}{\sqrt{R}} \cdot \left( \cos \frac{\phi}{2} + i \sin \frac{\phi}{2} \right) \quad (12)$$

$$\text{Bidir. Wave-(3)\&(4)} \quad \sigma = \sigma_+ e^{+ikx} + \sigma_- e^{-ikx}, \quad u = \frac{-K}{\rho_0 \omega} (\sigma_+ e^{+ikx} - \sigma_- e^{-ikx}) \quad (13)$$

$$(10-b)\&(13-a\&b) \quad \sigma = \Sigma (e^{+ikx} + e^{-ikx}), \quad u = \frac{-K \Sigma}{\rho_0 \omega} (e^{+ikx} - e^{-ikx}) \quad (14)$$

• ————— •

Velocity (High Impedance) Driver

$$(10-c)\&(14-a\&b) \quad U_0 e^{-i\omega t} = \frac{-2ik\Sigma}{\rho_0 \omega} \sin(KL) \quad \& \quad \sigma = 2\Sigma \cos(Kx) \quad (15)$$

$$(15-a\&b) \quad \sigma = i\rho_0 \omega U_0 \cos(Kx) \cdot e^{-i\omega t} / [K \sin(KL)] \quad (16)$$

• ————— •

Stress (Low Impedance) Driver

$$(10-d)\&(14-a\&b) \quad \epsilon_0 e^{-i\omega t} = 2\Sigma \cos(KL) \quad \& \quad u = \frac{-2ik\Sigma}{\rho_0 \omega} \sin(Kx) \quad (17)$$

$$(17-a\&b) \quad u = -ik\Sigma \sin(Kx) \cdot e^{-i\omega t} / [\rho_0 \omega \cos(KL)] \quad (18)$$

## SUBAPPENDIX B.H

### EIGENVALUE PROCEDURES FOR THE DAMPED ROD-ORGANPIPE

The concepts and analytical procedures involved in the analysis of the RO have been outlined from several viewpoints and in several applications in Subappendices B.A through B.G. Analyses of uncoupled components and of individual physical characteristics were used to demonstrate the effects of these features more clearly. In Appendix B.H all of the components and effects are combined in a single analysis.

The analysis here contains derivations of both the coupled characteristic equations and the procedure used to extract the eigenvalues from them. The original characteristic equation development was by Prof F.E.C. Culick of CIT. Several practical improvements were made to this routine during shakedown, and after some experience, on the computer. The generalized Newton's procedure was then applied to obtain the basis for an ITF computer program. An outline of the analysis is provided in the following pages.

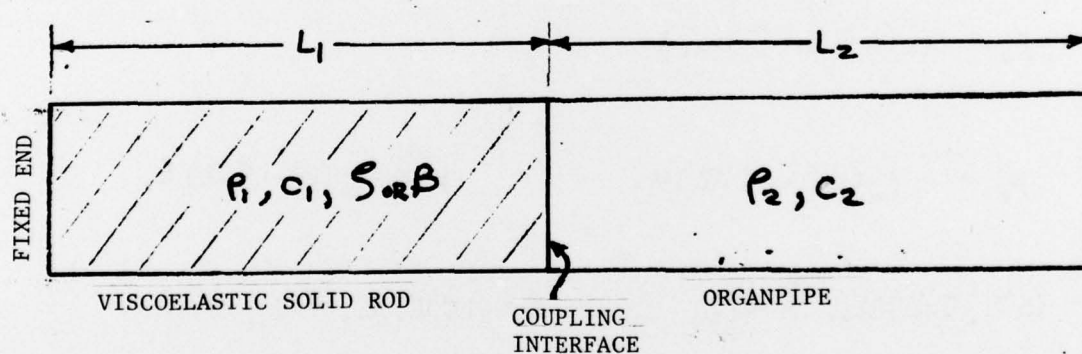


Figure B.H-1. Schematic of Rod-Organpipe

$$\text{Continuity} \quad \rho_t^{(a)} = -\rho_0 u_x \quad \epsilon = \epsilon_x \text{ \& } u = \epsilon_t \text{ so } \epsilon_t = u_x; \text{ also } \epsilon = -\frac{p}{\rho_0} \text{ so } \rho_t^{(f)} = -\rho_0 \epsilon_t \quad (1)$$

$$\text{Dynamic State} \quad p = c^2 \rho + \mathcal{S} \rho_t \quad c^2 = \frac{\mathcal{S} \rho_0}{\rho_0} \quad (2)$$

$$\text{Momentum} \quad \rho_0 u_t = -p_x \quad (3)$$

$$\text{Definition} \quad \Omega = \omega - i\alpha \quad (4)$$

$$\text{Linear System Characteristic} \quad \text{All variables} \sim e^{-i\Omega t} \quad (5)$$

$$(5) \quad u_t \quad u_t = -i\Omega u \quad (6)$$

$$(1), (2) \quad p_t = -\rho_0 (c^2 u_x + \mathcal{S} u_{xt}) \quad (7)$$

$$(6), (7) \quad p_t^{(a)} = -\rho_0 (c^2 - i\mathcal{S}\Omega) u_x \quad p^{(b)} = -\rho_0 (c^2 - i\mathcal{S}\Omega) \epsilon_x \quad (8)$$

$$(3)_t = -(8)_x \quad (c^2 - i\mathcal{S}\Omega) u_{xx} \stackrel{(a)}{=} u_{tt} \quad (c^2 - i\mathcal{S}\Omega) \epsilon_{xx} \stackrel{(b)}{=} \epsilon_{tt} + f(x) \quad (9)$$

$$(3)_x = -(8)_t \quad (c^2 - i\mathcal{S}\Omega) p_{xx} = p_{tt} \quad (10)$$

$$(5) \quad p_{tt} \quad p_{tt} = -\Omega^2 p \quad (11)$$

$$(11)=(10) \quad P_{xx} + \frac{\Omega^2}{(c^2 - i5\Omega)} \cdot P = 0 \quad (12)$$

$$\text{Definitions} \quad k = \frac{\Omega}{c} \quad , \quad \tau = \frac{5}{c^2} \quad (13)$$

$$(12), (13) \quad P_{xx} + \frac{k^2}{(1 - i5\Omega\tau)} P = 0 \quad (14)$$

$$\text{Hard B.C's. at } x=0, (L_1+L_2) \quad u^{(a)}(0) = u^{(b)}(L_1+L_2) = 0 \quad (15)$$

$$\text{Interface Conditions} \quad u^{(a)}(L_1^+) = u^{(b)}(L_1^-) \quad p^{(a)}(L_1^+) = p^{(b)}(L_1^-) \quad (16)$$

$$(14) \quad P_{1xx} + \frac{k_1^2 P_1}{(1 - i5\Omega\tau_1)} = 0 \quad 0 \leq x \leq L_1 \quad (17)$$

$$(14) \quad P_{2xx} + \frac{k_2^2 P_2}{(1 - i5\Omega\tau_2)} = 0 \quad L_1 \leq x \leq L \quad \text{where } L = L_1 + L_2 \quad (18)$$

$$\text{Definitions} \quad k_j = \frac{\Omega}{c_j} \quad , \quad \tau_j = \frac{5}{c_j^2} \quad , \quad K_j = k_j (1 - i5\Omega\tau_j)^{-\frac{1}{2}} \quad j=1,2 \quad (19)$$

$$\text{Bidir. Wave} \quad P_j = P_{j+} e^{+ik_j x} + p_{j-} e^{-ik_j x} \quad j=1,2 \quad (20)$$

$$(6), (3) \quad u = -i P_x / (e_0 \Omega) \quad (21)$$

$$(19), (21) \quad (20) \quad u_j = \frac{K_j}{e_0 \Omega} (P_{j+} e^{+ik_j x} - p_{j-} e^{-ik_j x}) \quad j=1,2 \quad (22)$$

$$(15), (22) \quad P_{1-} = P_{1+} = P_1 \quad P_{2-} = P_{2+} \cdot e^{2iK_2(L_1+L_2)} = P_2 \cdot e^{2iK_2(L_1+L_2)} \quad (23)$$



$$(23) \rightarrow (20) \quad p_1 = P_1 (e^{ik_1 x} + e^{-ik_1 x}) \quad p_2 = P_2 (e^{ik_2 x} + e^{-ik_2(x-2L)}) \quad (24)$$

$$(23), (24) \quad (20) \quad u_1 = \frac{\kappa_1 P_1}{\rho_1 \Omega} (e^{ik_1 x} - e^{-ik_1 x}) \quad u_2 = \frac{\kappa_2 P_2}{\rho_2 \Omega} (e^{ik_2 x} - e^{-ik_2(x-2L)}) \quad (25)$$

$$(16-a, b) \quad (24) \& \quad (25) \quad \frac{P_1}{P_2} = \frac{e^{ik_2 L_1} + e^{ik_2(2L_2+L_1)}}{e^{ik_1 L_1} + e^{-ik_1 L_1}} = \frac{(\rho_1 \kappa_2)}{(\rho_2 \kappa_1)} \frac{e^{ik_2 L_1} - e^{ik_2(2L_2+L_1)}}{e^{ik_1 L_1} - e^{-ik_1 L_1}} \quad (26)$$

$$\text{Rearrange (26)} \quad \frac{(e^{ik_1 L_1} - e^{-ik_1 L_1})}{(e^{ik_2 L_2} - e^{-ik_2 L_2})} \frac{(e^{ik_1 L_1} + e^{-ik_1 L_1})}{(e^{ik_2 L_2} + e^{-ik_2 L_2})} + \frac{(\rho_1 \kappa_2)}{(\rho_2 \kappa_1)} = 0 \quad (27)$$

$$\text{Trig. Form of (27)} \quad \frac{\tan(k_1 L_1)}{\tan(k_2 L_2)} + \left( \frac{\rho_1 \kappa_2}{\rho_2 \kappa_1} \right) = 0 \quad (28)$$

$$(4) \& (19-a) \quad (19-c) \quad K_j^{(a)} = \frac{\Omega / c_j}{\sqrt{1 - i\Omega \tau_j}} \stackrel{(b)}{=} \frac{(\omega - i\alpha) / c_j}{\sqrt{(1 - \alpha \tau_j) - i\omega \tau_j}} \stackrel{(c)}{=} \frac{(\omega - i\alpha) e^{i(\frac{\phi_j}{2})}}{c_j \sqrt{R_j}} \quad j=1, 2 \quad \text{where} \quad (29)$$

$$\text{Trig. Ident.} \quad \phi_j = \tan^{-1} \left( \frac{\omega \tau_j}{1 - \alpha \tau_j} \right) \quad \text{and} \quad \sqrt{R_j} = \left\{ (1 - \alpha \tau_j)^2 + (\omega \tau_j)^2 \right\}^{\frac{1}{4}} \quad j=1, 2 \quad (30)$$

$$(29) \quad j = 1, 2 \quad \frac{\rho_1 \kappa_2}{\rho_2 \kappa_1} = \frac{\rho_1 c_1}{\rho_2 c_2} \sqrt{\frac{R_1}{R_2}} e^{i(\phi_2 - \phi_1)/2} = \frac{\rho_1 c_1}{\rho_2 c_2} \sqrt{\frac{R_1}{R_2}} \text{cis} \left( \frac{\phi_2 - \phi_1}{2} \right) \quad (31)$$

$$\text{Expand 29} \quad K_j = \frac{1}{c_j \sqrt{R_j}} \left\{ [\omega \cos(\frac{\phi_j}{2}) + \alpha \sin(\frac{\phi_j}{2})] + i [\omega \sin(\frac{\phi_j}{2}) - \alpha \cos(\frac{\phi_j}{2})] \right\} \quad j=1, 2 \quad (32)$$

$$\text{Definitions} \quad Y_j^{(a)} = \frac{\omega \cos(\frac{\phi_j}{2}) + \alpha \sin(\frac{\phi_j}{2})}{c_j \sqrt{R_j}} \quad \& \quad X_j^{(b)} = \frac{\omega \sin(\frac{\phi_j}{2}) - \alpha \cos(\frac{\phi_j}{2})}{c_j \sqrt{R_j}} \quad j=1, 2 \quad (33)$$

$$(33) \rightarrow (32) \quad \tan(k_j L_j) = \tan(Y_j + iX_j) = \tan\{i(X_j - iY_j)\} = i \tanh\{X_j - iY_j\} \quad j=1,2 \quad (34)$$

$$\text{Definitions} \quad \tan(k_j L_j) = i(\theta_j - i\chi_j) \quad j=1,2 \quad \text{where} \quad (35)$$

$$(34), (35) \quad \theta_j = \frac{\sinh(2X_j)}{\cosh(2X_j) + \cos(2Y_j)} \quad \text{and} \quad \chi_j = \frac{\sin(2Y_j)}{\cosh(2X_j) + \cos(2Y_j)} \quad (36)$$

$$(31), (32), (35) \quad \frac{\theta_1 - i\chi_1}{\theta_2 - i\chi_2} + \left(\frac{P_1 C_1}{P_2 C_2}\right) \sqrt{\frac{R_1}{R_2}} \left\{ \cos\left(\frac{\phi_2 - \phi_1}{2}\right) - i \sin\left(\frac{\phi_2 - \phi_1}{2}\right) \right\} = 0 \quad (37)$$

& (36) in (28)

$$\text{Definition} \quad R = \left(\frac{P_1 C_1}{P_2 C_2}\right) \sqrt{\frac{R_1}{R_2}} \quad (38)$$

$$(33) \text{ R(37)} \quad \theta_1 + R \left\{ \theta_2 \cdot \cos\left(\frac{\phi_2 - \phi_1}{2}\right) + \chi_2 \cdot \sin\left(\frac{\phi_2 - \phi_1}{2}\right) \right\} = G_1(\alpha, f) = 0 \quad (39-a)$$

$$(33) \text{ Im(37)} \quad -\chi_1 + R \left\{ \theta_2 \cdot \sin\left(\frac{\phi_2 - \phi_1}{2}\right) - \chi_2 \cdot \cos\left(\frac{\phi_2 - \phi_1}{2}\right) \right\} = G_2(\alpha, f) = 0 \quad (39-b)$$

$$\text{Requirement} \quad \text{From estimate } F_0 = (\alpha_0, f_0) : G(F_0) \neq 0 \text{ find } \Delta F \text{ such that } G(F_0 + \Delta F) \stackrel{(c)}{=} 0 \quad (40)$$

$$\text{Definitions} \quad \Delta G \stackrel{(a)}{=} J \cdot \Delta F \quad \text{where} \quad J \stackrel{(b)}{=} \begin{bmatrix} G_{1\alpha} & G_{1f} \\ G_{2\alpha} & G_{2f} \end{bmatrix} \quad \text{and} \quad \Delta F \stackrel{(c)}{=} (\Delta\alpha, \Delta f) \quad (41)$$

$$G(F) \sim \text{Linear} \quad \text{Let } \Delta G = -G \quad \text{so} \quad G + \Delta G \stackrel{(b)}{=} G + J \cdot \Delta F \stackrel{(c)}{\approx} 0 \quad (42)$$

$$\text{Solve(42)} \quad \text{Then } \Delta F \stackrel{(a)}{\approx} -J^{-1} G \quad \text{and} \quad G(F) \approx 0 \quad \text{if} \quad F = F_0 - J^{-1} G. \quad (43)$$

This process is iterated, setting  $F_0 = F$  until  $G(F)$  is sufficiently small.

Defin.  $P_1(t) = \frac{P_0}{2} e^{-i\omega t}$  (44)

(24-a) & (44)  $P_1(x, 0) = P_0 \cdot \cos(k_1 x)$  (45)

(24-b), (26) & (44)  $P_2(x, 0) = P_0 \frac{\cos(K_1 L_1)}{\cos(K_2 L_2)} \cdot \cos[k_2(x-L)]$  (46)

(32) & (33)  $K_j = Y_j + i X_j$  (47)

$V_P = \frac{\omega}{K(K)}$  Phase Velocity =  $V_{Pj} = \frac{\omega}{Y_j}$   $j=1,2$  (48)

Trig-Hyp Identities  $\begin{cases} \cos(K_j L) = \cos\{i(X_j - iY_j)L\} = \cosh\{(X_j - iY_j)L\} \\ = \cosh(X_j L) \cdot \cos(Y_j L) - i \sinh(X_j L) \cdot \sin(Y_j L) \end{cases}$  (49)

$P_1(x, 0) = P_0 \cdot \{ \cosh(X_1 x) \cdot \cos(Y_1 x) - i \sinh(X_1 x) \cdot \sin(Y_1 x) \}$  (50)

(46), (49) & Defin.  $\left\{ \begin{array}{l} P_2(x, 0) = P_0 \frac{(A+iB)}{(C+iD)} (E+iH) = P_0 \frac{[(AC+BD)E + (AD-BC)H] + i[(AC-BD)H + (AD+BC)E]}{C^2 + D^2} \\ \text{where } \begin{array}{ll} A = \cosh(X_1 L_1) \cdot \cos(Y_1 L_1) & B = \sinh(X_1 L_1) \cdot \sin(Y_1 L_1) \\ C = \cosh(X_2 L_2) \cdot \cos(Y_2 L_2) & D = \sinh(X_2 L_2) \cdot \sin(Y_2 L_2) \\ E = \cosh[X_2(x-L)] \cdot \cos[Y_2(x-L)] & \\ H = \sinh[X_2(x-L)] \cdot \sinh[Y_2(x-L)] & \end{array} \end{array} \right. \quad (51)$

## SUBAPPENDIX B.I

## ANALYTICAL PROGRAM LISTING

```
00010 L1=10.000;  
00020 L2=10.000;  
00030 C1=6000.0;  
00040 C2=12000.0;  
00050 R01=1.6275E-4;  
00060 P=1500;  
00070 R02=1.1012E-5*P/1500;  
00080 RRO=10;  
00090 BET=.5;  
00100 A: PUT('      VAR0 VARE DVAR   F   ALP');  
00110 GET(VR0,VRF,DVR,FD,ALD);  
00120 IF(VRF<VR0 & DVR>0) DVR=-DVR;  
00130 PUT(' ');  
00140 ND=12;  
00150 DO VAR=VR0 TO VRF BY DVR;  
00160 RCL=VAR;  
00162 RCL=C2*L1/(C1*L2);  
00166 VRP=VAR;  
00168 RRC=RRO*C1/C2;  
00170 W=6.28318*FD;  
00180 ALP=ALD;  
00190 N=ND;  
00200 C: I=0;  
00210 DW=1;  
00220 DAL=1;  
00230 Q: I=I+1;  
00240 TST=0;  
00250 R: TAU=-BET/W;  
00260 FI1=ATAN(BET/(1-ALP*TAU));  
00270 FI2=0.0000;  
00280 SR1=SQRT(SQRT((1.000-ALP*TAU)**2+BET**2));  
00290 SR2=1.000;  
00300 X1=L1*(W*SIN(FI1/2.000)-ALP*COS(FI1/2.000))/(C1*SR1);  
00310 Y1=L1*(W*COS(FI1/2.000)+ALP*SIN(FI1/2.000))/(C1*SR1);  
00320 X2=L2*(W*SIN(FI2/2.000)-ALP*COS(FI2/2.000))/(C2*SR2);  
00330 Y2=L2*(W*COS(FI2/2.000)+ALP*SIN(FI2/2.000))/(C2*SR2);  
00340 XI1=COSH(2.00*X1)+COS(2.00*Y1);  
00350 TH1=SINH(2.00*X1)/XI1;  
00360 XI1=SIN(2.00*Y1)/XI1;  
00370 XI2=COSH(2.00*X2)+COS(2.00*Y2);  
00380 TH2=SINH(2.00*X2)/XI2;  
00390 XI2=SIN(2.00*Y2)/XI2;  
00400 F22=(FI2-FI1)/2.000;  
00410 C22=COS(F22);  
00420 S22=SIN(F22);  
00430 RZ=RRC*SR1/SR2;  
00440 E1=+TH1+RZ*(TH2*C22+XI2*S22);  
00450 E2=-XI1+RZ*(TH2*S22-XI2*C22);  
00460 IF TST>.5 GO TO S;  
00470 E10=E1;  
00480 E20=E2;  
00490 W0=W;  
00500 AL0=ALP;
```



```

00510 W=W+DW;
00520 TST=1;
00530 GO TO R;
00540 S: IF TST>1.5 GO TO T;
00550 E1W=(E1-E10)/DW;
00560 E2W=(E2-E20)/DW;
00570 W=W0;
00580 ALP=ALP+DAL;
00590 TST=2;
00600 GO TO R;
00610 T: IF TST>2.5 GO TO U;
00620 E1A=(E1-E10)/DAL;
00630 E2A=(E2-E20)/DAL;
00640 DET=(E1A*E2W-E1W*E2A);
00640 IF(DET=0) DET=2E-5;
00650 DAL=(E1W*E20-E10*E2W)/DET;
00660 DW=(E10*E2A-E1A*E20)/DET;
00670 ALP=AL0+DAL;
00680 W=W0+DW;
00690 ERS=.0002;
00695 RAL=ALP*RRR*100/(C2/L2);
00700 IF(ABS(DW/W)+ABS(DAL/ALP))<ERS GO TO U;
00710 IF 1<N-.5 GO TO Q;
00720 DF=DW/6.28318;
00730 F=W/6.28318;
00740 PUT EDIT(F,ALP,VRP,RCL,RAL,RZ,I)
00750 GO TO B;
00760 U: F=W/6.28318;
00770 RDF=(F-C2/(2*L2))*RRR*L2*1E4/C2;
00780 PUT EDIT(F,ALP,VRP,RCL,RAL,RDF,X1,Y1)
00790 B: FD=F;
00795 ALD=ALP;
00800 END;
00810 GO TO A;

```